Multi-Spherical Composite-Overwrapped Cryogenic Fuel Tanks for Hypersonic Aircrafts

Tapeinos, Ilias

DOI
10.4233/uuid:850a6ccc-7686-4536-8469-418691dc2dbb

Publication date
2019

Document Version
Final published version

Citation (APA)
Tapeinos, I. (2019). *Multi-Spherical Composite-Overwrapped Cryogenic Fuel Tanks for Hypersonic Aircrafts*. [Dissertation (TU Delft), Delft University of Technology]. https://doi.org/10.4233/uuid:850a6ccc-7686-4536-8469-418691dc2dbb

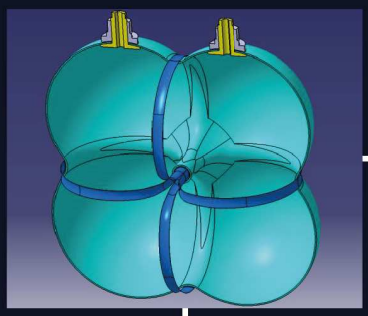

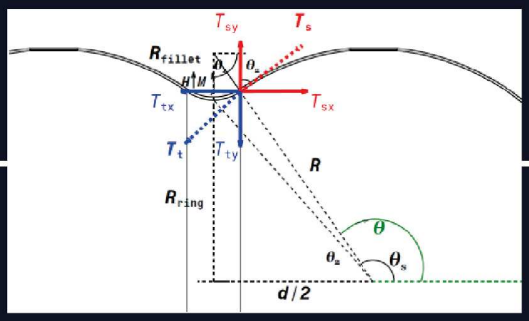

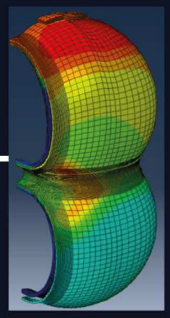

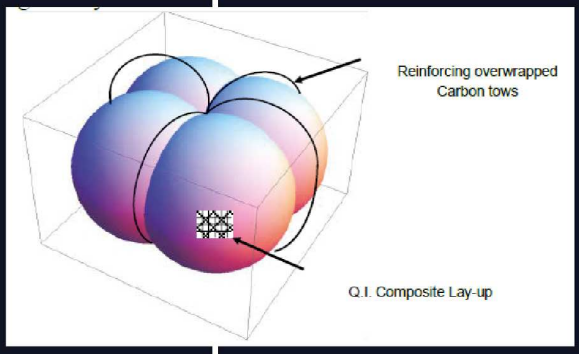

Multi-Spherical Composite-Ovewrapped Cryogenic Tanks for Hypersonic Aircrafts

Ilias Tapeinos

Multi-Spherical Composite-Overwrapped Cryogenic Fuel Tanks for Hypersonic Aircrafts

DISSERTATION

for the purpose of obtaining the degree of doctor at Delft University of Technology
by the authority of the Rector Magnificus prof.dr.ir. T.H.J.J. van der Hagen
chair of the Board for Doctorates to be defended publicly on

Thursday April 4, 2019 at 10:00 hours

by

Ilias TAPEINOS
Master of Science in Applied Mechanics, National Technical University of Athens, Greece
Born in Athens, Greece

This dissertation has been approved by the promotors.

Composition of the doctoral committee:

Rector magnificus,	Chair
Prof. dr. ir. R. Benedictus	Delft University of Technology, promotor
Dr. ir. S. Koussios	Delft University of Technology, copromotor

Independent members:

Prof. dr. S.C. Mantell	University of Minnesota, United States
Prof. dr. C. Kassapoglou	Delft University of Technology
Prof. dr. ir. R. Akkerman	University of Twente, Netherlands
Prof. dr. ir. W.A. Groen	Delft University of Technology

Other members:

Dr. ir. R.M. Groves	Delft University of Technology

This research was funded by the European Commission through the Cryogenic Hypersonic Advanced Tank Technologies (CHATT) Project.

Cover Design: K. Papamichou

ISBN:

Printed by: Ipskamp Printing (www.ipskampprinting.nl)

Summary

In the field of cryogenic storage, the medium inside the pressure vessel is in a liquid state and therefore cannot be further compressed. As a result, the storage tank should be designed in such a way, that it makes the best possible use of the available space (under a minimum weight) where it will be placed (e.g. within a reusable flight vehicle). Unlike conventional cylindrical pressure vessels, conformable pressure vessels provide an effective solution for this application in terms of volumetric and gravimetric efficiency. More specifically, conformable structures in the form of intersecting spheres (multi-sphere)-manufactured from composite materials- would be a beneficial configuration, since they can lead to weight savings associated with equal membrane strains when subjected to uniform pressure. Furthermore, because spheres have the minimum surface area for a given volume, they result in the minimization of passive heat in the tank and fuel boil-off, thus reducing the weight penalty associated with required thermal insulation thickness in cryogenic environments. Therefore a vessel configuration that incorporates partially merged spheres overwrapped with uni-directional (UD) carbon fiber straps applied at the merging points to introduce a uniform strain field would lead to a high volumetric efficiency at a low weight penalty.

The aim of this Dissertation is to increase the understanding of the behaviour of multi-spherical composite overwrapped pressure vessels (COPVs) with a polymeric liner under thermo-mechanical loading. This will enable the potential of multi-spherical COPVs to be examined for use as cryogenic fuel tanks.

Since the multi-sphere consists of merging shells, a stress analysis based on primary and secondary solutions at the sphere connecting areas (intersections) is sought. Mapping the stresses enables the derivation of the required number of UD straps to induce an equal strain field. In this work a method is presented to evaluate the exerted forces and bending moments uniformly distributed along the sphere/intersection boundary (junction) and to derive this required number of UD straps when the tank is loaded under internal pressure.

The geometric variables that control the design of a multi-spherical COPV and their effect on the laminate thickness at the intersections -needed for equal strain field at the cells- is hereby analysed. A method to evaluate the volumetric efficiency, weight and resulting performance of the multi-sphere is hereby presented. This enables a justification of whether the multi-sphere results in an enhancement of the volumetric efficiency and structural performance compared to packed cylinders when fitted in a prescribed box.

The effect of cryogenic chill-down, pressure cycling and draining on the thermal and structural response of the multi-sphere is analysed both numerically and experimentally. For the numerical part, a transient numerical thermo-mechanical model –based on Finite Elements (FE)- was developed that takes into account the temperature dependency of the liner and overwrap materials, as well as frost development at the outer surface and cryogen evaporation. A progressive failure algorithm was incorporated in the FE analysis to check the structural integrity of the liner and overwrap and to quantify the tank-pressure window under cryogenic operation. For the experimental part, hydrostatic burst testing at ambient conditions as well as pressure cycling at cryogenic conditions was performed by incorporating strain, temperature and damage accumulation monitoring techniques.

It is shown that a safe up-scale of the multi-sphere can be achieved for specific value intervals of the geometric variables and by following the strain compatibility principle, owing to the fact that the performance is nearly constant within these intervals. The structural performance and volumetric efficiency of the multi-sphere are linked in a stepwise linear inverse manner for increasing aspect ratio of the bounding box. In addition, the multi-sphere leads to a more

lightweight and volumetrically efficient tank configuration when fitted within a prescribed box compared to packed cylinders. It was shown both numerically and experimentally that localized cracking occurs in the liner at the central hollow cylinder throughout cryogenic chill-down, when employing polyamide (PA12) as the liner material. Therefore, polymer materials that can result in an intact liner throughout cryogenic operation need to be identified. However, the overwrap maintained its structural integrity, which along with the volumetric efficiency and weight savings can lead to the assumption that the multi-sphere can potentially be employed as a cryogenic fuel tank.

Samenvatting

Bij cryogene opslag is het medium binnenin het drukvat in vloeibare toestand en deze kan dus niet verder worden samengedrukt. Dientengevolge dient de opslagtank zo te worden ontworpen dat deze zo goed mogelijk gebruik maakt (tegen een minimum gewicht) van de beschikbare ruimte in de toepassing (bijv. binnenin een herbruikbaar vliegschip – RLV). Anders dan conventionele cilindrische drukvaten, bieden conformerende drukvaten een effectieve oplossing voor deze toepassing. Meer specifiek, conformerende constructies in de vorm van elkaar snijdende bollen – gemaakt van composiet materialen – zouden een gunstige configuratie zijn, aangezien zij kunnen leiden tot gewichtsbesparingen gerelateerd aan gelijke membraanrekken onder uniforme druk. Omdat bollen bovendien het minimale oppervlak voor een bepaald volume hebben, zorgen zij voor het minimaliseren van de passieve warmte in de tank en het verdampen van brandstof, en verminderen aldus de gewichtsbijdrage van de benodigde thermische isolatie voor de cryogene omgeving. Daarom zou een drukvat dat gedeeltelijk in elkaar geschaven bollen gecombineerd met omwikkelde unidirectionele (UD) koolstofvezel stroken (op de overlapspunten om een uniform rekveld te introduceren) leiden tot een hoge volumetrische efficiëntie tegen een laag gewicht.

Het doel van deze dissertatie is het vergroten van het begrip van het gedrag van multi-sferische composiet omwikkelde drukvaten (COPVs) met een polymeer voering onder thermo-mechanische belasting. Dit zal het mogelijk maken om het potentieel van multi-sferische COPVs als cryogene brandstoftanks te onderzoeken.

Aangezien de multi-sfeer bestaat uit samengesmolten schalen in elkaar geschaven, is een spanningsanalyse op basis van primaire en secondaire oplossingen bij de snijlijnen van de bollen (intersecties) gezocht. Het briellezen van de spanningen maakt het mogelijk om het benodigd aantal UD stroken voor een uniform verweld te bepalen. In dit werk is een methode gepresenteerd voor het evalueren van de kracht en het buigend moment langs de bol/intersectie grens (naad) die geschikte verplaatsing en verdraaiing compatibiliteit verzekert bij belasting volgens interne druk.

De geometrische variabelen die het ontwerp beheren van een multi-sferische COPV en hun effect op de laminaatdikte ter hoogte van de intersecties – benodigd voor een gelijk rekveld bij de cellen – is hiernevens geanalyseerd. Een methode om de volumetrische efficiëntie, het gewicht en de resulterend prestatie van de multi-sfeer af te leiden is hiernevens gepresenteerd. Dit maakt het mogelijk om te verdedigen of de multi-sfeer resulteert in het verbeteren van de volumetrische efficiëntie en zijn gewicht in vergelijking met gestapelde cilinders binnen een voorgeschreven inbouw ruimte.

Het effect van het cryogeen afkoelen, druk cycli en leegmaken op de thermische en structurele reactie van de multi-sfeer is zowel numeriek als experimenteel geanalyseerd. Voor het numerieke deel, is een transient numeriek thermisch-mechanisch model – gebaseerd op eindige elementen (FE) – ontwikkeld die tevens de temperatuurafhankelijkheid van de voering en de omwikkelde materialen, bevriezing op het buitenoppervlak en verdamping van de cryogene stof in beschouwing neemt. Een progressief bezwijkingsalgoritme was in de FE analyse geimplementeerd om de structurele integriteit van de voering en de omwikkeld materialen te verifiëren en om de drukgrenzen bij cryogeen gebruik te kwantificeren. Voor het experimentele deel zijn hydrostatische barsttesten bij omgevingscondities uitgevoerd en drukcycli doorlopen bij cryogene condities, beide met rek, temperatuur en schade accumulatie waarnemingstechnieken.

Er is aangetoond dat het opschalen van de multi-sfeer veilig kan plaatsvinden voor specifieke intervallen van de geometrische variabelen en dat door het rekcompatibiliteitsprincipe te volgen,

de prestatie vrijwel constant is binnen deze intervallen. De structurele prestatie en volumetrische efficiëntie van de multi-sfeer zijn gekoppeld op een stapsgewijze lineair-inverse wijze voor toenemende slankheidsverhoudingen van het omvattende inbouw ruimte. Bovendien leidt de multi-sfeer tot een lichtere en volumetrisch efficiëntere tankconfiguratie passend binnen een voorgeschreven inbouw ruimte in vergelijking met gestapelde cilinders. Het is zowel numeriek als experimenteel aangetoond dat lokale scheurgroei plaatsvindt in de voering bij de centrale holle cilinder gedurende cryogeen afkoelen wanneer polyamide (PA12) als voeringsmateriaal wordt gebruikt. Om die reden dienen polymeermaterialen die voor een intacte voering gedurende cryogene operatie kunnen zorgen te worden geïdentificeerd. De omwikkeling behield echter zijn structurele integriteit, wat samen met de volumetrische efficiëntie en gewichtsbesparing kan leiden tot de weloverwogen aanname dat de multi-sfeer potentieel gebruikt kan worden als een cryogene brandstoftank in de luchtvaart.

Nomenclature

Abbreviations

AE	Acoustic Emission
AIAA	American Institute of Aeronautics and Astronautics
ANSI	American National Standards Institute
APU	Auxiliary Power Unit
ASME	American Society of Mechanical Engineers
ASTM	American Society for Testing and Materials
BMDO	Ballistic Missile Defence Organization
BPVC	Boiler and Pressure Vessel Code
CAD	Computer-Aided-Design
CFD	Computational Fluid Dynamics
CFRP	Carbon-Fiber Reinforced Plastic
CH_4	Methane
CLT	Classical Lamination Theory
CO	Carbon Monoxide
CO_2	Carbon Dioxide
COPV	Composite-Overwrapped Pressure Vessel
CTE	Coefficient of Thermal Expansion
DC-X	Delta-Clipper Experimental
DIC	Digital Image Correlation
DOT	Department of Transportation (USA)
ET	External Tank
FBGs	Fiber Bragg Gratings
FEA	Finite Element Analysis
FPF	First Ply Failure
FRP	Fiber Reinforced Polymer
FV	Field Variable
GFRP	Glass-Fiber Reinforced Polymer
GH_2	Gaseous Hydrogen
GN_2	Gaseous Nitrogen
IM	Intermediate Modulus
IPC	Industrial Personal Computer
LEO	Low Earth Orbit
LBB	Leak-Before-Burst failure mode
LH_e	Liquid Helium
LH_2	Liquid Hydrogen

LN_2	Liquid Nitrogen
LNG	Liquefied Natural Gas
LO_2	Liquid Oxygen
MECO	Main Engine Cut-Off
MIE	Minimum Ignition Energy
MIL-STD	United States Military Standard
MLI	Multi-Layer Insulation
NASA	National Aeronautics and Space Administration
NDT	Non-Destructive Testing
NO_x	Nitrogen Oxides
PA	Polyamide
PC	Polycarbonate
PE	Polyethylene
PFA	Progressive Failure Analysis
PMMA	Polymethylmethacrylate
PP	Polypropylene
PS	Polystyrene
PTFE	Polytetrafluoroethylene (Teflon)
QI	Quasi-isotropic laminate
RLV	Reusable Launch Vehicle
RT	Room Temperature
RVE	Representative Volume Element
RVT	Reusable Vehicle Test
SDV	Solution-dependent variable
SSRT	Single-Stage Rocket Technology
SSTO	Single-Stage-To-Orbit vehicle
UD	Uni-directional
USDFLD	User Defined Field subroutine

Matrices & Vectors

$\mathbf{A}_{\text{sphere}}$	Extensional laminate stiffness matrix at the sphere
$\mathbf{A}_{\text{sphere}}(T)$	Extensional laminate stiffness matrix at the sphere as a function of temperature
$\mathbf{A}_{\text{torus}}$	Extensional laminate stiffness matrix at the intersection
$\mathbf{A}_{\text{torus}}(T)$	Extensional laminate stiffness matrix at the intersection as a function of temperature
$\mathbf{C}_{\text{lam}}$	Laminate stiffness matrix
$\mathbf{C}_{\text{o}}$	Layer stiffness matrix
$\mathbf{C}_{[0^o]}, \mathbf{C}_{[\pm 45^o]}$	Transformed (reduced) stiffness matrix of $[0^o]$ and $[\pm 45^o]$ plies respectively
$\mathbf{C}_{[\varphi]_k}$	Transformed (reduced) layer stiffness matrix

$\mathbf{C}_{[\varphi]_k}(T)$	Transformed (reduced) stiffness matrix of layer κ as a function of temperature
$\mathbf{D}_{\text{sphere}}$	Bending laminate stiffness matrix at the sphere
$\mathbf{D}_{\text{torus}}$	Bending laminate stiffness matrix at the intersection
$\mathbf{D}_{\text{torus}}(T)$	Bending laminate stiffness matrix at the intersection as a function of temperature
$\mathbf{e}_{\text{free}}^{[0^o]}, \mathbf{e}_{\text{free}}^{[90^o]}$	Free expansion strain vector for [0^o] and [90^o] ply
$\mathbf{M}_{\text{junction}}^{\text{T}}$	Thermal moment vector at the intersection
$\mathbf{M}_{\text{junction}}$	Mechanical moment vector at the intersection
$\mathbf{N}_{\text{junction}}$	Mechanical forces vector at the intersection
$\mathbf{N}_{\text{junction}}^{\text{T}}$	Thermal forces vector at the intersection
$\mathbf{N}_{\text{sphere}}$	Mechanical forces vector at the sphere
$\mathbf{N}_{\text{sphere}}^{\text{T}}$	Thermal forces vector at the sphere
$\mathbf{S}_{\text{lam}}$	Laminate compliance matrix
$\mathbf{T}_{[\varphi]_k}$	Transformation matrix of *k* ply
$\boldsymbol{\varepsilon}_{\varphi,\theta\_\text{junction}}^{[k]}(T,P)$	Strain vector at the intersection of ply *k* in the laminate coordinate system (φ,θ,φθ) due to *P* and ΔT
$\boldsymbol{\varepsilon}_{1,2\_\text{junction}}^{[k]}(T,P)$	Strain vector at the intersection of ply *k* in the material axis system due to *P* and ΔT
$\boldsymbol{\varepsilon}_{\varphi,\theta\_\text{sphere}}^{[k]}(T,P)$	Strain vector at the sphere of ply *k* in the laminate coordinate system (φ,θ,φθ) due to *P* and ΔT
$\boldsymbol{\varepsilon}_{1,2\_\text{sphere}}^{[k]}(T,P)$	Strain vector at the sphere of ply *k* in the material axis system due to *P* and ΔT
$\boldsymbol{\varepsilon}_{\text{junction}}$	Strains vector at the laminate at the sphere/intersection boundary
$\boldsymbol{\varepsilon}_{\text{sphere}}$	Strains vector at the laminate at the sphere
$\boldsymbol{\sigma}_{1,2\_\text{junction}}^{[k]}(T,P)$	Stress vector at the intersection of ply *k* in the material axis system due to *P* and ΔT
$\boldsymbol{\sigma}_{1,2\_\text{sphere}}^{[k]}(T,P)$	Stress vector at the sphere of ply *k* in the material axis system due to *P* and ΔT

Mathematical Operations & Derivatives

∇T	Temperature gradient
·	Vector inner product

Scalars (Latin)

a	Approximation function constant Spline coefficient

A_{cap}	Cross-sectional area formed by the fillet radius at the intersection
A_{liner}	Cross-sectional area of liner at central hollow cylinder
$A_{triangle}$	Cross-sectional area of the triangle formed at the intersection
A_{UD}	Cross-sectional area of UD strap
a_{ratio}	Box aspect ratio (l_{box}/w_{box})
$a_{[0o]}$	Required number of [0^o] layers at the intersection of the multi-sphere
$2a_{[\pm\varphi]}$	Required number of [$\pm\varphi$] layers at the intersection of the multi-sphere
	Approximation function constant
b	Distance between the two junctions
	Spline coefficient
B_F	Burst factor
$BOR_{allowable}$	Allowable hourly fuel boil-off of the cryogenic propellant
BOR_{multi}	Hourly cryogenic propellant boil-off in the multi-bubble
$BOR_{cycling}$	Boil-off rate throughout pressure cycling at the multi-sphere
	Polar opening radius
c	Approximation function constant
	Spline coefficient
C_1, C_2, C_3, C_4	Constants of integration to be evaluated based on BCs at the spherical cell edge
C_{RT}^{E}	Constant used for calculation of strain-rate dependency of ply engineering properties
C_{RT}^{S}	Constant used for calculation of strain-rate dependency of ply strength allowables
$Cp_{N2vapour}$	Specific heat capacity of nitrogen vapour at constant pressure
d	Centroid distance at the multi-sphere
	Spline coefficient
dP	Pressure difference between first damage onset (P_{FPF}) and global failure (P_{LPF})
dP_fast_FE	Pressure difference between P_{FPF} and P_{LPF} of the multi-sphere when loaded at a high pressure rise rate (from FE analysis)
dP_fast_exp	Pressure difference between P_{FPF} and P_{LPF} of the multi-sphere when loaded at a high pressure rise rate (from experiment)
dP_slow_FE	Pressure difference between P_{FPF} and P_{LPF} of the multi-sphere when loaded at a low pressure rise rate (from FE analysis)
dP/dt	Pressure rise rate
$d_{\varphi torus}, d_{\theta torus}, d_{\varphi\theta torus}$	Bending laminate compliance at the intersection in the meridional (φ), hoop (θ) and in-plane shear (φθ) directions
e	Spline coefficient
E_{11}	Tensile modulus of a composite layer parallel to the fibers
E_{22}	Tensile modulus of a composite layer transverse to the fibers
E_{f1}	Fiber modulus of elasticity
$E_{\varphi torus}$	Equivalent laminate modulus at the multi-sphere junction in the meridional direction
$E_{\theta torus}$	Equivalent laminate modulus at the multi-sphere junction in the hoop direction

E_{liner}	Young's modulus of the liner material
$E_{\text{RT}[0^o,45^o,90^o]}$	Strain rate adjusted ply modulus at orientations [0^o], [45^o] and [90^o] at tensile or compression loading
$E_{\text{o}[0^o,45^o,90^o]}$	Quasi-static ply modulus at orientations [0^o], [45^o] and [90^o] at tensile or compression loading
E_{sphere}	Equivalent laminate membrane modulus at the sphere
$E^{\text{b}}_{\theta\text{sphere}}$	Equivalent laminate bending modulus in the hoop direction at the sphere
$E^{\text{b}}_{\varphi\text{sphere}}$	Equivalent laminate bending modulus in the meridional direction at the sphere
$E_{\varphi\text{torus}}, E_{\theta\text{torus}}$	Equivalent laminate membrane modulus at the intersection in the meridional (φ) and hoop (θ) directions
f	Spline coefficient
F_{ij}	View factor
g	Gravitational acceleration
G_{12}	In-Plane shear modulus of a composite layer
G_{23}	Out-of-Plane shear modulus of a composite layer
h	Height of triangle formed when filleting the intersection
H	Edge force at sphere/intersection junction
h_{box}	Height of the prescribed box
h_{cap}	Height of the spherical caps at the intersections
h_{center}	Height of the spherical cap in the tank center
H_{coefrot}	Edge rotation coefficient for the toroidal shell due to edge force (H)
h_{e}	Specific enthalpy of the incoming GN_2 in the system
h_{fg}	Specific enthalpy of the saturated vapor
h_{inter}	Intersection spherical cap height
$h_{\text{interface}}$	Thermal contact conductance
h_{junction}	Height from centroid to junction point
h_{LN2}	Liquid boiling heat transfer coefficient
h_{out}	Free convection heat transfer coefficient
h_{tip}	Height at intersection axis from centroid to intersection tip
h_{vapour}	Heat transfer coefficient at the vapour region
i_{ratio}	Ratio between [0^o] and angle-ply layers at intersection
k	Thermal conductivity
K_1	Tank design safety factor associated to external loading
K_2	Tank design safety factor associated to thermal stresses
K_3	Tank design safety factor associated to pressure-induced stresses
k_{11}	Thermal conductivity of a composite ply parallel to the fibers
k_{22}	Thermal conductivity of a composite ply transverse to the fibers
k_{air}	Thermal conductivity of air
k_{comp}	Thermal conductivity of the composite overwrap
k_{e}	Material orthotropy parameter

k_{edge}	Spherical edge parameter
k_{frost}	Conductivity of frost layer
k_g	internal heat exchange coefficient between the wall and the gas
k_{ins}	Thermal conductivity of the thermal insulation material
$k_{overlap}$	Hoop ring overlapping parameter
L	Actual length of cylindrical part of the cylindrical COPV
l_{box}	Length of the prescribed box
l_{cyl}	Length of the central hollow tube at the multi-sphere
L_{hoop}	Dimensionless length of the hoop windings
L_{polar}^{c}	Dimensionless length of the polar windings at the cylindrical part of the COPV
L_{polar}^{d}	Dimensionless length of the polar windings at the dome of the COPV
L_{polar}	Total dimensionless length of the polar windings
$\dot{m}$	Mass flow rate
M	Bending moment at the sphere/intersection junction
m_{cells}	Number of spheres in the longitudinal/axial direction at the multi-sphere
$m_{cylcells}$	Number of cylinders in the axial direction of the cylindrical COPV
$M_{coefrot}$	Edge rotation coefficient for the toroidal shell due to edge bending moment (M)
M_{cryo}	Total multi-sphere COPV mass (with insulation)
m_g	Mass of GN_2 within the tank
M_{hoop}	Mass of the hoop windings
$M_{insulation}$	Thermal insulation mass
$M_{intersection}$	Mass of one intersection at the multi-sphere
M_{polar}	Mass of the polar windings
$M_{structural}$	Mass of the composite overwrap at the multi-sphere
M_{strcyl}	Mass of the composite overwrap at the cylindrical COPV
$multi_{cells}$	Total number of spheres at the multi-sphere
$multi_{centers}$	Total number of junction meeting points at the multi-sphere
$multi_{junctions}$	Total number of junctions at the multi-sphere
M_θ	Hoop membrane moment
M_φ	Meridional membrane moment
$M_{\varphi\theta}$	Shear membrane moment
n_{cells}	Number of spheres in the transverse direction at the multi-sphere
$n_{cylcells}$	Number of cylinders in the transverse direction of the cylindrical COPV
n_{hoop}	Required number of hoop windings at the cylindrical COPV
n_{PF}	Structural performance of a pressure vessel
n_{polar}	Required number of polar windings at the cylindrical COPV
n_x,n_z, n_{radial}	Acceleration in x, z and radial directions

$N_{\varphi}, N_{\theta}, N_{\varphi\theta}$	Meridional (φ), hoop (θ) and in-plane shear (φθ) forces
$N_{\varphi junction}$	Meridional membrane force at the sphere/intersection junction due to pressure
$N_{\theta junction}$	Hoop membrane force at the sphere/intersection junction due to pressure
P	Internal pressure
P_{bottom}	Pressure at the bottom of the tank
$P_{\varphi crit}$	Buckling pressure of the intersection at the meridional direction
$P_{\theta crit}$	Buckling pressure of the intersection at the hoop direction
$P_{coefrot}$	Edge rotation coefficient for the toroidal shell due to pressure (P)
p_{cells}	Number of spheres in the height direction at the multi-sphere
P_{FPF}	Pressure at first ply failure
P_{FPF_fast}	Pressure at first ply failure under high pressure rise rate
P_{FPF_slow}	Pressure at first ply failure under low pressure rise rate
P_{LPF}	Pressure at last ply failure
P_{LPF_fast}	Pressure at last ply failure under high pressure rise rate
P_{LPF_slow}	Pressure at last ply failure under low pressure rise rate
P_{MEOP}	Maximum expected operating pressure
P_{proof}	Proof pressure
p_{φ}, p_{θ} , p_{r}	Pressure in the meridional (φ), hoop (θ) and radial (r) directions respectively
P_{ull}	Pressure at the ullage region
$P(x), P'(x), P''(x)$	Function of intersection shape coordinate, tangency and curvature respectively
Q	Heat leakage
Q_{θ}	Edge shear force at the sphere/intersection junction
q_{cond}	Conductive heat flux at the surface of a tank wall layer
q_{conv}	Convective heat flux at the surface of a tank wall layer
q_{rad}	Radiative heat flux between two surfaces of two tank wall layers
R	Sphere radius Gas constant
r	Dimensionless fillet radius of the multi-sphere intersection
R_{cryo}	Sphere radius after the addition of a thermal insulation layer
r_{cyl}	Radius of the central hollow tube at the multi-sphere
R_{cyl}	Radius of cylindrical COPV
$R_{cylcryo}$	Radius of cylindrical COPV after the addition of a thermal insulation layer
R_{fillet}	Intersection fillet radius
R_{in}	Liner inner surface
R_{m}	Radius of curvature at the meridional direction
R_{out}	Liner outer surface
R_{p}	Radius of curvature at the parallel direction
R_{ring}	Intersection radius
$R_{ringfinal}$	Spheres Intersection radius with fillet radius correction
s	Width of the hoop ring

S	In-plane shear strength of composite ply Total surface area of the multi-sphere
S_{c}	Surface area of the cylinder of the cylindrical COPV
S_{centers}	Surface area of all the 3D lenses in the junction meeting points
S_{cryo}	Surface area of the multi-sphere after the addition of a thermal insulation layer
S_{CylCOPV}	Total surface area of the cylindrical COPV
$S_{\mathrm{cylinders}}$	Surface area of all the hollow cylinders at the multi-sphere
S_{dome}	Surface area of the dome of the cylindrical COPV
S_{external}	Tank stresses associated to external loading
S_{F}	Safety factor
S_{fillets}	Surface area of all the junctions
S_{i}	Internal surface of the tank in contact with gas
S_{lenses}	Surface area of the enclosed spherical caps in all the junctions
$S_{\mathrm{lensjunction}}$	Surface area of the enclosed spherical caps in one junctions
S_{pressure}	Tank stresses associated to internal pressure
$S_{\mathrm{o}[0^{\mathrm{o}},45^{\mathrm{o}},90^{\mathrm{o}}]}$	Quasi-static ply strength at orientations [0^{o}], [45^{o}] and [90^{o}] at tensile or compression loading
$S_{\mathrm{RT}[0^{\mathrm{o}},45^{\mathrm{o}},90^{\mathrm{o}}]}$	Strain rate adjusted ply strength at orientations [0^{o}], [45^{o}] and [90^{o}] at tensile or compression loading
S_{spheres}	Surface area of the spheres
$S_{\mathrm{spherescenter}}$	Common surface area in the meeting point of four intersections
$S_{\mathrm{spheresfillet}}$	Surface area of all the spherical segments subtracted due to filleting an intersection
S_{thermal}	Tank stresses associated to thermal loading
S_{torus}	Surface area of one intersection
t	Shell thickness Time
T	Temperature at any point of solid, gaseous or liquid medium
$T_{1,2}$	Temperature of a surface
T_{ex}	Ambient temperature
T_{frost}	Temperature at frost layer
T_{g}	Glass transition temperature
T_{in}	Temperature at liner inner surface
t_{ins}	Thickness of the thermal insulation layer
t_{junction}	Junction thickness
t_{liner}	Liner thickness
T_{s}	Temperature at the surface of the outer tank wall
t_{ply}	Thickness of a composite layer
t_{polar}	Dimensionless polar roving thickness
T_{sy}	Vertical membrane force component at the sphere
T_{ty}	Vertical membrane force component at the torus

T_{vapor}	Vapor temperature
T_{wi}	Temperature of the wall in contact with the gas
U	Overall tank coefficient of heat transfer of the tank wall
UTS_{liner}	Liner ultimate tensile strength
v	Air kinematic viscosity
V	Multi-sphere internal volume Angle of edge rotation
V_{box}	Volume of prescribed box
V_c	Volume of the cylinder of the cylindrical COPV
$V_{centers}$	Volume of all the 3D lenses in the junction meeting points
$V_{centerlens}$	Common volume to lenses in the meeting point of four intersections
V_{cryo}	Multi-sphere internal volume after the addition of the thermal insulation layer
$V_{cylinder}$	Volume of one central hollow tube at the multi-sphere
$V_{cylinders}$	Total volume of all the central hollow tubes at the multi-sphere
$V_{CylCOPV}$	Total volume of the cylindrical COPV
$V_{CylCOPV\_cryo}$	Total volume of the cylindrical COPV after the addition of the thermal insulation layer
V_{dome}	Volume of the dome of the cylindrical COPV
V_{eff}	Volumetric efficiency of a pressure vessel within a prescribed box
v_f	Specific volume of saturated LN_2
v_{fg}	Specific volume of saturated vapour
$V_{fillets}$	Added volume from filleting the junctions at the multi-sphere
V_{lenses}	Volume of all the 3D lenses at the multi-sphere junctions
V_{min}	Required fuel volume
V_{sH}, V_{sM}, V_{sP}	Angle of rotation at the edge of the spherical cell due to *H*, *M* and *P* respectively
V_{stotal}	Total angle of rotation at the edge of the spherical cell
$V_{spheres}$	Volume of spheres at the multi-sphere
V_{tH}, V_{tM}, V_{tP}	Angle of rotation at the edge of the toroidal cell due to *H*, *M* and *P* respectively
V_{ttotal}	Total angle of rotation at the edge of the toroidal cell
$v_{xytorus}$	Major Poisson's ratio of laminate at intersection
w_{box}	Width of the prescribed box
W	Weight
X_c	Longitudinal compressive strength of composite ply
X_t	Longitudinal tensile strength of composite ply
y	Dimensionless centroid distance at the multi-sphere
Y	Dimensionless radius coordinate of the dome in the cylindrical COPV
Y_{min}	Minimum dimensionless radius coordinate of the dome in the cylindrical COPV
Y_c	Transverse compressive strength of a composite ply
Y_{eq}	Dimensionless ratio of the radius of the equator and polar opening radius in the

	cylindrical COPV
Y_t	Transverse tensile strength of composite ply
z	Thickness coordinate in a laminate
Z	Dimensionless height coordinate of the dome in the cylindrical COPV
z_κ	Distance of ply κ from the mid-plane of a laminate

Scalars (Greek)

α	Winding angle over the dome of the cylindrical COPV
α_o	Coefficient of thermal expansion of the composite ply or liner at [0^oC]
α_{11}	Coefficient of thermal expansion of a composite ply parallel to the fibers
α_{22}	Coefficient of thermal expansion of a composite ply transverse to the fibers
α_{comp}	Coefficient of thermal expansion of the composite laminate
α_{liner}	Coefficient of thermal expansion of the liner material
α_{QI}	Thermal expansion coefficient of quasi-isotropic laminate at the sphere
α_{torusL}	Thermal expansion coefficient of laminate at intersection in longitudinal direction
α_{torusT}	Thermal expansion coefficient of laminate at intersection in transverse direction
β_{GN2}	Thermal expansion coefficient of GN_2
γ_{cyl}	Angle relative the intersection axis and liner connecting centroid and cylinder
δ	Air gap between liner and composite overwrap
ΔH_{vapLN2}	Enthalpy of vaporization of LN_2
ΔT	Temperature change
ΔT_1	Temperature change at the internal liner surface
ΔT_2	Temperature change at the external liner surface
ε	Emissivity of surface
$\varepsilon_{\theta\theta inter}$	Common strain of overwrap and liner at central cylinder region
$\dot{\varepsilon}$	Effective strain rate
$\dot{\varepsilon}_o$	Reference strain rate
$\varepsilon_\varphi, \varepsilon_\theta, \varepsilon_{\varphi\theta}$	Strain in meridional (φ), hoop (θ) and in-plane shear (φθ) directions
ε_{sphere}	Strain at the sphere in the meridional/hoop directions
$\varepsilon_{ultliner}$	Elongation at break
ε_{xt}	Ultimate longitudinal tensile strain of composite ply
ε_{yt}	Ultimate transverse tensile strain of composite ply
$\varepsilon_{\varphi junction}$	Strain at the sphere/intersection junction in the meridional direction
$\varepsilon_{\theta junction}$	Strain at the sphere/intersection junction in the hoop direction
θ_1	Angle between intersection axis and line connecting sphere and fillet centroids
θ_2	Angle between sphere tangent and intersection axis
θ_{memb}	Angle where secondary loads become negligible
θ_{reinf}	Angle relative to UD strap arc length

θ_s	Angle relative to horizontal intersection axis and line connecting sphere and fillet radius centroids
κ	Ply number within the laminate
$\kappa_{\varphi junction}$	Curvature at the sphere/intersection junction in the meridional direction
$\kappa_{\theta junction}$	Curvature at the sphere/intersection junction in the hoop direction
$\kappa_{\varphi\theta junction}$	Curvature at the sphere/intersection junction in the in-plane shear direction
Λ	Dimensionless length parameter of the cylinder in the cylindrical COPV
μ	Dimensionless distance from intersection tip to sphere/intersection junction
ν_{12}	Major Poisson's ratio of a composite layer
ν_{21}	Minor Poisson's ratio of a composite layer
ν_{f12}	Poisson's ratio of fiber
$\nu_{\varphi\theta sphere}$	Major Poisson's ratio of the sphere
$\nu_{\varphi\theta torus}$	Major Poisson's ratio of the intersection
ρ_{comp}	Density of the composite material
ρ_{frost}	Density of frost
ρ_{ins}	Density of the thermal insulation material
σ	Stefan-Boltzmann constant
$\sigma_{allowable}$	Strength allowable of a quasi-isotropic lay-up
σ_1, σ_2, τ_{12}	Stress in a composite ply in the parallel, transverse to fibers and in-plane shear directions
σ_{ii}	Stress at the liner in the *ii* direction
σ_{fa}	Fiber strength
σ_{liner_in}, σ_{liner_out}	Stress at the inside and outside surface of the liner at the central hollow tube
σ_{ult}	Strength allowable
φ_k	Angle of a composite layer *k*
φ_o	Initial angle of a composite layer in a quasi-isotropic laminate

Contents

Chapter 1: Introduction

1.1 Need for Green Aviation: Liquid Hydrogen as Fuel

Over the last few decades, the issues of developing a low emission economy and de-carbonization have been of primary concern in the aviation transport sector, as highlighted by the European Commission in 2010 [1]. Air traffic is expected to have an annual growth of 4-5 [%] over the next decades [2] and the associated environmental impact of conventional aviation hydrocarbon fuel is predicted to be substantial. The pollutants from current aircraft engines (carbon dioxide-CO_2, carbon monoxide-CO, oxides of nitrogen-NO_x,etc., see Fig. 1-1), contribute to the deterioration of local air quality. While aircraft emissions represent only a fraction of the global atmospheric pollution footprint (1-2 [%] percent [3]), their impact on the environment cannot be neglected [4].

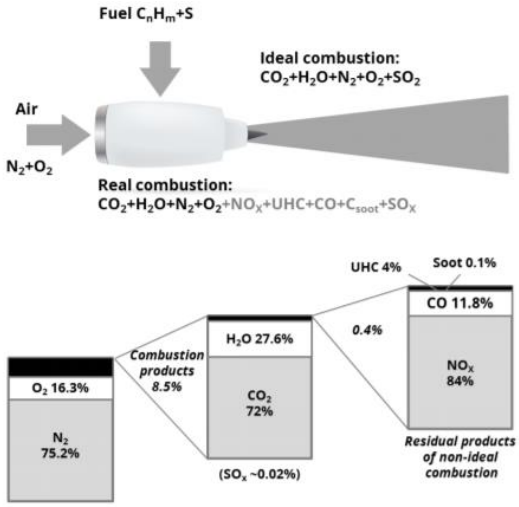

Fig. 1-1: Emissions released during aircraft fuel consumption [5].

Hydrogen (H_2) is an outstanding candidate for an environmentally acceptable future aviation fuel [4]. The gravimetric energy density (heat content per mass unit-MJ/kg) of gaseous hydrogen (GH_2) is 3 times higher than that of kerosene (JP-8), making it ideal for long duration flights [6].

The volumetric energy density (heat content per volume unit-MJ/L) of GH_2 is roughly a quarter of kerosene (Fig. 1-2) and thus the storage of sufficient amounts of hydrogen in fuel tanks becomes the most significant problem regarding its utilization in aviation [6]. The volumetric energy density of hydrogen can be increased by compression or liquefaction. Despite the weight penalty of the fuel tank insulation required to keep Liquid Hydrogen (LH_2) below its boiling point (-253 [^oC]), LH_2 has a two-fold higher volumetric energy than GH_2 when pressurized at 700 [bar] and a three-fold higher volumetric energy than GH_2 when pressurized at 350 [bar] [7].

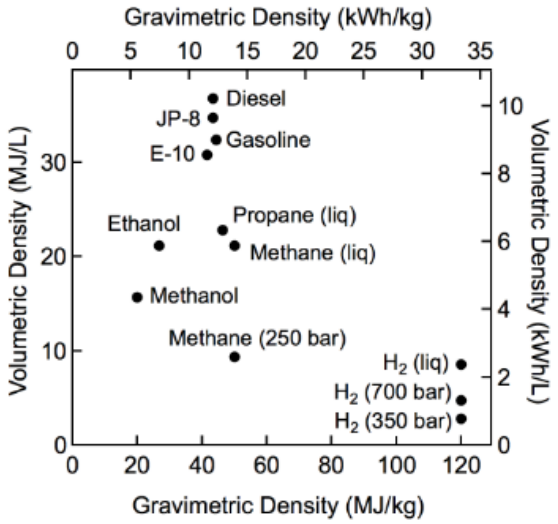

Fig. 1-2: Gravimetric and volumetric energy densities of common fuels based on lower heating values calculated for ambient temperature conditions [8].

Given the greater payload and lower carbon emissions linked to LH_2 use, liquid hydrogen-fueled vehicles are considered an excellent alternative to today's conventional fuel-powered vehicles [9], and sub-sonic aircrafts [10].

In the attempt to transition from kerosene to hydrogen-fueled aircrafts, the Cryoplane Project [11] analyzed different aircraft configurations by varying the position of the LH_2 tank. Fig. 1-3 depicts two promising configurations for LH_2 utilization from this study: a blended wing body and a twin-boom configuration. The hydrogen tanks are depicted in blue. In this study it was shown that Concept (a) is not suitable for pressure vessel application, due to the cylindrical shape of the fuel tanks – resulting in a relatively large unused volume. Furthermore, it was proven for Concept (b) that large external tanks lead to high profile and interference drag.

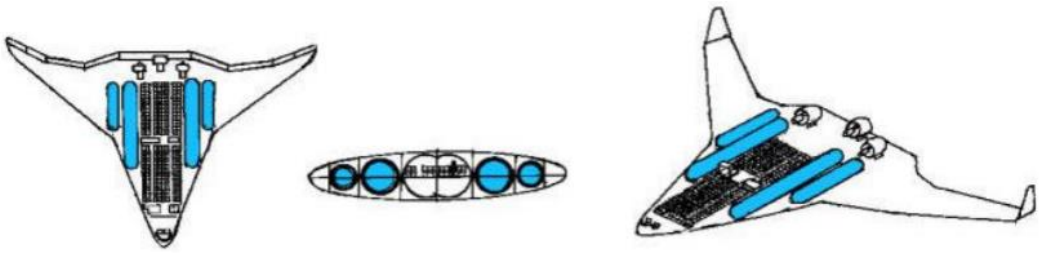

(a)

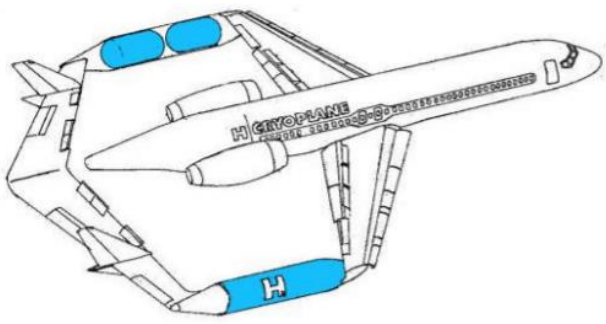

(b)

Fig. 1-3: a) Blended Wing Body aircraft configuration with integral LH_2 tanks and b) twin-boom aircraft configuration with non-integral LH_2 tanks [11].

1.2 Need for Efficient Conformal Structures for Fuel Storage

Based on the CryoPlane example [11], it is essential to investigate lightweight structures for LH_2 storage that can conform to a given space in the aircraft better than cylindrical pressure vessels. Conformable pressurized structures - in the form of intersecting cells joined together - are a lightweight and volumetrically efficient solution in the field of fuel containment. Jackson and Stone [12] were the first to propose the concept of intersecting metallic spherical tanks for storage of liquids or gases under pressure. The tank configuration proposed, consisted of separate spherical chambers with a welded diaphragm at the intersection, in an attempt to mimic the soap bubble cluster principle. Elliot et al [13] proposed using the low weight-to-displacement ratio of intersecting spherical shells and their high resistance to external hydrostatic pressures, in deep submergence vessels. This study addressed for the first time the use of orthotropic unidirectional fiber-reinforced polymers (FRPs) at the spherical membranes and stiffening rings at the junctions of the intersecting pressurized structures. However the manufacturability of intersecting spheres has always been an issue [14]-[15], and thus no commercial applications of such configurations have been reported so far.

Conformal pressurized structures in the form of intersecting cylinders -rather than spheres- have been conceptually analyzed in several studies [16]-[18]. In 2000, Thiokol Aerospace & Industrial Technologies [19] developed intersecting composite overwrapped cylindrical pressure vessels for gaseous hydrogen for fuel cell-powered vehicles. Fig. 1-4a depicts a finalized prototype, in which each cell was individually wound with carbon fiber-reinforced rovings and a final hoop overwrap was applied to join the different cells. The volumetric efficiency of intersecting cylindrical vessels when fitted in a rectangular envelope - compared to separate cylindrical vessels - can be seen in Fig. 1-4b. It is clear that with increasing envelope aspect ratio (width/length) the volumetric efficiency of the conformable configuration has a asymptotic trend, while separate cylinders show a discontinuous (zig-zag) pattern.

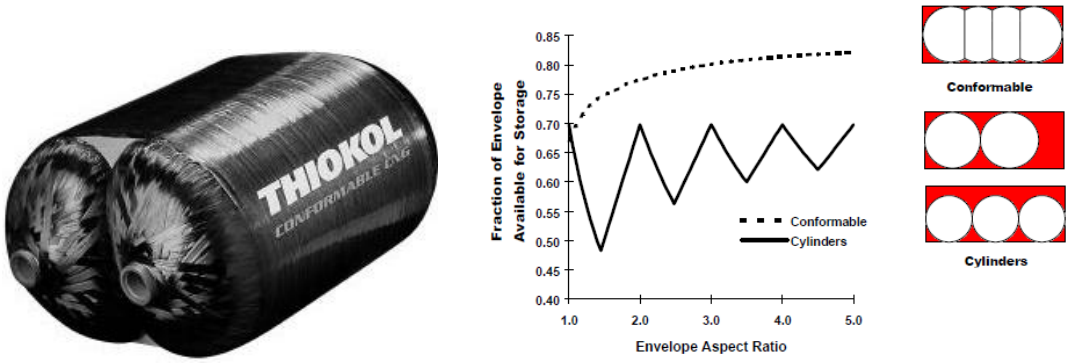

(a) **(b)**

Fig. 1-4: a) Conformable tank prototype and b) comparison of storage efficiencies within a prescribed rectangular envelope [19].

The downside of the multi-lobe configuration is the weight penalty introduced by the added hoop windings at the cylindrical body, which are necessary to have deformation compatibility between the dome and cylinder under pressure [20]. Furthermore, in cryogenic storage applications, the cylindrical section leads to excessive passive heat and cryogenic propellant boil-off due to the relatively large surface area to volume ratio. Therefore, it is imperative to develop new tank designs that could efficiently utilize the allowable space within an aircraft without adding extra weight while minimizing fuel boil-off, i.e. novel, gravimetrically and volumetrically efficient pressure vessel configurations.

A configuration based on intersecting composite overwrapped spherical membranes (multi-sphere) can lead to weight savings associated to (i) equal membrane strains when subjected to uniform pressure and (ii) the fact that spheres have the minimum surface area for a given volume. The latter characteristic leads to minimization of passive heat in the tank and fuel boil-off, thus limiting the weight penalty associated with required insulation thickness in cryogenic environments. Analysis of multi-spherical composite overwrapped pressure vessels (COPVs) for cryogenic storage is scarce or non-existing. To date, the development and testing of such structures - to evaluate their performance at a given load regime - has not been carried out.

1.3 Thesis Topics

All issues related to conformal COPV development and performance assessment need to addressed. Therefore the following objectives are to be analysed:

- Structural analysis of the multi-sphere under thermo-mechanical loads
- Development and testing of a multi-sphere sub-scale demonstrator
- Experimental verification of multi-sphere behaviour under cryogenic operation loads
- Identification of drawbacks and points for improvement for Type IV (plastic-lined) multi-sphere

1.4 Thesis Outline

A literature review on the use of COPVs in the field of LH_2 fuel storage is hereby presented in Chapter 2. Issues like tank shape, tank integration, required insulation, results from thermal and structural analysis and experimental behaviour under cryogenic conditions are investigated. Additionally, the load cases that a cryogenic propellant tank is subjected to during operation are presented. The common practises of COPVs proof-testing for spaceflights are provided and the design features of a cryogenic tank that lead to a safe operation are outlined.

Chapter 3 presents the knowledge gaps in the field of cryogenic tanks and conformal composite overwrapped vessels and the arising research questions, based on the literature survey of Chapter 2. The methodology incorporated in this Thesis to address these research questions is presented.

Chapter 4 is dedicated to the development of a method to analyse the stresses at the multi-spherical COPV when loaded under internal pressure. The basic tank geometry is presented and the geometrical variables that control the multi-sphere design are identified. A method to introduce equal strain field between the cells is provided. Furthermore, the effect of the geometrical parameters on the tank behaviour are evaluated.

Chapter 5 deals with the derivation of the multi-sphere internal volume, surface area and corresponding weight, based on the findings of Chapter 4 on the homogenization of the strain field. A comparison of the multi-sphere with cylindrical COPVs will show whether an enhancement in performance was achieved under cryogenic conditions.

Chapter 6 provides the approximation functions that describe the temperature dependency of the liner and composite overwrap materials. The approximation functions are based on results from material testing.

Chapter 7 consists of the developed transient numerical thermo-mechanical model of the cryogenic chill-down and pressure cycling of the multi-sphere. A progressive failure analysis model is developed to quantify the tank-pressure window at ambient and cryogenic conditions, based on tank wall material allowables obtained from Chapter 6.

Chapter 8 outlines the manufacturing process and the experimental testing of the multi-spherical COPV prototypes. The procedure steps and the results from a hydro-burst pressure test and pressure cycling at cryogenic temperatures are discussed. The approximation functions described in Chapter 6 and the results of Chapter 7 are compared with experimental results.

Finally, the conclusions of this work and recommendations for future research are presented in Chapter 9.

References

[1] European Commission, NN: Work Programme, Cooperation Theme 7 Transport (including Aeronautics), 2010.

[2] Airbus Report, 'Growing Horizons 2017/2036: Global Market Forecast', 2017.

[3] European Environmental Agency Report, 'Air pollutant emission inventory guidebook', 2017.

[4] H.L. Rogers, D.S. Lee, D.W. Raper, P.M. Foster, C.W. Wilson and P.J. Newton, 'The Impacts of Aviation on the Atmosphere', *The Aeronautical Journal*, **106**, 521-546, 2002.

[5] D. Wuebbles, M. Gupta and M. Ko, 'Evaluating the impacts of aviation on climate change', *EOS Transactions of the American Geophysical Union*, **88**, 157-168, 2007.

[6] G.D. Brewer, 'Hydrogen Aircraft Technology', CRC Press, 1991.

[7] A. Westenberger, 'Final Technical Report: Liquid hydrogen fuelled aircraft - system analysis', 2003.

[8] US Department of Energy, 'Report on Hydrogen Storage for Fuel Cell Applications', 2017.

[9] A. Silverstein and E.W. Hall, 'Liquid hydrogen as a jet fuel for high altitude aircraft', NASA-RM-E55C28a, 1955.

[10] G.D. Brewer, R.E. Morris, R.H. Lange and J.W. Moore, 'Study of the application of hydrogen fuel to long-range subsonic transport aircraft', vols. I and II; NASA-CR-132558-VOL-1 and NASA-CR-132559-VOL-2, 1975.

[11] A. Westenberger, 'Liquid hydrogen fuelled aircraft – system analysis. Final Technical Report-CryoPlane Project', GRD1-1999-10014, 2003.

[12] O.J. Jackson and C.L. Stone, 'Intersecting spherical pressure tank', USA Patent 2341044, 1944.

[13] D.R. Elliot, E. Francois and D. McDonald, 'Deep submergence vessels of interconnected radial-filament spheres', USA Patent 3608767, 1970.

[14] F.J.J.M.M. Geuskens, O.K. Bergsma, S. Koussios and A. Beukers, 'Analysis of conformable pressure vessels: introducing the multibubble', *AIAA Journal*, **49**, 1683-1692, 2011.

[15] C.-C. Liang, S.W. Shiah, C.-Y. Jen and H.-W. Chen, 'Optimum design of multiple intersecting spheres deep-submerged pressure hull', *Ocean Engineering*, **31**, 177-199, 2004.

[16] M.J. Warner, 'End closure modules for multi-cell pressure vessels and pressure vessels containing the same', USA Patent 6412650, 2002.

[17] M.D. Blair, D.G. Turner, R.K. Kunz, M.J. Warner, K.W. Davis, F.E. Wolcott and J.D. Bennett, 'Composite conformable pressure vessel', USA Patent RE41412E, 2010.

[18] K.W. Richards and N.G. Christensen, 'Seamless multi-section pressure vessel', USA Patent 8020722B2, 2011.

[19] A. Haaland, High-Pressure Conformable Hydrogen Storage for Fuel Cell Vehicles, *Proceedings of the U.S. DOE Hydrogen Program Review, California*, 2000.

[20] V.V. Vasiliev, *Composite Pressure Vessels: Analysis, Design and Manufacturing*, Bull Ridge Publishing, 2009.

Chapter 2: Literature Review on Cryogenic Storage Tanks

2.1 Early Applications of Liquid Hydrogen Containment in the Aerospace Sector

One of the earliest documented applications of hydrogen storage tanks for a flight vehicle (subsonic bomber) was reported in 1955 by Silverstein and Hall [1]. A twin-engine kerosene-powered bomber was converted to a single engine bomber operating on liquid-hydrogen that enabled the Martin B-57 bomber to extend its flight radius by 60 [%] at the same gross weight. A milestone for LH_2 propellant tanks in aerospace was their utilization in the Saturn V rocket in the 1960s and 1970s [2]. Saturn V was a heavy three-stage launch vehicle developed by NASA to support initially the Apollo program for moon exploration and later the launch the Skylab space station. Liquid hydrogen (LH_2) and liquid oxygen (LO_2) were used as propellants at the upper two stages. The LH_2 tank shell consisted of an aluminium-based single-wall tank with foam infiltrated with a honeycomb core insulation [2].

From the 1980s till 2010, the Space Shuttle was used as NASA's heavy launch vehicle. The Space Shuttle incorporated an external lightweight LH_2 fuel tank, which was also a load-bearing structure of the shuttle system as it had to withstand the i) weight of propellants (LO_2, LH_2), ii) internal tank pressures, iii) loads from the shuttle orbiter and the iv) loads from the solid rocket boosters (Fig. 2-1). An aluminium-lithium alloy was used for the pressure vessel wall, providing an increase in specific strength in comparison to the previously used aluminium alloy 2219 and a spray-on foam was applied at the external surface as thermal protection. The complete semi-monocoque tank structure was composed of different barrel sections, fusion-welded together [3].

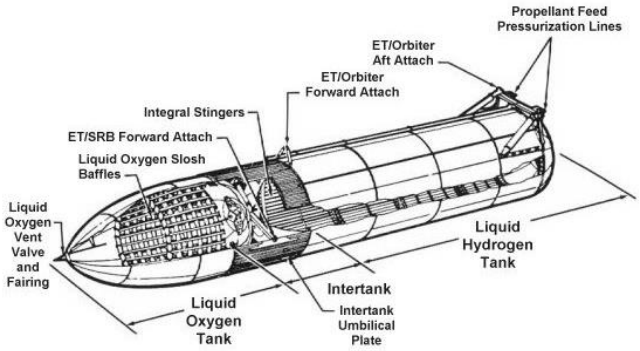

Fig. 2-1: Lay-out of the Space Shuttle External Tank (ET) [3].

The Space Shuttle hydrogen containment system was an external tank that however was complex and had a heavy three-stage configuration that was not re-usable. NASA, in cooperation with the Ballistic Missile Defence Organization (BMDO) and McDonnell-Douglas, initiated the Single-Stage Rocket Technology (SSRT) technology program, in order to seek a replacement of the Space Shuttle and to develop a fully reusable single-stage-to-orbit (SSTO) vehicle [4]. The result of this technology program was the development of the DC-X (Delta-Clipper Experimental) demonstrator that consisted of a LH_2 tank with an aluminium-lithium shell.

2.2 Introduction of Composites in Cryogenic Tanks

In all the above cases of hydrogen-fuelled space vehicles, the storage tanks were manufactured out of metals, which resulted in structures with relatively low structural efficiency. This however changed with the introduction of composites in the field of pressure vessels.

The primary reason for using composites is their higher strength and stiffness-to-weight ratios as compared to isotropic materials, which can be seen in the Ashby diagram below (Fig. 2-2). It is evident that the composites cluster together and more specifically, that the CFRPs (carbon fiber-reinforced polymers) rank higher than metals in both specific modulus and strength.

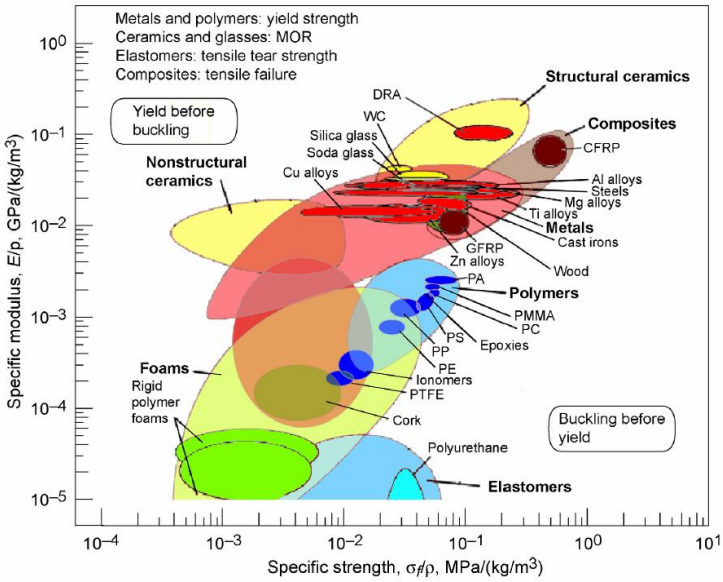

Fig. 2-2: Specific stiffness vs specific strength for various engineering materials [5].

Composites in the form of unidirectional strands/rovings can be tailored to reinforce a structure along the principal direction of the load that it is subjected to, thus making them ideal for applications such as pressure vessels [6]. Composite Overwrapped Pressure Vessels (COPVs) manufactured from filament winding on a metallic or plastic liner [6] have shown excellent potential for lightweight structural design in the field of fuel containment [7]-[8]. One way to assess their performance and to compare it to vessel configurations from isotropic materials is to employ the structural efficiency index:

$$\left(n_{\mathrm{PF}} = \frac{PV}{W} \right) \tag{2.1}$$

where P is the tank internal pressure, V is the tank's internal volume and W is the structural weight (in principal only the weight of the reinforcement is considered here). Fig. 2-3 depicts the gravimetric efficiencies of pressure vessels incorporating different reinforcement materials. It is evident that steel vessels lead to the lowest efficiency and CFRP based on IM-7 (intermediate modulus) carbon fibers results to the highest efficiency, which is more than seven times the value of steel-reinforced vessels.

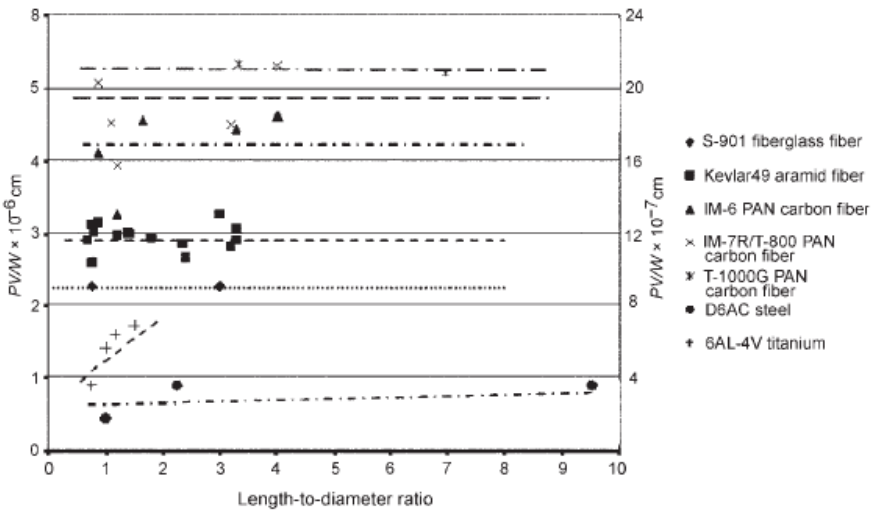

Fig. 2-3: Comparison of structural efficiency of pressure vessels from different reinforcement materials [9].

Composites were eventually utilized for cryogenic storage in the aerospace sector, based on the attributes presented above. Already the hydrogen tank in the updated DC-X vehicle had been changed to a composite one with low density reinforced foam internal insulation in 1997 [10]. In addition, the i) composite intertank, ii) the gaseous hydrogen/oxygen auxiliary power unit (APU) and iii) the feedline/valve assembly were some of the systems that had been converted from metallic to composite based structures (Fig. 2-4).

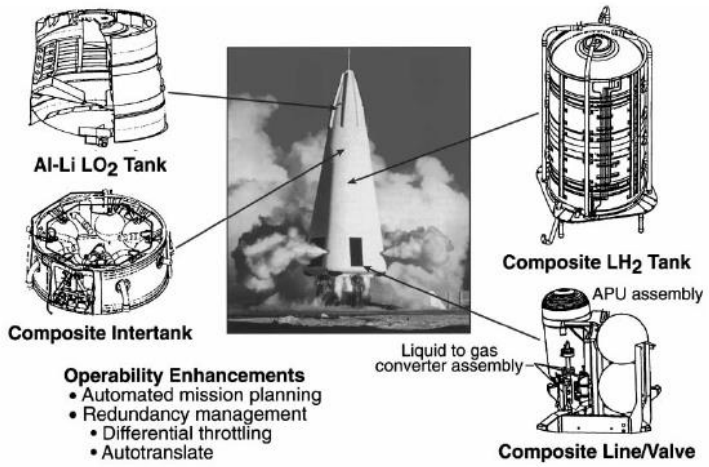

Fig. 2-4: Outline of DC-XA sub-components [10].

One of the most recent applications of composite overwrapped vessels for liquid hydrogen storage was reported in the X-33 vehicle (Fig. 2-5). The sub-orbital X-33 was developed to i) increase launch vehicle reliability, ii) minimise the cost of launching payloads to Low Earth Orbit (LEO) and essentially iii) show the potential of incorporating a novel tank design and advanced materials (composites) [11]. It consisted of two linerless multi-lobe LH_2 tanks based on conical configurations with a sandwich composite applied at the tank wall employing a CFRP inner and outer facesheets and a honeycomb core. Woven composite joints were used as reinforcement of the intersections. After successful manufacturing, the obtained configuration was tested according to the load it would face throughout operation (thermal and mechanical). Failure occurred during LH_2 draining in the form of microcracking of the inner facesheet and continuous GH_2 infiltration in the sandwich core, that led to higher than expected core pressure.

Essentially, hydrogen permeation -due to matrix microcracks- was the driving parameter for tank failure [11].

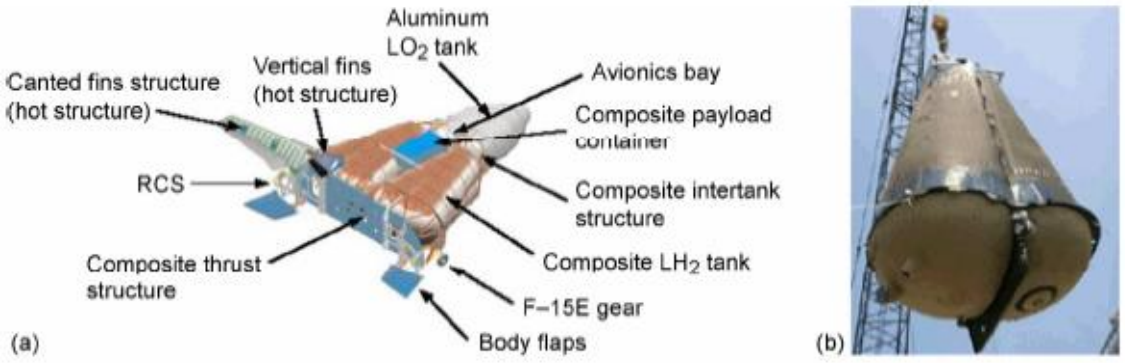

Fig. 2-5: Lay-out of a) X-33 vehicle components and b) multi-lobe LH_2 tank [11].

Despite failure during testing of this tank, multiple issues were addressed and lessons were learned. The use of a conformal tank within the SSTO vehicle and made out of composites was of significant importance. It was concluded that a liner was needed to be incorporated for gas tightness purposes and that the issue of composite microcracking at these low temperatures should be tackled. Finally, the effect of manufacturing on tank performance needs to be further investigated [11].

2.3 Cryogenic Tank Configurations

In this section, governing issues regarding cryogenic fuel tank conceptual design are presented. In particular, integral and non-integral cryogenic tanks are analysed and their corresponding operational loads throughout a flight are presented. Furthermore, different tank wall architectures and existing thermal insulation strategies are outlined.

2.3.1 Integral vs Non-Integral

Integral tanks are essentially part of the basic airframe structure and thus besides the thermal and mechanical loads from the fuel containment, they have to withstand fuselage loads as derived from the vehicle's accelerations and aerodynamic events. These loads are transferred to the vessel through an interconnected truss framework [12]. A CAD model of the SpaceLiner Reusable Launch Vehicle (RLV) is depicted in Fig. 2-6, with its integral LO_x and LH_2 orbiter tanks being incorporated in the fuselage.

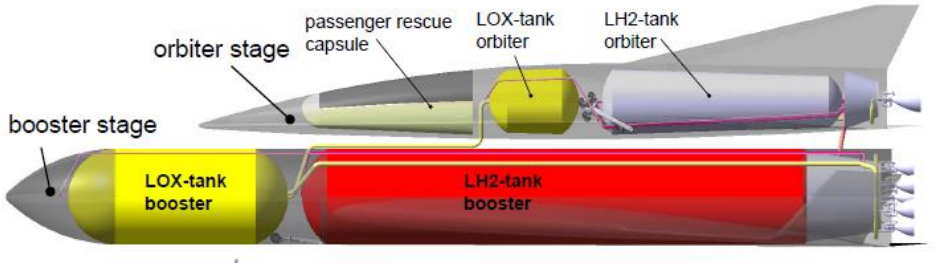

Fig. 2-6: Lay-out of SpaceLiner reusable launch vehicle (RLV) [13].

Throughout operation, the LH_2 orbiter tank of the SpaceLiner is subjected to a combined thermo-mechanical loading scenario as well as loading induced by gravitational accelerations during all the flight stages [13]. The different load cases of the tank are the following: i) nominal cryogenic operation at maximum expected temperature or ii) nominal empty operation after main-engine-cut-off (MECO) and iii) off-nominal operation after early MECO with remaining

LH_2 inside (Fig. 2-7). The maximum expected internal operating pressure (P_{MEOP}) is 3.8 [bar], while the most severe thermal loading at the tank wall is induced during regular cryogenic operation (T_{in} = -253 [°C], T_{ex} = RT (room temperature) with a ΔT = -276 [°C]). The symbols T_{in} and T_{ex} correspond to the inner tank wall and ambient temperatures respectively. The *x*-axis (n_x), *z*-axis (n_z) represent the horizontal and vertical gravitational accelerations respectively while n_{radial} is the radial acceleration. The symbols P_{ull} and P_{bottom} correspond to the pressure at the ullage and bottom surface respectively.

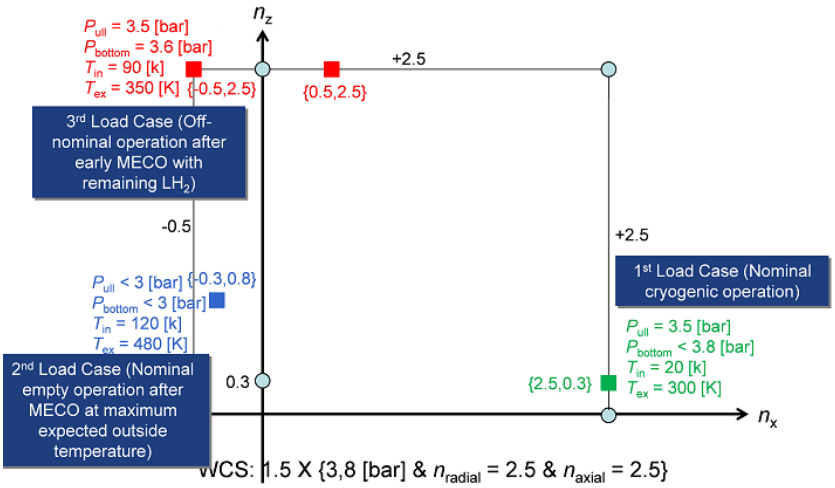

Fig. 2-7: Simplified flight load cases of the Space Liner LH_2 orbiter tank [14].

Non-integral tanks only have to sustain the loads associated with fuel storage, fuel dynamics (sloshing) and thermal stresses from thermal gradients arising at the tank wall. However the issue of effective attachment to the aircraft fuselage becomes critical due to the fact that the attachments must handle the thermal contraction/expansion difference between the inner and outer tank wall. Another implication is that a large non-integral tank would mean higher frontal and surface areas, resulting in higher drag [15].

The main drivers for the selection between integral and non-integral tanks are: i) weight savings, ii) effective utilization of the allowable space, iii) manufacturability, iv) drag and v) inspection and maintenance accessibility. Due to the fact that integral tanks carry part of the fuselage loads, their utilization results in aircraft weight savings. This can also be understood by the fact that they utilize more efficiently the available space within the aircraft, leading to a smaller fuselage and increased weight savings [16]. Furthermore, inspection for cracks and maintenance is easier to perform in integral tanks since the only step required is to remove the outer heat shield in order to have direct access to their external thermal insulation layer [17]. However, integral tanks require a complex architecture in order to conform to the aircraft shape, which will pose many manufacturing difficulties unlike the non-integral tanks that can have a simple geometry (e.g. sphere, cylinder).

2.3.2 Tank Wall Architecture

As mentioned above, the tank is subjected to several different mechanical loads throughout operation (inner pressure, fuel weight, vehicle acceleration loads and fuel sloshing). Consequently, the tank wall needs to provide effective reinforcement without adding too much weight, while minimising passive heat transmission in the liquid and thus fuel boil-off. The use of composites (Section 2.2) introduced significant weight savings in cryogenic tanks and provided improved insulation capabilities. The tank wall architecture would have a strong impact on the behaviour of the cryogenic tank.

The two main approaches for tank wall design are the single-wall [18] and double wall [16] geometries. In the single wall configuration, the single tank wall bears the inner pressure and an external thermal insulation layer (usually rigid foam) is applied through bonding on the outside surface of the tank (Fig. 2-8a). On the contrary, a double wall consists of an inner and an outer vessel with a vacuum-based insulation layer in-between (Fig. 2-8b). The main role of the inner layer is fluid containment while the outer layer is primarily used to keep the vacuum between the two shells. Joining elements are present to provide a load path to the outer structure but these lead to thermal bridging. A variation of the double-walled configuration is a sandwich construction that incorporates a core that has either load-bearing capabilities or thermal insulating potential (Fig. 2-8c). The symbol MLI in Fig. 2-8b represents multi-layer thermal insulation, which are layers of thin sheets used to minimize heat loss by radiation [16].

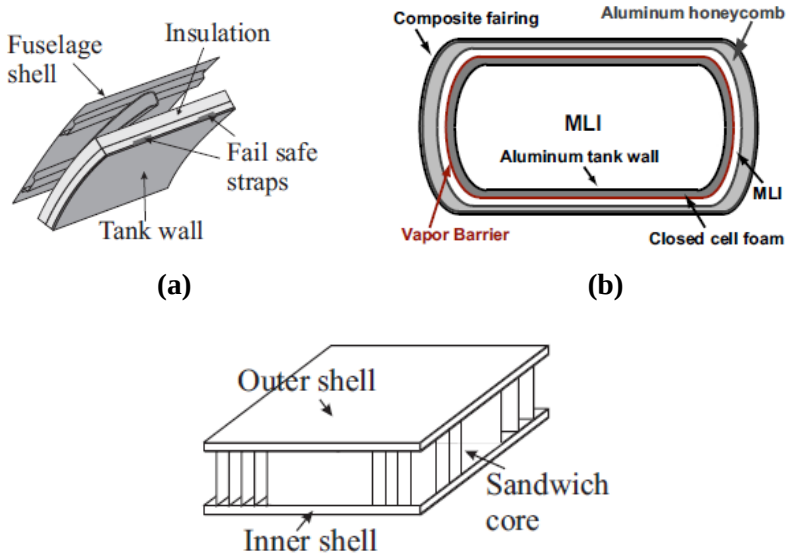

Fig. 2-8: a) Single-walled [18], b) double-walled [16] and c) sandwich [19] tank configurations.

Single-walled structures have the advantage of being simple and less costly [18]. However, they provide limited options for thermal insulation and they represent a sub-optimal solution in terms of weight minimisation. Double-walled configurations show the potential for weight minimisation and allow for a lot of insulation options, but they are very complicated and costly to fabricate. As a variation on this theme, sandwich structures provide an effective solution in terms of reducing the weight of a cryogenic tank, are ideal for both in-plane and bending loads but they are complex and costly to construct [20].

The insulation layers minimize the heat transmitted into the cryogenic fuel due to their minimal thermal conductivity. The three main insulation strategies are: i) rigid foams, ii) MLI and iii) aerogels. Materials used in insulation foams have higher thermal conductivity values than the other two options and do not require any vacuum. MLI is composed of multiple layers of thin sheets of very low conductivity. Despite being a very efficient and lightweight solution, it requires very high vacuum to operate properly [15]. Finally, aerogels are the ultra-light solution since they are primarily composed of air and have exceptional insulating properties. However, their disadvantage lies on the fact that they are very brittle; this is a severe drawback for cryogenic applications [15].

2.4 Analysis Procedures of Cryogenic COPVs

In this section, issues like analysis of the heat transfer phenomena occurring at the tank during chill-down, formation of a frost layer and the corresponding thermal stresses are outlined.

2.4.1 Thermal Analysis

One of the issues associated with the simulation of the behaviour of the multi-sphere cryogenic storage tank is the challenge of evaluating the temperature profile at the tank contour. In order to do so, the different heat transfer phenomena occurring at a cryogen need to be addressed. The heat transfer modes in a tank are in principle the following: i) conduction, ii) convection and iii) radiation [18]. Heat conduction occurs though the tank wall layers, tank supports, polar openings bosses and any other element that is connected to the tank. This heat mode can be described by the Fourier equation:

$$q_{\text{cond}} = -k\nabla T \tag{2.2}$$

where q_{cond} is the conductive heat flux at one of the surfaces of a tank wall layer, k is the thermal conductivity of the employed material(s) and ∇T is the temperature gradient in any direction.

Natural convection takes place at both the outer composite surface due to the temperature difference to the ambient environment and at the inner liner surface at the ullage region (unfilled tank space with liquid fuel).

$$q_{\text{conv}} = h_{\text{out}}\left(T_{\text{s}} - T_{\text{ex}}\right) \tag{2.3}$$

where q_{conv} is the convective heat flux, h_{out} is the free convection heat transfer coefficient and $T_{\text{s}} - T_{\text{ex}}$ is the difference between the outer tank wall and ambient temperatures. The heat transfer coefficient depends on the conditions of the boundary layer and nature of fluid motion. Essentially, the heat transmission from the exterior by convection must be decreased to minimise heat flux in the liquid and thus excessive fuel boil-off.

The last heat transfer mechanism is radiation between tank wall surfaces. The heat flux by radiation, between two bodies with temperatures T_1 and T_2 correspondingly with $T_1 > T_2$, is described by:

$$q_{\text{rad}} = \sigma\varepsilon\left(T_1^4 - T_2^4\right) \tag{2.4}$$

where q_{rad} is the radiative heat flux between two surfaces of two tank wall layers, σ is the Stefan-Boltzmann constant, ε is the emissivity of the surface and T_1 and T_2 are the surface temperatures. The view factor (F_{ij}) is the fraction of radiation leaving the inner shell surface and being intercepted by outer shell surface. The value of F_{ij} varies from 0 to 1 and it is directly dependent on the coefficient of thermal expansion (CTE) mismatch of the inner and outer shell and consequently on the air gap formed between them throughout chill-down. Heat radiation between surfaces can be reduced by applying radiation shields between them. This can be seen in Fig. 2-9, where a type IV (COPV with a plastic liner) tank is used for cryogenic storage (Liquefied Natural Gas-LNG). The complete lay-out of a cryogenic tank wall (double-walled) is shown in Fig. 2-9.

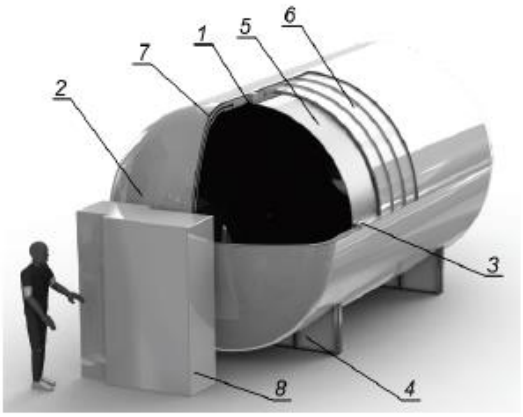

Fig. 2-9: Layout of a type IV cryogenic tank: 1) inner tank, 2) outer tank, 3) inner supports, 4) outer supports, 5) insulation, 6) radiation shields, 7) vacuum and 8) fittings [21].

By taking the above into consideration, Lisowski and Czyzycki [21] assessed the heat flux imposed on the fuel from the environment and the corresponding temperature distribution of Type IV tanks (plastic-lined fully overwrapped vessels) by FE analysis. The tank had a 50 [%] fill ratio with an ambient temperature at 15 [^{o}C]. A thermal contact resistance condition was applied in their model between the tank and the supports, while the only heat transfer pattern in the vacuum was radiation between tank wall layers. Additionally, a natural convection scenario was applied at the external tank surface. As a last step, the heat leakage and resulting storage time were also evaluated leading to the Type IV having the highest storage time compared to Type I (all metal vessel), Type II (metallic liner with only hoop windings) and Type III (composite overwrap with a metallic liner).

The effect of filling and draining with a cryogenic fuel on the temperature profile of a tank is of significant importance. Stephens et al. [22] assessed numerically the effect of both filling and draining with a cryogenic fuel (Liquid Nitrogen-LN_2), as well as aerodynamic heating on the tank wall for a fill ratio of 75 [%]. A two-dimensional finite-difference thermal-fluid model was developed to simulate the filling and draining phases. It was shown that the temperature field changed according to the following three ways of heat transfer as a function of the contained liquid level: i) tank wall cooling through vapour-free convection, ii) circumferential thermal conduction within the vessel wall coupled with vapour-free convection and iii) boiling heat transfer at the moment the liquid level reached the considered level in the tank. With the liquid level increasing, the temperature values at all measurement points dropped while an equilibrium was obtained at approximately 77 [K] (Fig. 2-10). It is evident that the temperature at location 300 (top of the tank) did not drop to the same value, due to the fact that it was in contact with the vapour region.

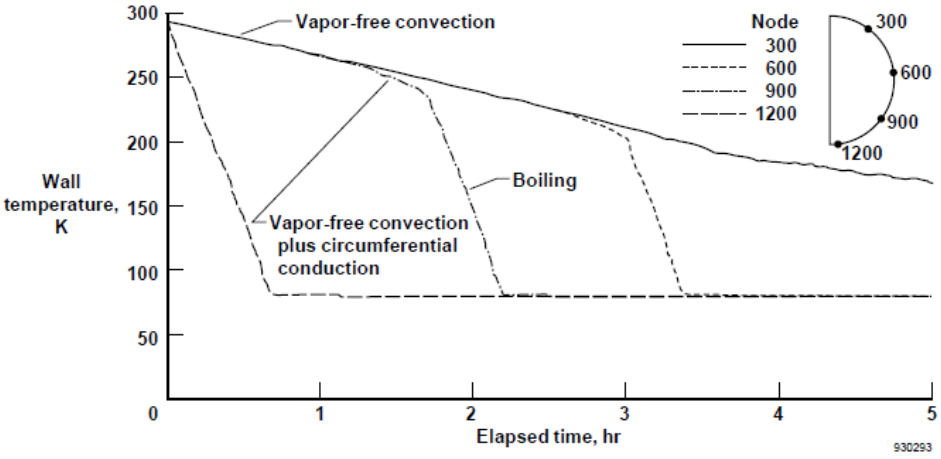

Fig. 2-10: Tank wall temperatures at different positions, as a function of time for a 75 [%] fill ratio [22].

The same two-dimensional computational model was applied to the same vessel configuration for storing both LN_2 and LH_2 at different fill ratios (15, 50 and 85 [%]) in [23]. This parametric study enabled the prediction of i) boil-off rates, ii) cryogenic fluid and wall temperatures and iii) surface heat fluxes. Tank wall and vapour temperatures increased while boil-off decreased with decreasing tank fill level. Kim et al. [24] performed a transient heat transfer analysis of a cryogenic oxidizer tank analysing the effect of prelaunch helium gas pressurization on the tank pressure and ullage gas temperature and evaporation of liquid oxygen.

In the absence of external thermal insulation, a frost layer is formed which will have a significant effect on the temperature gradient at the tank wall, due to its very low effective thermal conductivity, thus it functions as a thermal insulation layer [25]. This phenomenon cannot be neglected and must be taken into consideration in cryogenic tank systems that do not incorporate an insulation layer. Frost layer formation is associated with the fact that the surrounding humid air comes in contact with the colder tank wall surface. This leads to water vapour condensation and, since the temperature is below water freezing point, a frost layer is formed. J.D Yonko et al. [25] analysed frost thermal conductivity on a flat horizontal plate as a function of frost density and surface temperature. The frost thickness varies with time and location at the tank contour, and depends on i) the rate of water deposition from the ambient air to the frost surface, ii) frost density iii) air humidity and iv) air velocity [26]. Mago et al. [26] and K-H. Kim et al. [24] developed a semi-empirical and a numerical model method respectively to obtain the frost layer thickness and surface temperature of a cryogenic cylinder as a function of time. However, numerical derivation of the global temperature field of a multi-spherical tank configuration at cryogenic conditions -by taking into account the formation of a frost layer- has not been carried out yet.

2.4.2 Structural Analysis

Understanding the effect of tank wall temperature gradients on the pressure vessel's mechanical response -due to thermal restraints and friction between tank parts with different CTEs- is crucial at all stages of the cryogenic storage tank design. The stress state at any given position on a cryogenic tank wall is dependent on the temperature difference that point has experienced, as well as any other induced mechanical load throughout tank operation.

Xu et al. [27] performed a structural design study -based on FE analysis- of a LH_2 tank in remotely-operated aircraft, by incorporating both a thermal and mechanical analysis of the given configuration, while the tank was subjected to i) thermal loads, ii) pressure and iii) gravitational

acceleration loads. The configuration of interest was a metallic spherical tank, consisting of an inner and an outer wall, with support structures, vacuum and MLI in between. The heat transfer modes considered were convection and radiation on the outside of the tank and convection only on the inside wall that was in contact with LH_2. Derivation of the temperature profile and corresponding thermal stresses and their superposition at the stresses from pressurization and acceleration, enabled a realistic evaluation of the stress state of the tank at every operation point. Murugan et al. [28] performed a transient heat transfer analysis to evaluate the temperature at the tank contour of a metallic cylindrical LH_2 tank during chill-down. This enabled the evaluation of thermally induced stresses and their coupling with stresses induced during pressurization. Thermally induced stresses in a LH_2 tank from chill-down were also studied in [29]. A computational fluid dynamics (CFD) model analysed the effect of inflow rate and the state of cryogen inside the tank where the findings were used to derive the tank's temperature profile. The temperature output of the CFD study was then introduced to the FE-based structural analysis, where the resulting stress state of the tank was obtained.

The structural performance of cylindrical COPVs under cryogenic (LH_2) storage was investigated in [30]. In particular, an FE-based computational model was developed to perform a stress analysis of the overwrap -on a ply level- due to inertial and pressurization loads throughout operation. The thermo-mechanical properties at -253 [^{o}C] of the fiber and matrix of the composite overwrap were derived through coupon tests. Additionally, a progressive failure analysis at the macro-scale was carried out for i) static and ii) cyclic loading. A safety factor of 1.8 (damage initiation) and a burst factor of 5.35 (burst) as compared to the maximum expected operating pressure (P_{MEOP}) were achieved. Fig. 2-11 depicts the damage state at its initiation and prior to burst state at -253 [^{o}C]. The blue colour shows all the un-damaged regions, with damage at the red regions.

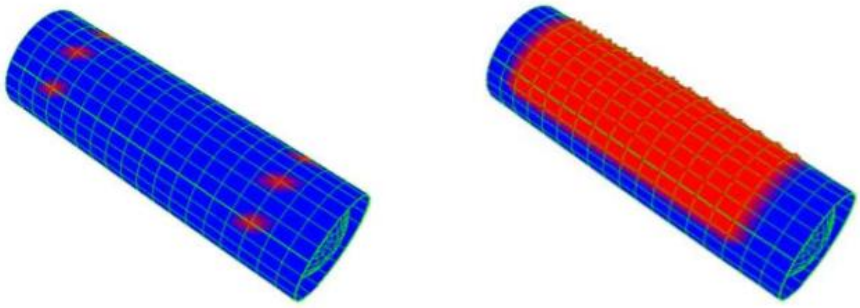

(a) **(b)**

Fig. 2-11: a) Damage initiation (P = 54 [psi]) and b) damage prior to burst (P = 160.5 [psi]) for a composite overwrapped LH_2 tank at -253 [^{o}C] [30].

Ju et al. [31] also performed a progressive failure analysis (PFA) of a COPV for LH_2 storage, incorporating the Classical Lamination Theory (CLT) and by employing the maximum stress criterion to check for ply failure. Loads associated with accelerations from launch, internal pressure, exposure to cryogenic fuel and residual stresses from curing of the laminate were considered. It was concluded that the thermal residual stresses were 80-98 [%] of the total stress in the direction transverse to the fibers. Additionally, it was concluded that thermal residual stresses are very sensitive to the CTE and that a more accurate measurement of that material property would lead to a more precise design. A micro-mechanics approach was performed in [32]-[33] to analyse the COPV behaviour for LH_2 storage applications, based on the use of a representative volume element (RVE) with a hexagonal array configuration. In [32], an exponential relationship was used between the CTE, engineering properties and the temperature.

In the next section, a review of the published works on testing of cryogenic tanks is outlined. The different testing approaches and monitoring techniques are presented.

2.5 Experimental Assessment of Cryogenic COPVs

2.5.1 Literature Survey

There are two basic approaches for an experimental evaluation of the performance of a cryogenic storage tank: i) investigation of the safety and burst factor under static pressure loading and ii) damage assessment during pressure or thermal cycling (durability) in an attempt to simulate tank refuelling and draining operations.

Several studies have been performed to assess the burst pressure values of pressure vessels at cryogenic temperatures [34]-[35]. It was shown in [35], that for the case of Type IV tanks, the pressure loss is initiated from cracks appearing at the liner/boss interface caused by high stresses associated with different CTE values of the metallic boss and plastic liner. This damage mode is considered as unsafe, since it can lead to ejection of the metallic boss [36]. Werlink and Pena [37] incorporated Fiber Bragg Gratings (FBGs) at the surface of a COPV filled with LN_2 that was burst tested in order to record axial/hoop strain and temperature data, thereby evaluating the tensile strength of the composite tows by parallel FBG alignment. Schneider et al. [38] developed a split disk test fixture to obtain the burst pressure of the cylindrical section of a COPV at a cryogenic temperature (Fig. 2-12a). The burst pressure findings of this test were compared to the corresponding ones from a burst test of a COPV. The fact that similar results were shown by both methods verified the accuracy of the new test fixture.

(a) **(b)**

Fig. 2-12: a) Composite ring mounted on a split disk fixture prior to LN_2 submersion and b) cryogenic COPV during cryo-testing [38].

Ray et al. [39] performed tests to evaluate the performance of spherical Type III COPVs at cryogenic temperatures and also analysed the effect of the metallic material of the liner. The tank was subjected to the following steps: i) proof pressure testing at 1.25 times the P_{MEOP} at -196 [°C] with LN_2 and GN_2 being the pressurant, ii) thermal cycling (5 times) with LN_2 with no applied pressure, iii) pressure cycling (100 times) from 0 to 4500 [psi] at -196 [°C] and finally iv) burst testing at the same temperature. It was shown that a burst factor (B_F) of 2.7 (compared to P_{MEOP}) was obtained with the composite overwrap failing on the top of the welded region of the liner, between the boss and the dome.

As mentioned above, pressure or thermal cycling of cryogenic COPVs is performed to simulate the tank refuelling and draining operation. This testing scenario provides proof of

whether the tank will withstand pressure loading-unloading at P_{MEOP} while simultaneously exposed to the cryogenic propellant. A number of published works have reported pressure and thermal cycling of filament wound pressure vessels while storing a cryogenic medium [40]-[42]. Messigner and Pulley [43] studied the effect of pre-cycling, at 1.5 times the P_{MEOP}, a cylindrical COPV (with LN_2) and then cycling at P_{MEOP} (with LH_2). The Acoustic Emission (AE) technique employed, recorded a significant number of damage hits during each LH_2 and LN_2 filling cycle due to thermal stresses that were caused by cold shock at the tank wall. Kang et al. [44] performed an experimental study that revealed a correlation between the temperature gradient and the cool down pattern for different locations at the tank. Lei et al. [45] analyzed the effect of active pressurization at the tank thermal response. Mizutani et al. [46] performed a real-time strain measurement of a composite LH_2 tank with FBG (Ormocer coated) sensors during rocket operations. Fig. 2-13b depicts the FBG and strain gage output during all flight stages of the flight vehicle shown in Fig. 2-13a.

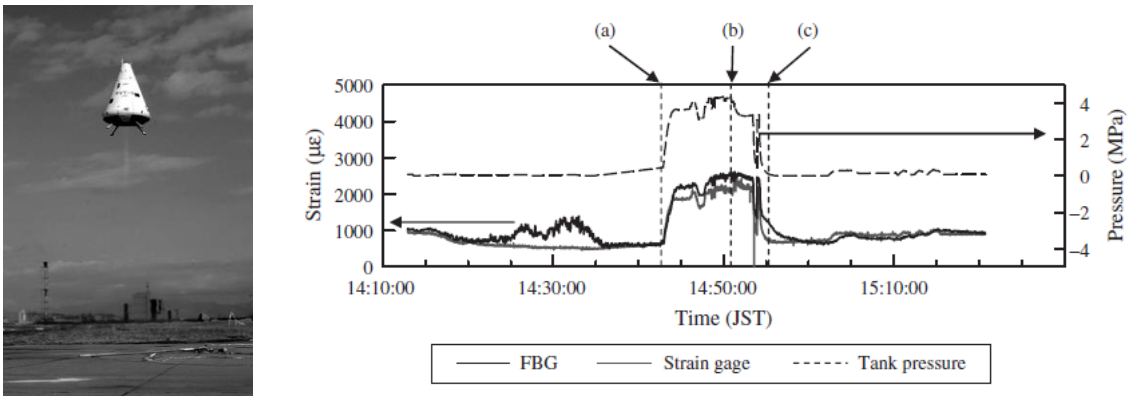

(a) **(b)**

Fig. 2-13: a) Flight experiment of reusable vehicle test (RVT) and b) strain monitoring of the LH_2 tank throughout all flight stages: a) pressurization, b) take-off and landing and c) de-compression [46].

In the following section all the issues related to the safe operation of cryogenic tanks are presented. This is crucial due to the fact that sudden cryogenic evaporation can lead to increased pressure and tank rupture, unless safety precautions are met.

2.5.2 Safety Issues in Testing

The most significant safety issue in the operation of cryogenic storage tanks is the vaporization of the cryogenic liquid [47]. Vaporization is associated with heat being transmitted to the cryogenic liquid, no matter how effective the thermal insulation in the tank configuration, due to the large temperature difference between the cryogenic medium and the ambient environment. The vaporized medium will accumulate in the vapor space and the pressure will increase. The absence of a venting path for the vaporized liquid results in a significant pressure build-up which can eventually rupture the cryogenic tank. This excessive pressure rise can be understood by considering that a large volume of gas is generated from the vaporization of a small volume of liquid (expansion ratio), due to large differences in density. Table 2-1 presents the liquid-to-gas expansion ratios and the corresponding boiling points of various media. Pressure relief devices are used to avoid entrapment of the cryogenic liquid at any point in the system.

Table 2-1: Expansion ratios and boiling points of different gases [47].

Cryogenic Medium [-]	Expansion Ratio [-]	Boiling Point [°C]	Gas Type [-]
Argon	860	-186	Inert
Helium	780	-269	Inert
Hydrogen	865	-253	Flammable
Methane	650	-196	Flammable
Nitrogen	710	-183	Inert
Oxygen	875	-161	Oxidizer

Even with the use of pressure relief valves, release of any of the above substances in a confined space could affect the air and thus the surroundings and exposed personnel. The release of argon (Ar), helium (He) and nitrogen (N_2) would result in an oxygen-deficient atmosphere, which can lead to asphyxiation. Release of liquid oxygen leads to an oxygen-enriched atmosphere increasing the potential for a fire to occur. Finally, hydrogen (H_2) and methane (CH_4) are flammable and require extensive safety measures. Fig. 2-14 depicts the measured minimum ignition energy (MIE) of a hydrogen-air mixture, showing the minimum amount of energy required to ignite a combustible vapor (air). A slight increase of H_2 concentration in the air raises the possibility of fire onset significantly [48].

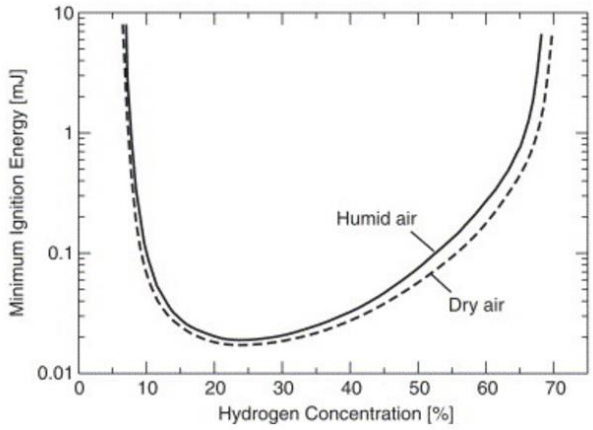

Fig. 2-14: Minimum ignition energy of hydrogen-humid air (relative humidity: 90[%]) and hydrogen-dry-air [48].

Embrittlement of tank wall materials can occur from exposure to high concentrations of hydrogen [49]. This leads to deterioration of the material's strain allowables and a reduction of the load-carrying capability of the tank, so that catastrophic failures can take place without significant deformation of the tank wall. In order to overcome this issue, the introduction of advanced material technologies at the tank wall must be assessed. Most cryogenic vessels are designed according to ASME Boiler and Pressure Vessel Code (BPVC Section VIII) [50] and Pressure (process) Piping Code (ASME B31.3) [51] to overcome these issues. In addition, they outline the design, manufacturing and assembly/inspection requirements. Moreover, they provide the specifications for the reinforcement calculation of a tank subjected to repeated thermal cycling or welding of piping sections.

The complete layout of all the components of a cryogenic storage tank can be seen in Fig. 2-15. Usually it is a double-walled vessel with an annular space (between the inner and outer vessel) under very high vacuum. This operates as a thermal insulation layer, thus minimizing the heat leak and cryogenic liquid boil-off. An internal vaporizer is a heat exchanger that functions as a gas vaporizing coil to convert the liquid product to gas but it is rarely used since the

cryogenic fuel must be withdrawn at a liquid state. Finally, general features can include a ring and post for easier handling and a liquid level gauge

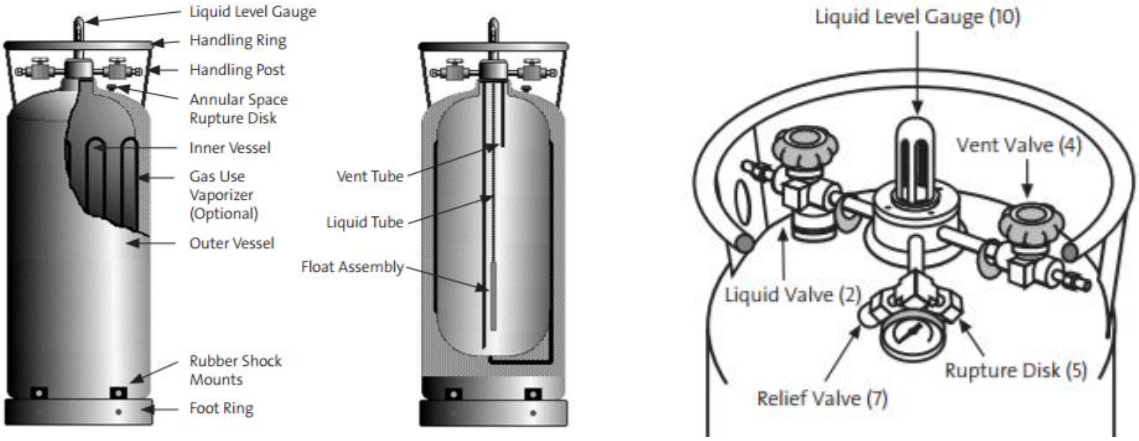

(a) **(b)**

Fig. 2-15: a) Side and b) top view of a cryogenic container [52].

For proper and safe flow of cryogenic liquid a number of different components are incorporated in the tank system. The liquid valve is used for filling and draining of the tank, while the vent valve is meant for venting the vapor space during the filling stage and for venting excess pressure during storage. Increasing the pressure within the internal vessel can be performed through self-pressurization by ambient heat input to the cryogenic medium under sealed vessel conditions, or by active pressurization through a gaseous medium by the vent valve. Pressure within the tank is monitored through the use of a pressure gauge. A relief valve is a spring-loaded safety valve that allows the pressure fluid to flow to an auxiliary route at a predetermined pressure value. Ultimately, the rupture disc is a metal-based membrane that has a one-time use and fails at a predetermined differential pressure. Liquid and vent tubes are incorporated –all the way to the tank bottom- for filling and draining of the tank.

It is important however to know the testing campaign required for certification of a pressure vessel in order to be used for cryogenic storage. The next section will provide an outline of the various key requirements imposed by Pressure Vessel Regulation Codes for integration in RLVs.

2.5.3 Testing Guidelines for Space-Flight COPVs

This section presents the different key requirements applicable to COPVs for integration in RLVs. These requirements are linked to the load environment that the COPV will experience during operation. In order for the COPV to be considered as an acceptable tank configuration for use in spaceflight missions, it needs to be subjected to a testing campaign and pass.

In the earlier space systems, - in which pressure vessels were based on metals (high-strength steel, Inconel alloys and titanium) - the original guideline used (MIL-STD-1522 [53] United States Air Force) did not include any safe-life (required period/number of cycles a metal tank can sustain containing a crack) demonstration, nor requirements for the pressure vessels that contain hazardous fluids or exhibit a brittle fracture failure mode; these were included later in [54]-[55]. The design requirements for metallic pressure vessels (e.g. main propellant tank for launch) and metallic pressurized structures (such as battery cases, heat pipes etc.) are incorporated in ANSI/AIAA S-080-1998 [56]. In 2000, ANSI/AIAA S-081 [57] was the first standard to include detailed requirements for composite overwrapped pressure vessels with a metallic liner, which are structures that are susceptible to impact damage and rupture of the composite parts under a long operational period. Additionally, requirements were included in the same standard about the

leak-before-burst (LBB) tank failure mode, which is a design approach where cracks in a metallic liner only grow through the thickness (with increasing number of cycles at MEOP) instead of growing in the in-plane shell direction. Under this approach pressure loss occurs before final catastrophic fracture takes place. However, standards for COPVs with plastic liners for spaceflight vehicles have not yet been established. The Aerospace Corporation issued in 2003 a technical report to provide guidelines on how to implement the requirements of ANSI/AIAA S-081 for an acceptable tank design [57].

Based on [58], in the design, analysis, testing, inspection, operation and maintenance phases of COPVs used in RLVs, the following elements are considered essential and must be addressed to assure the safety of crew and passengers: i) system analysis, ii) vessel strength, iii) fracture control, iv) Leak-Before-Burst (LBB) Failure Mode, v) fatigue (safe-life), vi) damage tolerance, vi) inspection, vii) acceptance proof tests, viii) qualification tests, ix) operation and maintenance, x) composite material strength design allowables, xi) stress rupture life and xii) impact damage control. However, within this study, only the requirements related to vessel strength, acceptance and qualification tests are considered. The strength requirements correspond to the evaluation of the static strength of a pressure vessel and are hereby presented. It is stated in [58], that COPVs should be capable of withstanding internal pressure levels in the expected operating environment without experiencing rupture or collapse. COPVs in RLVs with crew and passengers should have a minimum design ultimate safety factor of 1.5. Compliance to strength specifications should be verified by both structural analysis and testing. For the structural analysis, the detailed geometry, mechanical properties and load environment should be included. Furthermore, the structural analysis should determine stresses (or strains) and displacements resulting from the combined effects of ground and flight external loads, internal pressure and temperature gradients at the tank wall. The flowing stress combination needs are recommended in [58]:

$$K_1 S_{\text{external}} + K_2 S_{\text{thermal}} + K_3 S_{\text{pressure}} \leq \sigma_{\text{ult}} \tag{2.5}$$

where K_1, K_2 and K_3 are design safety factors associated with external loading, thermal stresses and pressure-induced stresses respectively, and S_{external}, S_{thermal} and S_{pressure} are stresses due to external and inertial loads, thermally induced loads and internal pressure correspondingly and σ_{ult} is the tank strength allowable.

Acceptance tests are required to ascertain that materials, manufacturing and hardware are acceptable for use, while qualification tests are used to demonstrate that the design, analysis and manufacturing have led to a design that meets the specification requirements [58]. The steps that need to be performed, are outlined in Fig. 2-16. There are two different approaches: within Approach “A” the ASME Code or DOT Title 49 is not followed and a design and analysis study needs to be coupled to the verification testing. Approach “B” is based on the ASME Code or DOT Title 49 and prescribes an acceptance test (proof testing at 1.5 times the P_{MEOP}) and evaluation of vibration, pressure cycling and burst.

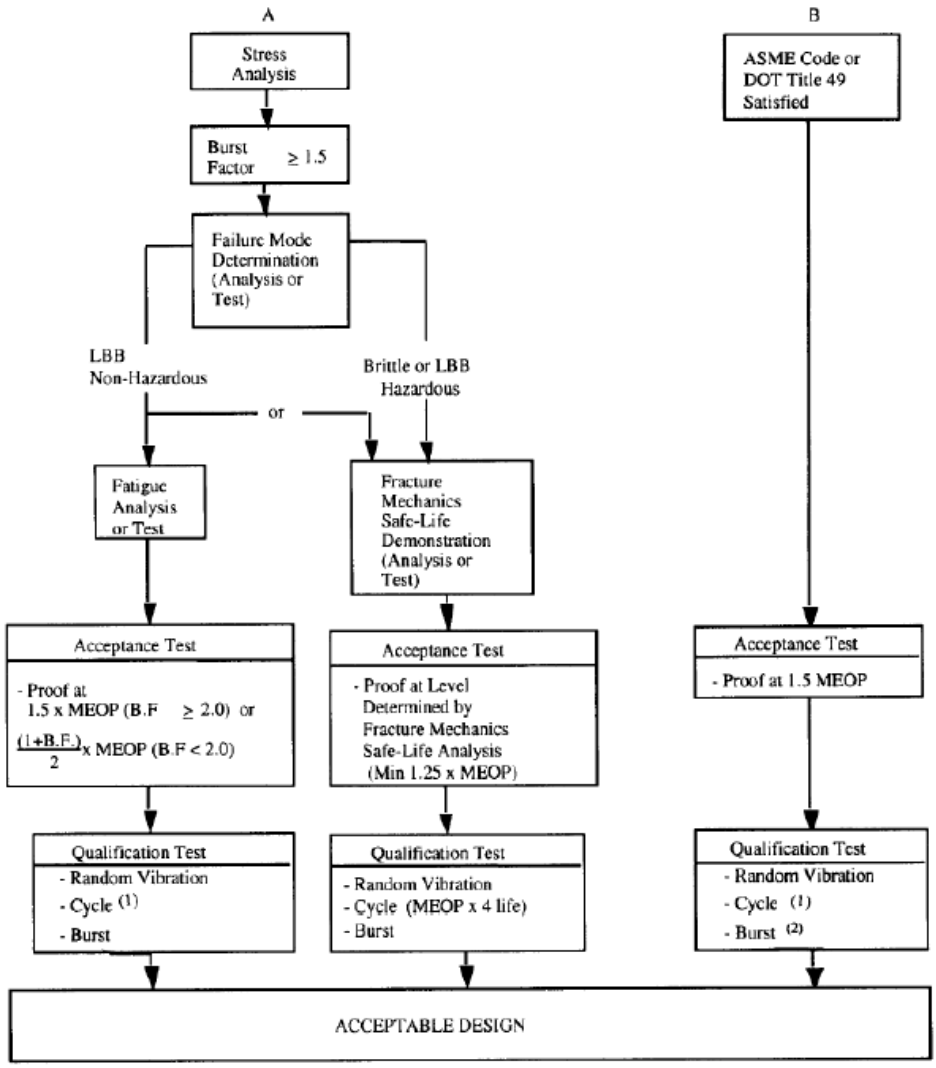

Fig. 2-16: Pressure vessel verification process [58].

As shown in Fig. 2-16, acceptance tests include proof testing and safe-life analysis. Proof testing is carried out at the following pressure:

$$P_{\text{Proof}} = \text{Min}\left[1.5P_{\text{MEOP}}, \frac{\left(1+B_{\text{F}}\right)P_{\text{MEOP}}}{2}\right] \tag{2.6}$$

where B_{F} is the factor applied to P_{MEOP}, to obtain the design pressure. It is essential that no material yielding, damage or pressure loss occurs within this load regime. Safe-life requirements are imposed on a pressure vessel with a non-LBB or hazardous LBB failure mode. For testing purposes, an initial flaw should be incorporated in the liner of the vessel and its size must be identified by non-destructive testing (NDT).

A fracture mechanics growth study should be performed to verify that the COPV has adequate safe-life (a minimum burst factor of 1.25 times the P_{MEOP} for a number of cycles that is four times the service life). Qualification tests consist of random vibration and burst testing as well as pressure cycling at either four times the service life at P_{MEOP} or two times the service life at 1.5 times the P_{MEOP}. For the case of pressure cycling at cryogenic temperatures, no pressure

loss –signifying fuel loss- is allowed to occur within this number of cycles. For burst testing, no burst should occur at B_F times the P_{MEOP}, which implies that at least a safety factor of 1.5 needs to be demonstrated.

2.6 Concluding Remarks

The main goal of this chapter was to provide a literature survey on the common practices and published works in the field of design, analysis and experimental assessment practices of composite cryogenic tanks.

It was shown that extensive work has been carried out on the derivation of the temperature profile of the tank wall as a function of the cryogen state, position and the type of COPV (Type III, Type IV etc.). Additionally, arising thermal stresses and their effect on tank structural integrity has been investigated numerically with the use of Progressive Failure Algorithms. The mechanical behaviour of COPVs under cryogenic environment has been assessed in several works by employing pressure cycling with several cryogens. Fiber Bragg grating (FBG) and acoustic emission (AE) techniques have been incorporated for strain and damage evolution monitoring purposes.

However the issue of employing plastic lined composite overwrapped intersecting spheres (Type IV) for cryogenic storage has not been addressed yet. Issues like understanding the geometrical parameters that control its design and its mechanical and thermal response when subjected to cryogenic chill-down and pressure cycling are yet to be performed.

References

[1] A. Silverstein and E.W. Hall, 'Liquid hydrogen as a jet fuel for high-altitude aircraft', NACA-RM-E55C28a, 1955.

[2] R.L. Middleton, J.M. Stuckey, J.T. Schell, L.B. Mulloy and P.E. Dumire, 'Development of a lightweight external insulation system for liquid-hydrogen stages of the Saturn V vehicle', *Advances in Cryogenic Engineering*, **10**, 216-222, 1964.

[3] http://www.aerospaceweb.org/question/spacecraft/q0285.shtml

[4] W.A. Gaubatz, 'DC-X results and the next step', *AIAA-94-4674*, 1994.

[5] M.F. Ashby, '*Materials selection in mechanical design*', Elsevier Butterworth-Heinemann, 2005.

[6] V.V. Vasiliev, *Composite Pressure Vessels: Analysis, Design and Manufacturing*, Bull Ridge Publishing, 2009.

[7] J. Schneider, M. Dyess, C. Hastings, J. Patterson, J. Noorda and T. DeLay, 'Lightweight cryogenic Composite Over-wrapped Pressure Vessels (COPVs) for launch vehicle applications, *Proceedings of the 48th AIAA Conference*, Hawaii, 2007.

[8] D. Emerson, M. Ruby, D. Almond, M. Turner and A. Clarke, 'All-thermoplastic composite hydrogen storage cylinders for fuel-cell powered passenger vehicles', *Proceedings of the 14th Automotive Composites Conference & Exhibition (ACCE)*, Detroit, 2014.

[9] S.T. Peters, Composite Filament Winding, ASM International Materials Park, 2011.

[10] D.C. Freeman and T.A. Talay, 'Reusable launch vehicle technology program', *Acta Astronautica*, **41**, 777-790, 1997.

[11] 'Final Report of the X-33 Liquid Hydrogen Tank Test Investigation', NASA Marshall Space Flight Center, Huntsville, 2000.

[12] G.D. Brewer, ‘Aviation usage of liquid hydrogen fuel-prospects and problems’, *International Journal of Hydrogen Energy*, **1**, 65-88, 1976.

[13] CHATT Project, ‘Final Report’, 2015.

[14] I.G. Tapeinos, S. Koussios and R.M. Groves, 'Design and analysis of a multi-cell subscale tank for liquid hydrogen storage', *International Journal of Hydrogen Energy*, **41**, 3676-3688, 2016.

[15] S.K. Mital, J.Z. Gyekenyesi, S.M. Arnold, R.M. Sullivan, J.M. Manderscheid and P.L.N. Murthy, ‘Review of Current State of the Art and Key Design Issues With Potential Solutions for Liquid Hydrogen Cryogenic Storage Tank Structures for Aircraft Applications’, *NASA/TM-214346*, 2006.

[16] D. Verstraete, P. Hendrick, P. Pilidis and K. Ramsden, ‘Hydrogen fuel tanks for subsonic transport aircraft’, *International Journal of Hydrogen Energy*, **35**, 11085-11098, 2010.

[17] J. Ingram, J. Nahon, Y. Amouyal and P. Stadler, ‘ Cryogenic fuel tanks for the Clip-Air plane’, Clip-Air: Engineering Report, EPFL University, 2012.

[18] R.D. McCarty, ‘Thermophysical properties of Helium-4 from 2 to 1500K with pressures to 1000 atmospheres’, US Department of Commerce: National Bureau of Standards, 1972.

[19] L. Raffaelli, ‘PhD Thesis: Thermomechanics of Fiber Reinforced Epoxies for Cryogenic Pressurized Contaiment’, TU Munich, 2006.

[20] J.T. Wang, T.F. Johnson, D.W. Sleight and E. Saether, ‘Cryogenic tank structure sizing with structural optimization method’, *Proceedings of the 19th Applied Aerodynamics Conference*, Anaheim, 2001.

[21] E. Lisowski and W. Czyzycki, ‘Transport and storage of LNG in container tanks’, *Journal of KONES Powertrain and Transport*, **18**, 193-201, 2011.

[22] C.A. Stephens, G.J. Hanna and L. Gong, ‘Thermal-fluid analysis of the fill and drain operations of a cryogenic fuel tank’, NASA Technical Memorandum 104273, 1993.

[23] G.J. Hanna and C.A. Stephens, ‘Predicted thermal response of a cryogenic fuel tank exposed to simulated aerodynamic heating profiles with different cryogens and fill levels’, NASA Contractor Report 4395, 1991.

[24] K-H. Kim, H-J. Ko, K. Kim, Y-W. Kim and K-J. Cho, ‘Analysis of heat transfer and frost layer formation on a cryogenic tank wall exposed to the humid atmospheric air’, *Applied Thermal Engineering*, **29**, 2072-2079, 2009.

[25] J.D. Yonko and C.F. Sepsy, ‘An investigation of the thermal conductivity of frost while forming on a flat horizontal plate’, *ASHRAE Transactions*, **73**, 1-11,1967.

[26] P.J. Mago and S.A. Sherif, ‘Frost formation and heat transfer on a cold surface in ice fog’, *International Journal of Refrigeration*, **28**, 538-546, 2005.

[27] W. Xu, Q. Li and M. Huang, ‘Design and analysis of liquid hydrogen storage tank for high-altitude long-endurance remotely-operated aircraft’, *International Journal of Hydrogen Energy*, **40**, 16578-16586, 2015.

[28] S. Murugan, M.S. Starvin and K. Muruga Dhas, ‘Thermo-structural analysis of high pressure cryogenic tanks’, *International Journal of Engineering Research & Technology*, **2**, 1730-1738, 2013.

[29] Z. Kang, L. Yanzhong, X. Mengjian and W. Lei, ‘Investigation of the chill-down behavior and thermal stress distribution of a cryogenic tank during the filling process’, *Physics Procedia*, **67**, 342-347, 2015.

[30] G.H. Abumeri, D.N, Kosareo and J.M. Roche, ‘Cryogenic composite tank design for next generation launch technology’, *Proceedings of the 40th AIAA/ASME/SAE/ASEE Joint Propulsion Conference and Exhibit*, 2004.

[31] J. Ju, B.D. Pickle, R.J. Morgan and J.N. Reddy, 'An initial and progressive failure analysis for cryogenic composite fuel tank design', *Journal of Composite Materials*, **41**, 2545,-2568, 2007.

[32] M. Ren, X. Change, H.Y. Xu and T. Li, 'Trans-scale analysis of composite ovewrapped pressure vessel at cryogenic temperature', *Composite Structures*, **160**, 1339-1347, 2017.

[33] S. Choi and B.V. Sankar, 'Micromechanical analysis of composite laminates at cryogenic temperatures', *Journal of Composite Materials*, **40**, 1077-1091, 2007.

[34] S.M. Aceves, J. Martinez-Frias and O. Garcia-Villazana, 'Analytical and experimental evaluation of insulated pressure vessels for cryogenic hydrogen storage', *International Journal of Hydrogen Energy*, **25**, 1075-1085, 2000.

[35] N.L. Newhouse, 'Development of improved composite pressure vessels for hydrogen storage', Hexagon Lincoln Annual Report, 2013.

[36] J.P.B. Ramirez, D. Halm, J.-C. Grandidier, S. Villalonga and F. Nony, '700 bar type IV high pressure hydrogen storage vessen burst-simulation and experimental validation', *International Journal of Hydrogen Energy*, **40**, 13183-13192, 2015.

[37] R.J. Werlink and F. Pena, ' NASA Prototype All Composite Tank Cryogenic pressure tests to Failure with Structural Health Monitoring', *Proceedings of the 10th International Workshop on Structural Health Monitoring*, California, 2015.

[38] J. Schneider, M. Dyess, C. Hastings, J. Patterson, J. Noorda and T. DeLay, 'Lightweight cryogenic composite over-wrapped pressure vessels (COPVs) for launch vehicle applications', Proceedings of the *49th AIAA/ASME/ASCE/AHS/ASC Structures, Structural Dynamics and Materials Conference*, 2007.

[39] D.M. Ray, N.J. Greene, D. Revilock, S. Sneddon and E. Anselmo, 'High pressure composite overwrapped pressure vessel (COPV) development tests at cryogenic temperatures', *Proceedings of the 49th AIAA/ASME/ASCE/AHS/ASC Structures, Structural Dynamics and Materials Conference*, 2008.

[40] R.W. Frischmuth and P.T. Hacker, 'Investigation of plastic tape for lining filament-wound fiber-glass cryogenic propellant tanks', *NASA Technical Note D-3206*, 1966.

[41] R.L. Conder and N.L. Newhouse, 'Cyclic pressure test of a filament-wound vessel containing liquid nitrogen', *Cryogenics*, **20**, 697-701, 1980.

[42] S.M. Aceves, G.D. Berry, G. Petitpas and V. Switzer, 'Thermomechanical Cycling of Thin Liner High Fiber Fraction Cryogenic Pressure Vessels Rapidly Refueled by LH_2 Pump to 700 bar', *Proceedings of the Annual Merit Review: Hydrogen and Fuel Cells*, 2016.

[43] R. Messinger and J. Pulley, 'Thermal-mechanical cyclic test of a composite cryogenic tank for Reusable Launch Vehicles', *Proceedings of the 44th AIAA/ASME/ASCE/AHS/ASC Structures, Structural Dynamics and Materials Conference*, 2003.

[44] Z. Kang, L. Yanzhong, M. Yuan, W. Lei, X. Fushou and W. Jiaojiao, 'Experimental study on coold down characteristics and thermal stress of cryogenic tank during LN2 filling process', *Applied Thermal Engineering*, **130**, 951-961, 2018.

[45] W. Lei, L. Yanzhong, J. Yonghua and M. Yuan, 'Experimental investigation on pressurization performance of cryogenic tank during high-temperature helium pressurization process', *Cryogenics*, **66**, 43-52, 2015.

[46] T. Mizutani, N. Takeda and H. Takeya, 'On-board Strain Measurement of a Cryogenic Composite Tank Mounted on a Reusable Rocket using FBG Sensors', *Structural Health Monitoring*, **5**, 205-214, 2006.

[47] 'Technical Report: Handling of cryogenic liquids', Princeton, 2008.

[48] R. Ono and T. Oda, ‘Minimum ignition energy of hydrogen-air mixture: Effects of humidity and spark duration’, *Journal of Electrostatics*, **65**, 87-93, 2007.

[49] S.K. Mital, J.Z. Gyekenyesi, S.M. Arnold, R.M. Sullivan, J.M. Manderscheid and P.L.N. Murthy, 'Review of Current State of the Art and Key Design Issues With Potential Solutions for Liquid Hydrogen Cryogenic Storage Tank Structures for Aircraft Applications', NASA/TM-214346, 2006.

[50] ASME, ‘Boiler and Pressure Vessel Code: An International Code’, (BPVC Section VIII), 2013.

[51] ASME, ‘B31.3: Process Piping Design’, 2016.

[52] Air Products, ‘Cryogenic liquid containers: Technical Report’, 36047, 2013.

[53] MIL-STD-1522, Standard General Requirements for Safe Design and Operation of Pressurized Missile and Space Systems, United States Air Force, 1972.

[54] MIL-STD-1522A, Standard General Requirements for Safe Design and Operation of Pressurized Missile and Space Systems, United States Air Force, 1984

[55] MIL-STD-1540C, Test Requirements for Launch, Upper-Stage and Space Vehicles, 1994.

[56] ANSI/AIAA S-080, ‘Space Systems—Metallic Pressure Vessels, Pressurized Structures, and Pressure Components’, 1998.

[57] ANSI/AIAA S-081, ‘Space Systems—Metallic Pressure Vessels, Pressurized Structures, and Pressure Components’, 2000.

[58] J.B Chang, ‘Implementation Guidelines for ANSI/AIAA S-081: Space Systems Composite Overwrapped Pressure Vessels’, 2003.

Chapter 3: Research Questions and Methodology

In Section 3.1 the state-of-the-art is summarized and knowledge gaps are identified. In Section 3.2 the research questions and sub-questions are formulated in a concise way. Section 3.3 presents and justifies the methodology that this Thesis will follow in addressing the research questions.

3.1 Discussion of State-of-the-Art

The most important requirements for cryogenic propellant tanks are the following: i) propellant storage at large quantities due to liquid incompressibility, ii) efficient conformation to a given space within the aircraft, iii) safe operation at cryogenic conditions and iv) small surface area to minimize the passive heat from the exterior and thus the propellant boil-off. As mentioned in Chapter 2, cylindrical pressure vessels have been utilized as cryogenic fuel tanks in several published works [1]-[3]. However it was shown in the Cryoplane Project [4] that these configurations are not always the optimal solution for fuel containment, since they result in a considerable unused volume within the aircraft. Haaland [5] showed that conformable tanks can lead to higher volumetric efficiency over packed cylinders when fitted in a prescribed rectangular envelope. In places where the aspect ratio of the enclosing box is closer to 1, the most volumetrically efficient solution is a pressure vessel arrangement that incorporates intersecting spheres (multi-sphere). A multi-spherical pressure vessel leads to weight savings associated with equal membrane strains when subjected to uniform pressure. Additionally, spheres have the minimum surface area for a given volume, which leads to minimization of fuel boil-off.

A novel composite overwrapped multi-spherical tank configuration with a polymer liner is proposed in this Thesis. The tank consists of four spheres partially merged, with uni-directional (UD) carbon fiber straps applied at the merging points to introduce strain compatibility between the spheres and intersections as well as a central hollow tube in which the fiber straps would pass through.

Since the multi-sphere consists of merging shells, a stress analysis based on primary and secondary solutions at the sphere connecting areas (intersections) needs to be sought. The intersection can be idealized as a toroidal shell owing to the fact that a fillet radius is introduced here to reduce stress concentrations locally. The joining of a spherical and a toroidal shell leads to edge bending owing to their non-equal shell deflections. The stress state in the vicinity of junctions and the effect of ring beams in shells have been analyzed in various studies [6]-[9]. Several published works have focused on providing analytical methods to evaluate junction stresses between isotropic intersecting shell elements by using either the principle of virtual work [10], finite difference method [11] or through assessing the exerted transverse shearing forces and moments with the use of an asymptotic integration method [12]-[13]. The theory of thin elastic shells was employed by Chernykh [14] to assess analytically and numerically the stress state developed at the junction of spheres supported on a cylinder and junctions of toroidal shells. Zingoni [15] developed a closed-form solution to calculate junction stress in general shells of revolution joined together on the basis of membrane hypothesis for shells. Intersecting composite shells have also been studied in [16]-[17]. Skopinsky [18] provided a systematic approach for the stress analysis of intersecting composite laminated cylindrical shells by using a Finite Elements (FE) analysis based on 2D laminated shell theory.

Despite the fact that many efforts have focused on the analysis of the junction stresses in various shell assemblies, there is a lack of a convenient analytical solution for the bending induced by merging a composite overwrapped spherical to a toroidal shell, as it relates to the

multi-sphere. Additionally the geometric variables that control the design of a multi-spherical COPV and their effect on the laminate thickness at the intersections -needed for equal strain field at the cells- has not been addressed.

As stated in Chapter 1, conformable pressurized structures have been used in the field of fuel containment as a lightweight and volumetrically efficient solution [19]-[22]. The use of a multi-lobe geometry with intersecting conical cells was reported in the LH_2 tank of X33 vehicle [23]. It was shown in [19] that composite overwrapped intersecting cylinders lead to to higher volumetric efficiency over packed cylinders when fitted in a prescribed rectangular envelope. However, the downside of a cylindrical configuration is the weight penalty introduced by the added hoop windings - to introduce deformation compatibility between the dome and cylinder [24]. On the other hand, spheres lead to weight savings, linked to equal membrane strain response to internal pressure. Furthermore, (as stated in the previous paragraph) spheres have the minimum surface area for a given volume, which results in minimal fuel boil-off. Therefore the intersecting spheres (multi-sphere) are expected to result in both high volumetric efficiency and low weight.

However the volumetric efficiency and the added weight (due to geometric complexity) of a composite overwrapped multi-sphere have not been addressed yet. A comparison of the performance and volumetric efficiency of the multi-sphere to packed cylindrical configurations when fitted in a prescribed box would reveal which configuration is more effective for cryogenic storage.

Thermal residual stresses at the tank wall during chill-down and pressure cycling are very sensitive to the CTE and the engineering properties of the tank wall materials, as it was mentioned in Section 2.4. Therefore the temperature dependency of these properties needs to be evaluated for a more accurate design. This was done previously by performing mechanical testing at several temperatures and by developing realistic fitting functions to interpolate over the entire temperature range of interest. Shrivastava et al. [25] employed a linear interpolation of the experimental measurement values of tensile strength of glass fiber-reinforced polymers (GFRP) under uniaxial loading at cryogenic temperatures, which does not describe accurately the viscoelastic behaviour of composites. The use of a polynomial relationship between composite mechanical properties and temperature was reported in [26].

However linear and polynomial relationships are inconvenient since they may only behave reliably only within the range of the fitted experimental data and would not capture the asymptotic behaviour of tank wall material properties at temperature extremes. The non-linear behaviour of engineering properties and strength indices as a function of temperature needs to be described with relationships that match testing results and behave reliably both inside and outside the measured data range. The obtained temperature dependency of the liner and overwrap materials will enable the accurate evaluation of the stress state at the tank wall throughout cryogenic operation and the derivation of the pressure allowable of the multi-sphere at cryogenic temperatures.

A thorough understanding of the multi-sphere behavior under thermo-mechanical loading through numerical simulation is a valuable asset. As stated in the Section 2.4, the chill-down process of cryogenic tanks has been addressed numerically in various published works [27]-[30]. The effect of pressurization on the ullage gas temperature and the evaporation of cryogenic propellant was analysed in [31] by employing a transient heat transfer analysis.

However, the effect of cryogenic chill-down, pressure cycling and draining at the thermal and structural response of a multi-spherical COPV by incorporating tank wall material properties fitting functions with a physical basis has not been performed yet. In addition, the heat transfer coming from the creation of a frost layer at the outer tank surface -in the absence of thermal insulation- is a critical factor for the evolution of tank wall temperature gradient and has been ignored in most studies.

The experimental assessment of the multi-sphere is crucial, in order to verify of the findings of numerical simulation. Hydrostatic pressure testing would enable the evaluation of strain, the difference between first damage onset and ultimate failure (pressure window) as well as corresponding damage locations. Furthermore, filling with a cryogen and pressure cycling would reveal the thermal and structural response of the multi-sphere under nominal cryogenic operation.

Hydrostatic pressure testing of composite overwrapped pressure vessels (COPVs) at ambient conditions has been reported in several studies [32]-[34]. Blassiau et al. [35] showed that progressive failure of COPVs is controlled by matrix relaxation during pressure increase that leads to an overload of the intact fibers and fiber break clustering.

For the case of cryogenic tanks, there have been several published works on the topic of filling and pressure cycling of COPVs to demonstrate safe operation. Kang et al. [36] performed an experimental study that revealed a correlation between the temperature gradient and the cool down pattern for different locations at the tank. Lei et al. [37] analyzed the effect of active pressurization at the tank thermal response. Strain monitoring through the use of FBGs has been employed in several published works [38]-[40].

Despite the fact that many efforts have focused on the study of progressive failure of composite overwrapped pressure vessels, the evaluation of strain evolution with increasing pressure values as well as the pressure window of composite overwrapped multi-spheres has not been addressed yet. Furthermore, the effect of cryogenic chill-down and pressure cycling on the thermal and structural response of the multi-sphere has not been assessed experimentally yet. Finally, the establishment of a relationship between strain and temperature at the composite overwrap based on obtained experimental results has been ignored.

3.2 Research Questions

In this section the research questions of this Thesis are outlined:

1) Which variables control the design of the multi-sphere?
2) What is the mechanical response of the multi-sphere when subjected to internal pressure?
3) Which is the required laminate thickness at the intersection for uniform strain field?
4) What is the effect of tank geometrical variables on the multi-sphere inner volume, surface area and mass?
5) Is there a combination of values of geometrical variables that leads to maximization of the tank structural performance at ambient and cryogenic conditions?
6) Does the multi-sphere introduce any volumetric efficiency and weight savings in the field of cryogenic fuel containment compared to cylinders?
7) How would the tank wall materials behave over the whole temperature range of tank operation?
8) How would the multi-sphere behave under normal cryogenic operation?
9) Is it feasible to manufacture and test a sub-scale multi-sphere demonstrator?

3.3 Research Methodology

The research methodology is hereby presented chapter by chapter. Each research question will be associated to a plan of actions.

Chapter 4

The composite overwrapped multi-sphere concept is introduced in this Chapter. The basic tank geometry is presented and the geometrical variables that control the multi-sphere design are identified. Stress analysis at the spheres –when subjected to internal pressure- is conducted by employing the linear membrane theory. On the other hand, the stress analysis at the sphere connecting areas (intersections) is based on the evaluation of the force (H) and bending moment (M) uniformly distributed along the sphere/intersection boundary (junction) that ensure the satisfaction of the deflection and rotation compatibility. In this work, the edge force (H) is obtained by subtracting the vertical component of the torus membrane force (T_{ty}) at the sphere/intersection boundary (junction) from the vertical component of the force of the neighboring sphere (T_{sy}). The edge bending moment (M) is calculated by applying rotational compatibility between the sphere and intersection. The required number of external UD straps at the intersections are defined on the basis of introducing equal strain field between the cells. Finally, the effect of the geometrical parameters on the stress state and required laminate thickness at the intersection is evaluated.

This Chapter addresses the first 3 research questions that are related to the analytical derivation of the stress field at the multi-sphere and required laminate thickness at the intersection.

Chapter 5

The derivation of the internal volume, surface area, weight and performance of the multi-sphere as a function of all the geometric variables is conducted in this Chapter. The assessment of the multi-sphere weight and resulting performance is carried out by taking into consideration the required laminate thickness at the intersection (calculated in Chapter 4). A relationship is hereby sought between volumetric efficiency and performance. A comparison study is performed between the multi-spherical and cylindrical COPVs on the basis of volumetric efficiency and structural performance when fitted in a rectangular envelope for cryogenic storage.

This Chapter answers research questions #4,5 and 6 that are related to the evaluation of the volumetric efficiency and performance of the multi-sphere.

Chapter 6

Approximation functions that describe the temperature dependency of the mechanical properties of the liner and overwrap materials are presented in Chapter 6. These functions are based on material testing and literature. The focus is to develop approximation functions that capture the asymptotic behaviour of the properties at temperature extremes, while behaving reliably within the given temperature regime. These extremes are (T_1 = -269 [^{o}C]) and curing temperature of the composite overwrap (T_2 = 125 [^{o}C]). A separate set of fitting constants {a, b, c} is assigned for every approximation function by employing a least squares fit where temperature (T) is the independent variable.

This Chapter addresses research question #7 about the temperature dependency of the tank wall materials.

Chapter 7

A transient numerical thermo-mechanical model –based on Finite Elements (FE)- is developed to simulate the tank wall response at both pressure increase at high and low displacement rate as well as cryogenic chill-down, pressure cycling and draining of the multi-sphere. The high displacement rate case is considered in accordance with the sudden excessive fuel boil-off that can occur in a cryogenic tank. Cryogenic chill-down, pressure cycling and draining are the loads a storage tank is subjected to throughout operation. The temperature dependency of the liner and overwrap materials -derived in Chapter 6- is hereby incorporated. A progressive failure algorithm is incorporated in the FE analysis to check the structural integrity of the liner and overwrap throughout thermo-mechanical loading to analyse the different damage mechanisms that occur at various loading scenarios and to quantify the tank-pressure window. Frost development at the outer surface and cryogen evaporation is taken into consideration for the case of cryogenic operation.

This Chapter answers research question #8 about the thermo-mechanical behaviour of the multi-sphere under cryogenic chill-down and pressure cycling. However this is performed only numerically within this Chapter, since the experimental assessment is carried out in Chapter 8.

Chapter 8

The manufacturing and testing campaign of a sub-scale multi-sphere demonstrator is presented in Chapter 8. The thermo-mechanical performance of the multi-spherical COPV is assessed through hydrostatic burst testing at ambient conditions and pressure cycling at cryogenic conditions (with the use of liquid nitrogen-LN_2 due to safety reasons). Strain evolution is obtained by Digital Image Correlation (DIC) and Fiber Bragg Gratings (FBGs) at room and cryogenic conditions respectively. Temperature is monitored with the use of thermocouples. The evaluation of strain and temperature profiles will enable the evaluation of the heat transfer phenomena at various tank locations (e.g. vapour-free convection, circumferential/tangent thermal conduction, convection associated with LN_2 boiling) as a function of time and their effect on tank behaviour. Additionally, the Acoustic Emission (AE) technique is utilized for damage monitoring during pressurization. The later method will enable the identification of the pressure value and location at which first damage onset and ultimate failure occurs (pressure window). In this chapter an answer is sought to the question of whether the accuracy of the approximation functions of Chapter 6 and results of Chapter 7 are met.

This Chapter answers research question #8 and 9 since the manufacturing and testing of a sub-scale multi-sphere demonstrator is hereby performed.

3.4 Concluding Remarks

The main goal of this chapter was to provide the state-of-the-art practices in the field of design, analysis and experimental assessment of composite cryogenic tanks to assist in identifying knowledge gaps in the analysis of thermo-mechanical loading of conformal structures. The research questions of this Thesis as well as the proposed research methodology to address these questions were presented in this Chapter.

References

[1] D. Verstraete, P. Hendrick, P. Pilidis and K. Ramsden, 'Hydrogen fuel tanks for subsonic transport aircraft' *International Journal of Hydrogen Energy*, **35**, 11085-11098, 2010.

[2] D. Verstraete, 'Long range transport aircraft using hydrogen fuel', *International Journal of Hydrogen Energy*, **38**, 14824-14831, 2013.

[3] B. Khandelwal and R. Singh, 'Hydrogen powered aircraft: the future of air transport', *Progress in Aerospace Sciences*, **60**, 45-59, 2013.

[4] A. Westenberger, 'Liquid hydrogen fuelled aircraft – system analysis. Final Technical Report-CryoPlane Project'. GRD1-1999-10014, 2003.

[5] A. Haaland, 'High-Pressure Conformable Hydrogen Storage for Fuel Cell Vehicles', *Proceedings of the U.S. DOE Hydrogen Program Review*, California, 463-469, 2000.

[6] D.S. Houghton, A.S.L. Chan, 'Discontinuity effects at the junction of a pressurized cylinder and end bulkhead', *Proceedings of the Institution of Mechanical Engineers*, **175**, 1847-1982, 1961.

[7] W.H. Wittrick, 'Non-linear discontinuity stresses in shells of revolution under internal pressure', *International Journal of Engineering Science*, **2**, 179-188, 1964.

[8] J. Jayaraman and K.P. Rao, 'Junction reinforced pressurized spherical shell with a conical nozzle', *Thin-Walled Structures*, **3**, 345-363, 1985.

[9] J.G. Teng 'Intersections in steel shell structures', *Progress in Structural Engineering and Materials*, **2**, 459-471, 2000.

[10] AK.Kulkarni, K.W. Neale and F. Ellyin, 'Consistent theories for intersecting shells', *Nuclear Engineering Design*, **35**, 377-385, 1975.

[11] H. Kraus, G.G. Bilodean and B.F. Langer, 'Stresses in thin-walled pressure vessels with ellipsoidal heads', *Journal of Engineering Industry*, **83**, 29-42, 1961.

[12] W. Flügge, 'Stresses in shells', *Springer*, 1960.

[13] S. Timoschenko and S. Woinowsky-Krieger, 'Theory of Plates and Shells', *Mc Graw-Hill*, 1959.

[14] K.F. Chernykh, 'Compound shells of revolution', **2**, 7-48, 1968.

[15] A. Zingoni, 'Stresses and deformations in egg-shaped sludge digestors: discontinuity effects', *Engineering Structures*, **23**, 1373-1382, 2001.

[16] H.V. Lakshminarayana, 'Finite element analysis of laminated composite shell junctions', *Computers and Structures*, **6**, 11-15, 1976.

[17] Z.A. Galishin, 'Analysis of the axi-symmetric thermoelastic state of branced laminated transversally isotropic shells', *International Applied Mechanics*, **31**, 275-280, 1995.

[18] N.V. Skopinsky, 'Theoretical analysis of composite shell intersection', *The Journal of Strain Analysis for Engineering Design*, **34**, 107-116, 1999.

[19] D.R. Elliot, E. Francois and D. McDonald, 'Deep submergence vessels of interconnected radial-filament spheres', USA Patent 3608767, 1970.

[20] M.J. Warner, 'End closure modules for multi-cell pressure vessels and pressure vessels containing the same', USA Patent 6412650, 2002.

[21] M.D. Blair, D.G. Turner, R.K. Kunz, M.J. Warner, K.W. Davis, F.E. Wolcott and J.D. Bennett, 'Composite conformable pressure vessel', USA Patent RE41412E, 2010.

[22] K.W. Richards and N.G. Christensen, 'Seamless multi-section pressure vessel', USA Patent 8020722B2, 2011.

[23] 'Final Report of the X-33 Liquid Hydrogen Tank Test Investigation', NASA Marshall Space Flight Center, Huntsville, 2000.

[24] V.V. Vasiliev, *Composite Pressure Vessels: Analysis, Design and Manufacturing*, Bull Ridge Publishing, 2009.

[25] A.K. Shrivastava, MDN. Hussain, 'Effect of low temperature on mechanical properties of bidirectional glass fiber composites', *Journal of Composite Materials* , **42**, 2407-2432, 2008.

[26] J. Bausano, S. Boyd, J. Lesko, S. Case, 'Composite Life under Sustained Compression and One Sided Simulated Fire Exposure: Characterization and Prediction' *Proceedings of Composites in Fire-3*, Newcastle, 2003.

[27] S. Murugan, M.S. Starvin and K. Muruga Dhas, 'Thermo-structural analysis of high pressure cryogenic tanks', *International Journal of Engineering Research & Technology*, **2** 1730-1738, 2013.

[28] A. Hedayat, W. Cartagena and A.K. Majumdar, 'Modeling and analysis of chill and fill processes for the cryogenic processes for the cryogenic storage and transfer engineering development unit tank', *Cryogenics*, **74**, 106-112, 2016.

[29] K.A. Keefer and J. Hartwig, 'Development and validation of an analytical charge-hold-vent model for cryogenic tank chill-down', *International Journal of Heat Mass Transfer*, **101**, 175-189, 2016.

[30] C.A. Stephens, G.J. Hanna and L. Gong, 'Thermal-fluid analysis of the fill and drain operations of a cryogenic fuel tank', NASA Technical Memorandum 104273, 1993.

[31] K.H. Kim, H.-J. Ko, K. Kim, Y.-S. Jung, S.-H. Oh and K.-J. Cho, 'Transient thermal analysis of cryogenic oxidizer tank in the liquid rocket propulsion system during the prelaunch helium gas pressurization', *Journal of Engineering Thermophysics*, **21**, 1-15, 2012.

[32] W.H. Tam, P.S. Griffin and A.C. Jackson, 'Design and manufacture of a composite overwrapped pressurant tank assembly', *Proceedings of the 38th AIAA/ASME/SAE/ASEE Joint Propulsion Conference & Exhibit*, Indiana, 2002.

[33] L. Wang, C. Zheng, H. Luo, S. Wei and Z. Wei, 'Continuum damage modeling and progressive failure analysis of carbon fiber/epoxy composite pressure vessel', *Composite Structures*, **134**, 475-482, 2015.

[34] J.P.B. Ramirez , D. Halm, J-C. Grandidier, S. Villalonga and F. Novy, '700 bar type IV high pressure hydrogen storage vessel burst – Simulation and experimental validation', *International Journal of Hydrogen Energy*, **40**, 13183-13192, 2015.

[35] S. Blassiau, A.R. Bunsell and A. Thionnet, 'Micromechanics, damage and life prediction of carbon fibre composite pressure vessels', *Proceedings of the 11th ECCM*, Rhodes, 2004.

[36] Z. Kang, L. Yanzhong, M. Yuan, W. Lei, X. Fushou and W. Jiaojiao, 'Experimental study on cool down characteristics and thermal stress of cryogenic tank during LN2 filling process', *Applied Thermal Engineering*, **130**, 951-961, 2018.

[37] W. Lei, L. Yanzhong, J. Yonghua and M. Yuan, 'Experimental investigation on pressurization performance of cryogenic tank during high-temperature helium pressurization process', *Cryogenics*, **66**, 43-52, 2015.

[38] W. Blazejewski, A. Czulak, P. Gasior, J. Kaleta, R. Mecha, 'SMART composite high pressure vessels with integrated Optical Fiber Sensors', *Proceedings of SPIE*, **7647**, 2010.

[39] A. Güemes, M. Frovel, J.M. Pintado, I. Baraibar, E. del Olmo, 'Fiber optic sensors for hydrogen cryogenic tanks', *Proceedings of the 2nd European Conference on Structural Health Monitoring*, Munich, 2004.

[40] I. Latka, W. Ecke, B. Höfer, C. Chojetzki and A. Reutlinger, 'Fiber optic sensors for the monitoring of cryogenic spacecraft tank structures', *Proceedings of SPIE*, **5579**, Bellingham-WA, 2004.

Chapter 4: Introduction to Multi-Spherical COPVs

This section contains the stress analysis of a novel thin-walled composite over-wrapped multi-cell structure when considering only internal pressure loads. It is crucial to perform this analysis since the spheres and the sphere connecting areas (intersections) must have the same radial expansion as the spheres, in order to eliminate secondary loading (bending) effects. A method is hereby presented to address the loads exerted at the multi-sphere that relies on the deformation compatibility between the spheres and intersections and takes into account the secondary loads exerted at the intersections. Additionally, the geometrical variables that control the design of the multi-spherical structure are identified and their effect on the tank's mechanical behavior are analyzed.

4.1 Basic Geometry

A multi-sphere can consist of any given number of intersecting spherical cells. A conceptual design of the multi-cell structure of interest (quadri-spherical tank in this case) is depicted in Fig. 4-1, with all centroids in the same plane and with all spherical elements of the same radius. This configuration is hereinafter referred to as a multi-sphere. It can be seen that every sphere connecting area (intersection) is a curve that lies in a single plane composed of two circular cross sections. The main parameters that control this tank geometry are the radius of the spheres (R), the distance between the centroids (d) and number of cells in the axial (m_{cells}), transverse (n_{cells}) and height (p_{cells}) directions.

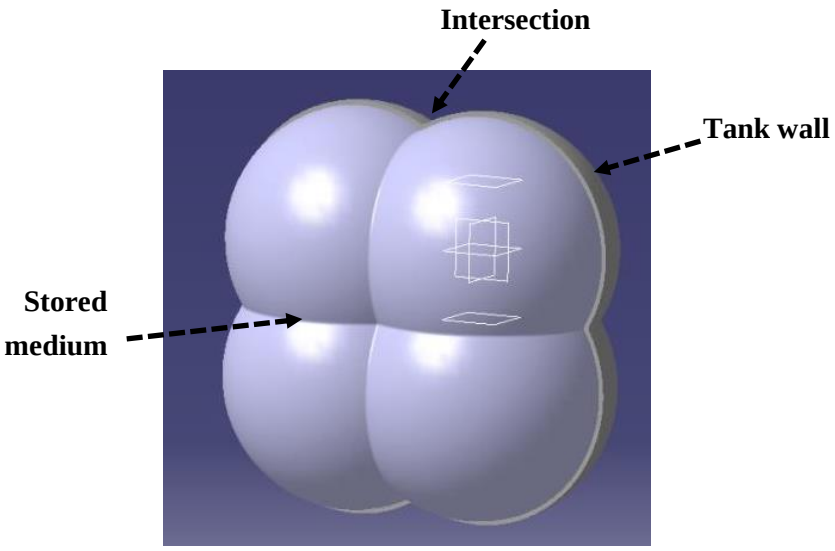

Fig. 4-1: Quadri-spherical tank with equal shell radius for all cells (multi-sphere).

Due to internal pressure imposed on the thin tank wall, a membrane response will be exerted on the spherical elements while a resultant outward radial load will cause significantly higher deformations and stress concentrations at the intersections [1]. Therefore, the issue of reinforcement of the intersections to meet the structural requirements becomes crucial. The intersection must have the same expansion as the spheres to eliminate secondary loading (bending) at the intersection regions. The reinforcement can be established by two different methods: internal webs (Fig. 4-2a) and external reinforcing rings (UD straps) (Fig. 4-2b). Reinforcement webs introduce a large weight penalty on the tank and are considered complex from a manufacturing point of view [2]. On the other hand, the configuration with external reinforcing rings relies on the tailorability of the composite laminate at the intersection, leading to minimum added weight and reducing manufacturing complexity [3]-[5]. Therefore, the second

reinforcing strategy is chosen as the junction reinforcing strategy and is thus adopted in corresponding calculations.

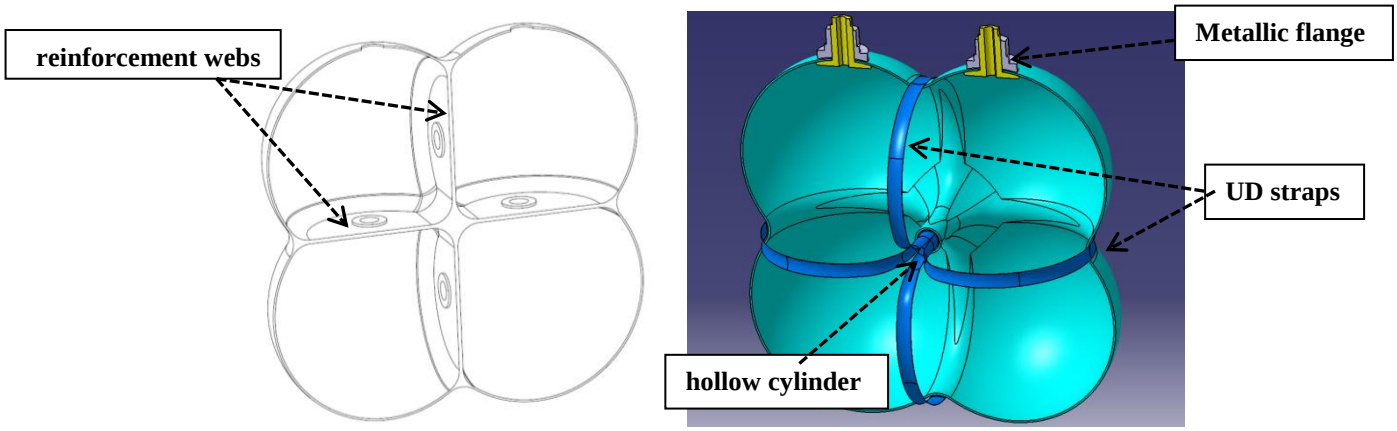

Fig. 4-2: Two different approaches for intersection reinforcement: a) internal webs and b) external UD carbon straps.

A hollow section in the tank center is required to ensure the continuity of the reinforcing straps by letting them pass through, thereby allowing them to form a continuous 3D curve (Fig. 4-2b). The hollow cylinder should allow space for all necessary rovings to pass through, whereby the number is determined by deformation compatibility requirements. Additionally, metallic flanges are introduced to the geometry, for tank filling, draining and fuel delivery throughout operation.

4.2 Intersection Geometry

A fillet radius is needed at the intersection to reduce the stresses at the region, owing to the fact that the pressure is distributed over a larger surface area. This section investigates the effect of the intersection morphology on its curvature as a function of arc length.

The initial approach was to employ a constant radius at the intersection. This will result in a transition from a positive to negative curvature with constant values at the sphere and junction areas respectively. The formed shape at the sphere joining area can now be idealized as a toroidal shell (Fig. 4-3). The symbols h_{tip} and $h_{junction}$ correspond to the height of the intersection at its tip and the height of the junction respectively, R is the sphere radius, R_{fillet} is the fillet radius at the intersection and μR and yR the dimensionless tip-junction and tip-centroid distances respectively. A strain jump is expected at the sphere-torus boundary owing to the fact that the joining elements consist of different geometry and curvature and will deflect differently under uniform pressure [6].

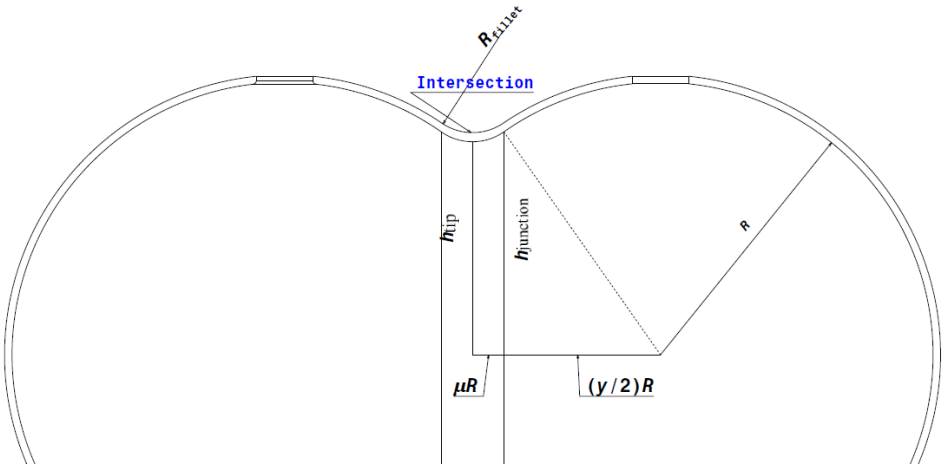

Fig. 4-3: Schematic of the sphere connecting area (intersection).

An interpolating spline can be employed at the intersection to introduce a curvature match between the sphere and the intersection at the junction point. This match will result in a smooth strain increase at the intersection instead of a strain jump. A fifth order polynomial function can be used owing to the position, tangency and curvature compatibility conditions at the intersection tip and the junction point (Table 4-1):

$$P(x) = a + bx + cx^2 + dx^3 + ex^4 + fx^5 \tag{4.1}$$

Table 4-1: Spline-sphere shape compatibility equations.

Compatibility	Intersection Tip	Junction
Location	$P(0) = Rh_{\text{tip}}$	$P(\mu R) = Rh_{\text{junction}}$
Tangency	$P'(0) = 0$	$P'(\mu R) = \dfrac{\frac{y}{2} - \mu}{\sqrt{1 - \left(\frac{y}{2} - \mu\right)^2}}$
Curvature	$\dfrac{P''(0)}{\left(1 + P'(0)^2\right)^{3/2}} = \dfrac{1}{R_{\text{fillet}}}$	$\dfrac{P''(\mu R)}{\left(1 + P'(\mu R)^2\right)^{3/2}} = -\dfrac{1}{R}$

where $h_{\text{tip}} = \left(\sqrt{1 - \left(\frac{y}{2}\right)^2}\right)$ and $h_{\text{junction}} = \left(\sqrt{1 - \left(\frac{y}{2} - \mu\right)^2}\right)$. The coefficients *a*, *b*, *c*, *d*, *e*, *f* of the interpolating spline can be identified by solving the system of equations outlined in Table 4-1. A cubic spline can also be incorporated for the case that there is not a constraint in the coordinate and curvature values at the sphere-intersection joining point. The new position, tangency and curvature compatibility conditions are presented in Table 4-2:

$$P(x) = a + bx + cx^2 + dx^3 \tag{4.2}$$

Table 4-2: Spline-sphere shape compatibility equations.

Compatibility	Intersection Tip	Junction
Location	-	$P(\mu R) = Rh_{\text{junction}}$
Tangency	$P'(0) = 0$	$P'(\mu R) = \dfrac{\frac{y}{2} - \mu}{\sqrt{1 - \left(\frac{y}{2} - \mu\right)^2}}$
Curvature	-	$\dfrac{P''(\mu R)}{\left(1 + P'(\mu R)^2\right)^{3/2}} = -\dfrac{1}{R}$

A cubic spline with a linear strain distribution can be obtained by considering $\mu = y/2$ in Eq.(4.2) and the conditions of Table 4-2. A comparison of the behaviour between the intersection with a constant radius (R_{fillet} = 315 [mm]) and a cubic spline for R = 145 [mm] is presented in Fig. 4-4a, for a small difference in the intersection profile. It can be seen in Fig. 4-4b that indeed a linear variation of curvature was obtained for the spline, while a constant fillet radius led to a very sudden curvature change at the junction point.

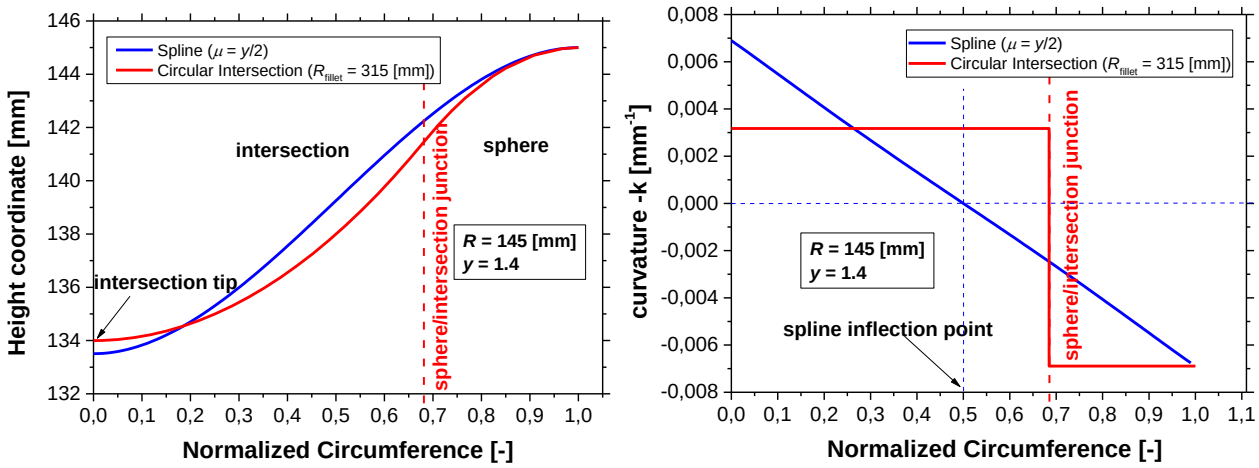

(a) **(b)**

Fig. 4-4: a) Intersection profile and b) corresponding curvature for a circular intersection (R_{fillet} = 315 [mm]) and b) a spline ($\mu = y/2$).

The distribution of the meridional and hoop membrane forces over the spherical cell and intersection from a static structural FE analysis (ABAQUS Software Package) is shown in Fig. 4-5. The tank was subjected to P = 5.7 [bar], which corresponds to 1.5 times the maximum expected operating pressure (P_{MEOP}) of the SpaceLiner LH_2 tank (Fig. 2-7). The composite ply engineering properties listed in Table 4-3 were utilized, where E_{11} is the ply longitudinal modulus, E_{22} is the transverse modulus, G_{12} is the in-plane shear modulus and ν_{12} is the major Poisson's ratio. It is shown that the intersection with a spline led to a linear meridional force distribution, while a sudden force jump was obtained for the circular intersection at the junction.

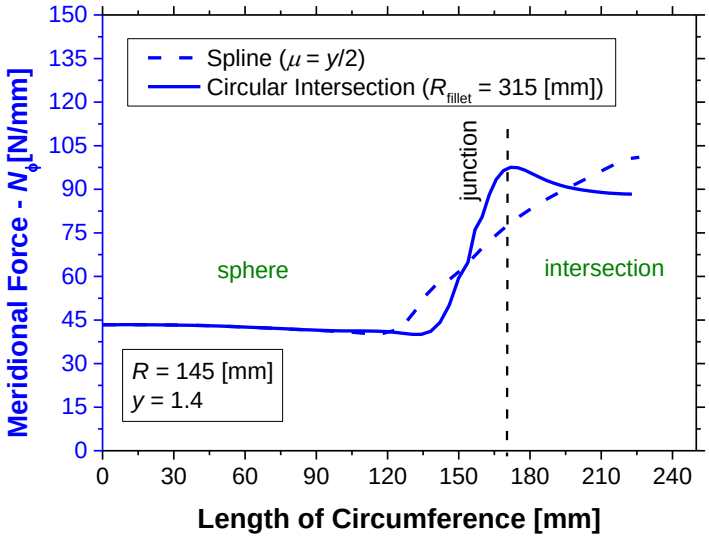

Fig. 4-5: Distribution of the meridional force (N_φ) over the spherical shell and intersection for a) a circular intersection (R_{fillet} = 315 [mm]) and b) a spline ($\mu = y/2$) based on FE analysis.

Table 4-3: Ply engineering properties (USN150A/K51) [7].

E_{11} (GPa)	E_{22} (GPa)	G_{12} (GPa)	ν_{12}	t_{ply} (mm)
128	8.7	4.74	0.28	0.14

It is shown in Fig. 4-5 that the peak force was very similar for both intersection profiles. Based on this outcome and geometrical simplicity the focus of this Thesis will be from now on intersections with a circular cross-sections.

4.3 Stress Analysis

4.3.1 Spherical Membranes

The stress analysis of the spheres relies on the consideration of a simple, rotationally symmetric shell of revolution, which is obtained by rotating a curve (meridian) about an axis of revolution. Fig. 4-6 depicts the meridian of a shell of revolution with R_m, R_p being the radii of curvature of the meridian and the parallel directions respectively. The distance of a point on the shell with the axis of rotation is given by $R = R_p \sin\varphi$. A membrane element is formed by two adjacent meridians and two parallel circles (Fig. 4-6). The meridional force (per unit length) is denoted as N_φ, while N_θ and $N_{\varphi\theta}$ correspond to the hoop and in-plane shear forces at the element. The angle $d\theta$ is defined by the two meridians, while the angle $d\varphi$ is defined by the two parallels.

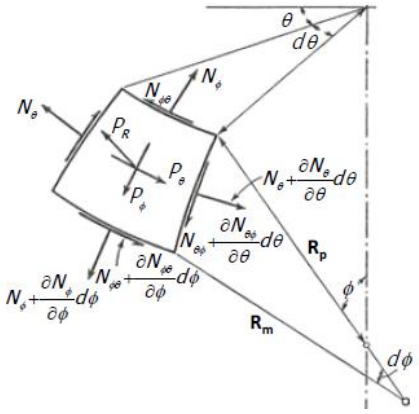

Fig. 4-6: Stress equilibrium at an element of a shell of revolution [5].

The equilibrium of in-plane stresses on that membrane element will result in three equations to determine three unknown forces:

$$\sum F_{\varphi}=0\Rightarrow\frac{\partial N_{\varphi}}{\partial\varphi}+R_{\mathrm{m}}\frac{\partial N_{\varphi\theta}}{\partial\theta}-N_{\theta}R_{\mathrm{m}}\cos\varphi+p_{\varphi}RR_{\mathrm{m}}=0 \tag{4.3}$$

$$\sum F_{\theta}=0\Rightarrow R_{\mathrm{m}}\frac{\partial RN_{\theta}}{\partial\theta}+\frac{\partial\left(N_{\varphi\theta}\right)}{\partial\varphi}+N_{\varphi\theta}R_{\mathrm{m}}\cos\varphi+p_{\theta}RR_{\mathrm{m}}=0 \tag{4.4}$$

$$\sum F_{\mathrm{r}}=0\Rightarrow\frac{N_{\varphi}}{R_{\mathrm{m}}}+\frac{N_{\theta}}{R_{\mathrm{p}}}=p_{\mathrm{r}} \tag{4.5}$$

where p_φ and p_θ correspond to pressure in the meridional and hoop directions respectively and p_r is pressure in the radial direction. Since pressure p_r is uniform and $p_\varphi = p_\theta = 0$, the applied loads are rotationally symmetric which means that all derivatives of θ are zero in Eq. (4.3). Therefore Eq. (4.4) can be eliminated and Eq. (4.3) becomes:

$$\frac{\partial RN_{\varphi}}{\partial\varphi}=N_{\theta}R_{\mathrm{m}}\cos\varphi \tag{4.6}$$

Solving for N_θ in Eq. (4.5) and subsequently substituting it in Eq.(4.6) results in N_φ being:

$$N_{\varphi}=\frac{p_{\mathrm{r}}}{R_{\mathrm{p}}\sin^{2}\varphi}\int_{0}^{R}RdR \tag{4.7}$$

Replacing $R=R_{\mathrm{p}}\sin\left(\varphi\right)$ in Eq. (4.7) and considering the integration constant as zero for axi-symmetric shells leads to:

$$N_{\varphi}=\frac{p_{\mathrm{r}}R_{\mathrm{p}}}{2} \tag{4.8}$$

Substitution of Eq. (4.8) in Eq. (4.5) results in:

$$N_{\theta}=\frac{p_{\mathrm{r}}R_{\mathrm{p}}\left(2R_{\mathrm{m}}-R_{\mathrm{p}}\right)}{2R_{\mathrm{m}}} \tag{4.9}$$

Division of Eq. (4.9) by Eq. (4.8) provides the ratio of shell line forces and by dividing the forces by the shell thickness (t) provides the ratio of membranes stresses:

$$\frac{\sigma_\theta}{\sigma_\varphi} = 2 - \frac{R_\mathrm{p}}{R_\mathrm{m}} \tag{4.10}$$

where σ_φ, σ_θ are the in-plane shell stresses in the meridian and parallel directions respectively. It is evident in the above equation that the shell stresses depend on the radii of curvature of the shell. For the case of the spherical shell $R_\mathrm{m} = R_\mathrm{p}$ and thus the stress ratio $\sigma_\theta/\sigma_\varphi$ becomes 1.

For the composite plies are employed at the membrane, the stiffness matrix of a single layer at the tank wall ($\mathbf{C}_\mathrm{o}$) can be derived from [8]:

$$\mathbf{C}_\mathrm{o} = \begin{bmatrix} \frac{E_{11}}{1-\nu_{12}\nu_{21}} & \frac{\nu_{12}E_{22}}{1-\nu_{12}\nu_{21}} & 0 \\ \frac{\nu_{12}E_{22}}{1-\nu_{12}\nu_{21}} & \frac{E_{22}}{1-\nu_{12}\nu_{21}} & 0 \\ 0 & 0 & G_{12} \end{bmatrix} \tag{4.11}$$

where the minor Poisson's ratio is given by: $\nu_{21} = \frac{\nu_{12}E_{22}}{E_{11}}$, ν_{12} is the major Poisson's ratio and E_{11}, E_{22} and G_{12} are the ply tensile moduli in the parallel and transverse directions and the in-plane shear modulus respectively. The resulting stiffness of the laminate is given by [8]:

$$\mathbf{C}_\mathrm{lam} = \frac{1}{\sum_{k=1}^{n} t_\mathrm{ply}} \sum_{k=1}^{n} \mathbf{C}_{[\varphi]_k} t_\mathrm{ply} \tag{4.12}$$

where:

$$\mathbf{C}_{[\varphi]_\mathrm{k}} = \mathbf{T}_{[\varphi]_\mathrm{k}} \cdot \mathbf{C}_\mathrm{o} \cdot \mathbf{T}^\mathrm{T}_{[\varphi]_\mathrm{k}} \,,\; \mathbf{T}_{[\varphi]_\mathrm{k}} = \begin{bmatrix} \cos^2\varphi & \sin^2\varphi & \sin 2\varphi \\ \sin^2\varphi & \cos^2\varphi & -\sin 2\varphi \\ -\cos\varphi\sin\varphi & \cos\varphi\sin\varphi & \cos 2\varphi \end{bmatrix}_\mathrm{k} \tag{4.13}$$

whereby φ represents the different lamina angles, t_ply is the ply thickness, n the number of layers, $\mathbf{T}_{[\varphi]_\mathrm{k}}$ is the stress transformation matrix and $\mathbf{C}_{[\varphi]_\mathrm{k}}$ is the rotated ply stiffness matrix. The shell stresses vector is given by multiplying the laminate stiffness matrix by the shell strains vector:

$$\begin{bmatrix} \sigma_\varphi \\ \sigma_\theta \\ 0 \end{bmatrix} = \mathbf{C}_\mathrm{lam} \cdot \begin{bmatrix} \varepsilon_\varphi \\ \varepsilon_\theta \\ 0 \end{bmatrix} \tag{4.14}$$

where ε_φ and ε_θ are shell strains in the meridional and parallel directions respectively. Finally, the layer stresses of the material coordinate system can be expressed as:

$$\begin{bmatrix} \sigma_1 \\ \sigma_2 \\ 0 \end{bmatrix} = \mathbf{C}_\mathrm{o} \cdot (\mathbf{T}^\mathrm{T}_{[\varphi]_\mathrm{k}})^{-1} \cdot \mathbf{S}_\mathrm{lam} \cdot \begin{bmatrix} \sigma_\varphi \\ \sigma_\theta \\ 0 \end{bmatrix} \tag{4.15}$$

whereby $\mathbf{S}_\mathrm{lam} = \mathbf{C}^{-1}_\mathrm{lam}$ is the laminate compliance matrix. As a result the layer strains are derived from:

$$\begin{bmatrix} \varepsilon_1 \\ \varepsilon_2 \\ 0 \end{bmatrix} = \mathbf{C}_{\text{lam}} \cdot \begin{bmatrix} \sigma_1 \\ \sigma_2 \\ 0 \end{bmatrix} \tag{4.16}$$

According to Vasiliev et al. [4] the structural efficiency in any pressurized shape is maximal when the laminate is in a state of equal biaxial extension. Therefore the condition $\varepsilon_\varphi = \varepsilon_\theta$ leads to the optimal solution, which can be obtained with a quasi-isotropic (QI) lay-up for a sphere owing to equal in-plane stiffness in all directions.

4.3.2 Intersections

The joining of a sphere and a torus at the intersection region leads to edge bending owing to their non-equal deflections. The assessment of the stress state at the intersections relies on the evaluation of the bending loads and superposition on the membrane stresses, since membrane solutions cannot always satisfy the boundary conditions of displacement and rotations compatibility. As stated previously, adding UD straps will change the deflection of the intersection and the right number of UD straps will even lead to strain compatibility between the cells. An approach to evaluate the stress state at the junction and the required number of UD straps at the meridional and hoop directions -based on the asymptotic integration method [9]- is presented below.

The required number of UD straps at the multi-sphere is directly related to membrane forces and moments in the meridional (N_φ, M_φ) and hoop (N_θ, M_θ) directions at the sphere-junction boundary, which in turn is dependent on the exerted shear force per unit length (Q_θ) and angular rotation (V) at that edge.

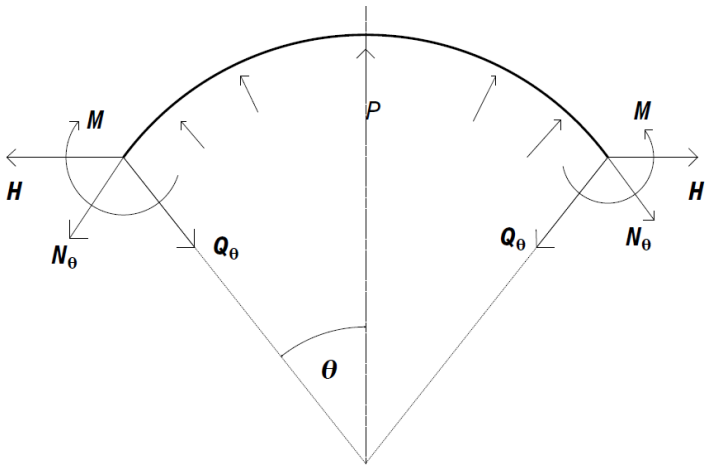

Fig. 4-7: Edge forces and bending moment at a shallow spherical cell.

Membrane forces are dependent on the exerted shear force per unit length (Q_θ) at that edge (Fig. 4-7), while moments are dependent on the edge angular rotation (V) according to shell equilibrium considerations [10]:

$$N_\varphi = -\frac{dQ_\theta}{d\theta}, N_\theta = -Q_\theta \cot(\theta), M_\varphi = \nu M_\theta, M_\theta = -\frac{E^{\text{b}}_{\theta\text{sphere}} dV}{R d\theta} \tag{4.17}$$

where $E^{b}_{\theta sphere}$ is the equivalent bending modulus of the laminate in the hoop direction (θ) at the sphere given by by Eq.(4.18) [11]:

$$E^{b}_{\theta sphere} = \frac{12\left(D_{\varphi\varphi}D_{\theta\theta} - D^{2}_{\varphi\theta}\right)}{t^{3}D_{\varphi\varphi}} = E^{b}_{\varphi sphere} \tag{4.18}$$

$$\text{where } \mathbf{D}_{sphere} = \frac{1}{3}\sum_{k=1}^{n}\mathbf{C}_{[\varphi]_k}\left(z_k^3 - z_{k-1}^3\right)$$

and $\mathbf{D}_{sphere}$ corresponds to the [3x3] bending stiffness matrix of the laminate at the sphere, z_k is the distance of a ply from the laminate mid-plane, t_{ply} is the cured ply thickness (Fig. 4-8), κ is the layer number and n is the number of layers (at least 3). Additionally $D_{\varphi\varphi}$, $D_{\theta\theta}$, $D_{\varphi\theta}$ are terms from the bending stiffness terms of the laminate ($\mathbf{D}_{sphere}$).

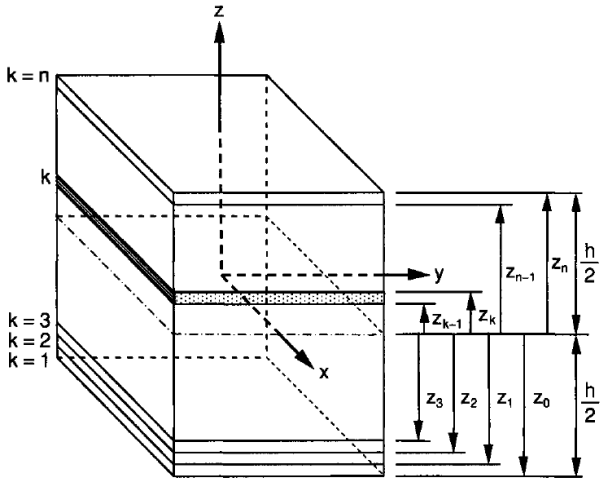

Fig. 4-8: Geometry of an n-layer laminate.

The steps to derive Q_θ are provided hereby. For thin shells that are not shallow, the shell equilibrium governing equations are given below [5]:

$$\frac{d^2Q_\theta}{d\theta^2} = E_{sphere}tV\,,$$
$$\frac{d^2V}{d\theta^2} = -\frac{R}{E^{b}_{sphere}}Q_\theta \tag{4.19}$$

where R is the sphere radius, t is the shell thickness, E_{sphere} is the equivalent laminate membrane modulus of the spherical shell respectively given by Eq.(4.20) [11]:

$$E_{sphere} = \frac{1}{t}\frac{\mathbf{A}_{sphere\varphi\varphi}\mathbf{A}_{sphere\theta\theta} - \mathbf{A}^{2}_{sphere\varphi\theta}}{\mathbf{A}_{sphere\theta\theta}} \tag{4.20}$$

$$\text{where } \mathbf{A}_{sphere} = \sum_{k=1}^{n}\mathbf{C}_{[\varphi]_k}t_{ply}\,,\ \varphi_k = \frac{k\pi}{n} + \varphi_o$$

and $\mathbf{A}_{sphere}$ corresponds to the [3x3] extensional stiffness matrix of the sphere, n is the number of layers and φ_o is an arbitrary initial angle.

By eliminating V from Eq.(4.19) we obtain:

$$\frac{d^4 Q_\theta}{d\theta^4} + 4k^4 Q_\theta = 0,$$

$$\text{where } k = \sqrt[4]{3\left(1-\nu^2_{\varphi\theta\text{sphere}}\right)\left(\frac{R}{t}\right)^2} \tag{4.21}$$

and $\nu_{\varphi\theta\text{sphere}}$ is the Poisson's ratio of the laminate at the sphere. The general solution of Eq. (4.21) is given below:

$$Q_\theta = e^{k\theta}\left(C_1\cos(k\theta)+C_2\sin(k\theta)\right)+e^{-k\theta}\left(C_3\cos(k\theta)+C_4\sin(k\theta)\right) \tag{4.22}$$

where C_1,C_2, C_3 and C_4 are constants of integration to be evaluated from boundary conditions at the edges. The terms C_3 and C_4 can be omitted owing to the consideration that the shell is bent by forces and moments uniformly distributed along the edge [9].

Flügge [6] derived Q_θ as a function of angle θ after determining the two constants C_1 and C_2 from boundary conditions at the spherical cell edge. The application of an equal and opposite force (H) and a bending moment (M) uniformly distributed along the junction edge (boundary) ensures the satisfaction of the compatibility boundary conditions (Fig. 4-7). Q_θ for the applied edge bending moment (M) and radial load (H) is:

$$Q_\theta = H\left(-\sqrt{2}\sin(\theta_s)e^{-k\theta}\cos\left(k\theta+\frac{\pi}{4}\right)\right) \text{ for applied } H \tag{4.23}$$

$$Q_\theta = M\left(\frac{2k}{R}e^{-k\theta}\sin(k\theta)\right) \text{ for applied } M \tag{4.24}$$

The meridional (N_φ) and hoop (N_θ) membrane forces as a function of angle θ are given by utilizing Eqs. 4.17, 4.23, 4.24 [12]:

$$N_\varphi = H\left(2k\sin(\theta_s)e^{-k\theta}\cos(k\theta)\right)+M\left(\frac{2\sqrt{2}k^2}{R}e^{-k\theta}\cos\left(k\theta+\frac{\pi}{4}\right)\right)+\frac{PR}{2} \tag{4.25}$$

$$N_\theta = -H\left(-\sqrt{2}\sin(\theta_s)e^{-k\omega}\cos\left(k\theta+\frac{\pi}{4}\right)\right)\cot(\theta_s)+M\left(\frac{2k}{R}e^{-k\theta}\sin(k\theta)\right)\cot(\theta_s)+\frac{PR}{2} \tag{4.26}$$

A damped oscillatory character is expected for the membrane forces based on the above equations. Membrane forces can be obtained as a function of length of circumference by replacing $\theta = s/R$ in Eq.(4.25) and Eq.(4.26). The meridional (M_φ) and hoop (M_θ) membrane moments as a function of angle θ are given by the following equations [12]:

$$M_\varphi = 2\nu M_\theta + H\left(-\frac{R}{k^2\sqrt{2}}\sin(\theta_s)e^{-k\theta}\sin\left(k\theta+\frac{\pi}{4}\right)\right)+M\left(\frac{1}{k}e^{-k\theta}\cos(k\theta)\right) \tag{4.27}$$

$$M_\theta = H\left(\frac{R\sin(\theta_s)e^{-k\theta}\sin(k\theta)}{k}\right)+M\left(\sqrt{2}e^{-k\theta}\sin\left(k\theta+\frac{\pi}{4}\right)\right) \tag{4.28}$$

A schematic of the exerted loads at the multi-sphere is depicted in Fig. 4-9. A toroidal shell is formed from the introduction of a fillet. The sphere/intersection (torus) boundary is given for θ = 0. The symbols θ_2 and θ_s represent the angle between the sphere tangent and the intersection axis and the angle relative to the horizontal intersection axis and the line connecting sphere and fillet radius centroids respectively.

$$\theta_2 = \arccos\left(\frac{d/2}{R + R_{\text{fillet}}}\right) \tag{4.29}$$

$$\theta_s = \pi - \theta_2 \tag{4.30}$$

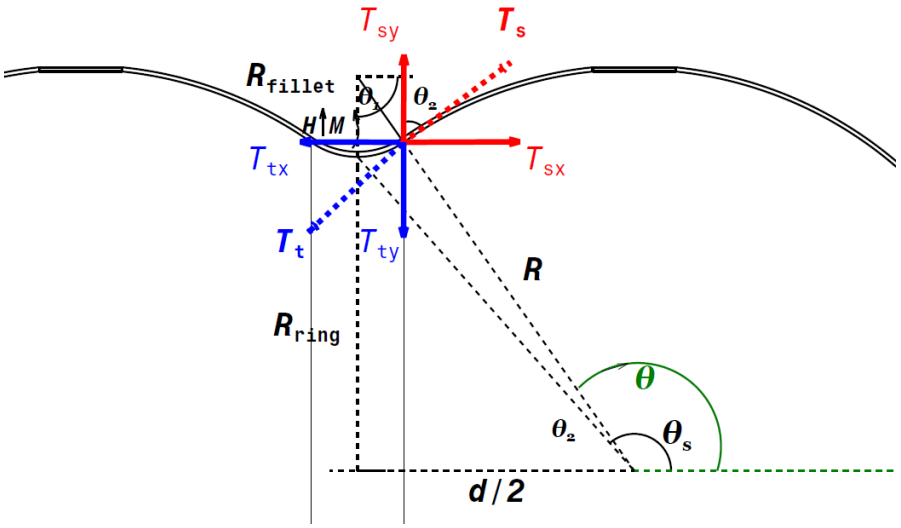

Fig. 4-9: Analysis of forces at the junction of the multi-sphere.

For the case of the multi-sphere, the resultant radial load (H) at the junction can be derived from the subtraction of the vertical component of the torus membrane force (T_{ty}) from the vertical component of the force of the neighboring sphere (T_{sy}) (Fig. 4-9):

$$H = T_{sy} - T_{ty}$$

$$\text{where } T_{sy} = \frac{PR}{2}\cos(\theta_2), \tag{4.31}$$

$$T_{ty} = \frac{PR_{\text{fillet}}\left(\left(R_{\text{ring}} + R_{\text{fillet}}\right) - \frac{R_{\text{fillet}}\sin(2\pi - \theta_2)}{2}\right)}{\left(\left(R_{\text{ring}} + R_{\text{fillet}}\right) - R_{\text{fillet}}\sin(2\pi - \theta_2)\right)}\cos(\theta_2)$$

The rotational compatibility equation below is solved for the moment M:

$$V_{\text{stotal}} = V_{\text{ttotal}} \Leftrightarrow V_{\text{sH}}H + V_{\text{sM}}M + V_{\text{sP}}P = V_{\text{tH}}H + V_{\text{tM}}M + V_{\text{tP}}P$$

$$\text{where } V_{\text{sH}} = \frac{2k^2\sin(\theta_s)}{E_{\text{sphere}}tk_1}, V_{\text{sM}} = -\frac{4k^3}{E_{\text{sphere}}Rtk_1}, V_{\text{sP}} = 0, \tag{4.32}$$

$$k_1 = 1 - \frac{1-2\nu}{2k}\cot(\theta_s)\ ,\ k_2 = 1 - \frac{1+2\nu}{2k}\cot(\theta_s),$$

$$V_{\text{tH}} = \frac{H_{\text{coefrot}}}{E_{\varphi\text{torus}}R_{\text{fillet}}}, V_{\text{tM}} = \frac{M_{\text{coefrot}}}{E_{\varphi\text{torus}}R_{\text{fillet}}^2}, V_{\text{tP}} = \frac{P_{\text{coefrot}}}{2E_{\varphi\text{torus}}}$$

and $E_{\varphi\text{torus}}$ is the effective laminate stiffness at the intersection in the meridional direction, t_{junction} is the shell thickness at the same location and M_{coefrot}, H_{coefrot} and P_{coefrot} are the edge rotation coefficients for toroidal shell of negative curvature as obtained from Galletly [13]. These edge rotation coefficients are dependent on the R/t and $(R_{\text{fillet}}+R_{\text{ring}})/R_{\text{fillet}}$ ratios. The value of T_{ty} becomes zero in the case that there is no fillet radius at the intersection (R_{fillet} = 0 [mm]). A

relationship between the edge radial load and bending moment was established in [14] based on edge rotational compatibility (Eq.(4.33)):

$$M = -HRsin(\theta_s) / {k_{edge}}^2,$$

$$\text{where } k_{edge} = \sqrt[4]{3\left(1-\nu_{\varphi\theta torus}^2\right)\left(\frac{R}{t_{junction}}\right)^2} \tag{4.33}$$

In both Eq. (4.32) and Eq. (4.33) a dependency of M on H, R and $t_{junction}$ is obtained. The equivalent laminate modulus of the toroidal shell at the meridional ($E_{\varphi torus}$) and hoop ($E_{\theta torus}$) directions is derived as follows:

$$E_{\varphi torus} = \frac{1}{t_{junction}} \frac{\mathbf{A}_{torus\varphi\varphi}\mathbf{A}_{torus\theta\theta} - \mathbf{A}^2_{torus\varphi\theta}}{\mathbf{A}_{torus\theta\theta}}$$

$$E_{\theta torus} = \frac{1}{t_{junction}} \frac{\mathbf{A}_{torus\varphi\varphi}\mathbf{A}_{torus\theta\theta} - \mathbf{A}^2_{torus\varphi\theta}}{\mathbf{A}_{torus\varphi\varphi}} \tag{4.34}$$

$$\text{where } \mathbf{A}_{torus} = \sum_{\kappa=1}^{n} \mathbf{C}_{[\varphi]_\kappa} t_{ply} = t_{ply}\left[\alpha_{[0^o]}\mathbf{C}_{[0^o]} + \alpha_{[\pm\varphi]}\left(\mathbf{C}_{[\varphi]} + \mathbf{C}_{[-\varphi]}\right)\right], \tag{4.35}$$

$$t_{junction} = a_{[0^o]} + 2a_{[\pm\varphi]}$$

and $\mathbf{A}_{torus}$ corresponds to the [3x3] extensional stiffness of the torus, $a_{[0^o]}$ and $a_{[\pm\varphi]}$ are the number of plies needed at the intersection to ensure strain compatibility at meridional and hoop directions. The angle of the angle-ply layer is selected to be in the value range of $[5^o] \leq \varphi \leq [75^o]$, owing to the complexity of the application of UD-prepreg straps with $\varphi > [75^o]$ over the intersection.

By replacing ($\theta = 0$) at Eq.(4.25-4.28) we obtain the loads and moments at the junction of sphere/intersection:

$$\mathbf{N}_{sphere} = \begin{bmatrix} \frac{PR}{2} \\ \frac{PR}{2} \\ 0 \end{bmatrix}, \mathbf{N}_{junction} = \begin{bmatrix} H\left(2k\sin\left(\theta_s\right)\right) + M\left(\frac{2k^2}{R}\right) + \frac{PR}{2} \\ H\left(\cos\left(\theta_s\right)\right) + \frac{PR}{2} \\ 0 \end{bmatrix}, \mathbf{M}_{junction} = \begin{bmatrix} \frac{M}{k} + Mv_{\varphi\theta sphere} - \frac{HR\sin\left(\theta_s\right)}{2k^2} \\ M \\ 0 \end{bmatrix} \tag{4.36}$$

The minimum required number of UD straps at $[0^o]$ and $[\pm\varphi]$ orientations is determined by solving the following system of strain compatibility equations (Eq.(4.37)) at the junction ($\theta = 0$) in the meridional and hoop directions for $a_{[0^o]}$ and $a_{[\pm\varphi]}$.

$$\boldsymbol{\varepsilon}_{sphere} = \boldsymbol{\varepsilon}_{junction} \Rightarrow \begin{bmatrix} \varepsilon^o_{\varphi sphere} \\ \varepsilon^o_{\theta sphere} \\ \gamma^o_{\varphi\theta sphere} \end{bmatrix} = \begin{bmatrix} \varepsilon^o_{\varphi junction} \\ \varepsilon^o_{\theta junction} \\ \gamma^o_{\varphi\theta junction} \end{bmatrix} + z\begin{bmatrix} \kappa_{\varphi junction} \\ \kappa_{\theta junction} \\ \kappa_{\varphi\theta junction} \end{bmatrix}, \tag{4.37}$$

where $\varepsilon^{o}_{\varphi sphere} = \varepsilon^{o}_{\theta sphere} = \frac{N_{\varphi sph}}{E_{sphere}t} - \frac{\nu_{\varphi\theta sphere} N_{\theta sph}}{E_{sphere}t}$, $\varepsilon^{o}_{\varphi junction} = \frac{N_{\varphi junction}}{E_{\varphi torus} t_{junction}} - \frac{\nu_{\varphi\theta torus} N_{\theta junction}}{E_{\varphi torus} t_{junction}}$,

$$\varepsilon^{o}_{\theta junction} = -\frac{\nu_{\varphi\theta torus} N_{\varphi junction}}{E_{\varphi torus} t_{junction}} + \frac{N_{\theta unction}}{E_{\theta torus} t_{junction}}, \kappa_{\varphi junction} = d_{\varphi\varphi torus} M_{\varphi junction} + d_{\varphi\theta torus} M_{\theta junction},$$

$$\kappa_{\theta junction} = d_{\varphi\theta torus} M_{\varphi junction} + d_{\theta\theta torus} M_{\theta junction}, \kappa_{\varphi\theta junction} = 0$$

and the terms $\varepsilon^{o}_{\varphi sphere} = \varepsilon^{o}_{\theta sphere}$ are the equal mid-plane meridional and hoop strains and $\gamma^{o}_{\varphi\theta sphere}$ at the sphere, while $\varepsilon^{o}_{\varphi junction}, \varepsilon^{o}_{\theta junction}$ $\gamma^{o}_{\varphi\theta junction}$ are the mid-plane strains and $\kappa_{\varphi junction}$, $\kappa_{\theta junction}$, $\kappa_{\varphi\theta junction}$ are curvatures in the meridional, hoop and in-plane shear directions at the intersections.

The laminate at the torus is designed to be balanced and symmetric to avoid un-wanted coupling between in-plane loads and out-of-plane strain responses or even between curvatures and twists throughout thermo-mechanical loading [11]. Fig. 4-10 depicts an idealization of the laminate, where within each layer several [0°] and [±φ] plies can be obtained. The idealization follows the laminate design practices outlined in [15], whereby no more than 4 plies of approximately the same orientation are expected to be placed on top of each other when enforcing strain compatibility conditions at the multi-sphere.

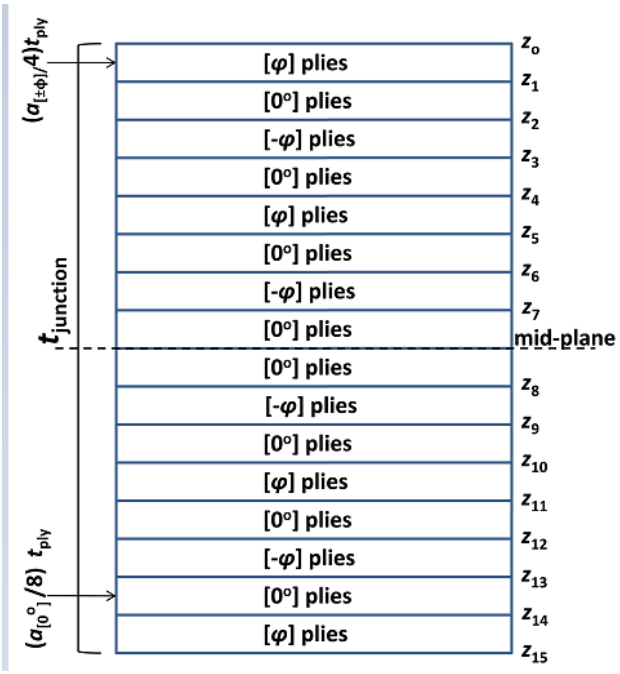

Fig. 4-10: Idealization of laminate at the toroidal shell (intersection).

The bending stiffness matrix at the intersection is obtained by employing Eq. (4.38):

$$\mathbf{D}_{torus} = \frac{1}{3}[\mathbf{C}_{[0^o]}\left[\left(z_2^3 - z_1^3\right) + \left(z_4^3 - z_3^3\right) + \left(z_6^3 - z_5^3\right) + \left(z_7^3\right) + \left(z_8^3\right) + \left(z_{10}^3 - z_9^3\right) + \left(z_{12}^3 - z_{11}^3\right) + \left(z_{14}^3 - z_{13}^3\right)\right] +$$
$$+\mathbf{C}_{[\varphi]}\left[\left(z_1^3 - z_0^3\right) + \left(z_5^3 - z_4^3\right) + \left(z_{11}^3 - z_{10}^3\right) + \left(z_{15}^3 - z_{14}^3\right)\right] + \qquad (4.38)$$
$$\mathbf{C}_{[-\varphi]}\left[\left(z_3^3 - z_2^3\right) + \left(z_7^3 - z_6^3\right) + \left(z_9^3 - z_8^3\right) + \left(z_{13}^3 - z_{12}^3\right)\right]]$$

The resulting values of the z_k coordinates of the laminate depicted in Fig. 4-10 are given below (Table 4-4):

Table 4-4: Thickness coordinates of the laminate at the intersection.

Above Mid-plane		Below Mid-plane	
z_o	$-\left(\frac{a_{[0^o]}}{2}+a_{[\pm\varphi]}\right)t_{ply}$	z_{15}	$\left(\frac{a_{[0^o]}}{2}+a_{[\pm\varphi]}\right)t_{ply}$
z_1	$-\left(\frac{a_{[0^o]}}{2}+\frac{3a_{[\pm\varphi]}}{4}\right)t_{ply}$	z_{14}	$\left(\frac{a_{[0^o]}}{2}+\frac{3a_{[\pm\varphi]}}{4}\right)t_{ply}$
z_2	$-\left(\frac{3a_{[0^o]}}{8}+\frac{3a_{[\pm\varphi]}}{4}\right)t_{ply}$	z_{13}	$\left(\frac{3a_{[0^o]}}{8}+\frac{3a_{[\pm\varphi]}}{4}\right)t_{ply}$
z_3	$-\left(\frac{3a_{[0^o]}}{8}+\frac{a_{[\pm\varphi]}}{2}\right)t_{ply}$	z_{12}	$\left(\frac{3a_{[0^o]}}{8}+\frac{a_{[\pm\varphi]}}{2}\right)t_{ply}$
z_4	$-\left(\frac{a_{[0^o]}}{4}+\frac{a_{[\pm\varphi]}}{2}\right)t_{ply}$	z_{11}	$\left(\frac{a_{[0^o]}}{4}+\frac{a_{[\pm\varphi]}}{2}\right)t_{ply}$
z_5	$-\left(\frac{a_{[0^o]}}{4}+\frac{a_{[\pm\varphi]}}{4}\right)t_{ply}$	z_{10}	$\left(\frac{a_{[0^o]}}{4}+\frac{a_{[\pm\varphi]}}{4}\right)t_{ply}$
z_6	$-\left(\frac{a_{[0^o]}}{8}+\frac{a_{[\pm\varphi]}}{4}\right)t_{ply}$	z_9	$\left(\frac{a_{[0^o]}}{8}+\frac{a_{[\pm\varphi]}}{4}\right)t_{ply}$
z_7	$-\left(\frac{a_{[0^o]}}{8}\right)t_{ply}$	z_8	$\left(\frac{a_{[0^o]}}{8}\right)t_{ply}$

It is important to avoid buckling at the intersection. Buckling is a consideration owing to the fact that the toroidal shell -formed from adding a fillet radius- has negative curvature and it becomes a very thin shell for high R_{fillet} and R/t values. With the required number of UD straps known, the buckling pressure of the intersection at the meridional and hoop directions can be evaluated. The equation for critical external pressure used in isotropic materials [16] is adapted by considering the equivalent laminate properties:

$$P_{\varphi crit} > S_F P_{MEOP}\,,\; P_{\theta crit} > S_F P_{MEOP}$$

$$\text{where } P_{\varphi crit} = 2\sqrt{\left(3-\nu_{\varphi\theta}\right)^2}\,E_{\varphi torus}\left(\frac{t_{junction}}{R_{fillet}}\right)^2, \qquad (4.39)$$

$$P_{\theta crit} = 2\sqrt{\left(3-\nu_{\varphi\theta}\right)^2}\,E_{\theta torus}\left(\frac{t_{junction}}{R_{fillet}}\right)^2$$

and $P_{\varphi crit}$ and $P_{\varphi crit}$ are the buckling pressure in the meridional and hoop directions respectively and S_F is a safety factor. A contour plot of meridional and hoop membrane forces on the multi-sphere from a static structural FE analysis is shown in Fig. 4-11. A centroid distance of d = 200 [mm] was selected and since $d = yR$ the dimensionless centroid distance was y = 1.4.

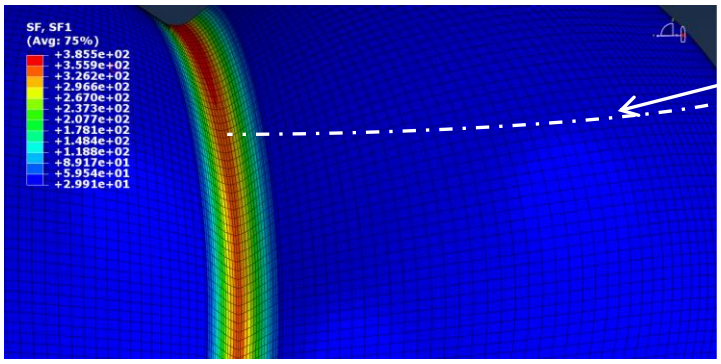

Path for N_φ evaluation

(a)

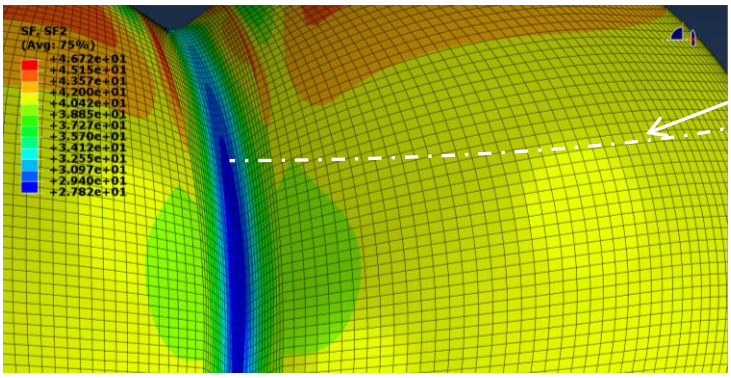

Path for N_θ evaluation

(b)

Fig. 4-11: a) Meridional (N_φ) and b) hoop (N_θ) membrane forces at the multi-sphere (y = 1.4, R = 145 [mm], R_{fillet} = 10 [mm]).

A comparison between the analytical solution and the FE analysis on the meridional and hoop membrane forces distribution at the spherical and toroidal cells is presented in Fig. 4-12 for the path shown in Fig. 4-11a,b. The damped oscillatory character of the edge bending solution near the junction can be seen. The results seem to be in very good agreement (average offset of 4 [%]), revealing the highly non-linear character when moving from the spherical to the toroidal cell. The magnitude of the membrane moments is rather low compared to the membrane forces.

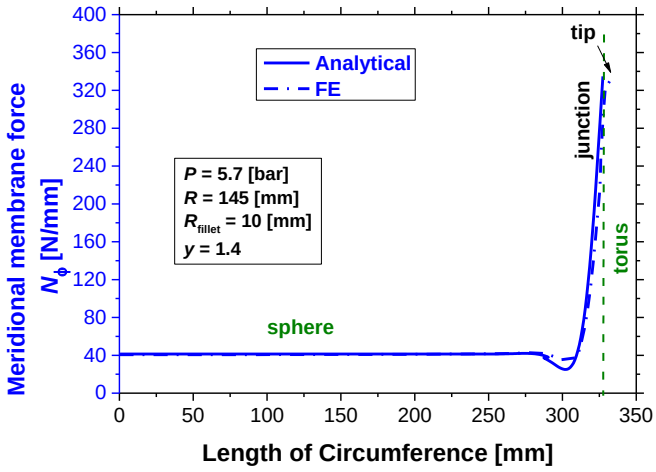

(a)

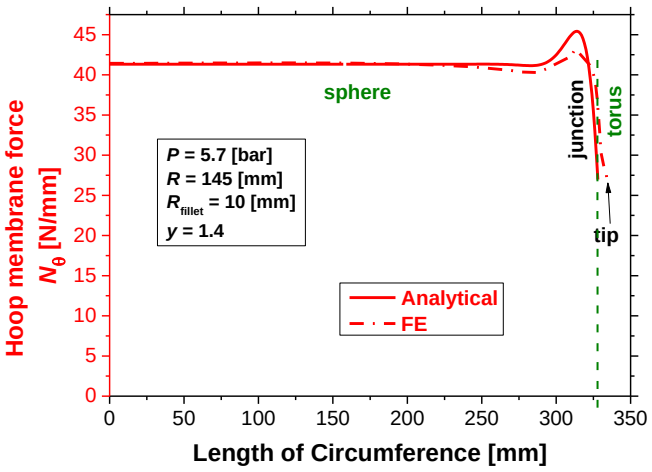

(b)

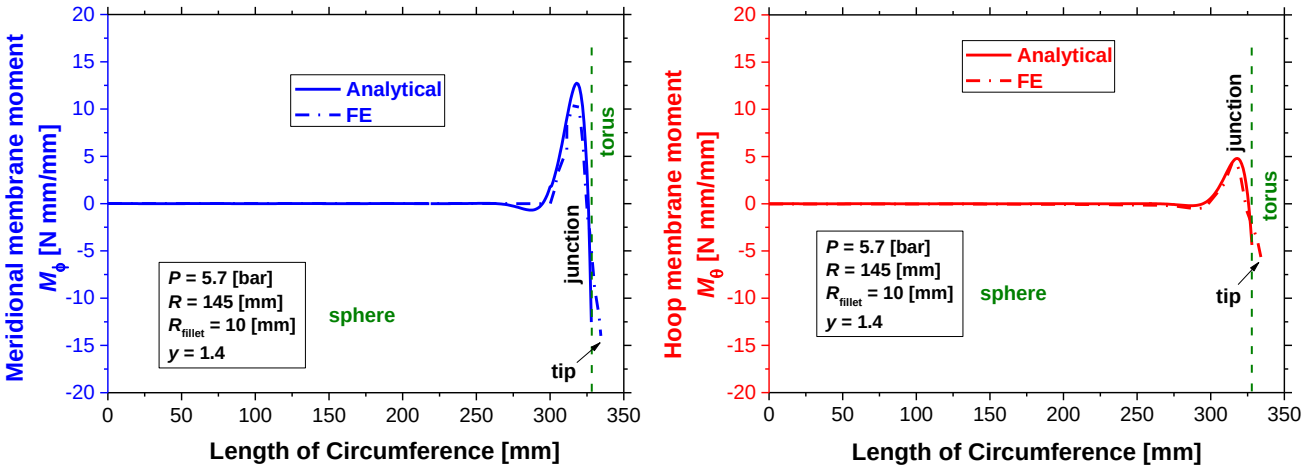

(c) **(d)**

Fig. 4-12: Comparison between the analytical solution and FE on a) meridional (N_φ), b) hoop (N_θ) membrane forces and c) meridional (M_φ) and b) hoop (M_θ) membrane moments over the spherical cell and intersection under P_{MEOP}.

A contour-plot of the required number of UD straps at both the meridional and hoop directions is depicted in Fig. 4-13. The intersection point of the two curves is the solution of the system in Eq. (4.37).

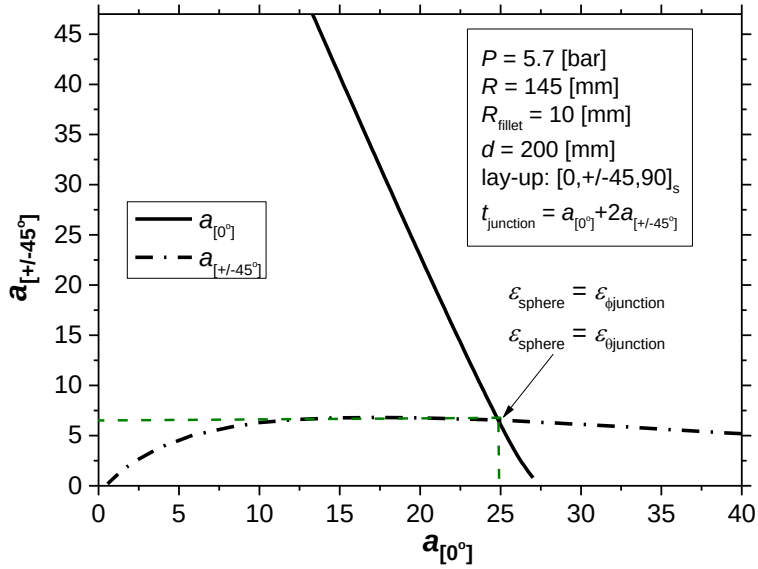

Fig. 4-13: Required number of a) [0°] and b) [+/-45°] UD straps for strain compatibility at meridional and hoop directions respectively (P = 5.7 [bar], R = 145 [mm], R_{fillet} = 10 [mm]).

The meridional and hoop strain distribution -based on FE analysis- for an increasing number of [0°] and [±φ] UD straps is illustrated in Fig. 4-14a and b. In this case ±φ was assumed to be [±45°]. Significant strain jumps are depicted near the junction for the case of $a_{[0]} = 2a_{[\pm45]} = 2$. Strain compatibility in both the meridional and hoop directions was achieved with $a_{[0]} = 25$, $2a_{[\pm45]} = 12$, which verifies the findings of the analytical solution presented above.

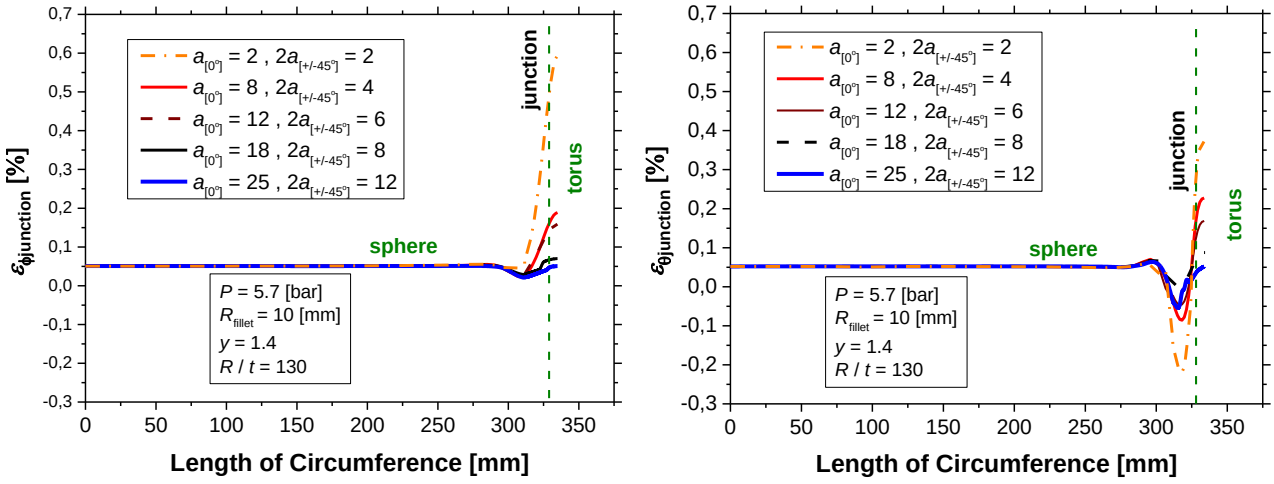

Fig. 4-14: Effect of UD straps on the strain distribution over the spherical cell and junction in the a) meridional and b) hoop directions (FE analysis).

4.4 Effect of Geometrical Parameters

The identification of the geometrical properties that control the design of the multi-sphere is crucial towards understanding its behavior when subjected to inner pressure. This section presents the effect of the geometry parameterization on the exerted loads and required laminate thickness at the intersection.

4.4.1 Centroid Distance

A cross-section in the *xy* plane of two intersecting spheres with radii *R* with their centroids at a distance *d* is depicted in Fig. 4-15. The intersection of the two spheres leads to the formation of two spherical caps and thus a three-dimensional biconvex lens shape with the intersecting cross-section being a circle with radius R_{ring}.

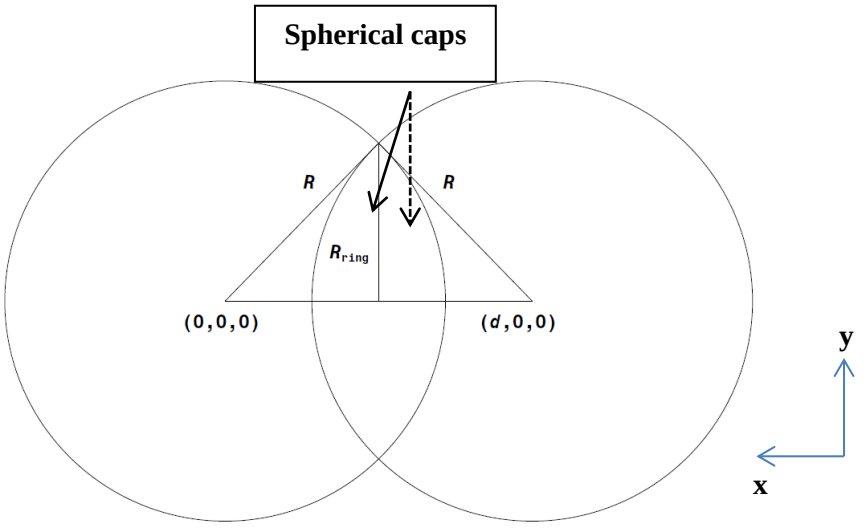

Fig. 4-15: Cross-section of two intersecting spheres with equal radii (*R*) with their centroids at the same plane (0,0,0) and (*d*,0,0).

The equations of the two spheres are:

$$x^2 + y^2 + z^2 = R^2 \tag{4.40}$$

$$(x-d)^2 + y^2 + z^2 = R^2$$

where $d = yR$ with $0 < y < 2$, The intersection radius (R_{ring}) in the yz plane is given by:

$$R_{ring} = \sqrt{R^2 - \left(\frac{d}{2}\right)^2} \tag{4.41}$$

Fig. 4-16 depicts the normalized radius of the intersecting curve as a function of normalized centroids distance (y). For $y = 0$ this leads to $R_{ring} = R$ due to the formation of a single sphere, while for $y = 2$ the formation of distinct spheres results in $R_{ring} = 0$.

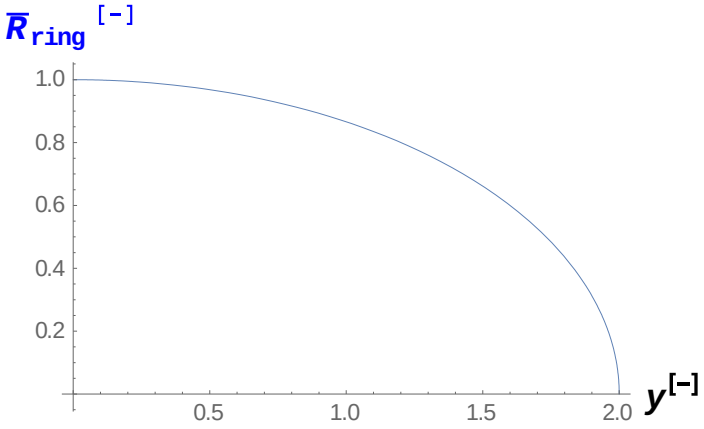

Fig. 4-16: Normalized radius of intersecting curve (with respect to R) as a function of normalized centroids distance (y).

It was shown in Eq. (4.31) that the edge force (H) depends on the angle between the spherical cell and intersection axis (θ_2). This angle decreases with increasing centroid distance and becomes zero for $y = 2$ (Fig. 4-17a). This results in a linear increase of H within this regime owing to the fact that $\cos(\theta_2)$ controls the trend of H. Nullification of H for $y = 2$ occurs since two distinct spheres are created and edge displacements vanish.

The edge bending moment (M) has a highly non-linear decreasing trend –reaching a minimum value at $y = 1.45$ approximately- and being zero for $y = 0$ and $y = 2$. A very similar trend was obtained for solving for M in Eq (4.32) and by employing Eq (4.33). This behaviour of M can be associated to the fact that the term $-H\sin(\theta_s)$ defines its trend. From now on, Eq.(4.33) will be used for simplicity. In the graphs below, no fillet radius was considered ($r = R_{fillet}/R = 0$) to focus on the effect of y at this point.

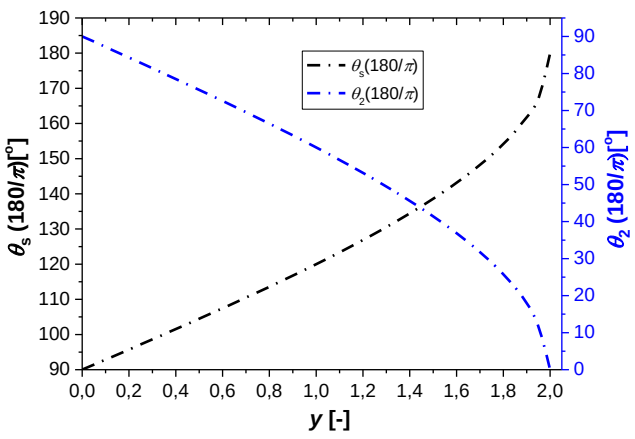

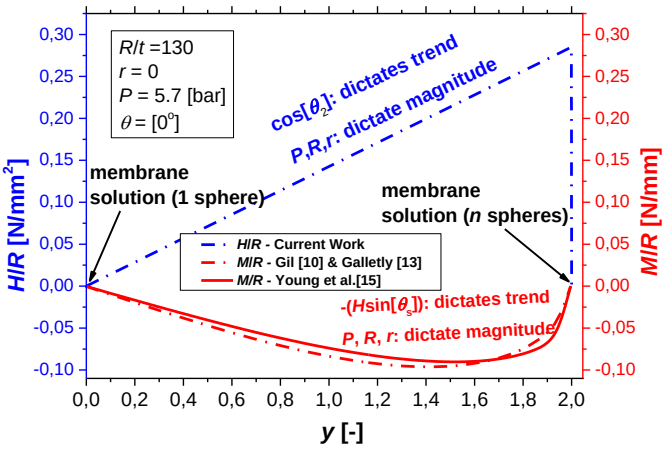

(a) **(b)**

Fig. 4-17: a) Angle between the tangent of the sphere and the intersection axis and b) normalized radial load (*H*) and c) normalized edge moment (*M*) versus dimensionless centroid distance (*y*).

The ratio of the junction and sphere meridional and hoop membrane forces is shown in Fig. 4-18. As expected, both curves become 1 for $y = 0$ and $y = 2$ since the membrane solution is attained there. A peak is obtained for $N_{\varphi junction}$ at $y = 1.46$. This peak can be explained by the fact that the trend and magnitude of $N_{\varphi junction}$ is mainly dependent on the term $H\sin(\theta_s)$ (Eq. (4.25)) and is maximized at that y value (Fig. 4-18b).

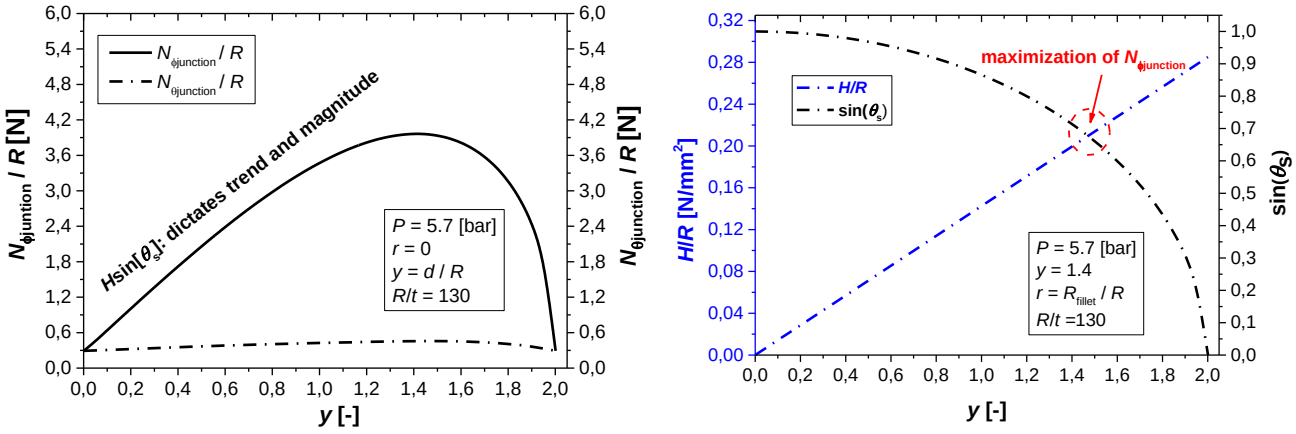

(a) **(b)**

Fig. 4-18: Normalized meridional (N_φ) and hoop (N_θ) line forces at the junction and the sphere as a function of *y*.

Apart from the magnitude of the junction forces, it is also important to assess the angle (θ_{reinf}) at which they fade out. This will enable us to know the arc length (s) in the hoop direction that needs to be reinforced with UD straps (Fig. 4-19). This is done by solving $N_\varphi = N_{\varphi sph}$ (Eq. (4.25)) and $N_\theta = N_{\theta sph}$ (Eq. (4.26)) for an angle $\theta = \theta_{memb}$ and keeping the maximum angle of the two. This resulting angle value is added to θ_1:

$$\theta_{reinf} = 2\left(\theta_{memb} + \theta_1\right)$$

$$\text{where } \theta_1 = \arcsin\left(\frac{d/2}{R + R_{fillet}}\right) \tag{4.42}$$

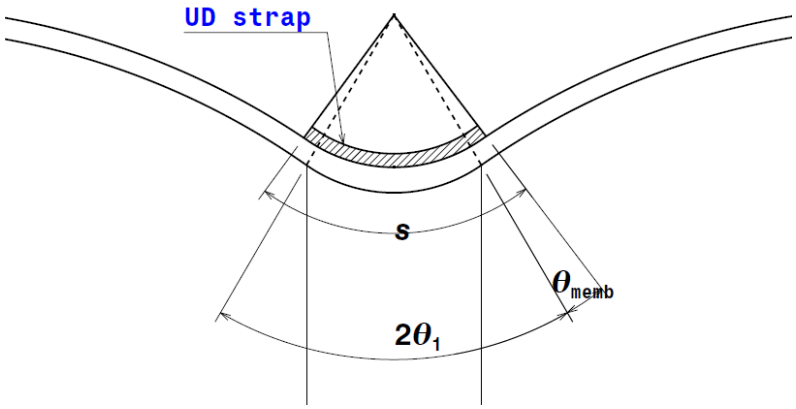

Fig. 4-19: Schematic of UD straps over the intersection.

The resulting arc length of reinforcement can be derived from $s = \theta_{reinf} R_{fillet}$. The effect of y on s is presented below (Fig. 4-20). The arc length of the reinforcement attains a fairly constant value for the interval $0.3 < y < 2$, while it nullifies at $y = 0$ and $y = 2$.

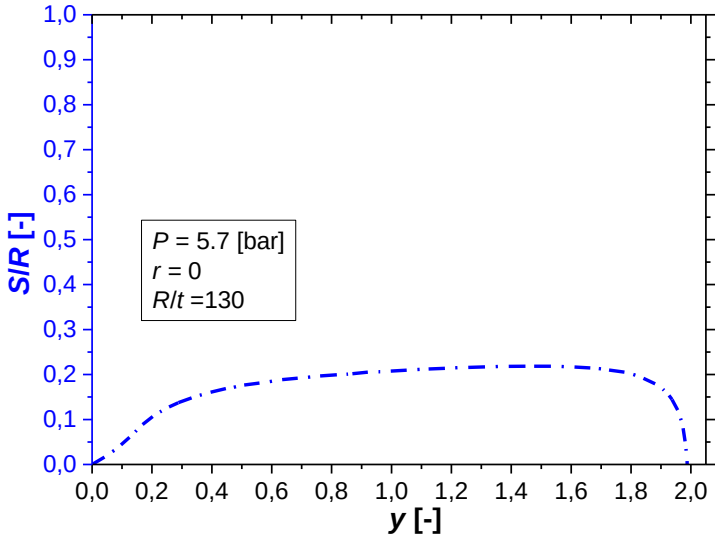

Fig. 4-20: Arc length (s) that the secondary loads become negligible as a function of y.

It was shown that the trend and magnitude of the laminate thickness and arc length as a function of centroid distance (y) is primarily dependent on the exerted radial load H and angle θ_s, thus leading in a non-linear behaviour that attains the membrane solution for $y = 0$ and $y = 2$. It is important to analyse the effect of the intersection fillet radius (R_{fillet}) and sphere radius (R) on the mechanical behaviour of the tank.

4.4.2 Intersection Fillet Radius

The introduction of a fillet radius leads to the pressure load being carried by both the spherical and toroidal cells at the intersection, which in turn leads to the reduction of the magnitude of the exerted membrane forces at the region. The effect of the fillet radius (R_{fillet}) on the forces at the junctions is captured by Eq. (4.31). From now on the fillet radius will be referred to in its dimensionless format ($r = R_{fillet}/R$).

The normalized meridional ($N_{\varphi junction}/R$) and hoop ($N_{\theta junction}/R$) junction forces for various r values are presented in Fig. 4-21. An exponential decay was obtained for the meridional case, where a 50 [%] reduction in the $N_{\varphi junction}$ magnitude occurs within $0 \leq r \leq 0.075$. Additionally, an asymptotic ratio value of 1.5 approximately can be seen for $r > 0.2$. The increasing trend of the $N_{\theta junction}$ versus r can be described by an inverse hyperbolic function owing to the increase of r. The asymptotic value of $N_{\theta junction}/R$ is slightly above 0.3.

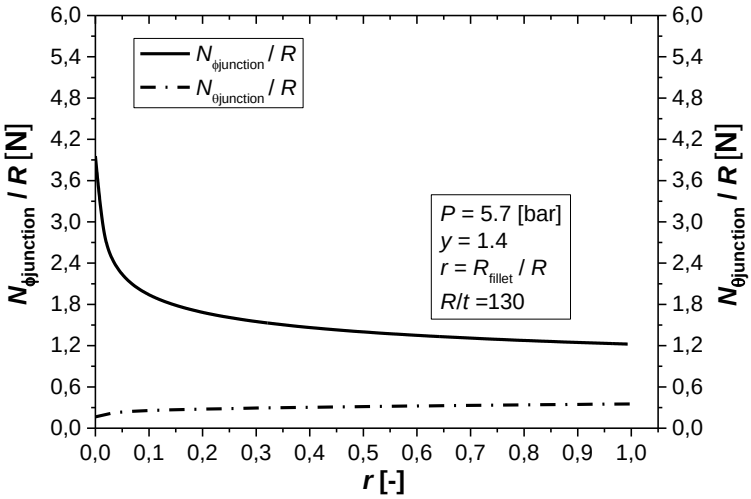

Fig. 4-21: Normalized meridional and hoop line forces at the junction and the sphere as a function of *r*.

The effect of r on θ_{reinf} and normalized arc length of reinforcement (s/R) is presented below (Fig. 4-22). An exponential decay is attained for $\theta_{reinf.}$. On the other hand, it is clear that an increasing r results in a non-linear rise of the arc length that can be approximated by an inverse hyperbolic function, owing to Eq. (4.42).

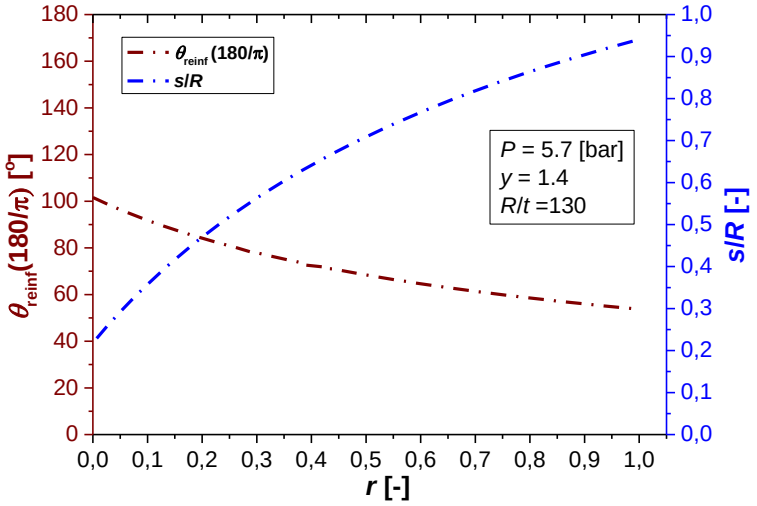

Fig. 4-22: Angle and resulting arc length that the secondary loads become negligible as a function of *r*.

The increasing s for larger y and r values will lead to significant mass penalties. The mass of the intersection is provided by:

$$M_{\text{intersection}} = \rho_{\text{comp}} \int_0^{\gamma_{\text{cyl}}} st_{\text{junction}} d\gamma \,, \qquad \gamma_{\text{cyl}} = \arcsin\left(\frac{l_{\text{cyl}}}{2R_{\text{ringfinal}}}\right) \tag{4.43}$$

where ρ_{comp} is the density of the composite material, l_{cyl} is the length of the central hollow cylinder, γ_{cyl} is the angle relative to the cylinder length from the centroid and $R_{\text{ringfinal}}$ is the intersection radius incorporating the effect of the fillet radius (see Eq.(5.7) in the next Chapter).

Therefore the arc length (s) and thickness ($t_{junction}$) values of the intersection should be selected upon minimizing the cross-sectional area of the UD strap ($A_{UD} = st_{junction}$). A minimum A_{UD} value for a given dimensionless centroid distance (y) value can be identified for a specific set of fillet radius (r), lamina angle ($\pm\varphi$) and ratio between [0^o] and [$\pm\varphi$] layers at the intersection ($i_{ratio} = a_{[0]}/2a_{[\pm\varphi]}$).

The resulting required normalized fillet radius (r), ratio of the [0^o] and [$\pm\varphi$] layers (i_{ratio}) and angle of angle-ply layers ($\pm\varphi$) as a function of varying dimensionless centroid distance (y) is depicted in Fig. 4-23a,b,c. It can be seen that a decreasing trend is obtained for r, while i_{ratio} , $t_{junction}$ and θ_{reinf} have an increasing trend up to a certain y value and then decrease. The opposite effect is shown for φ. This trend can be interpreted as follows: for $0 < y < 1.45$ approximately a steep increasing slope is obtained for the meridional force at the junction ($N_{\varphi junction}$)-(Fig. 4-18a) and hence more layers are needed to ensure strain compatibility. As result, φ tends to come closer to [0^o] but then more [$\pm\varphi$] layers are needed to ensure strain compatibility in the hoop direction and i_{ratio} becomes larger than 1. Fillet radius (r) values attain a decreasing tendency to counteract the increase of $t_{junction}$ within the same interval ($0 < y < 1.45$) and lead to cross-sectional area (A_{UD}) minimization. For $1.1 < y < 1.6$ approximately a plateau is attained for r and φ. For $1.6 < y < 2$ the lower $N_{\varphi junction}$ values result in an increase of φ and a decrease of i_{ratio}. The resulting angle of reinforcement is decreasing in the interval $1.8 < y < 2$. The resulting normalized $t_{junction}$ is illustrated in Fig. 4-23d.

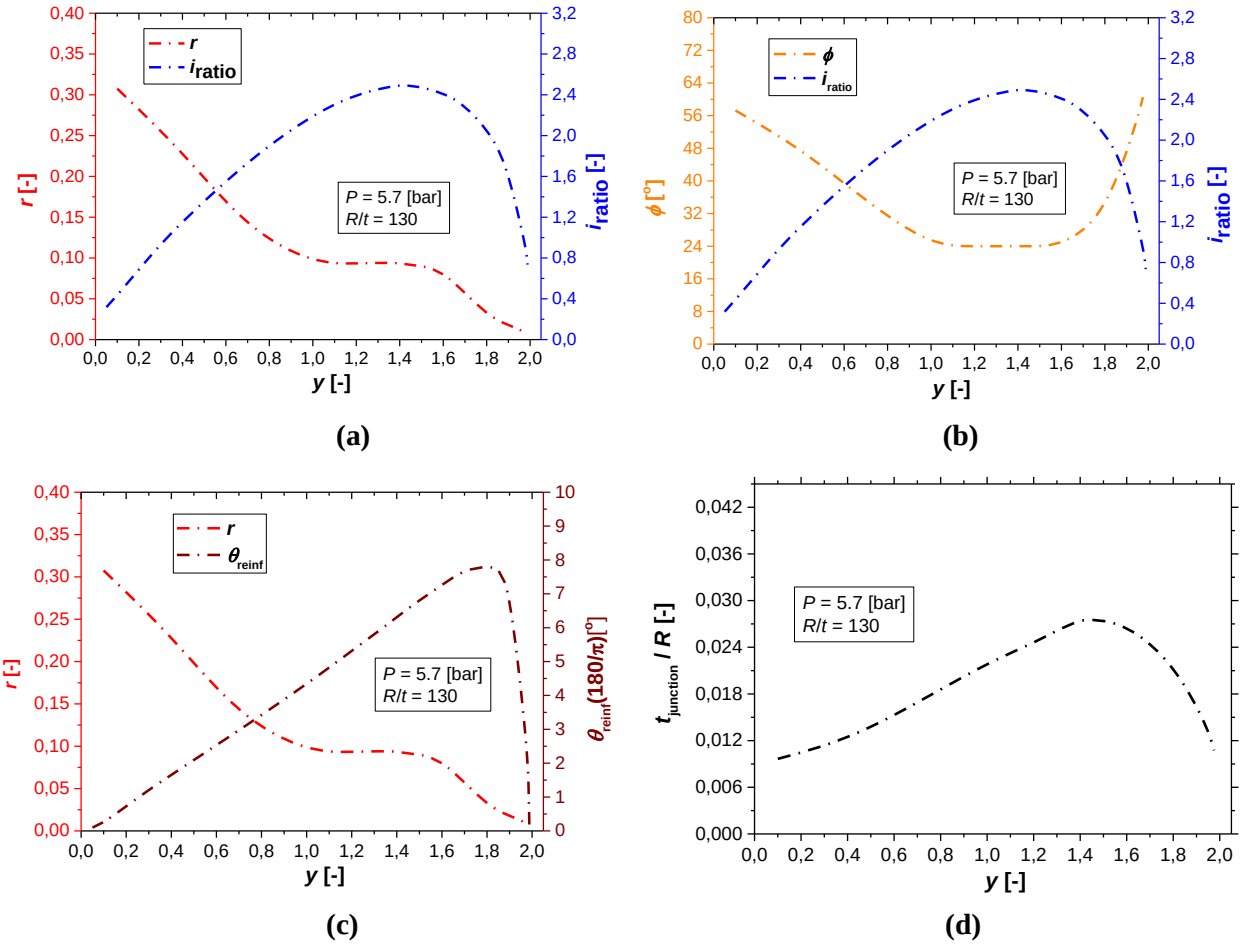

Fig. 4-23: Resulting normalized fillet radius (r), ratio between [0^o] and [$\pm\varphi$] layers, lamina angle (φ), reinforcement angle (θ_{reinf}) and intersection thickness ($t_{junction}$) from minimization of cross-sectional area (A_{UD}) as a function of y for R/t =130.

The effect of the sphere radius-to-thickness ratio (R/t) on the normalized laminate thickness at the intersection ($t_{junction}$/R) is presented in Fig. 4-24. It can be seen that $t_{junction}$ decreases exponentially with higher R/t values, reaching a plateau for R/t > 130. This behaviour can be associated with the fact that a low R/t value leads to stiffer sphere which leads to a thicker laminate at the intersection. On the other hand, very high R/t values can lead to buckling of the intersection (Eq. (4.39))

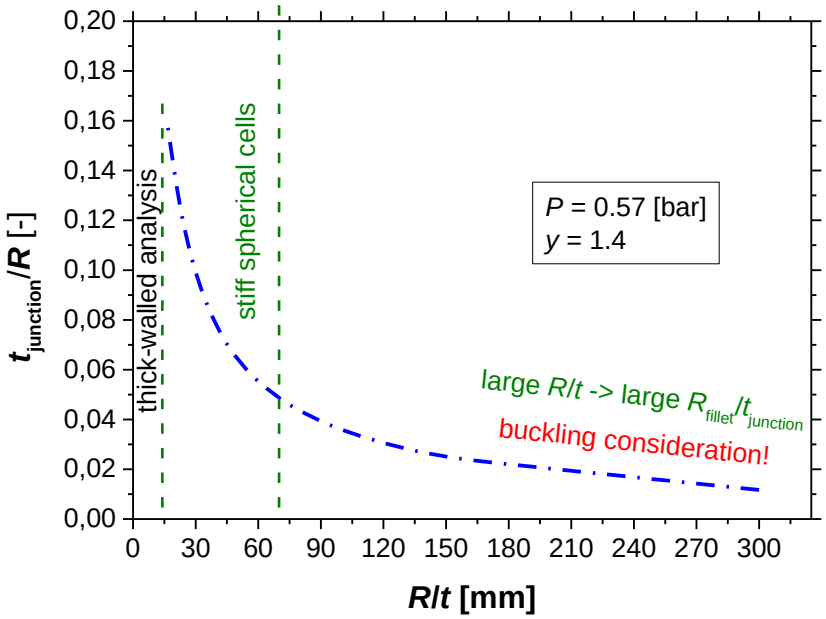

Fig. 4-24: Normalized laminate thickness at the intersection as a function of the sphere radius-to-thickness ratio (R/t).

4.4.3 Sphere Radius

In this section the effect of sphere radius (R) on the tank's mechanical response to internal pressure is analyzed by evaluating the exerted junction line forces in the meridional ($N_{\phi junction}$) and hoop ($N_{\theta junction}$) directions. The R/t ratio was kept constant. The meridional and hoop membrane forces as a function of R can be seen in Fig. 4-25 where it is shown that a linear dependency is attained.

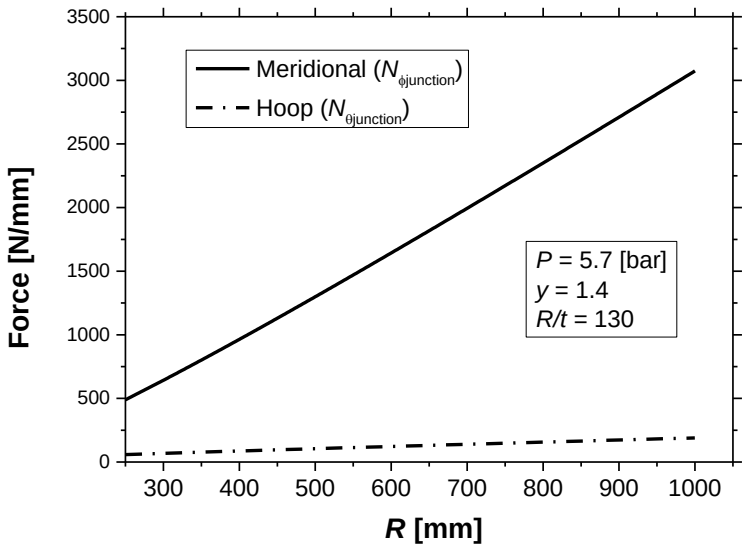

Fig. 4-25: Meridional ($N_{\phi junction}$) and hoop ($N_{\theta junction}$) forces for variable sphere radius (R) (y = 1.4, P = 5.7 [bar], R/t = 130).

In the next Chapter the effect of R on the structural performance of the multi-sphere will be analysed.

4.5 Concluding Remarks

The main goal of this chapter was the introduction of the multi-spherical COPV concept and the identification of the geometrical variables that control the tank design. The assessment of the edge disturbances at the spherical cell junctions enabled the determination of the number of straps, needed to achieve deformation compatibility at the junction areas. External UD hoop rings were incorporated at the junctions, to introduce stain compatibility between the spherical membranes and intersections. The stress state at the junctions of the multi-sphere is controlled by the following variables: i) centroid distance (y), ii) fillet radius (r), iii) sphere radius (R). This has a direct effect on the: i) lamina angle (φ) and ii) ratio between [0^o] and [$\pm\varphi$] layers (i_{ratio}) and thus iii) laminate thickness at the junctions.

It was shown that the meridional line force ($N_{\varphi junction}$) has a dominant effect -compared to other membrane forces- on the required number of UD straps. A highly non-linear relationship was obtained between N_φ and the centroid distance (y), with N_φ reaching a peak value for y = 1.5 approximately owing to its dependency on edge force (H) and the angle relative to horizontal intersection axis and the line connecting sphere and fillet radius centroids (θ_s). For y = 0 and y = 2, $N_{\varphi junction}$ is approaching the value of the membrane solution. $N_{\varphi junction}$ is decreasing exponentially versus the increasing r values, which verifies that the maximum stress concentration is obtained for r = 0.

Variables r, φ and i_{ratio} for a given y value were chosen upon minimizing the product of junction thickness ($t_{junction}$) and the arc length of the UD strap (s). It was shown that with increasing y, φ tends to comes closer to [0^o] and hence more [0^o] layers were needed to ensure strain compatibility in the hoop direction which leads to the increase of i_{ratio}. The fillet radius (r) obtained a decreasing tendency to counteract the increase of $t_{junction}$ within the same interval. Finally, it was shown that higher R/t ratios lead to a reduction in the stiffness of the spheres and thus an exponential decrease of the laminate at intersection ($t_{junction}$).

References

[1] D. Fryer and J.F. Harvey, 'High Pressure Vessels', Springer-Science + Business Media, 1998.

[2] F.J.J.M.M. Geuskens, O.K. Bergsma, S. Koussios and A. Beukers, 'Analysis of conformable pressure vessels: introducing the multibubble', *AIAA Journal*, **49**, 1683-1692, 2011.

[3] G.G. Love, 'Structural Analysis of Orthotropic Shells', *AIAA Journal*, **1**, 1843-1847, 1963.

[4] V.V. Vasiliev, 'Composite pressure vessels – analysis, design and manufacturing', *Bull Ridge Corporation*, 2009.

[5] G. Gerard, 'Comparative Efficiencies of Aerospace Pressure Vessel Design Concepts', *AIAA Journal*, **4**, 2081–2089, 1966.

[6] W. Flügge, 'Stresses in Shells', Springer- Verlag Berlin Heidelberg GmbH, 1960.

[7] SK Chemicals, 'Material Datasheet'.

[8] S. Koussios, 'Chapter 3: Integral Design for Filament Winding—Materials, Winding Patterns, and Roving Dimensions for Optimal Pressure Vessels' Composite filament winding. ASM International Materials Park, 2011.

[9] S. Timoshenko and S. Woinowsky-Krieger, 'Theory of plates and shells', McGraw-Hill, 1959.

[10] S.S. Gill, 'The stress analysis of pressure vessels and pressure vessel components', Pergamon Press, 1970.

[11] E.J. Barbero, 'Introduction to Composite Materials Design', *Taylor & Francis Group*, 1999.

[12] E.H. Baker and L. Kovalevsky, 'Structural analysis of shells', Mc-Graw-Hill, 1972.

[13] G.D. Galletly, 'Edge influence coefficients for Toroidal Shells of Negative Gaussian Curvature', *Journal of Engineering for Industry*, 69–75, 1960.

[14] W. Young and R.G. Budynas, 'Roark's Formulas for Stress and Strain', *McGraw-Hill* (Seventh Edition), 2002.

[15] C. Kassapoglou, 'Design of Composite Structures', *John Wiley & Sons*, 2010.

[16] S. Timoshenko and J.M. Gere, 'Theory of Elastic Stability', McGraw-Hill Book, 1961.

Chapter 5: Volumetric Efficiency & Structural Performance of a Multi-spherical COPV

As mentioned in the previous chapter, conformable structures lead to the enhancement of the volumetric efficiency of a pressure vessel within a prescribed space. Fig. 5-1 shows the expected benefits in terms of the volumetric efficiency of the conformable tank concept compared to multiple cylinders in a rectangular envelope in the automotive industry [1]. The cross-section of the pressure vessels is depicted, and for all aspect ratios (envelope length/width) the conformal vessel concept surpasses the respective cylindrical one in terms of volumetric efficiency.

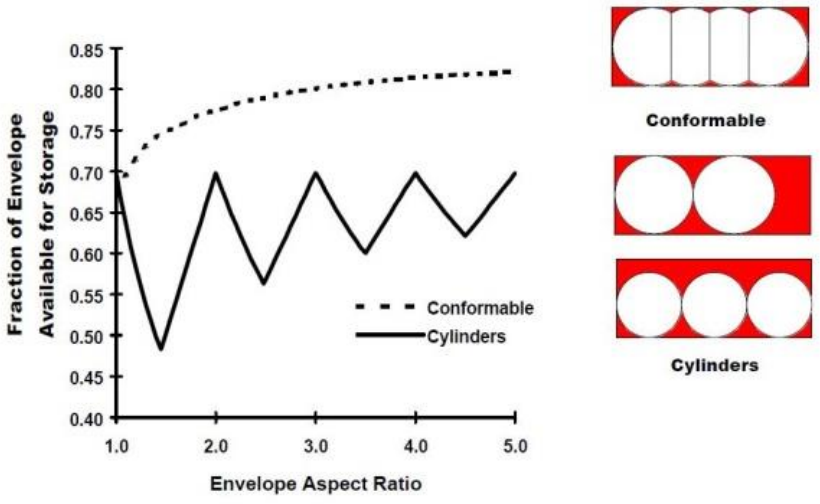

Fig. 5-1: Comparison of the volumetric efficiency between cylindrical and conformable tanks in a rectangular envelope [1].

In this section the internal volume, surface area, mass and structural performance of the multi-sphere are derived analytically. The effect of all these geometrical parameters on those entities is analyzed. A comparison is performed between the multi-sphere and cylindrical COPVs in terms of volumetric efficiency when fitted within a prescribed allowables space and the resulting performance under cryogenic environment.

5.1. Geometrical Calculations

5.1.1 Multi-sphere

i. Internal Volume

In this section, the internal volume is obtained as a function of all the geometrical independent variables: i) membrane element radius (R), ii) the dimensionless centroids distance from the intersecting axis (y), iii) number of membrane elements in the length (m_{cells}), width (n_{cells}) and height (p_{cells}) directions and iv) the dimensionless fillet radius (r). A multi-cell tank consists of $multi_{\text{cells}}$ cells (Fig. 5-2):

$$multi_{\text{cells}} = \left(m_{\text{cells}}\right)\left(n_{\text{cells}}\right)\left(p_{\text{cells}}\right) \tag{5.1}$$

The resulting volume of all the spheres can be derived from:

$$V_{\text{spheres}} = multi_{\text{cells}} \frac{4}{3} \pi R^3 \tag{5.2}$$

The total number of junctions ($multi_{\text{junctions}}$) and junction meeting points ($multi_{\text{centers}}$) is given by the following relationships (Fig. 5-2):

$$multi_{\text{junctions}} = \left[n_{\text{cells}} \left(m_{\text{cells}} - 1 \right) + m_{\text{cells}} \left(n_{\text{cells}} - 1 \right) \right] p_{\text{cells}} + m_{\text{cells}} n_{\text{cells}} \left(p_{\text{cells}} - 1 \right) \tag{5.3}$$

$$multi_{\text{centers}} = \left[\left(m_{\text{cells}} - 1 \right) \left(n_{\text{cells}} - 1 \right) \right] p_{\text{cells}} + \left(p_{\text{cells}} - 1 \right) \left(n_{\text{cells}} - 1 \right) \tag{5.4}$$

As stated in Chapter 4, the junction of two spheres leads to the formation of two spherical caps and together they form a three-dimensional (3D) lens (Fig. 4-15). The volume of one 3D lens (V_{lens}) along with the total volume of all the lenses (V_{lenses}) is given below [2]:

$$V_{\text{lenses}} = multi_{\text{junctions}} V_{\text{lensjunction}}$$

$$\text{where } V_{\text{lensjunction}} = \frac{\pi (2R - d)^2 (d^2 + 4dR)}{12d} \tag{5.5}$$

and d is the centroid distance. A complete example lay-out of a multi-bubble configuration is depicted in Fig. 5-2, where nine different spherical cells are joined together with the number of junctions being 12 and the number of junction meeting points being 4. In this case $m_{\text{cells}} = 1$.

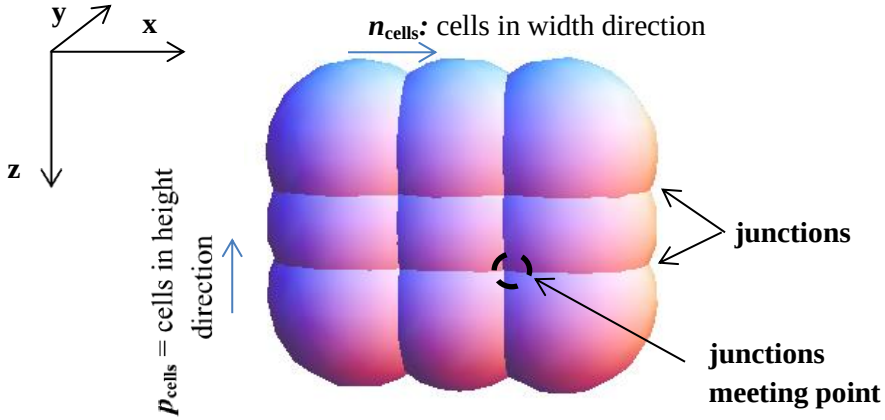

Fig. 5-2: Arrangement of a multi-spherical tank.

The spherical caps overlap each other at the junctions meeting points which results in the formation of common 3D lenses (Fig. 5-3). The coarse grid pattern represents the spherical caps (3D lens) created at the junction, while the fine grid pattern corresponds to the common lens formed at the junction meeting point.

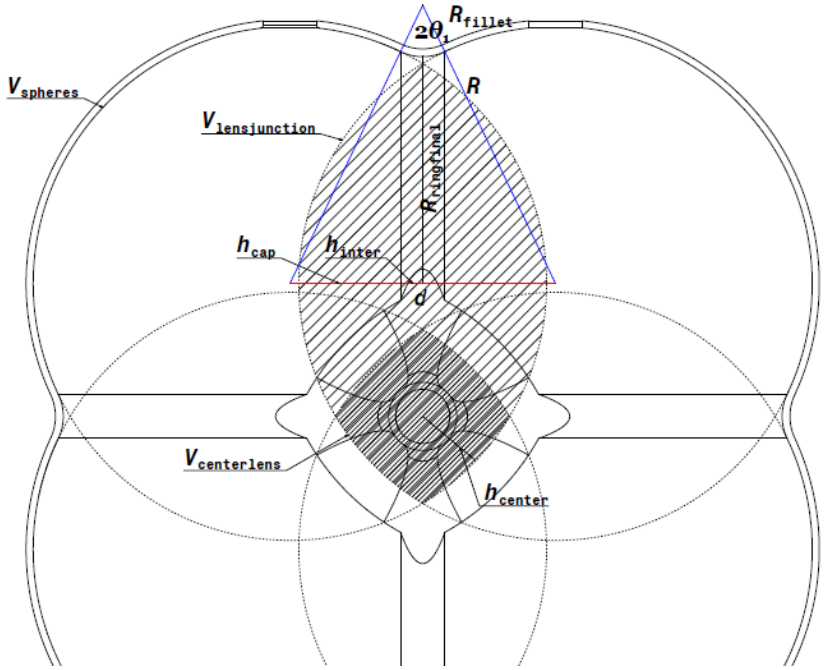

Fig. 5-3: Volume of spheres and intersection spherical caps.

The volume of all the 3D lenses at the junction meeting points can be defined by:

$$V_{\text{centers}} = multi_{\text{centers}} V_{\text{centerlens}},$$

$$\text{where } V_{\text{centerlens}} = \frac{\pi(2R_{\text{ringfinal}} - d)^2 (d^2 + 4dR_{\text{ringfinal}})}{12d},$$

$$R_{\text{ringfinal}} = R_{\text{ring}} + \left[\left(R\cos(\theta_1) - R_{\text{ring}} \right) - \left(h_{\text{inter}} \tan\left[\frac{\theta_1}{2} \right] \right) \right] \tag{5.6}$$

$$h_{\text{inter}} = R_{\text{fillet}} \sin(\theta_1)$$

and $V_{\text{centerlens}}$ is the volume of the lens at a junctions meeting point, $R_{\text{ringfinal}}$ is the intersection radius incorporating the fillet radius correction and h_{inter} is the spherical cap height defined by the intersection axis and the vertical plane at the sphere-junction boundary (Fig. 5-3). An increase of the centroid distance (y) leads to the reduction of the height of the spherical caps at the intersections (h_{cap}) and thus reduction of V_{lenses} and V_{centers}.

Every junction meeting point consists of a hollow section for the reinforcement loops to pass through (Fig. 4-2). The volume of this section (idealized as a cylindrical cell) must be evaluated and subtracted from the tank internal volume. The total volume of all the hollow cylinders within the multi-sphere ($V_{\text{cylinders}}$) is given by:

$$V_{\text{cylinders}} = multi_{\text{centers}} V_{\text{cylinder}},$$

$$\text{where } V_{\text{cylinder}} = \pi r_{\text{cyl}}^2 l_{\text{cyl}},\ r_{\text{cyl}} = \text{Max}\left[\frac{4sk_{\text{overlap}}}{2\pi}, 2t_{\text{junction}}, h_{\text{center}} \right] \tag{5.7}$$

$$l_{\text{cyl}} = \sqrt{R_{\text{ringfinal}}^2 - \left(\frac{d}{2} - r_{\text{cyl}} \right)^2},\ h_{\text{center}} = \frac{2R - d\sqrt{2}}{2}$$

and $k_{overlap}$ being a UD strap arc length overlap parameter where $k_{overlap} = 0$ for a full ring overlap and $k_{overlap} = 1$ for no overlap. The constraint imposed on the radius of the cylinder: $r_{cyl} = 4sk_{overlap}/2\pi$ can be understood by the fact that its perimeter must accommodate the ring cross-sectional areas of the four junctions. At the same time, the cylinder radius should be at least twice the junction laminate thickness ($r_{cyl} = 2t_{junction}$). Furthermore, the radius should be at least equal to the height of the spherical cap formed between two intersecting spheres at the junction meeting point ($r_{cyl} = h_{center}$).

The multi-sphere top view and the cross-section at the intersection are illustrated in Fig. 5-4a and Fig. 5-4b respectively. A top view of the 3D lens formed by the two spherical caps at the intersection can be seen in Fig. 5-4a. For $y = 1$ the height of a spherical cap equals half the centroid distance ($h_{cap} = d/2$). The hollow cylinder in the tank center is shown in Fig. 5-4b.

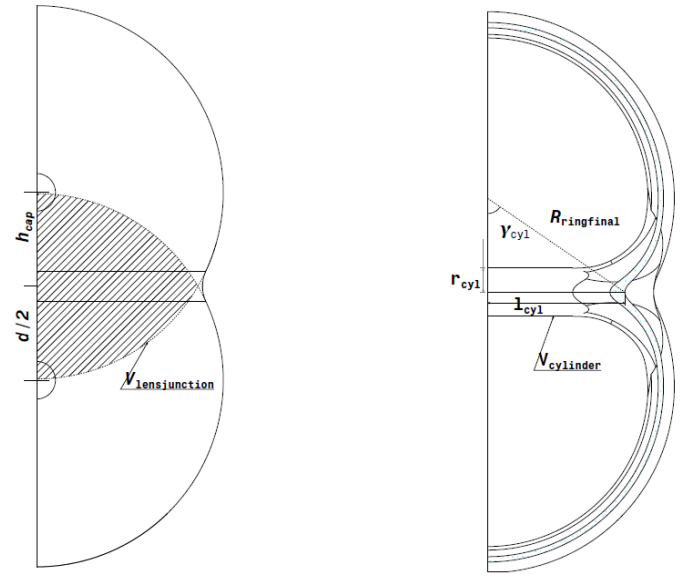

(a) **(b)**

Fig. 5-4: Tank a) top view and b) intersection cut.

The effect of the dimensionless centroid distance (y) on the central cylinder radius (r_{cyl}) can be seen in Fig. 5-5. For $0 < y < 1.5$, r_{cyl} follows the structural constraint of ($r_{cyl} = 4sk_{overlap}/2\pi$) and it follows the decreasing trend of dimensionless fillet radius (r) - seen in Fig. 4-23c. For higher y values, the geometrical constraint ($r_{cyl} = h_{center}$) at the junction meeting point is adopted (Fig. 5-3).

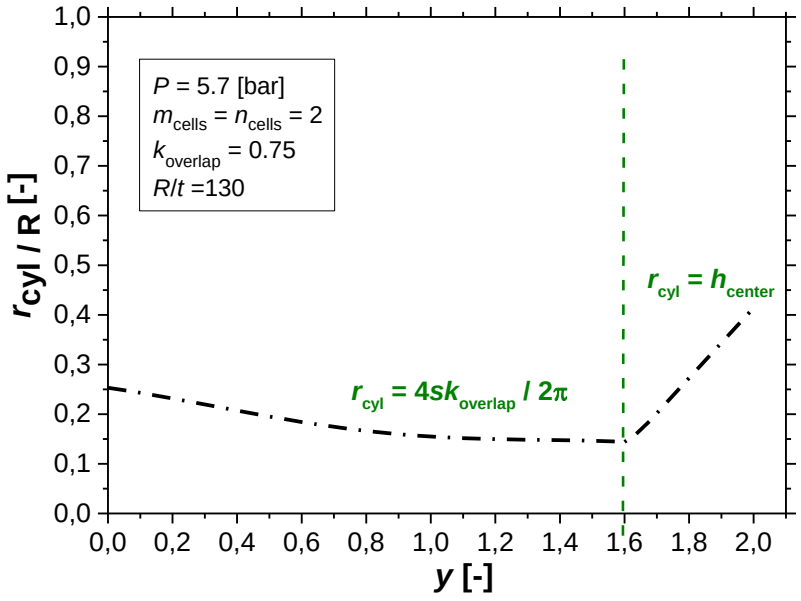

Fig. 5-5: Normalized radius of central hollow tube as a function of *y*.

The introduction of a fillet radius at the intersections leads to an increase of the total internal volume. The added volume from all the junctions (V_{fillets}) is obtained by projecting a triangular face over the toroidal shell formed at the junction (Fig. 5-6), which can be derived as follows:

$$V_{\text{fillets}} = multi_{\text{junctions}} V_{\text{fillet}},$$

$$\text{where } V_{\text{fillet}} = \left(A_{\text{triangle}} - A_{\text{cap}}\right)\left(2\pi R_{\text{ring}}\right), \tag{5.8}$$

$$A_{\text{triangle}} = \frac{bh}{2} = \frac{\left(2R_{\text{fillet}}\sin\left(\theta_1\right)\right)\left(R\cos\left(\theta_1\right) - R_{\text{ring}}\right)}{2}, A_{\text{cap}} = \frac{R_{\text{fillet}}^2}{2}\left(2\theta_1 - \sin(2\theta_1)\right)$$

and b is the distance between the two junctions, h is the height of the triangle, A_{triangle} is the cross-sectional area of the triangle formed at the intersection and A_{cap} is the cross-sectional area formed by the fillet radius at the intersection.

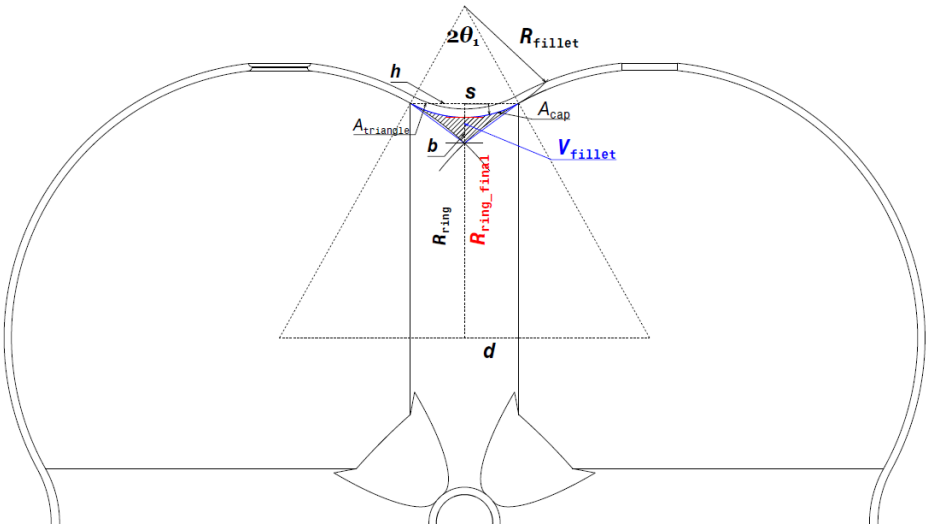

Fig. 5-6: Added volume due to filleting of an intersection.

The internal volume of the multi-sphere tank is found by combining the volumes calculated in Eqs. (5.2), (5.5), (5.6), (5.7) and (5.8):

$$V = V_{\text{spheres}} + V_{\text{centers}} + V_{\text{fillets}} - V_{\text{lenses}} - V_{\text{cylinders}} \tag{5.9}$$

The effect of the dimensionless centroid distance (y) on the normalized volume is illustrated in Fig. 5-7. As an example, two cells were considered across the length and width ($m_{\text{cells}} = n_{\text{cells}} = 2$). Higher values of y lead to an increase of V in a non-linear fashion. It can be seen from the slope of the normalized volume (Fig. 5-7b) that V obtains its global maximum value near $y = 2$, owing to the fact that V_{fillets} is maximized at that point.

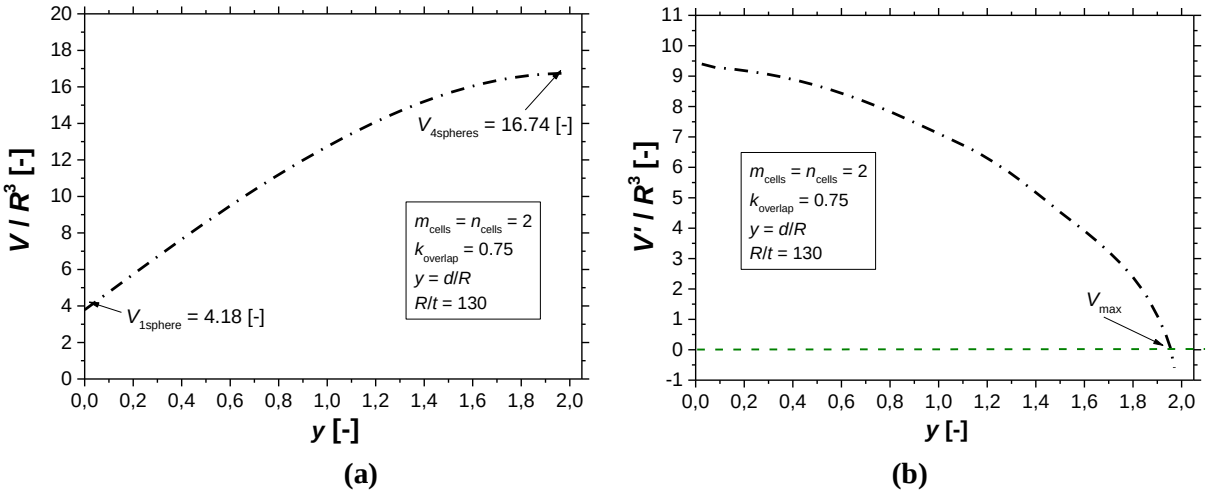

Fig. 5-7: a) Normalized Internal volume and b) its derivative as a function of y.

A correlation between the normalized volume and the number of spherical cells is illustrated in Fig. 5-8. An m_{cells}^2 dependence can be seen, which is a useful consideration for tank up-scaling.

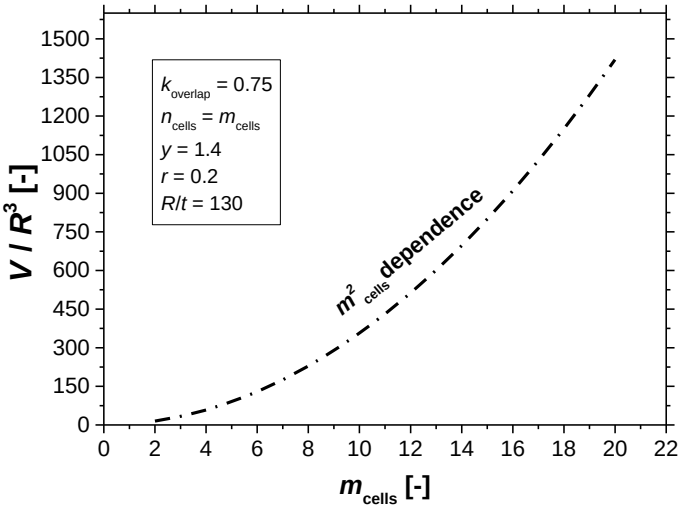

Fig. 5-8: Normalized internal volume as a function of m_{cells}.

ii. Surface Area

A large surface area leads to an increase of composite overwrap weight and insulation thickness. The latter is attributed to more passive heat intake at the cryogenic liquid and thus faster fuel boil-off during operation [3]. Spheres can be beneficial due to their minimal surface area for a given volume. The surface area of the spherical cells -without considering the intersections- is given by:

$$S_{\text{spheres}} = multi_{\text{cells}} 4\pi R^2 \tag{5.10}$$

The surface area of the two spherical caps formed in an intersection is obtained by:

$$S_{\text{lenses}} = multi_{\text{junctions}} S_{\text{lensjunction}},$$
$$\text{where } S_{\text{lensjunction}} = 2(2h_{\text{cap}}),\ h_{\text{cap}} = R - \sqrt{R^2 - R_{\text{ring}}^2} \tag{5.11}$$

and h_{cap} is the height of the spherical cap at the intersection and $S_{\text{lensjunction}}$ is the surface area of one lens formed at an intersection. As mentioned in the previous Chapter, one intersection (up to the cylindrical hollow tube) is idealized as a toroidal shell. Hence, the total surface area of all junctions (S_{fillets}) can be derived from:

$$S_{\text{fillets}} = multi_{\text{junctions}} S_{\text{torus}},$$
$$\text{where } S_{\text{torus}} = 2\pi s R_{\text{ringfinal}} \left(\frac{2\pi - \gamma_{\text{cyl}}}{2\pi} \right) \tag{5.12}$$

and S_{torus} is the surface area of one intersection. The surface area of the spherical cells below the intersections needs to be evaluated ($S_{\text{spheresfillet}}$) and subtracted from the total tank surface area. That surface area of two spherical caps with cap height (h_{inter}) (therefore a 3D lens) and can be given by the following equation:

$$S_{\text{spheresfillets}} = multi_{\text{junctions}} S_{\text{spherefillet}},$$
$$\text{where } S_{\text{spherefillet}} = 2\left[2\pi R h_{\text{inter}}\right] \tag{5.13}$$

At the junction meeting point, a common region is formed in the shape of two spherical caps with equal cap height (h_{center}) (Fig. 5-9). The corresponding surface area of all the 3D lenses in the junction meeting points (S_{centers}) is given by:

$$S_{\text{centers}} = multi_{\text{centers}} S_{\text{center}},$$
$$\text{where } S_{\text{center}} = 2\left[2\pi R h_{\text{center}}\right] \tag{5.14}$$

The surface area of all the central hollow cylindrical shells can be derived from:

$$S_{\text{cylinders}} = multi_{\text{centers}} S_{\text{cylinder}},$$
$$\text{where } S_{\text{cylinder}} = 2\pi\left(r_{\text{cyl}} l_{\text{cyl}} + r_{\text{cyl}}^2\right) \tag{5.15}$$

Finally, the total surface area can be formulated as:

$$S = S_{\text{spheres}} + S_{\text{fillets}} + S_{\text{cylinders}} + S_{\text{centers}} - S_{\text{lenses}} - S_{\text{spheresfillets}} \tag{5.16}$$

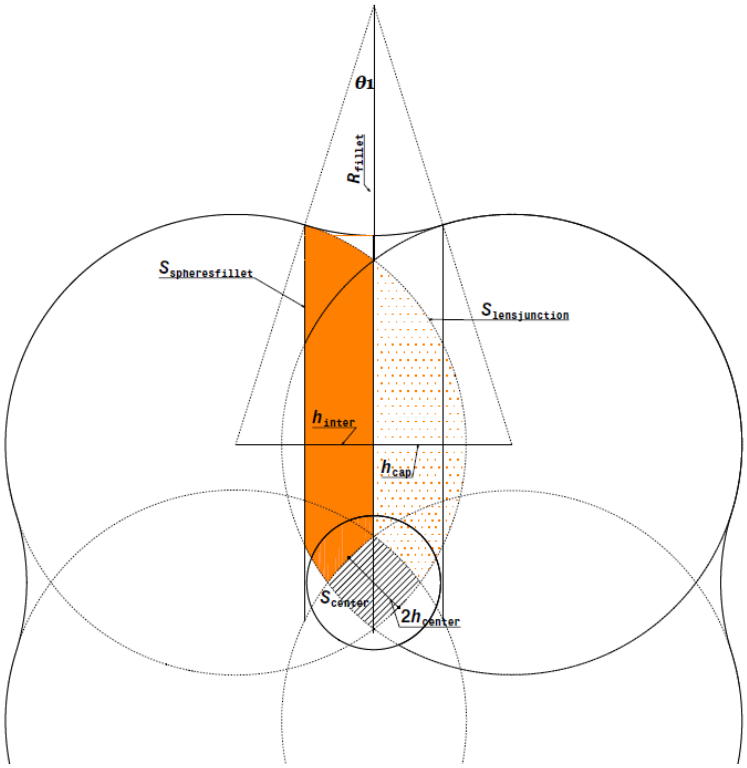

Fig. 5-9: Schematic of various surface area regions.

The effect of the dimensionless centroid distance (y) on the normalized surface area of the multi-sphere is depicted below (Fig. 5-10a). A near bi-linear increasing trend is identified with increasing y values. The decreasing trend of r_{cyl} for $0 < y < 0.7$ (Fig. 5-5) is followed by the surface area. The transition from the structural ($r_{cyl} = 4sk_{overlap}/2\pi$) to the geometrical constraint ($r_{cyl} = h_{center}$) for the cylinder has a strong impact on the surface area, which can be primarily seen at the trend of its slope in Fig. 5-10b.

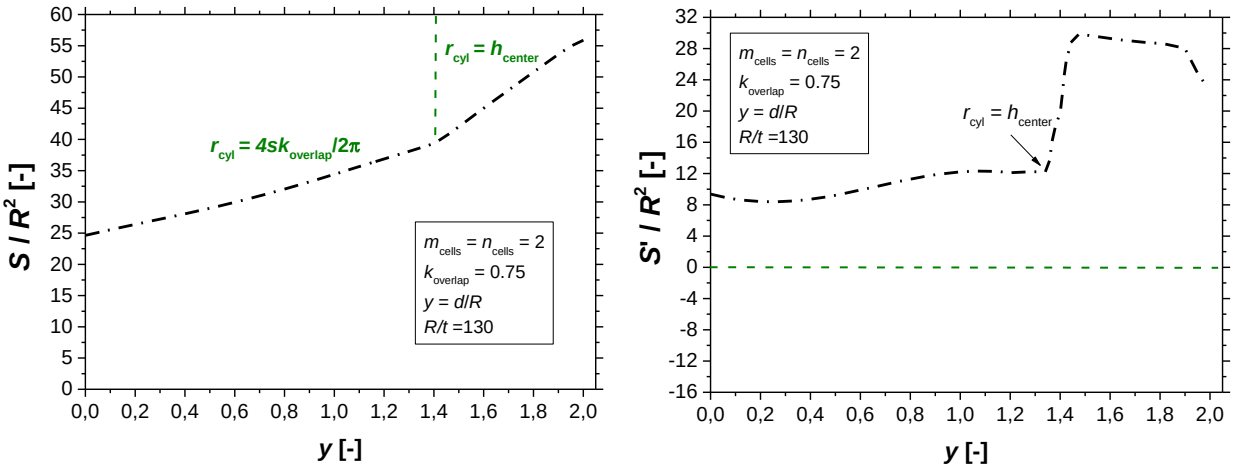

Fig. 5-10: a) Normalized surface area and b) its derivative as a function of *y*.

iii. Mass

The mass of the composite overwrap of the multi-sphere is a function of surface area and the thickness of the tank wall. It can be derived by the following equation by considering the density and thickness of the tank wall (based on the thin-walled assumption):

$$M_{\text{structural}} = \rho_{\text{comp}} t \left(S_{\text{spheres}} + S_{\text{centers}} - S_{\text{lenses}} - S_{\text{spheresfillets}} \right) + \rho_{\text{comp}} t_{\text{junction}} \left(S_{\text{fillets}} + S_{\text{cylinders}} \right) \tag{5.17}$$

As mentioned in Section 4.3.1, a balanced and symmetric quasi-isotropic (QI) lay-up is employed at the spheres to introduce a uniform strain response when subjected to internal pressure. Therefore at least 6 plies are required to also obtain a balanced and symmetric lay-up. For a QI lay-up, the minimum required thickness for a spherical cell is obtained from the following relationship [4]:

$$t = \text{Max}\left[\frac{PR}{2\sigma_{\text{allowable}}}, 6t_{\text{ply}} \right] \tag{5.18}$$

where t_{ply} is the cured ply thickness and $\sigma_{\text{allowable}}$ is the strength allowable of the laminate. At least three plies are required to form a QI laminate. The strength allowable of the laminate ($\sigma_{\text{allowable}}$) can be identified by utilizing the ply engineering constants and strength allowables of the employed composite [4]-[5]. The normalized mass as a function of centroid distance is presented in Fig. 5-11a. A non-linear trend is obtained, similar to the one of intersection laminate thickness (Fig. 4-23d). Unlike the peak of surface area at y = 2, the peak value for mass is achieved for y = 1.6 approximately (Fig. 5-11b), owing to the decreasing trend of t_{junction} for y > 1.6.

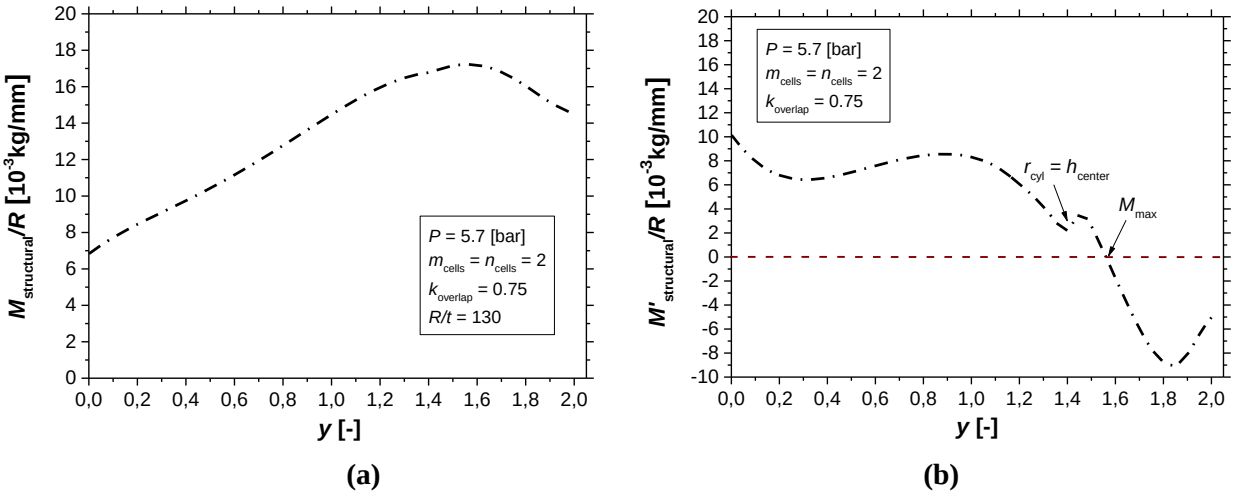

Fig. 5-11: : a) Normalized structural mass and b) its derivative as a function of *y*.

iv. Insulation Thickness

When the tank operates in a cryogenic environment the total mass (M_{cryo}) can be derived accordingly:

$$M_{\text{cryo}} = M_{\text{structural}} + M_{\text{insulation}} = M_{\text{structural}} + \rho_{\text{ins}} t_{\text{ins}} S_{\text{cryo}} \tag{5.19}$$

where t_{ins} is the tank insulation thickness and S_{cryo} is the total multi-cell surface area obtained by replacing R by ($R_{\text{cryo}} = R - t_{\text{ins}}$) in Eqs. (5.10-5.17). The addition of an insulation layer leads to the reduction of volumetric efficiency of the fuel tank within a prescribed box. The evaluation of the required t_{ins} is based on the maximum allowable fuel boil-off hourly rate -in terms of mass- $BOR_{\text{allowable}}$. Mital et al. [6] stated that only 1.6 [%] of the total fuel weight is allowed to evaporate per hour as the fuel is consumed quickly. In the following system the heat transfer from the exterior surface to the liquid (Q) is given by [7]:

$$Q = US_{\text{cryo}}(\Delta T),$$

$$\frac{1}{U} = \frac{t}{k_{\text{comp}}} + \frac{t_{\text{ins}}}{k_{\text{ins}}} + \frac{1}{h_{\text{out}}} \tag{5.20}$$

where U is the overall tank coefficient of heat transfer (containing all layers of thermal resistance as a series of thermal barriers), k_{comp} and k_{ins} are the CFRP ply out-of-plane and insulation thermal conductivities respectively, t_{ins} is the insulation thickness and h_{out} is the free convection film heat transfer coefficient of the exterior. To evaluate the required insulation thickness, the following equation needs to be solved for t_{ins}:

$$BOR_{\text{multi}} = BOR_{\text{allowable}} \tag{5.21}$$

where BOR_{multi} is the hourly fuel boil-off in the multi-bubble tank (given by $BOR_{\text{multi}} = Q / \Delta H_{\text{vap}}$) and ΔH_{vap} is the heat of vaporization of the liquid. The new internal volume of the multi-sphere (V_{cryo}) can be obtained by replacing R with R-t_{ins} in Eqs.(5.1-5.6).

v. Structural Performance

The performance factor $n_{\text{PF}} = PV / W$ is utilized as an index for rating pressure vessels, where $W = Mg$ is the shell weight and g is the gravitational acceleration. Performance and its derivative as a function of y are provided in Fig. 5-12. Unlike the mass curve (Fig. 5-11a), the performance reaches a plateau value from y = 0.7 till 1.4 approximately (Fig. 5-12a).

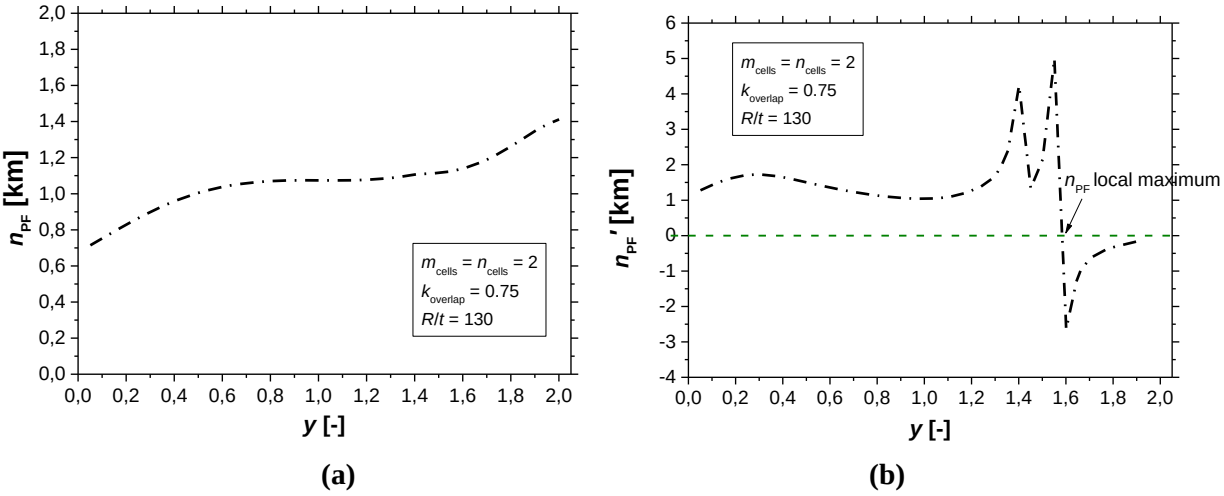

Fig. 5-12: a) Normalized performance and b) its derivative as a function of *y*.

The performance parameter (n_{PF}) as a function of the independent scaling variables: y, m_{cells} is depicted in Fig. 5-13. As stated in the previous section an increasing m_{cells} value results in a quadratic increase of the number of sphere intersections and thus a larger weight penalty. This also leads to an asymptotic behavior. It is shown that the peak performance value is obtained for m_{cells} = 2. The performance in the interval y = {0.7,1.4} and m_{cells} = {6 , ∞} remains within a ± 10 [%] value range.

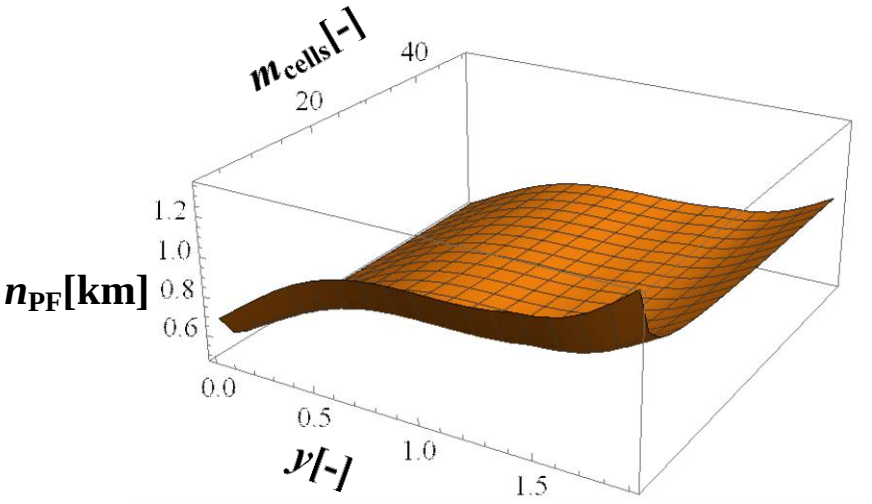

Fig. 5-13: Joined effect of y and m_{cells} on the performance (n_{PF}) for R/t = 130.

The most important outcome of this analysis is that the performance in the interval y = {0.7, 1.4} and m_{cells} = {6 , ∞} remains within a ± 10 [%] value range. Therefore it can be concluded that a safe up-scale of the tank can be achieved by keeping these geometrical variables within these intervals and by following the strain compatibility principle.

5.1.2 Cylindrical COPV with geodesic-isotensoid domes

In this section a summary of the method to derive the internal volume, surface and mass of a conventional cylindrical COPV with isotensoid domes is provided. This derivation will enable the comparison of cylindrical with multi-spherical COPVs in terms of volumetric efficiency and performance, when fitted in a prescribed box. The equations of this section are taken from [8].

i. Internal Volume

The first step is to evaluate the meridian profile as a function of the i) dimensionless radius coordinate (Y), ii) the dimensionless ratio of cylinder radius / polar opening radius (Y_{eq}), iii) the dimensionless axial force (r), iv) the radius of the polar opening (c) and v) the material orthotropy parameter (k_e). The optimal meridian is given by integration of the following differential equation:

$$Z'(Y) = \pm \frac{Y\left(Y^2 + rY_{eq}^2\right)}{\sqrt{\left(\frac{k_e + Y^2 - 1}{k_e + Y_{eq}^2 - 1}\right)^{k_e - 1} (1+r)^2 Y_{eq}^6 - Y^2\left(Y^2 + rY_{eq}^2\right)^2}}, \qquad (5.22)$$

$$k_e = \frac{E_{22}\left(1+\nu_{12}\right)}{E_{11}\left(1+\nu_{21}\right)}, Y_{eq} = \frac{R_{cyl}}{c}$$

where R_{cyl} is the radius of the cylinder. The upper limit of integration is Y_{eq} while the lower limit (Y_{min}) is derived by the following condition:

$$Y_{min} = Max\left[\left(\frac{k_e + Y^2 - 1}{k_e + Y_{eq}^2 - 1}\right)^{k_e - 1} (1+r)^2 Y_{eq}^6 - Y^2\left(Y^2 + rY_{eq}^2\right)^2 = 0 \quad ; \quad 1\right] \qquad (5.23)$$

which states that Y_{min} is the largest number between the Y value that nullifies the denominator of Eq. (5.23) or 1. Fig. 5-14 illustrates the resulting dimensionless meridian profile when the contribution of the matrix is considered ($k_e = E_2(1+\nu_{12})/E_1(1+\nu_{21}) = 0.0856$) and for $Y_{eq} = 5$.

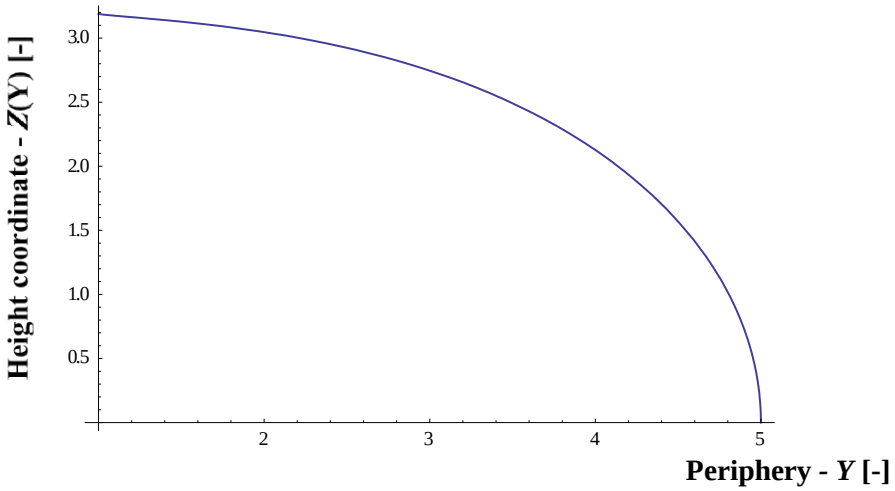

Fig. 5-14: Meridian profile of the cylindrical COPV for $Y_{eq} = 5$ and $k_e = 0.0856$.

With the meridian profile known, the internal volume of the COPV can be derived by:

$$V_{CylCOPV} = c^3\left(2V_{dome} + V_c\right),$$
$$\text{where } V_{dome} = \pi \int_{Y_{min}}^{Y_{eq}} Y^2 Z'(Y)\,dY, \quad V_c = \pi Y_{eq}^2\left(2\Lambda Y_{eq}\right), \Lambda = L/cY_{eq} \tag{5.24}$$

where V_c is the volume of the cylindrical body, Λ is the dimensionless length of the cylindrical body and L is actual length of the cylinder.

ii. Surface Area

The surface area of a cylindrical COPV is calculated as follows:

$$S_{CylCOPV} = c^2\left(2S_{dome} + S_c\right),$$
$$\text{where } S_{dome} = 2\pi \int_{Y_{min}}^{Y_{eq}} Y\sqrt{1+Z'(Y)}\,dY \quad , \quad S_c = 2\pi Y_{eq}\left(2\Lambda Y_{eq}\right) \tag{5.25}$$

where S_c is the surface area of the cylindrical body and S_{dome} is the surface area of the dome.

iii. Mass

The mass of the composite overwrap is a function of the number and total length of the hoop and polar windings over the cylinder and dome respectively (Fig. 5-15). The number of polar (n_{polar}) and hoop (n_{hoop}) windings is derived by imposing a strain compatibility scenario between the dome and the cylindrical body [8].

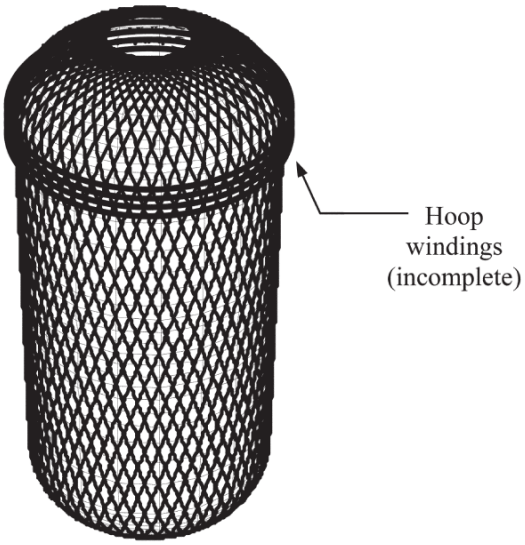

Fig. 5-15: Polar and hoop windings on a dome-cylinder combination [8].

The total mass is obtained by summing the mass of the hoop and polar windings:

$$M_{\text{strcyl}} = M_{\text{polar}} + M_{\text{hoop}} = n_{\text{polar}} L_{\text{polar}} + n_{\text{hoop}} L_{\text{hoop}} \ ,$$

$$\text{where } L_{\text{polar}} = 2L^{\text{d}}_{\text{polar}} + L^{\text{c}}_{\text{polar}} = 2\left(2\int_{Y_{\min}}^{Y_{\text{eq}}} \frac{\sqrt{1+Z^{'}(Y)}}{\cos(a)}\, dY \right) + \left(2\frac{2\Lambda Y_{\text{eq}}}{\cos(a)} \right), \tag{5.26}$$

$$L_{\text{hoop}} = 2\pi Y_{\text{eq}} \ , \ a = \text{Arc}\,\text{Sin}\left[\frac{1}{Y} \right]$$

where α is the winding angle over the dome, $L^{\text{c}}_{\text{polar}}$ and $L^{\text{d}}_{\text{polar}}$ are the dimensionless lengths of the polar windings at the cylinder and dome respectively and L_{polar}, L_{hoop} are the total dimensionless lengths of the polar and hoop windings respectively. The mentioned entities are derived analytically in [8].

5.2. Parametric Study on COPV Volumetric Efficiency and Performance

In this section a study is carried out on the evaluation of the i) insulation thickness, ii) volumetric efficiency and iii) performance of multi-spherical and cylindrical COPVs when fitted within a prescribed rectangular envelope. This prescribed box can have a variable aspect ratio ($a_{\text{ratio}} = l_{\text{box}}/w_{\text{box}}$) of length ($l_{\text{box}}$) and width ($w_{\text{box}}$). A comparison is performed between the multi-spherical COPV and the conventional cylindrical COPV based on the above aspects at both ambient and cryogenic conditions. A single row of shells is considered along the height direction (h_{box}) of the prescribed box for all the configurations.

5.2.1 Ambient Conditions

i. Constraints

For the case of the multi-sphere, an integer number of cells has to fit along the length and width of the box. This will lead to a zig-zag pattern in volumetric efficiency (V_{eff}) versus increasing

aspect ratio (a_{ratio}). The design constraints of the multi-sphere within the prescribed box are established below:

$$\text{i)}\ R = \frac{h_{box}}{2}\ ,\ \text{ii)}\ 0 < R_{fillet} \le R\ ,\ \text{iii)}\ 0 < y < 2$$

$$\text{iv)}\ m_{cells} = \frac{Ry - 2R + a_{ratio} w_{box}}{Ry}\ \ \text{v)}\ m_{cells} \in Z_{+}\ , \tag{5.27}$$

$$\text{vi)}\ n_{cells} = \frac{Ry - 2R + w_{box}}{Ry}\ ,\ \text{vii)}\ n_{cells} \in Z_{+}\ ,\ \text{viii)}\ V \ge V_{min}$$

where h_{box} is the box height. The values of R, R_{fillet} and h_{box} are positive real numbers. A single row of intersecting spheres was considered in this study (constraint (i)), while constraints (iv) and (vi) state that the total length of the intersecting spheres should be equal to the box length and width.

The approach followed hereby is to identify the y, m_{cells} *and* n_{cells} values and corresponding required r, φ and i_{ratio} ($a_{[0o]}$/ $2a_{[\pm\varphi]}$), $t_{junction}$, s at the intersection to maximize the structural performance (n_{PF}) of the multi-sphere, by employing Eqs. (5.1 - 5.19) and by applying the constraints of Eq. (5.27). The QI lay-up employed at the spheres was $[60,0,-60]_s$. A minimum inner volume (V_{min}) is defined as a constraint, based on the required fuel volume (constraint (viii)). In this case the box consists of the following dimensions: $w_{box} = l_{box} = 4800$ [mm] and $h_{box} = 1200$ [mm]. A cross-section of the box and the integrated multi-sphere is depicted below (Fig. 5-16).

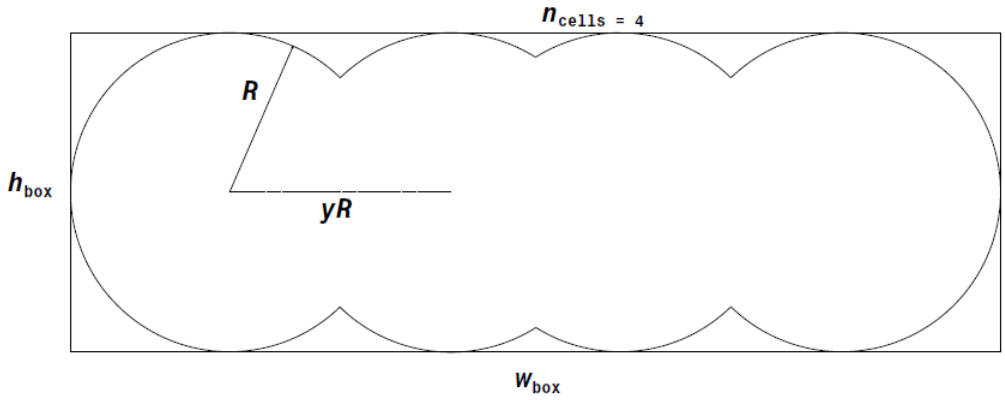

Fig. 5-16: Cross-section of the rectangular envelope and the integrated multi-sphere.

Unlike multi-spherical COPVs, cylindrical COPVs can be arranged in two different ways: i) at a longitudinal (Fig. 5-17a) and ii) at a transverse arrangement (Fig. 5-17b). Only the cylindrical section of these COPVs is hereby depicted. An integer number of cylindrical cells will lead to a zig-zag pattern in V_{eff} versus increasing a_{ratio} or the transverse arrangement, while a continuous line is expected for longitudinally packed cylinders.

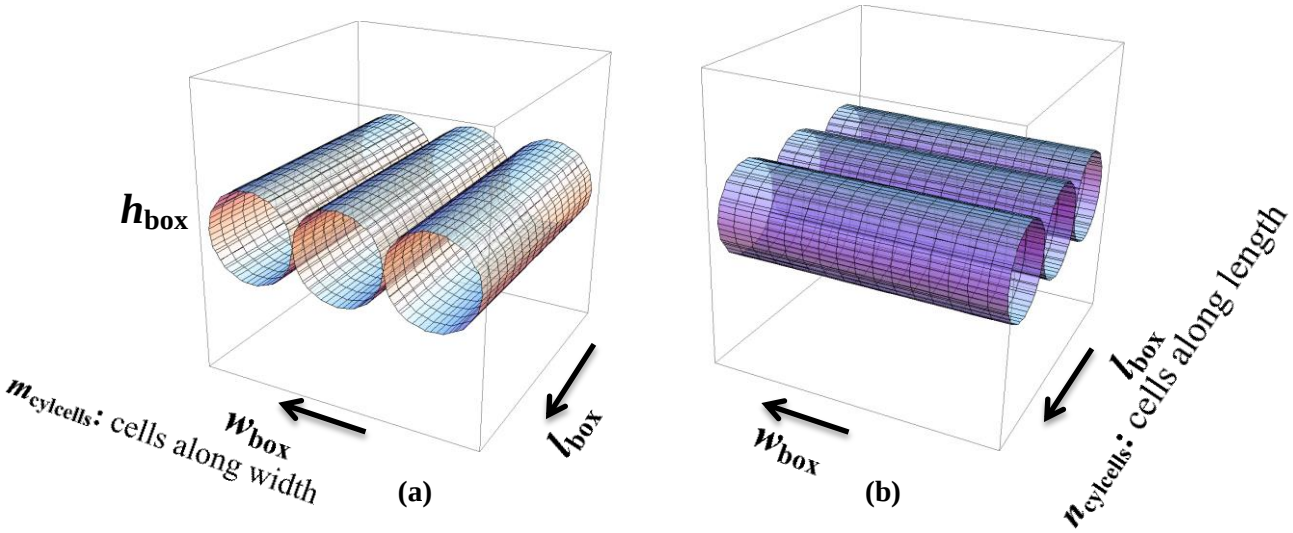

Fig. 5-17: a) Longitudinal/axial and b) transverse arrangement of cylinders.

The design constraints for the longitudinally-packed cylinders are related to the cylinder dimensionless length (Λ), equator radius (R_{cyl}), number of cylinders along the width ($m_{cylcells}$), polar opening (c) as well as dome height ($\bar{Z}$). A single row of packed cylinders was considered in this study (constraint (i)). The cylinders with the isotensoid domes need to fit along the length (constraint ii) and width (constraint iii) of the box.

$$\text{i) } R_{cyl} = \frac{h_{box}}{2}\text{, ii) } 2\Lambda Y_{eq} c + 2\bar{Z} = l\text{,}$$
$$\text{iii) } m_{cylcells} = \frac{w}{2R_{cyl}} \text{ iv) } m_{cylcells} \in Z_{+}\text{, v) } m_{cylcells} V_{cyclCOPV} \geq V_{min} \tag{5.28}$$

On the other hand, the design constraints for the transversely-packed cylinders rely on the number of cylinders along the box length ($n_{cylcells}$) are given below:

$$\text{i) } R_{cyl} = \frac{h_{box}}{2}\text{, ii) } \left(2Y_{eq} c\right)\text{Integer}\left[l/\left(2Y_{eq} c\right)\right] = w_{box}$$
$$\text{iii) } n_{cylcells} = \frac{a_{ratio} w_{box}}{2R_{cyl}}\text{, iv) } n_{cylcells} \in Z_{+}\text{, v) } n_{cylcells} V_{cyclCOPV} \geq V_{min} \tag{5.29}$$

By using Eqs. (5.22 - 5.26) and by applying the constraints of Eqs (5.28-5.29), the maximum number of cells and a global optimum of the performance (n_{PF}) is sought for the cylindrical COPVs in both longitudinal and transverse arrangement.

ii. Results

The total number of cells for the multi-sphere that can fit within the box is depicted below (Fig. 5-18). Eqs. (5.1 - 5.9) were used for the multi-sphere volume calculation keeping into consideration the constraints of Eq. (5.27). A stepwise linear increase was obtained.

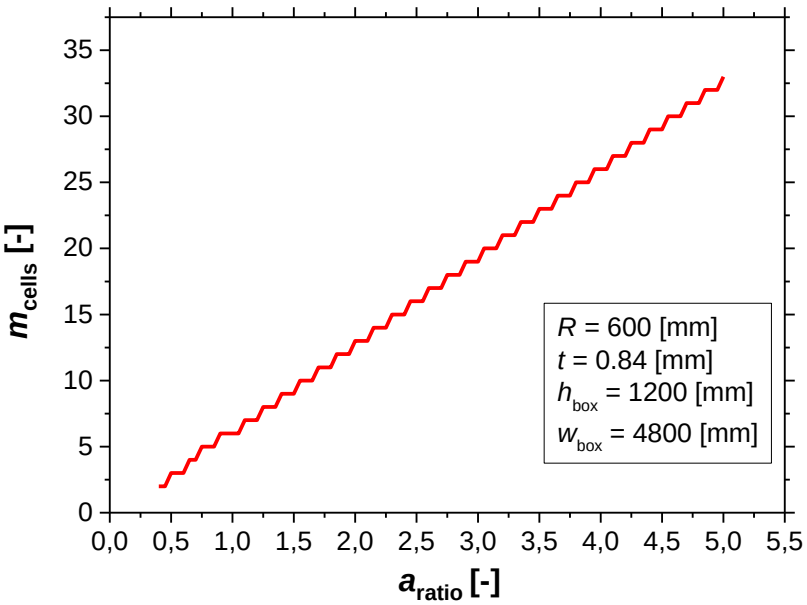

Fig. 5-18: Number of spherical cells along the box length (m_{cells}) as a function of a_{ratio} at ambient conditions for P = 5.7 [bar].

The resulting volumetric efficiency (V_{eff}) of multi-spherical and cylindrical pressure vessels in longitudinal/axial as well as transverse arrangement for $0.4 \leq a_{ratio} \leq 5$ is illustrated in Fig. 5-19. For $0.4 \leq a_{ratio} \leq 1.5$, the variation in the number of contained cells in both multi-spherical, and cylindrical COPVs with transverse packaging is quite high while V_{eff} values of cylindrical COPVs with axial packaging show a more stable behaviour. This is explained by the fact that only the length of the cylindrical body needs to be increased with higher box a_{ratio} values in the axial packaging configuration. For $a_{ratio} \geq 1.5$ it can be seen that the multi-spherical configuration leads to the highest V_{eff}, with the longitudinal packaging being the second best option. It can also be seen that the V_{eff} of the transverse arrangement does not exceed 75 [%]. All configurations show an asymptotic behaviour with increasing values of a_{ratio}.

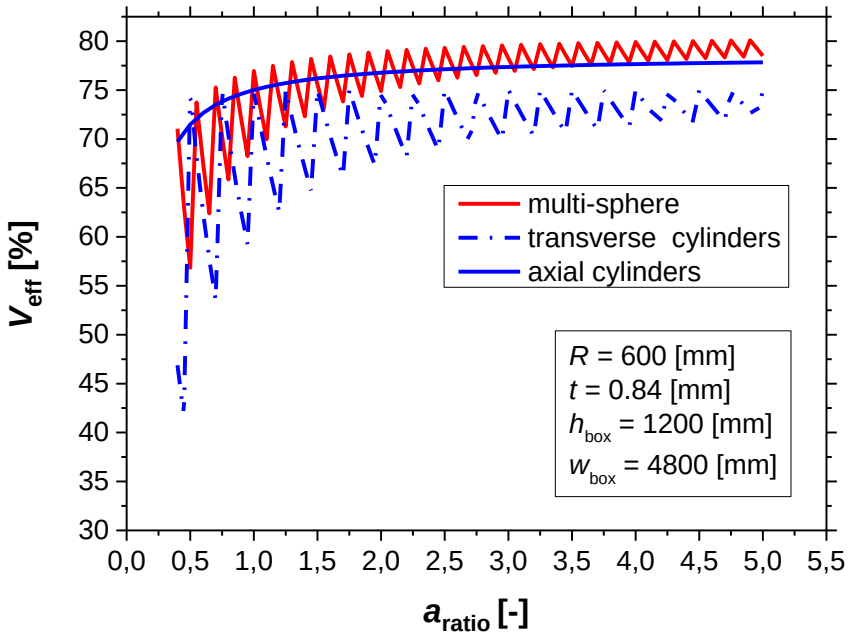

Fig. 5-19: Volumetric efficiency of i) multi-spherical, and cylindrical pressure vessels in ii) axial and iii) transverse packaging for a box with variable a_{ratio} at ambient conditions.

A comparison between the three different tank configurations on the basis of structural mass is illustrated in Fig. 5-20. A stepwise linear increase is obtained for all three configurations associated with a stepwise linear increase of the number of cells (Fig. 5-19). The multi-sphere is the lightest of the three with the axially and transversely packed cylindrical being the heaviest one. The lower weight of the multi-sphere can be attributed to the equal stress behaviour at the sphere and the fact that it consists of 67 [%] of the cylindrical body surface area. Additionally, the weight penalty from reinforcing the intersections is very small in the multi-sphere while in the cylindrical COPVs it can be considerable due to the large surface area of the cylinder (Sec. 5.1.2).

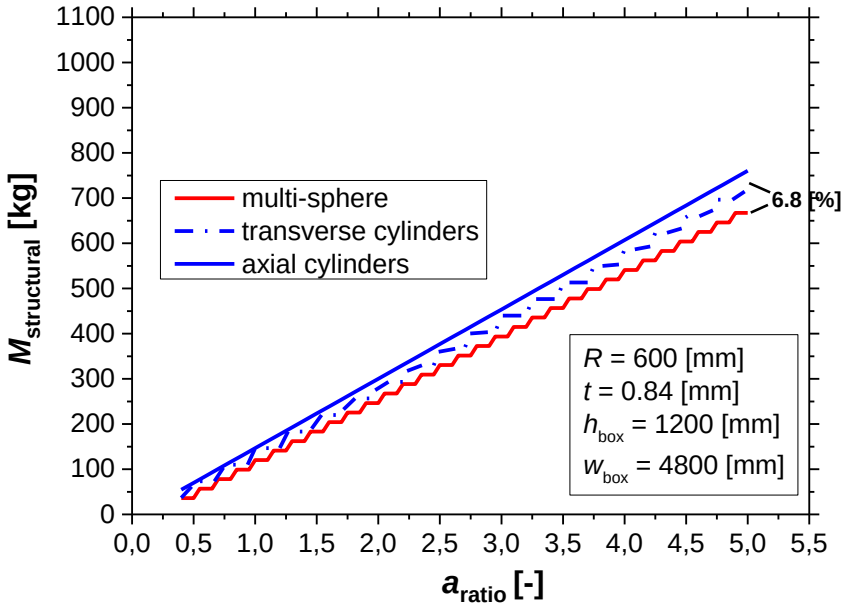

Fig. 5-20: Structural mass of i) multi-spherical, and cylindrical pressure vessels in ii) axial and iii) transverse packaging for a box with variable a_{ratio} at ambient conditions for P = 5.7 [bar].

The resulting performance (n_{PF}) of the vessels is illustrated in Fig. 5-21. The longitudinal and transverse arrangement resulted in similar n_{PF} magnitude and trend. However, the changes in efficiency of these configurations with varying a_{ratio} are negligible compared to the multi-sphere (Fig. 5-21). Owing to the enhancement of the internal volume and weight savings, a larger n_{PF} is obtained for the multi-sphere at ambient conditions. In contrast to the rise of volumetric efficiency, the performance is decreasing in an exponential decay. This can be attributed to the stepwise linear increase of mass (Fig. 5-20) while volume is increasing at a smaller extent in an inverse hyperbolic manner (Fig. 5-19) with increasing box a_{ratio}.

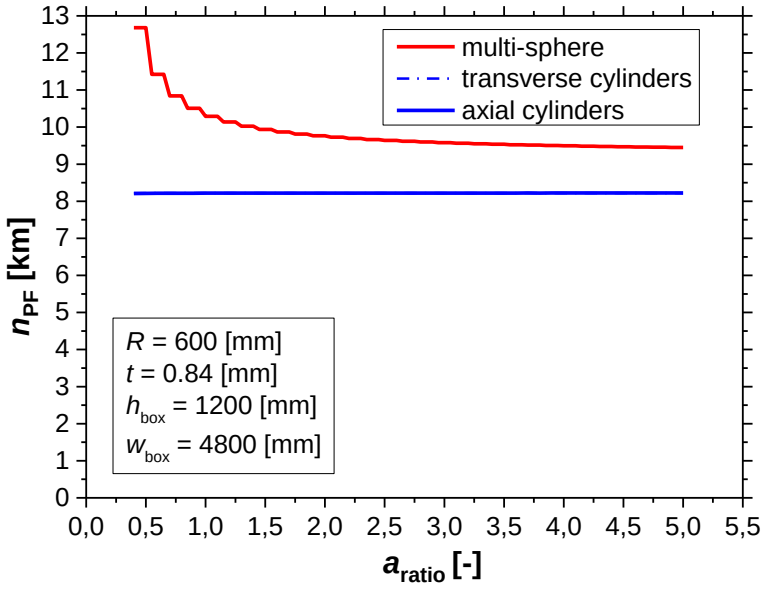

Fig. 5-21: Structural performance of i) multi-spherical, and cylindrical pressure vessels in ii) axial and iii) transverse packaging for a box with variable a_{ratio} at ambient conditions for P = 5.7 [bar].

It is important to evaluate the performance of these configurations when storing LH_2 and establish whether the multi-sphere is still a more beneficial configuration compared to cylindrical COPVs at cryogenic conditions.

5.2.2 Cryogenic Conditions

Unlike operation under ambient conditions, when storing a cryogenic propellant, a thermal insulation layer needs to be added in the tank configuration, which alters the tank design. Therefore the design constraints for the multi-sphere under cryogenic conditions become:

$$\begin{gathered}
\text{i)}\ R_{\text{cryo}} + t_{\text{ins}} = \frac{h_{\text{box}}}{2}\ \ \&\ \text{ii)}\ \ 0 < y < 2 \\
\text{iii)}\ \left(m_{\text{cells}} - 1\right) y\left(R_{\text{cryo}} + t_{\text{ins}}\right) + 2\left(R_{\text{cryo}} + t_{\text{ins}}\right) = a_{\text{ratio}} w_{\text{box}},\ \ \text{iv)}\ \ m_{\text{cells}} \in \mathrm{N} \\
\text{v)}\left(n_{\text{cells}} - 1\right) y\left(R_{\text{cryo}} + t_{\text{ins}}\right) + 2\left(R_{\text{cryo}} + t_{\text{ins}}\right) = w_{\text{box}}, \\
\text{vi)}\ n_{\text{cells}} \in Z_{+},\ \text{vii)}\ V_{\text{cryo}} \geq V_{\min}
\end{gathered} \tag{5.30}$$

whereby R_{cryo} is the reduced radius when employing thermal insulation. The new design constraints for the longitudinally packed cylinders under cryogenic conditions become:

$$\begin{gathered}
\text{i)}\ R_{\text{cylcryo}} + t_{\text{ins}} = \frac{h_{\text{box}}}{2}, \\
\text{iii)}\ \ 2\Lambda Y_{\text{eq}} c + 2\bar{Z} + 2t_{\text{ins}} = w_{\text{box}},\ \text{iv)}\ \ 2m_{\text{cylcells}}\left(R_{\text{cylcryo}} + t_{\text{ins}}\right) = w_{\text{box}} \\
\text{v)}\ \ m_{\text{cylcells}} \in Z_{+},\ \text{vi)}\ m_{\text{cylcells}} V_{\text{cyclCOPV_cryo}} \geq V_{\min}
\end{gathered} \tag{5.31}$$

where R_{cylcryo} is the reduced radius of the cylinder due to the addition of a thermal insulation layer. The corresponding design constraints for the transversely-packed cylinders under cryogenic conditions are:

$$\text{i)}\ R_{\text{cyl\_cryo}} + t_{\text{ins}} = \frac{h_{\text{box}}}{2}\ ,\ \text{ii)}\ Y_{\text{eq}} = \frac{R_{\text{cyl\_cryo}}}{c},$$

$$\left(2Y_{\text{eq}}c\right)\text{Integer}\left[l/\left(2Y_{\text{eq}}c\right)\right] = w_{\text{box}}\ ,\ \text{iv)}\ \ 2n_{\text{cylcells}}\left(R_{\text{cylcryo}} + t_{\text{ins}}\right) = a_{\text{ratio}}w_{\text{box}} \tag{5.32}$$

$$\text{v)}\ \ n_{\text{cylcells}} \in Z_{+}\ ,\ \text{vi)}\ n_{\text{cylcells}}V_{\text{cyclCOPV\_cryo}} \geq V_{\text{min}}$$

The required insulation thickness (t_{ins}) for LH_2 storage as a function of variable box a_{ratio} can be seen in Fig. 5-22. The hypothesis that the multi-sphere leads to a reduction of surface area and thus less passive heat coming from the exterior is hereby verified for $a_{\text{ratio}} \geq 1.5$. It can be seen that the cylindrical COPVs require approximately 7.3 [%] thicker thermal insulation for a_{ratio} =5 which will affect both their internal volume and weight.

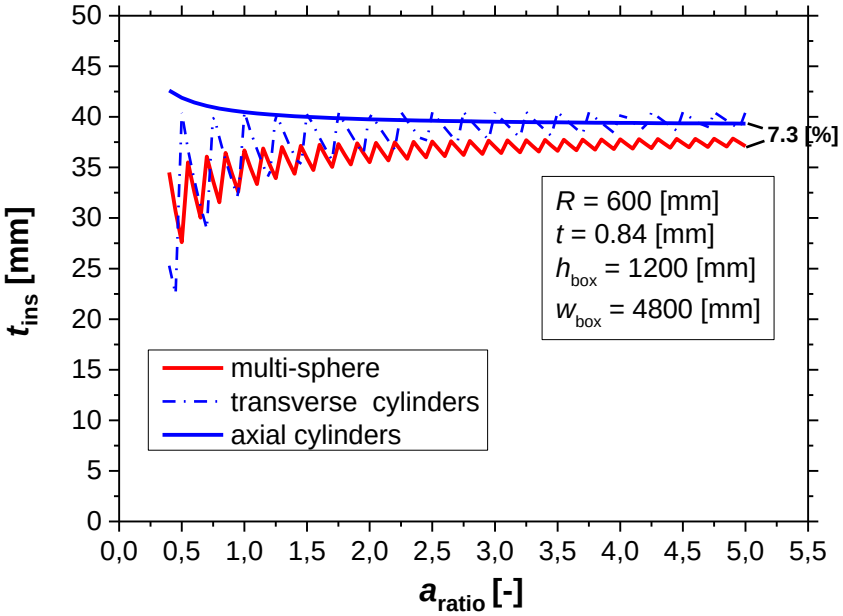

Fig. 5-22: Required insulation thickness of i) multi-spherical, and cylindrical pressure vessels in ii) axial and iii) transverse packaging for a box with variable a_{ratio} ratio for LH_2 storage.

The resulting volumetric efficiency for the three different configurations can be seen below (Fig. 5-23). The introduction of a thermal insulation layer leads to 10 [%] reduction approximately of the efficiency of all configurations (Fig. 5-19). The multi-sphere has the highest V_{eff} for $a_{\text{ratio}} \geq 1.5$ (compared to 3.5 at ambient conditions). A difference of 3.7 [%] is obtained for $a_{\text{ratio}} = 5$ between the multi-sphere and the axially packed cylinders.

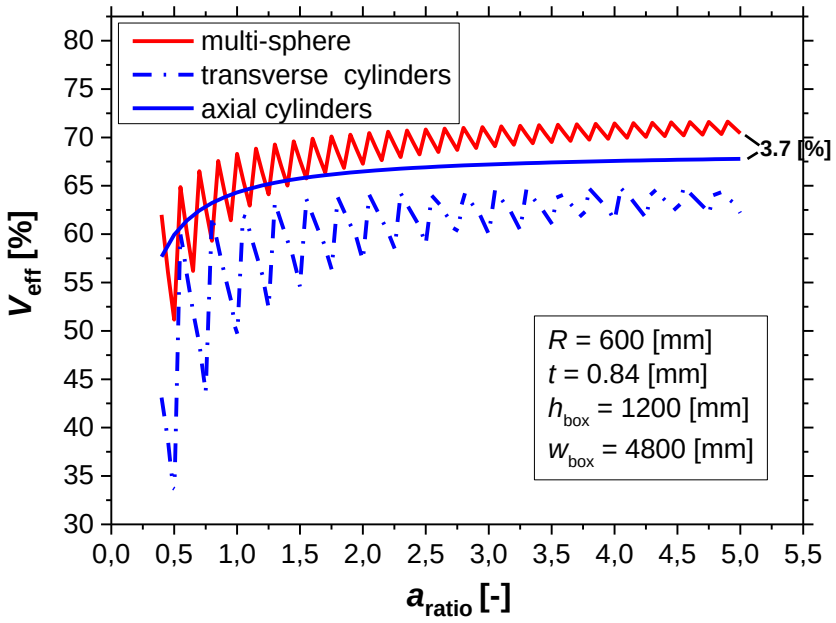

Fig. 5-23: Volumetric efficiency of i) multi-spherical, and cylindrical pressure vessels in ii) axial and iii) transverse packaging for a box with variable a_{ratio} for LH_2 storage.

The multi-sphere is the most weight-efficient configuration with weight reduction going up to 9.2 [%] for a_{ratio} = 5 compared to cylinders (Fig. 5-24). This can be linked to the thinner insulation layer and the less mass of reinforcement to introduce a uniform strain field. The addition of the thermal insulation layer leads to an average increase of 21 [%] approximately for the multi-sphere and a 26 [%] approximately for the cylinders (Fig. 5-20).

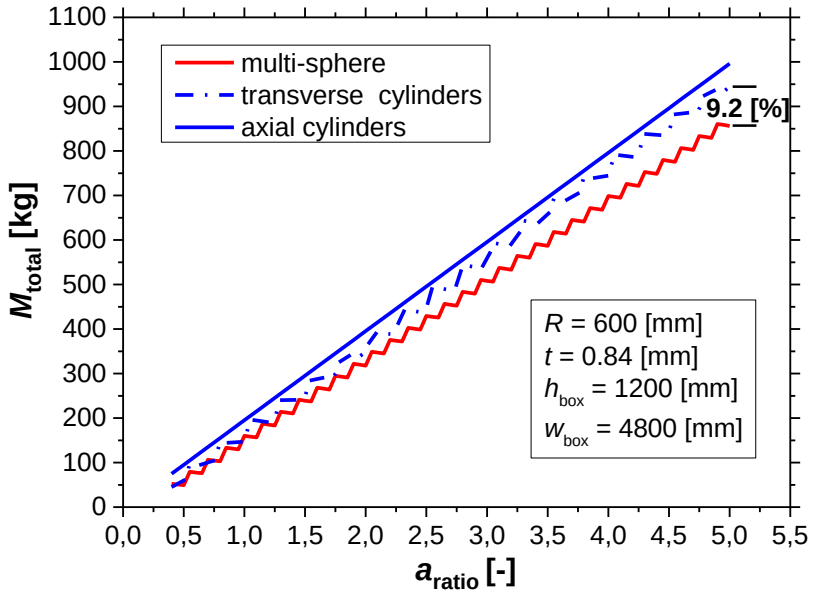

Fig. 5-24: Total tank weight of i) multi-spherical, and cylindrical pressure vessels in ii) axial and iii) transverse packaging for a box with variable a_{ratio} for LH_2 storage.

The resulting performance at cryogenic conditions is illustrated below (Fig. 5-25). It is shown that the addition of thermal insulation results in a reduction of n_{PF} by an average factor of 1.45 approximately for the multi-sphere and a factor of 1.55 approximately for the cylinders (Fig. 5-21). The multi-sphere is the most structurally efficient COPV with the n_{PF} difference ranging from 34.3 [%] for a_{ratio} = 0.4 to 17.1 [%] for a_{ratio} = 5.

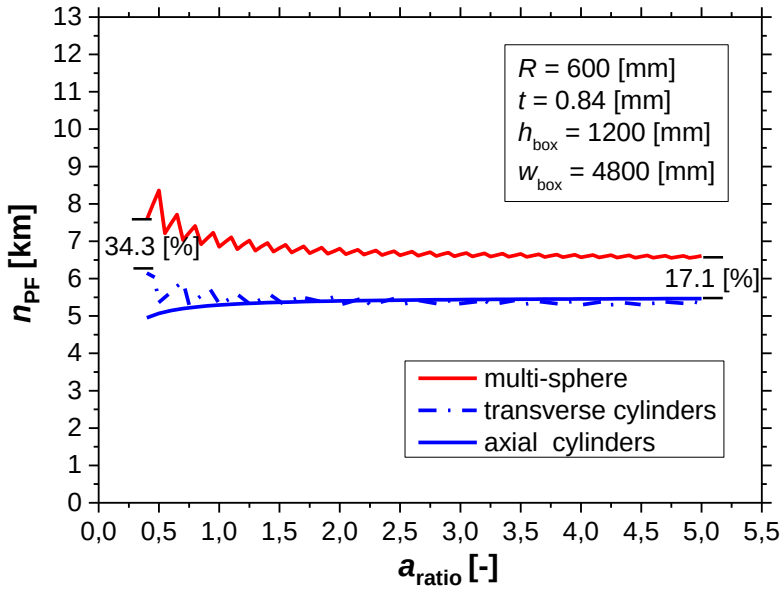

Fig. 5-25: Structural performance of i) multi-spherical, and cylindrical pressure vessels in ii) axial and iii) transverse packaging for a box with variable a_{ratio} for LH_2 storage.

A correlation between the normalized values of structural performance and volumetric efficiency of the multi-sphere for LH_2 storage is depicted below (Fig. 5-26). A stepwise linear inverse relationship is obtained for increasing a_{ratio} values. It is shown that maximization of n_{PF} leads to $V_{eff} = 0.73\ V_{effmax}$, while maximization of V_{eff} results in $n_{PF} = 0.78\ n_{PFmax}$ within the value range of a_{ratio} studied. It can be concluded that small a_{ratio} values lead to structural efficiency maximization, while large values result in the maximization of V_{eff}. It is however important that the structural efficiency cannot fall below $n_{PF} = 0.75\ n_{PFmax.}$

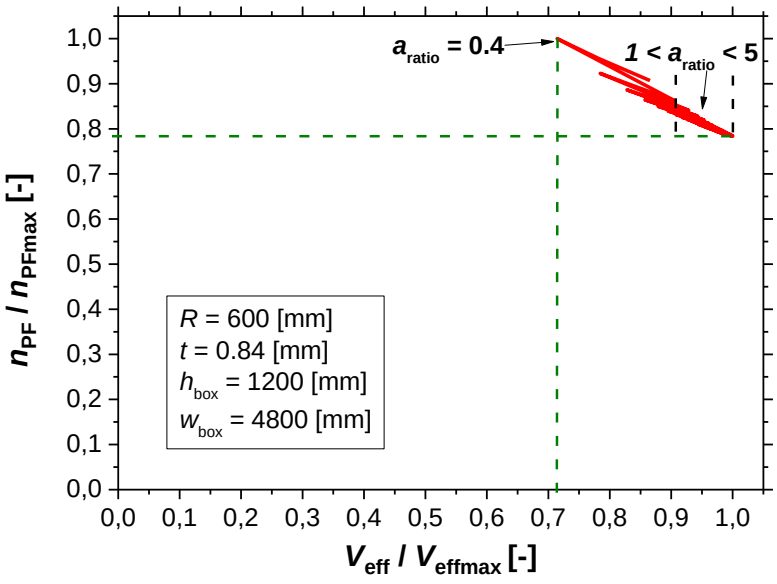

Fig. 5-26: Correlation between the normalized values of structural performance and volumetric efficiency for a box with variable a_{ratio} for LH_2 storage.

5.3. Concluding Remarks

This chapter dealt with the determination of the multi-sphere internal volume, surface area and corresponding mass based on the following variables i) number of cells (m_{cells}, n_{cells}, p_{cells}), ii) dimensionless centroid distance (y), iii) dimensionless fillet radius (r), iv) sphere radius (R), v)

lamina angle (φ) and vi) ratio between [0^o] and [$\pm\varphi$] layers at the junctions. The goal was to maximize performance (n_{PF}) for a given prescribed space. The findings of Chapter 4 on the required number of UD straps reinforcement for spheres/junction strain compatibility were incorporated in the weight calculations.

It was shown that the internal volume and mass of the multi-sphere have an increasing non-linear trend with increasing values of the dimensionless centroid distance (y). On the other hand, the multi-sphere performance reaches a plateau value from y = 0.7 till 1.6 approximately and maximizes near y = 2. When performance is plotted against increasing m_{cells} value it remains within a ± 10 [%] value range in the interval y = {0.7, 1.4} and m_{cells} = {6 , ∞}. As a result it can be concluded that a safe up-scale of the tank can be achieved by keeping these geometrical variables within these intervals and by following the strain compatibility principle.

A parametric study on the volumetric efficiency and performance of the multi-sphere -when fitted in a rectangular envelope with variable aspect ratio (l_{box}/w_{box})- was performed by changing the above mentioned parameters. Since an integer number of cells has to fit along the length and width of the box, the graph of the volumetric efficiency (V_{eff}) versus the box increasing aspect ratio attained a zig-zag pattern. A comparison to cylindrical COPVs revealed an enhancement in vessel in both V_{eff} and n_{PF} under ambient and cryogenic conditions. This is attributed to the fact that strain compatibility in a multi-spherical COPV is achieved with hoop rings applied at the small sections (intersections), while hoop windings in a cylindrical COPV are applied over the entire cylindrical region. Additionally, spheres have a smaller surface area for a given volume when compared to cylinders, which results in less passive heat from the exterior to the cryogenic fuel. As a result, a thinner layer of thermal insulation needs to be applied that results in better volumetric efficiency and less insulation weight. Finally, an inverse stepwise linear relationship between V_{eff} and n_{PF} for increasing box aspect ratio was attained.

References

[1] A. Haaland, High-Pressure Conformable Hydrogen Storage for Fuel Cell Vehicles, *Proceedings of the U.S. DOE Hydrogen Program Review, California*, 463-469, 2000.

[2] Wolfram Mathworld.

[3] T.L. Bergman, A.S. Lavine, F.P. Incropera and D.P. Dewitt, 'Fundamentals of heat and mass transfer', *John Wiley and Sons* (Seventh Edition), 2011.

[4] E.J. Barbero, 'Introduction to Composite Materials Design', *Taylor & Francis Group*, 1999.

[5] I.M. Daniel and O. Ishai, 'Engineering mechanics of composite materials, (Second Edition) Oxford University Press, 2006.

[6] S. Mital, J. Gyekenyesi, S. Arnlod, R. Sullivan, J. Manderscheid and P. Murphy, 'Review of current state of the art and key design issues with potential solutions for liquid hydrogen cryogenic storage tank structures for aircraft applications', NASA-TM, 2006.

[7] T.L. Bergman, A.S. Lavine, F.P. Incropera and D.P. Dewitt, ' Fundamentals of heat and mass tranfer', (Seventh Edition) John Wiley & Sons, 2011.

[8] S. Koussios, 'Chapter 3: Integral Design for Filament Winding—Materials, Winding Patterns, and Roving Dimensions for Optimal Pressure Vessels' S.T. Peters, Composite filament winding. ASM International, Materials Park, 2011.

Chapter 6: Engineering Properties at Cryogenic Temperatures

The multi-spherical COPV is expected to have a plastic liner serving as a gas diffusion barrier, which has a significantly higher coefficient of thermal expansion (CTE) compared to the composite overwrap. The CTE mismatch can lead to considerable stresses throughout chill-down. Additionally, material embrittlement of the tank wall occurs due to exposure to cryogenic environments thus affecting strain evolution and pressure allowables. Therefore the derivation of temperature dependent properties is required in order to assess accurately the stress field at both the liner and composite overwrap throughout cryogenic operation. This section deals with the evaluation of the engineering properties of the liner and overwrap materials through approximated functions. The approximation functions are based on the results from material testing and literature. This chapter is based on the work conducted in [1].

6.1 Material Testing

The stiffness and strength of the composite overwrap and polymeric liner materials are expected to increase while the ultimate failure strain is expected to decrease substantially when tested at cryogenic temperatures compared to their behaviour at ambient conditions [1]. For this research, uniaxial tensile and compression loading was conducted at coupon level under various temperatures in accordance to the ASTM 3039 [3] and ASTM 6641 [4] standards to derive the engineering properties and respective strength indices of the overwrap and liner materials. The laminate specimen lay-ups were $[0^o]_8$, $[+/-45^o]_{2s}$, $[90^o]_{16}$ and consisted of a rectangular geometry: length: 250 [mm], width: 25 [mm] in accordance to ASTM 3039 [3]. The liner samples consisted of a dog-bone geometry: length: 165 [mm], gauge length: 50 [mm], width: 19 [mm], gauge width: 13 [mm] in accordance to ASTM 638 [5]. The temperatures at which the composite (CFRP) and liner specimens were tested can be seen below (Table 6-1). Each sample was tested five times in order the examine the repeatability of results.

Table 6-1: Outline of temperatures employed for coupon testing.

Specimen	Temperatures
$[0^o]_8$	{-40 [^{o}C], -10 [^{o}C], 23 [^{o}C]}
$[+/-45^o]_{2s}$	{-40 [^{o}C], -10 [^{o}C], 23 [^{o}C]}
$[90^o]_{16}$	{-40 [^{o}C], -10 [^{o}C], 23 [^{o}C]}
PA12	{-70 [^{o}C],-40 [^{o}C], -10 [^{o}C], 23 [^{o}C], 60 [^{o}C], 90 [^{o}C]}

An overview of a cryo-tensile test with the use of a climate chamber is depicted in Fig. 6-1. Cooling on the sample was induced by forced convection through a fan. The lowest possible temperature of testing was -70 [^{o}C], owing to the testing machine limitations. The sample was kept in the climate chamber for 30 [minutes] prior to testing to obtain the preferred temperature. Strain gages at longitudinal and transverse directions along with thermocouples were attached to the specimen surface to monitor strain and temperature evolution throughout the experiment. Mechanical grips were incorporated for clamping of the specimen. Finally, the specimen was loaded in tension or compression in a displacement control way.

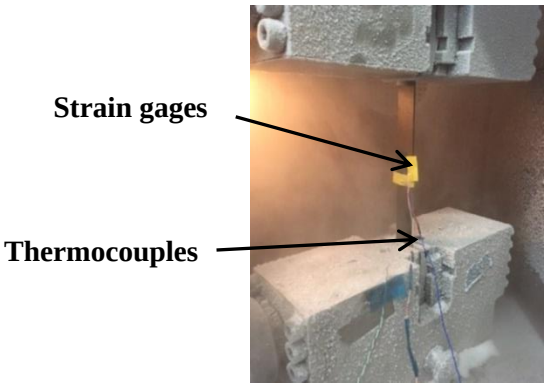

Fig. 6-1: Uniaxial tensile loading of a carbon fiber-reinforced polymer (CFRP) specimen at cryogenic conditions.

The obtained ply engineering properties (E_{11}, E_{22}, G_{12}, ν_{12}) can be seen in Table 6-2. Additionally, the strength allowables (X_t, Y_t, S), failure strain (ε_{xt}: parallel to the fibers, ε_{yt}: transverse to the fibers) of the CFRP material are given below. These values were used as a first step to extrapolate over a wider temperature range using a least squares fit approach.

Table 6-2: CFRP ply properties at various temperatures.

T [°C]	E_{11} [GPa]	E_{22} [GPa]	ν_{12} [-]	G_{12} [GPa]	X_t [MPa]	X_c [MPa]	Y_t [MPa]	Y_c [MPa]	S [MPa]	ε_{xt} [%]	ε_{yt} [%]
-40	132.8	10.4	0.251	5.6	2186	1193	79.3	278.3	80.2	1.49	0.51
-10	131.7	9.7	0.272	5.2	2125	1181	75.3	253.2	74.8	1.43	0.52
23	128.6	8.6	0.278	4.7	2067	1130	67.1	244.7	71.6	1.46	0.58

The values for the Young's modulus (E_{liner}), major Poisson's ratio ($\nu_{12lienr}$), ultimate tensile strength (UTS_{liner}) and elongation at break ($\varepsilon_{ultliner}$) of PA12 can be seen below (Table 6-3).

Table 6-3: PA12 properties at various temperatures.

T [°C]	E_{liner} [GPa]	$\nu_{12liner}$ [-]	UTS_{liner} [MPa]	$\varepsilon_{ultliner}$ [%]
-70	3.8	0.34	77.6	3.87
-40	2.9	0.34	69.3	5.51
-10	2.4	0.39	63.5	8.23
23	1.5	0.41	43.3	19.3
60	0.7	0.43	36.2	45.4
90	0.5	0.45	25.4	126.4

The polymer response to uniaxial tension at different temperatures can be seen in Fig. 6-2. This graph is determined after applying the gauge length and sample thickness values to the force-displacement relationship obtained from the experiment. Young's modulus and strength are increasing while elongation-at-break is decreasing at lower temperatures. While the material had a very ductile behaviour at room temperature (RT) and at elevated temperatures, at -40 [°C] and at -70 [°C] the plastic region was particularly small. Hartwig [6] concluded that PA12 has a very small plastic region at the LN_2 boiling point (-196 [°C]).

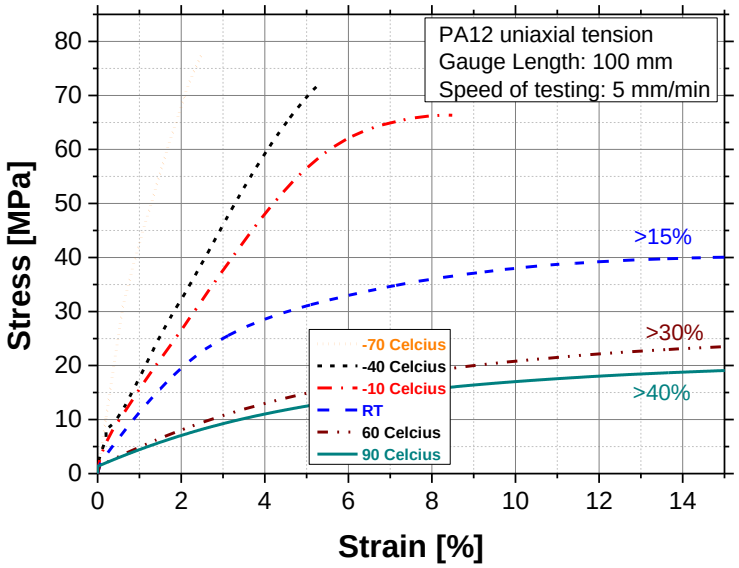

Fig. 6-2: PA12 response to uniaxial loading at different temperatures.

A cryogenic COPV can face a scenario of high strain-rate loading due to sudden excessive liquid fuel boil-off. The liner material was tested at four different strain rates owing to the polymer strain-rate sensitivity [7]. Strain-rates of 75 [mm/min], 100 [mm/min] and 125 [mm/min] were selected since they are close to common pressure rise rates (dP/dt) occurring throughout operation for tanks with a very thin thermal insulation layer [8] (although in this case we are analysing a non-insulated tank). The respective results can be seen in Fig. 6-3. A non-linear stress-strain response along with a very high elongation at break (19.3 [%]) is seen when testing at 5 [mm/min]; testing at 125 [mm/min] results in near linear-elastic behaviour with an elongation at break of 4.83 [%].

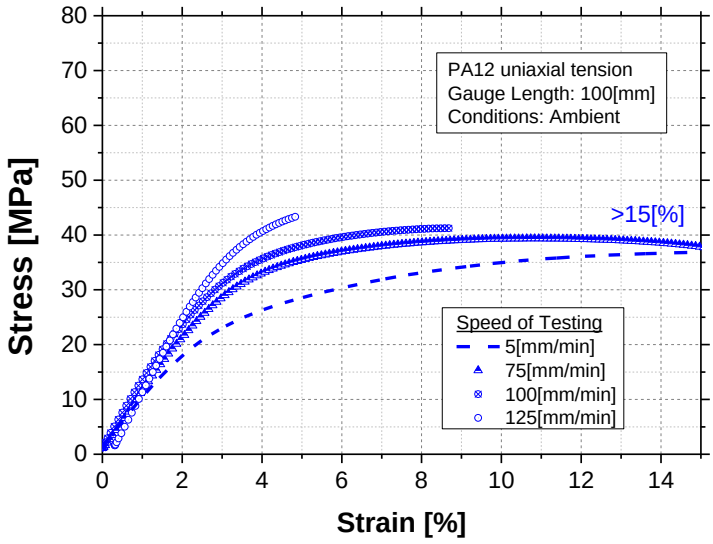

Fig. 6-3: PA12 response to uniaxial loading at room temperature at various speeds of testing.

Finally, the thermal expansion of both composite overwrap and polymeric liner materials was evaluated experimentally by employing ASTM 11359-2 [9] at -105 [^{o}C] < T < 100 [^{o}C]**.** The results are presented in the next section.

6.2 Material Properties at Temperature Extremes

Both the liner and overwrap material properties were investigated at temperature extremes by several published works. The temperature extremes of these functions are given by the LHe boiling point (T_1 = -269 [^{o}C]) and the curing temperature of the composite overwrap (T_2 = 125 [^{o}C]). The CTE values of both the liner and composite materials are assumed zero at T_1 = -269 [^{o}C] due to compaction of molecules and lack of free volume within the material. The values of the properties at temperature extremes (T_1 = -269 [^{o}C] and T_2 = 125 [^{o}C]) are given in Table 6-4, with the symbol T used as superscript to denote the temperature dependency of these properties:

Table 6-4: Property values at temperature extremes.

Property	**Unit**	**T_1 = -269 [^{o}C]**	**T_2 = 125 [^{o}C]**
$\varepsilon^{T}_{ultliner}$	[%]	< 1 [10]	> 500 [10]
E^{T}_{liner}	[GPa]	6.93 [11]	0.28 [12]
UTS^{T}_{liner}	[MPa]	117 [10]	16 [10]
α^{T}_{liner}	[mm/mm^{o}C]	0	175 10^{-6} [6]
ε^{T}_{xt}	[%]	1.51 [13]	1.43 [13]
ε^{T}_{yt}	[%]	0.31 [1]	0.73 [1]
E^{T}_{11}	[GPa]	137.8 [14]	126.5 [15]
E^{T}_{22}	[GPa]	10.78 [16]	6.81 [17]
G^{T}_{12}	[GPa]	8.92 [15]	3.72 [18]
X^{T}_{t}	[MPa]	2289 [15]	2007 [15]
X^{T}_{c}	[MPa]	1120.4 [14]	846 [17]
Y^{T}_{t}	[MPa]	84.3 [15]	48.57 [18]
Y^{T}_{c}	[MPa]	304.3 [15]	158 [17]
S^{T}	[MPa]	102.4 [15]	52.1 [18]
α^{T}_{11}	[mm/mm^{o}C]	0	-0.42 10^{-6} [19]
α^{T}_{22}	[mm/mm^{o}C]	0	67.85 10^{-6} [19]

The values presented above will be incorporated in the approximation functions of the following Section to accurately perform an interpolation study within the temperature range of interest.

6.3 Approximation Functions

Fitting functions were sought, which would behave reliably within the temperature range of interest. A separate set of fitting constants {*a*, *b*, *c*} was assigned for every approximation. These constants were derived from a least squares fit with temperature (*T*) as the independent variable.

Elongation at break of the liner material (PA12) and UD prepreg was approximated by employing a hyperbolic function. This is attributed to the fact that a close to zero value is expected at very low cryogenic temperatures while at temperatures relatively higher than the glass transition temperature (T_g), the ultimate strain is expected to be considerable as material softening occurs. The following equation was employed:

$$\left(\varepsilon_{\text{ultliner}}^{\text{T}}, \varepsilon_{\text{xt}}^{\text{T}}, \varepsilon_{\text{yt}}^{\text{T}}\right) = f\left(a,b,c \mid T\right) \Rightarrow \frac{1}{\left(a-bT\right)^{\text{c}}} \tag{6.1}$$

where *a*, *b* and *c* are independent fitting function constants.

The stiffness and strength of PA12 polymer and UD prepreg are expected to decrease gradually as temperature increases while cryogenic temperatures result in a gradual increase of these properties. As mentioned above, an asymptotic curve is expected for *E*(T) and *S*(T) at cryogenic temperatures due to freezing of the mobility of polymer molecules and at elevated temperatures due to material softening associated with glass transition. A sigmoid function was utilized to fit the experimental strength and stiffness values over temperature since it can accurately represent the asymptotic material behaviour over the entire temperature regime (Eq. (6.2)).

$$\left(E_{\text{liner}}^{\text{T}}, E_{11}^{\text{T}}, E_{22}^{\text{T}}, G_{12}^{\text{T}}, UTS_{\text{liner}}^{\text{T}}, X_{\text{t}}^{\text{T}}, X_{\text{c}}^{\text{T}}, Y_{\text{t}}^{\text{T}}, Y_{\text{c}}^{\text{T}}, S^{\text{T}}\right) = f\left(a,b,c \mid T\right) \Rightarrow \frac{a}{\left(1+be^{-\text{cT}}\right)} \tag{6.2}$$

where *a* represents the unrelaxed value of that property at the LHe boiling temperature (-269 [$^{\text{o}}$C]) while *b* and *c* capture stiffness/strength change. Unlike the CFRP ply behaviour at [45$^{\text{o}}$] and [90$^{\text{o}}$] orientations, temperature is expected to have a very small effect on the CFRP stiffness and strength at [0$^{\text{o}}$] orientation.

Finally, the coefficient of thermal expansion (CTE) of the liner material and the [90$^{\text{o}}$] composite strips was captured using a polynomial fit of a third order following the T^3 dependence of CTE, proposed by Hartwig [6].

$$\left(\alpha_{\text{liner}}^{\text{T}}, \alpha_{11}^{\text{T}}, \alpha_{22}^{\text{T}}\right) = f\left(a,b,c,\alpha^{o} \mid T\right) \Rightarrow aT^3 + bT^2 + cT + \alpha^{o} \tag{6.3}$$

where $\alpha_{\text{liner}}^{\text{T}}, \alpha_{11}^{T}, \alpha_{22}^{T}$ are the CTE of PA12, and the composite ply along the fiber and transverse to the fiber directions as a function of temperature respectively while α^{o} is the CTE at 0 [$^{\text{o}}$C].

The best-fit values for the coefficients *a*, *b*, *c* and a^{o} for all approximation functions are given in Table 6-5. It can be seen that fitting constants *b* and *c* obtained higher values in the matrix-dominated engineering properties ($E_{22}^{\text{T}}, G_{12}^{\text{T}}, X_{\text{c}}^{\text{T}}, Y_{\text{t}}^{\text{T}}, Y_{\text{c}}^{\text{T}}, S^{\text{T}}$) than the fiber dominated ones $\left(E_{11}^{T}, X_{\text{t}}^{\text{T}}\right)$ associated to strong temperature dependency. The error column corresponds to the percentile difference between the mean value of the experimental results and the value from the fitting functions for every mechanical property.

Table 6-5: Fitting constants of approximation functions.

Property	***Unit***	***a*** **[-]**	***b*** **[-]**	***c*** **[-]**	$\boldsymbol{\alpha^{\text{o}}}$ 10^{-6} [mm/mm $^{\text{o}}$C]	**Error [%]**
$\varepsilon_{\text{ultliner}}^{\text{T}}$	[%]	0.36	0.0026	2.36	-	± 5.88
$E_{\text{liner}}^{\text{T}}$	[GPa]	7.009	2.797	-0.0181	-	± 3.47
$UTS_{\text{liner}}^{\text{T}}$	[MPa]	117	1.164	-0.0127	-	± 4.11
$a_{\text{liner}}^{\text{T}}$	[mm/mm$^{\text{o}}$C]	$1.4 \cdot 10^{-12}$	$5.3 \cdot 10^{-10}$	$4.3 \cdot 10^{-7}$	$110.6 \cdot 10^{-6}$	± 3.73
$\varepsilon_{\text{xt}}^{\text{T}}$	[%]	3.45	0.0015	-0.3	-	± 2.09
$\varepsilon_{\text{yt}}^{\text{T}}$	[%]	1.55	0.0029	1.44	-	± 3.13

E_{11}^{T}	[GPa]	139.735	0.068	-0.0038	-	± 0.68
E_{22}^{T}	[GPa]	11.202	0.171	-0.0251	-	± 1.29
G_{12}^{T}	[GPa]	6.903	0.353	-0.0273	-	± 2.24
X_{t}^{T}	[MPa]	2372	0.116	-0.0049	-	± 1.31
X_{c}^{T}	[MPa]	1201	0.011	-0.0791	-	± 2.62
Y_{t}^{T}	[MPa]	87	0.145	-0.0231	-	± 2.15
Y_{c}^{T}	[MPa]	314	0.192	-0.0338	-	± 4.18
S^{T}	[MPa]	103	0.387	-0.0254	-	± 3.84
α_{11}^{T}	[mm/mm °C]	$5 \cdot 10^{-15}$	$4 \cdot 10^{-11}$	$-4.6 \cdot 10^{-10}$	$-0.613 \cdot 10^{-6}$	± 1.84
α_{22}^{T}	[mm/mm °C]	$2.93 \cdot 10^{-12}$	$8.1 \cdot 10^{-10}$	$0.12 \cdot 10^{-6}$	$32.15 \cdot 10^{-6}$	± 2.03

The approximation of PA12 engineering properties is illustrated in Fig. 6-4. The error bar in the graphs corresponds to the value variation (standard deviation) of a given mechanical property at a given testing temperature. It can be seen that the hyperbolic function captures accurately the asymptotic behaviour of elongation at break at both cryogenic and elevated temperatures (Fig. 6-4a).

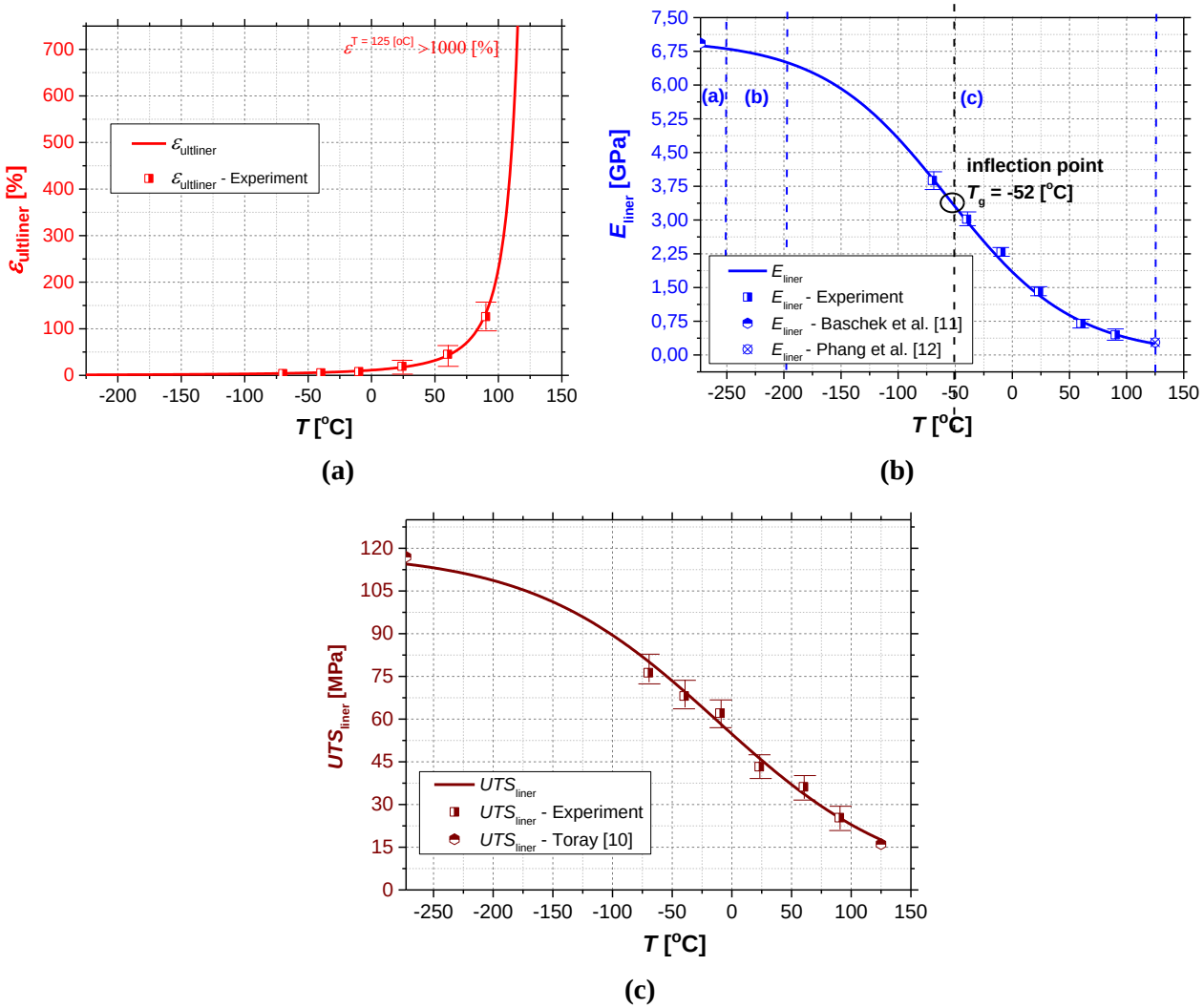

Fig. 6-4: a) Elongation at break, b) Young's modulus and c) tensile strength values of the liner material (PA12) as a function of temperature.

The increasing trend of Young's modulus and strength of PA12 with decreasing temperature is depicted in Fig. 6-4b,c. Below -253 [°C] (region (a)) the modulus is decreasing slightly as the temperature rises, while for region (b): -253 [°C] < $T \leq$ -196 [°C] a temperature-dependent elastic modulus was obtained. Finally, a more temperature-dependent elastic modulus can be seen for region (c): -196 [°C] < T < 125 [°C] where unfreezing of molecular motions of the polymer occur. The glass transition temperature is at T_g = -52 [°C] based on the inflection point of the curve in Fig. 6-4c.

The ply longitudinal and transverse failure strain, modulus, strength as a function of temperature is depicted in Fig. 6-5a, b and c respectively.

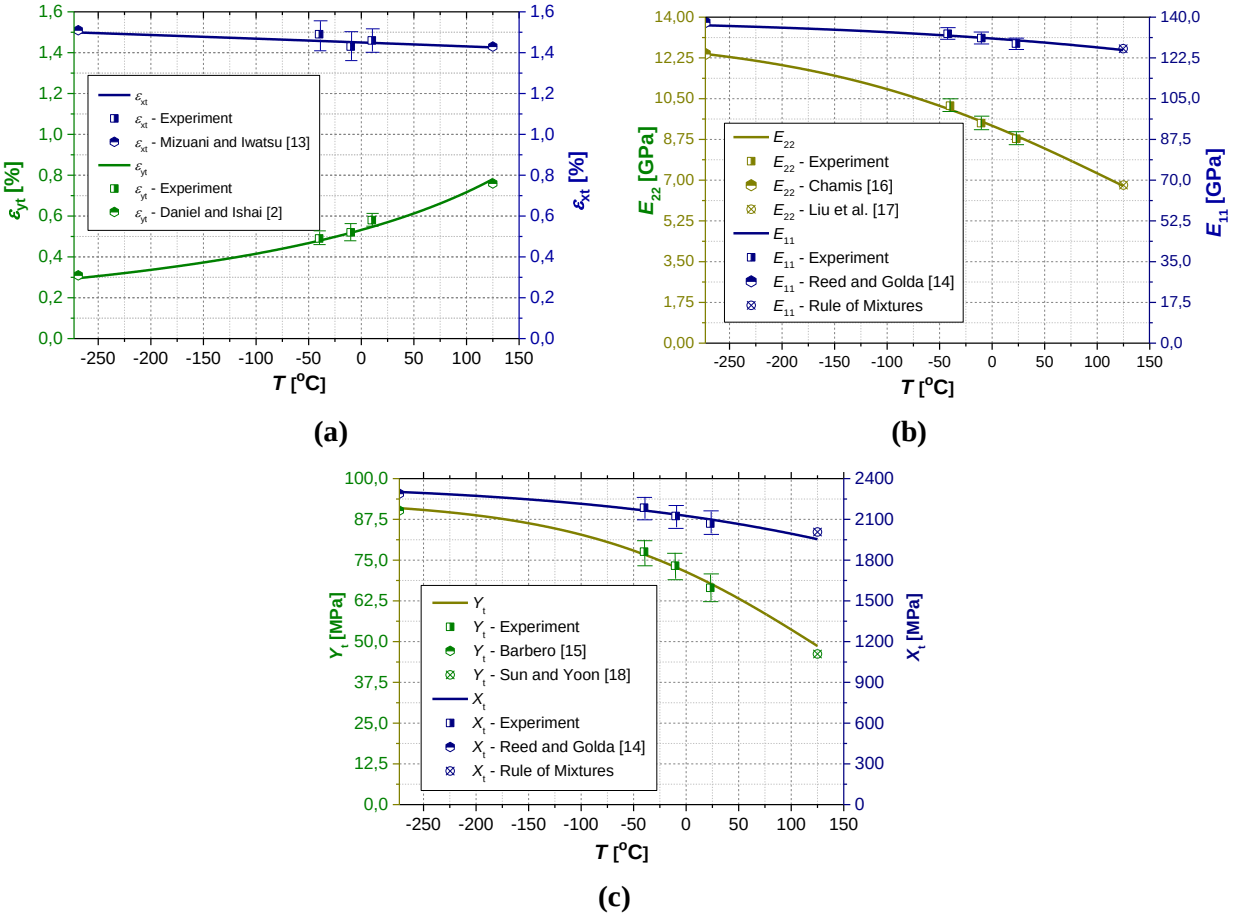

Fig. 6-5: Ply longitudinal and transverse a) failure strain, b) modulus and c) tensile strength as a function of temperature.

A considerable failure strain reduction in the transverse direction can be seen, which can be critical for the overwrap throughout chill-down. On the other hand, temperature had a very small effect at the composite properties in the longitudinal direction since it is fiber-dominated owing to the fact that the effect of temperature on the fiber engineering properties (E_{f1}, ν_{f12}, σ_{fa}) is negligible. A strong temperature dependence was obtained for matrix dominated engineering properties (E_{22} and Y_t).

The CTE of the liner and overwrap materials over -269 [°C] < T < 125 [°C] is shown in Fig. 6-6. A very good agreement was obtained between the approximation function and the experimental data at -75 [°C] $\leq T <$ 88 [°C]. Additionally, the approximation function matches the recordings of Baschek et al. [11] at -196 [°C] < T < -75 [°C]. A strong temperature dependence was found both for PA12 for -273 [°C] < $T \leq$ -160 [°C] as well as for the composite ply in the direction transverse to the fibers for T > 40 [°C]. The difference in CTE between PA12

and the composite specimen as well as the difference in CTE along the fiber and transverse to direction is evident and can lead to stress when the tank is exposed to chill-down.

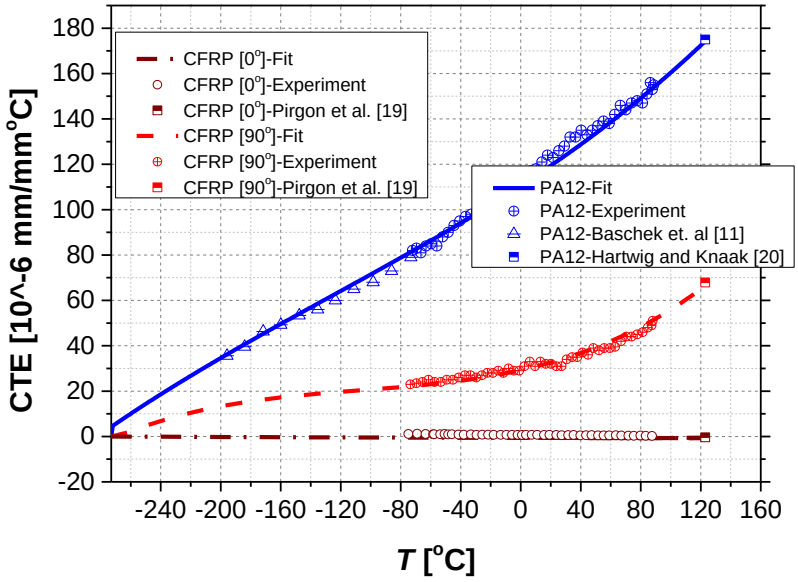

Fig. 6-6: Coefficient of thermal expansion (CTE) for the liner (PA12) and tank wall materials (CFRP) respectively.

The above approximation functions will be incorporated at the engineering properties and strength allowable definitions in the FE analysis of the next Chapter. This will enable a more accurate prediction of the response of the tank constituents to cryogenic chill-down and pressure cycling.

6.4 Concluding Remarks

In this chapter various functions were employed to derive the temperature dependency of the liner composite overwrap materials from measured values and material properties from literature. These functions are based on the results from coupon testing and the findings of literature. As expected matrix dominated properties (E_{22}, G_{12}, Y_t, S, ε_{yt}, α_{22}) showed a greater temperature dependency than the fiber dominated ones (E_{11}, X_t, ε_{xt}, α_{11}). A substantial CTE mismatch was obtained between the liner and composite overwrap materials at -160 [°C] < T < 125 [°C], which can lead to considerable stresses throughout chill-down in areas of liner-overwrap contact.

References

[1] I.G. Tapeinos, D.S. Zarouchas, O. Bergsma, S. Koussios and R. Benedictus, 'Evaluation of the Mechanical Performance of a Multi-Cell Tank for Cryogenic Storage: Part I- Tank Pressure Window based on Progressive Failure Analysis', *International Journal of Hydrogen Energy*, **44**, 3917-3930, 2019.

[2] I.M. Daniel and O. Ishai, 'Engineering mechanics of composite materials', Oxford University Press, 2006.

[3] ASTM 3039-17, 'Standard test method for tensile properties of polymer-matrix composite materials', 2017.

[4] ASTM 6641-14, 'Standard test method for compressive properties of polymer matrix composite materials using a combined loading compression (CLC) test fixture', 2014.

[5] ASTM 638-03, 'Standard test method for tensile properties of plastics', 2003.

[6] G. Hartwig, 'Polymer Properties at Room and Cryogenic Temperatures', *The International Cryogenics Monograph Series*, 1994.

[7] M.B. Ruggles-Wrenn and O. Ozmen, 'The rate(time)-dependent mechanical behaviour of the PMR-15 thermoset polymer at 316^{o}C: experiments and modeling', *Journal of Pressure Vessel Technology*, **132**, 908-914, 2010.

[8] G. Agrawal, J. Joseph, D.K. Agarwal and S.S. Kumar, 'Effect of insulation thickness on evolution of pressure and temperature in a cryogenic tank', *Proceedings of the 23rd National Heat and Mass Transfer Conference*, India, 2015.

[9] ASTM 11359-2, 'Determination of coefficient of linear thermal expansion and glass transition temperature'.

[10] Toray Plastics, 'Technical Report-Nylon Plastics'.

[11] G. Baschek, G. Hartwig and F. Zahradnik, 'Effect of water absorption in polymers at low and high temperatures', *Polymer*, **40**, 3433–3441, 1991.

[12] I.Y. Phang, T. Liu, A. Mohamed, K.P. Pramoda, L. Chen, L. Shen, S.Y. Chow, C. He, X. Lu and X. Hu, 'Morphology, thermal and mechanical properties of nylon 12/organoclay nanocomposites prepared by melt compounding', *Polymer International*, **54**, 456-464, 2005.

[13] K. Mizutani and T. Iwatsu , 'Temperature dependence of tensile properties of composites consisting of carbon fiber tow in thermosetting polymers', *Journal of Applied Polymer Science*, **25**, 2649-2652, 1980.

[14] R.P. Reed and M. Golda, 'Cryogenic properties of unidirectional composites', *Cryogenics*, **34**, 909-928, 1994.

[15] E.J. Barbero, 'Introduction to Composite Materials Design', *Taylor & Francis Group*, 1999.

[16] C.C. Chamis, 'Simplified Composite Micromechanics Equations for Hygral Thermal and Mechanical Properties', *SAMPE Quarterly*, **15**, 14–23, 1984.

[17] Z. Liu, Z. Guan, F. Liu and J. Xu, 'Time-temperature dependent mechanical properties of cured epoxy resin and unidirectional CFRP', *Proceedings of the 8th ICMAE*, Prague, 2017.

[18] C.T. Sun and K.J. Yoon, 'Technical Report: Mechanical properties of graphite/epoxy composites at various temperatures', 1988.

[19] O. Pirgon, G.H. Wostenholm and B. Yates, 'Thermal expansion at elevated temperatures IV. Carbon-fiber composites', *Journal of Physics D: Applied Physics*, **6**, 309-321, 1973.

[20] G. Hartwig and S. Knaak, 'Fibre-epoxy composites at low temperatures', *Cryogenics*, **24**, pp. 639-647, 1984.

Chapter 7: Transient Modeling and Progressive Failure Analysis of Type IV Cryogenic Multi-sphere

The scope of the previous chapters was to theoretically assess different design issues and structural requirements arising from mechanical loading of the multi-spherical COPV. However, in order to conduct a detailed design of the plastic lined multi-sphere, issues like the effect of the manufacturing process on the structure's behaviour throughout pressurization and nominal cryogenic operation (chill-down and pressure cycling) needs to be assessed.

This chapter's focus is to simulate the manufacturing process (draping) of the multi-sphere and to evaluate the local change of stiffness over the tank contour due to in-plane shearing of the draped patches. The optimum composite patch shape will be identified on the basis of minimization of in-plane shear deformation. Additionally a transient thermo-mechanical FE model is developed to analyse the temperature profile and arising stresses by taking into consideration the temperature dependent properties of Chapter 6. This chapter is based on the work conducted in [1].

7.1 Manufacturing Simulation

The complexity of the current vessel geometry does not permit the use of filament winding since a wound fiber strand from one dome to another would not reinforce the junction in between (fiber bridging) (Fig. 7-1). Therefore draping/laying composites at pre-defined geometries is one of the few options left.

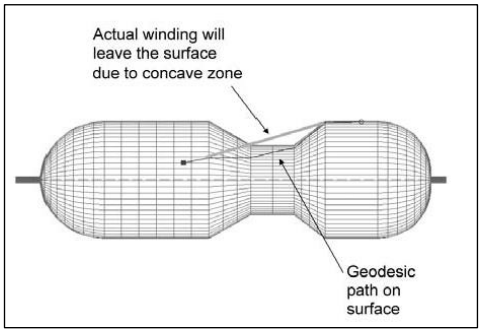

Fig. 7-1: Issue of bridging on a concave surface [2].

The current design -considered for manufacturing- incorporates a quasi-isotropic lay-up ($[0/\pm45/90]_s$) to introduce equal in-plane stiffness in all directions at the spheres. The design of composite patches -to be draped- is controlled by how uniform the membrane response of the shell will be. In practice, when mapping composite flat strips (patches) over a three dimensional surface of the multi-sphere, issues such as shear deformation of the fibers can occur. This leads to a local change of the angle of reinforcement and thus the composite lay-up will deviate slightly from being quasi-isotropic due to an angular offset of [45^o] not exactly met. A patch geometry that minimizes in-plane shear deformation will be identified.

The composite-overwrapping process is simulated through the use of the software DRAPE which evaluates the in-plane stiffness and strength throughout the whole contour [3]. Fig. 7-2 illustrates the draping of three different composite patch shapes. The narrowest patch has a maximum width at the sphere equator line of 50 [mm], while the widest reaches a width of 150 [mm]. The yellow colour represents no in-plane shearing, while blue represents [10-20^o] shearing and red more than [20^o] shearing. It is evident that the wider the patch the higher the risk for in-plane shearing; for the [0^o] patches the blue region could even evolve into wrinkles that affect the load transfer between plies.

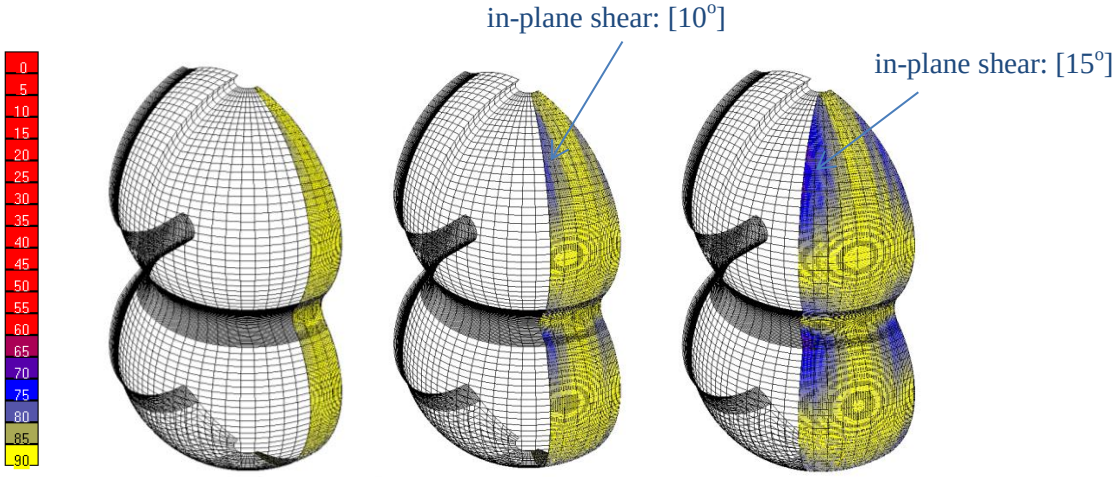

Fig. 7-2: Contour plot of in-plane shear of [0°] plies due to draping of i) narrow, ii) normal and iii) wide composite patches.

The resulting angular variability from draping patches will affect the stiffness of the laminate. The extensional stiffness of the laminate is given by:

$$\mathbf{A}_{\text{sphere}} = \sum_{k=1}^{n} \mathbf{C}_{[\varphi]_k} t_{\text{ply}} \tag{7.1}$$

where the rotated ply stiffness matrix $\mathbf{C}_{[\varphi]_k}$ is given by Eq (4.13). The effect of angular variability of the angle-ply layers on the extensional stiffness ratio ($A_{\varphi\varphi}/A_{\theta\theta}$) can be seen in Fig. 7-3. As expected, when there is no in-plane shear deformation of the fabric strip this will lead to a consistent QI lay-up. For a shear deformation of [20°] a stiffness ratio of 0.5 and 2 between the meridional and hoop directions is obtained.

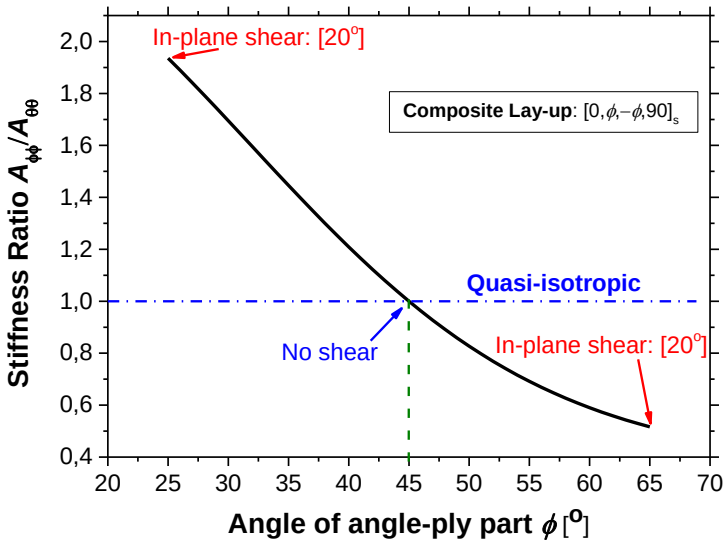

Fig. 7-3: Extensional stiffness ratio ($A_{\varphi\varphi}/A_{\theta\theta}$) as a function of angular variability of participating angle-ply layers.

The distribution of laminate stiffness over the contour in the vicinity of the polar opening is depicted in Fig. 7-4. It can be seen that the widest patch results in doubled stiffness in the meridional direction as compared to the hoop direction. The addition of more patches on the tank contour leads to the increase of in-plane shear fiber deformation for the two wider patch shapes which can be seen by the red colour in Fig. 7-2b,c (shear deformation > [30°]). It is shown that

the narrowest patch shape (of the three) leads to an equal in-plane stiffness and thus is selected as the flat fabric strip to be used for overwrapping of the multi-sphere. There is no need to utilize a narrower patch when employing draping as the manufacturing process, since that would slow-down the laying-up of the composite plies.

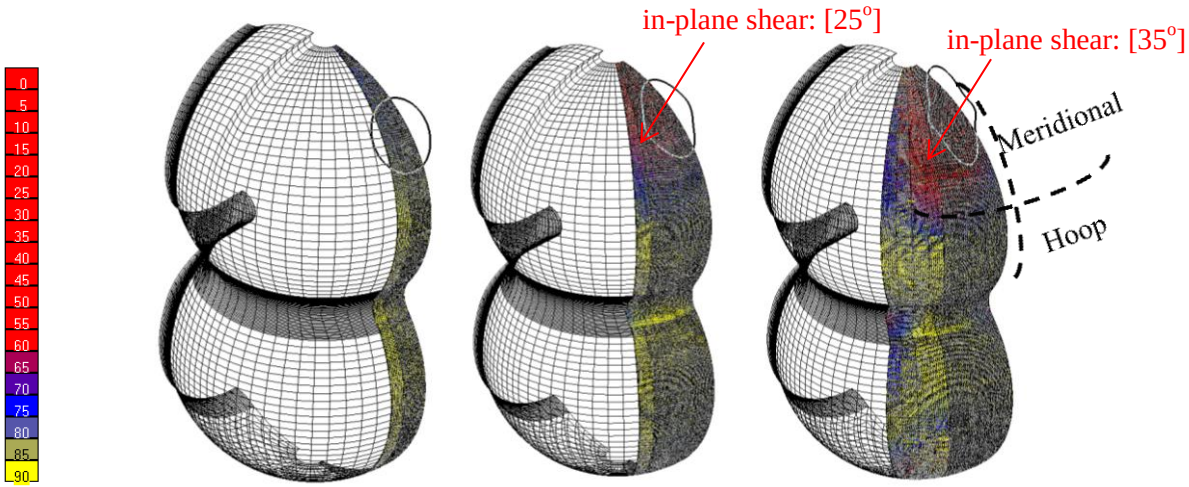

Fig. 7-4: Equivalent laminate stiffness over the contour for of a) narrow, b) normal and c) wide composite patches.

The optimal shape of the flat fabric to be draped on the multi-sphere is illustrated in Fig. 7-5. A variable width will lead to a straight line along the meridional direction when projected on the 3D surface. The narrowest part at the center of the patch is associated with the different radius of curvature of the intersection.

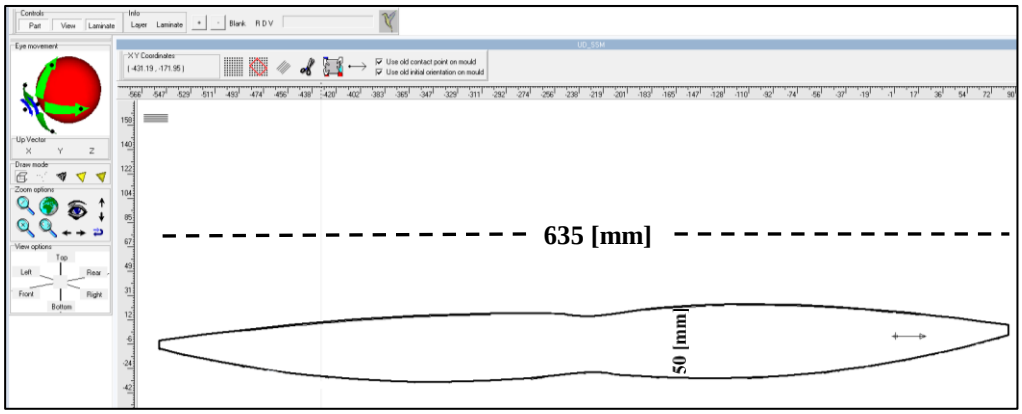

Fig. 7-5: Shape of the optimal patch (DRAPE software).

7.2 Modeling of Hydrostatic Pressure and Cryogenic Operation

7.2.1 Model

The 3D-shaped tank with draped patches was imported from the software DRAPE to a commercial FE Software Package (Abaqus). Composite sections were defined for every element. A local ply orientation and stiffness from DRAPE was introduced in every element in the FE analysis, associated with the shearing of the fabric strips when applied on top of the curved contour. Since the structure is a thin-walled vessel under uniform internal pressure, a plane stress approach was considered. A transient coupled temperature-displacement analysis was employed in all cases to accurately relate deformation with temperature at the tank wall. Conventional

linear temperature-displacement shell elements were used (S4RT) for the composite overwrap to evaluate the in-plane stress indices coupled to the temperature difference the element is experiencing. These elements are appropriate for modelling structures undergoing small membrane strains and finite rotations when subjected to thermo-mechanical loading [4]. The transverse principal stress entity (σ_3) was considered as negligible since the composite structure is a thin-walled shell [5]. On the other hand, a linear 8-node brick element (C3D8RT) was utilized for the liner to accurately predict any temperature and stress variation through-the-thickness [4]. The first load case that was analysed was pressurization at high and low displacement rates. This high pressure rise rate case was considered to be representative of the sudden excessive fuel boil-off that can occur in a cryogenic tank. The second case was related to the operational loads of a cryogenic propellant tank (cryogenic chill-down, pressure cycling, tank draining) (Fig. 2-7).

7.2.2 Failure Analysis

A Progressive Failure Algorithm (PFA) was incorporated to check for structural integrity of the plastic liner and composite overwrap throughout operation. The focus of this modelling approach was the evaluation of both the liner damage and intra-laminar failure at the composite overwrap. Localized failure was defined as damage that leads to a localized stiffness degradation, while a global one implies that the tank has no more load carrying capability. The following phenomena were considered as structural ultimate failure: cluster of composite fiber breaks and matrix cracking combined with liner fracture, since these lead to pressure loss [6]. It is desired that the first damage onset and the global failure will occur at the spherical cells (safe mode) and not at the intersections, inner hollow cylinder, or next to the fittings (unsafe modes). The reason for that is the difficulty to inspect any small damage onset at the junctions or the hollow cylinder, while damage onset next to the polar opening could lead to ejection of the fittings. The number of UD straps to be added was chosen by employing the findings of Section 4.3.2.

Since the multi-sphere was analysed as a thin-walled shell under plane stress, 2D failure criteria were used here. The selection of the failure criteria was based on a distinction between fiber and matrix failure modes. Initially, the maximum stress criterion was utilized to analyse fiber failure under tension and compression. All strength allowables are expressed as a function of temperature, denoted by the superscript T. The symbols σ_1, σ_2, τ_{12} correspond to ply stresses in the parallel, transverse to the fiber and in-plane shear directions respectively and are based on the integration points of any given element at the composite overwrap.

- *Fiber tensile failure* ($\sigma_1 > 0$)

$$\frac{\sigma_1}{X_t^T} = 1, \tag{7.2}$$

- *Fiber compressive failure* ($\sigma_1 < 0$)

$$-\frac{\sigma_1}{X_c^T} = 1 \tag{7.3}$$

The Hashin failure criterion [7] was used to determine matrix failure under tension and compression as well as fiber-matrix shear-out. This criterion considers the contribution of longitudinal shear stress to each failure mode.

- *Fiber-matrix shear out/debonding* ($\sigma_1 < 0$)

$$\left(\frac{\sigma_1}{X_c^T}\right)^2+\left(\frac{\tau_{12}^2}{S^{T2}}\right)=1 \tag{7.4}$$

- *Matrix cracking under tension* ($\sigma_2 > 0$)

$$\left(\frac{\sigma_2}{Y_t^T}\right)^2+\left(\frac{\tau_{12}^2}{S^{T2}}\right)=1 \tag{7.5}$$

- *Matrix cracking under compression* ($\sigma_2 < 0$)

$$\left(\frac{\sigma_2}{Y_c^T}\right)^2+\left(\frac{\tau_{12}^2}{S^{T2}}\right)=1 \tag{7.6}$$

The three-dimensional form of the Von Mises yield criterion was adopted to check for liner failure (Eq. (7.7)). The symbols σ_{11}, σ_{22}, σ_{33} represent the principal stresses while σ_{12}, σ_{13}, σ_{23} correspond to the shear stresses at the integration points of any given element at the liner.

$$UTS_{\text{liner}}^T=\sqrt{\frac{1}{2}\left[\left(\sigma_{11}-\sigma_{22}\right)^2+\left(\sigma_{22}-\sigma_{33}\right)^2+\left(\sigma_{33}-\sigma_{11}\right)^2+6\left(\sigma_{23}^2+\sigma_{31}^2+\sigma_{12}^2\right)^2\right]} \tag{7.7}$$

The damage initiation and progression was carried out by using a material subroutine (USDFLD-User Defined Field) utilizing solution-dependent variables (SDVs) in ABAQUS [4]. SDVs represent damage variables evaluated from stress and strain values obtained after every increment of the analysis. The first two solution-dependent variables (SDV1 and SDV2) were associated with matrix failure under tension and compression respectively, while the third one (SDV3) was attributed to compression-induced fiber -matrix debonding (shear-out). The last solution-dependent variables were linked with fiber failure under tension or compression (SDV4, SDV5) while SDV6 was used to describe the evolution of liner failure. Field variables (FVs) were used as damage flags linked with SDVs [4]. Their value was set equal to 0 for the undamaged state and to 1 with damage onset, at which point a degradation rule would be applied to the specific composite ply at that location. Fig. 7-6 depicts a flowchart of the progressive failure model of this study.

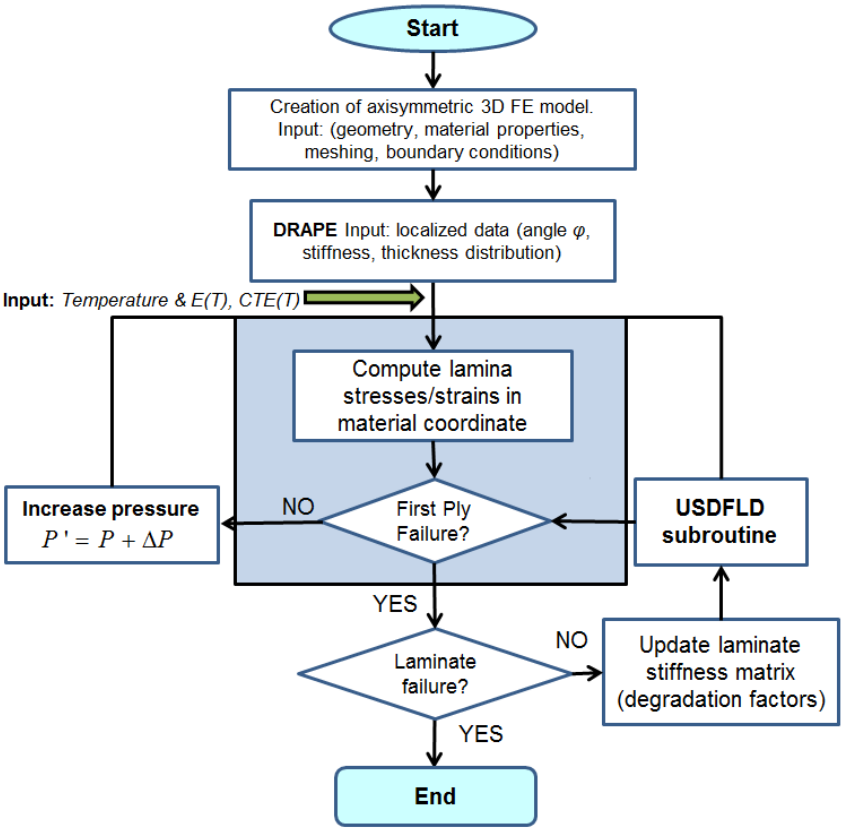

Fig. 7-6: Flowchart of the progressive failure analysis model.

A material model that involves direct degradation of elastic constants with discrete knock-down factors, was utilized. The degradation factors that were used can be seen in Table 7-1. Papanikos et al. [8] derived that there was an 80 [%] reduction in matrix-dominated elastic constants when in tension, and 60 [%] reduction when in compression. In this study, fiber fracture signifies nullification of all elastic constants as it is considered that the structure has no load carrying capability in that case.

Table 7-1: Degradation factors applied for stiffness degradation.

Failure Type	E_{11}	E_{22}	ν_{12}	G_{12}	G_{13}	G_{23}
Matrix cracking (tension)	1	0.2	1	0.2	0.2	0.2
Matrix cracking (compression)	1	0.4	1	0.4	0.4	0.4
Fiber/Matrix debonding (compression)	1	1	1	10^{-10}	1	1
Fiber fracture (tension)	10^{-10}	10^{-10}	10^{-10}	10^{-10}	10^{-10}	10^{-10}
Fiber fracture (compression)	10^{-10}	10^{-10}	10^{-10}	10^{-10}	10^{-10}	10^{-10}

7.2.3 Analysis

i. Burst Pressure at Room Temperature

The mechanical response of the multi-sphere when subjected to internal pressure at room temperature was hereby analysed. An FE analysis coupled with the progressive failure algorithm (7.2.2) was carried out to evaluate the i) strain behaviour and interaction of different tank constituents, ii) the pressure allowable of the structure and the iii) pressure difference (dP)

between the first damage onset and ultimate failure. The tank was loaded in the following way: i) cooling from 125 [°C] to room temperature (curing process) and ii) pressurizing the tank up to burst (Fig. 7-7a). Only cooling was considered from the curing face, owing to the fact this is the main phase where residual stresses are expected to arise in the overwrap and liner. The pressure load applied at the liner inner surface in conjunction with symmetric boundary conditions can be seen in Fig. 7-7b. The external pressure load -depicted in Fig. 7-7b corresponds to the ambient pressure.

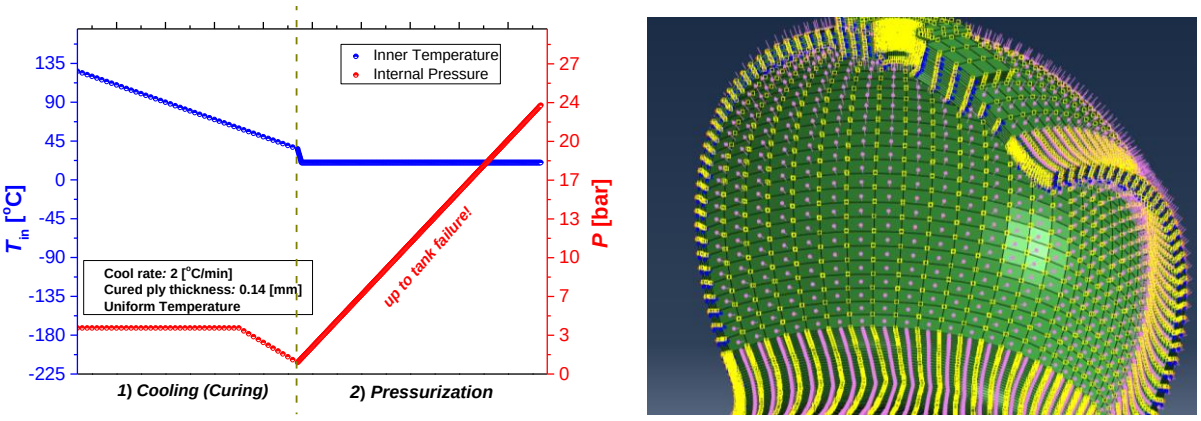

(a) **(b)**

Fig. 7-7: a) Internal pressure vs inner temperature loading and b) loads and boundary conditions at the 3D model for testing at ambient conditions.

As mentioned in 7.2.1, both the low and high pressure rate loading up to burst cases were considered, using the strain rate-dependent liner material properties as depicted in Fig. 6-3. Rates of pressure increase of $\frac{dP}{dt} = 0.05$ [bar/s] and $\frac{dP}{dt} = 1.35$ [bar/s] were applied to the low and high displacement rate cases respectively. The first displacement rate was arbitrarily chosen to represent a slow pressure rise. The second displacement rate corresponds to a fast pressure rate (dP/dt) that an LN_2 cryogenic tank is normally facing throughout evaporation of a vent-less tank with the lack of a thermal insulation barrier [9]. For this high strain rate case the model developed in [10] was employed to obtain the ply engineering properties based on the obtained experimental results in Section 6.1:

$$E_{\mathrm{RT}[0^o,45^o,90^o]} = E_{\mathrm{o}[0^o,45^o,90^o]}\left(1 + C^{\mathrm{E}}_{\mathrm{RT}} \ln \frac{\dot{\varepsilon}}{\dot{\varepsilon}_{\mathrm{o}}}\right) \tag{7.8}$$

$$S_{\mathrm{RT}[0^o,45^o,90^o]} = S_{\mathrm{o}[0^o,45^o,90^o]}\left(1 + C^{\mathrm{S}}_{\mathrm{RT}} \ln \frac{\dot{\varepsilon}}{\dot{\varepsilon}_{\mathrm{o}}}\right) \tag{7.9}$$

where $E_{\mathrm{RT}[0^o,45^o,90^o]}$ and $S_{\mathrm{RT}[0^o,45^o,90^o]}$ are the strain rate adjusted moduli and strengths respectively of the composite (at different orientations), $E_{\mathrm{o}[0^o,45^o,90^o]}$ and $S_{\mathrm{o}[0^o,45^o,90^o]}$ are the quasi-static laminate modulus and strength respectively, $\dot{\varepsilon}_{\mathrm{o}}$ is the reference stain rate and $\dot{\varepsilon}$ is the effective strain rate. The constants $C^{\mathrm{E}}_{\mathrm{RT}}$ and $C^{\mathrm{S}}_{\mathrm{RT}}$ for different ply orientations under tension, compression and in-plane shear were obtained from [11]. The results of this analysis are presented in Section 7.3.1.

ii. Cryogenic Operation

The loading conditions for this scenario can be seen in Fig. 7-8a. The cryogen that would be employed in the experiment (Chapter 8) would be liquid nitrogen-LN_2 (boiling point: -196 [^{o}C]) instead of LH_2 (boiling point: -253 [^{o}C]) for safety reasons so LN_2 is hereby assumed in the analysis. The chosen LN_2 filling rate of the tank is 0.0055 [l/s], in order to avoid any unwanted thermal stress peak at the tank wall [12]. A transient coupled temperature-displacement analysis was carried out to simulate the response of the tank wall to chill-down, pressure cycling and draining, since these are the load cases a cryogenic tank is experiencing [13]. More specifically, the various heat transfer mechanisms, temperature profile and strain evolution were analysed.

A natural convection boundary condition was applied to the liner inner surface above the gas-liquid interface with a heat transfer coefficient of h_{vapor} = 22.6 [W/m^2 K] and a ullage temperature of T_{vapor} = -146 [^{o}C] in accordance with the work of Stephens et. al [13] (Fig. 7-8b). As soon as the liquid front reaches a prescribed position at the liner inner surface, boiling heat transfer would be enforced to that location with a heat transfer coefficient (h_{LN2}) that is derived from Kida et al. [14].

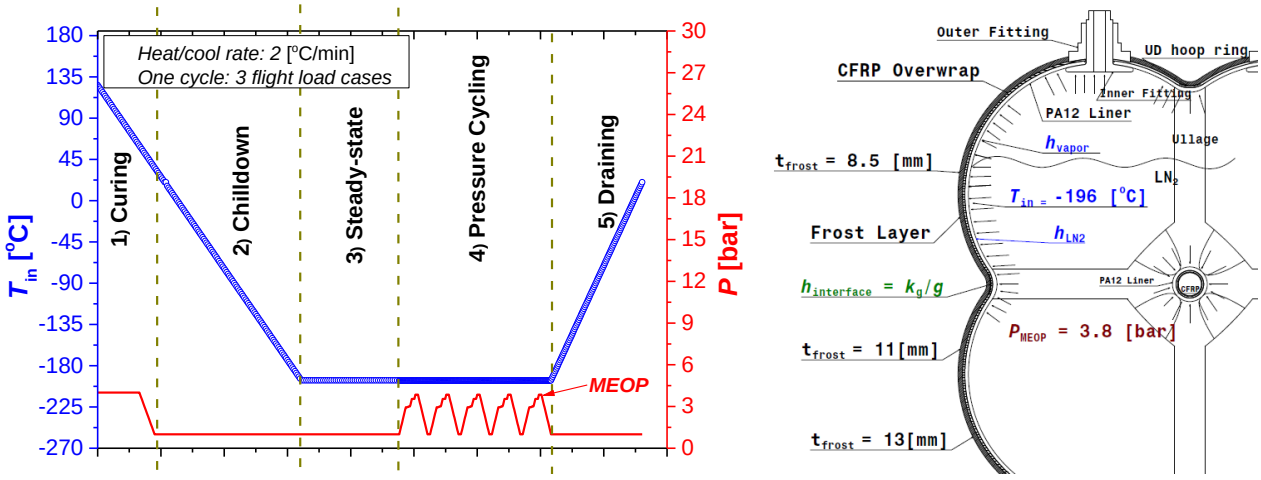

(a) **(b)**

Fig. 7-8: a) Internal pressure vs inner temperature loading and b) loads and boundary conditions for cryogenic operation.

The formation of a frost layer was considered at the tank external surface which is associated with water condensation and subsequent freezing during cryogenic chill-down. A varying thickness in the height direction was assigned to the frost layer in accordance to the expected exposure time of any tank region to LN_2 Fig. 7-8b. The frost layer thickness values were obtained from the findings of Kim et al. [15] (Fig. 7-9).

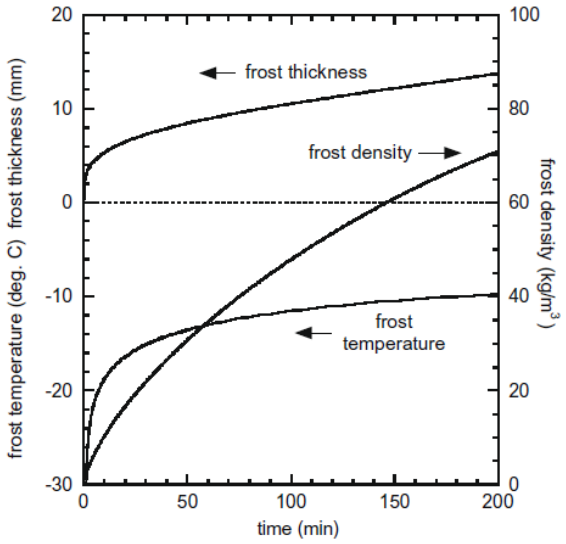

Fig. 7-9: Frost layer thickness as a function of time at LO_x tank wall [15].

Frost thermal conductivity and density was derived by the following equations:

$$k_{\text{frost}} = 0.024248 + 7.23 \cdot 10^{-4} \rho_{\text{frost}} + 1.183 \cdot 10^{-6} \rho_{\text{frost}}^2 \quad [16] \qquad (7.10)$$

$$\rho_{\text{frost}} = 650 e^{0.227 T_{\text{frost}}} \quad [17]$$

whereby k_{frost} ρ_{frost} are the frost thermal conductivity and density respectively and T_{frost} is the frost temperature. A natural convection boundary condition was applied at the external surface of the frost layer. The heat transfer coefficient (h_{out}) value of h_{out} = 30 [W/m^2 K] was obtained from the work of Schalla [18]. The ambient temperature was considered as T_{ex} = 23 [$^{\text{o}}$C].

The heat transfer at the liner/composite interface was assessed by considering a thermal contact conductance scenario, where an imperfect conduction can take place -between the two surfaces in contact- leading to a temperature drop. The heat flux along the surface contour, is not uniform because of the varying air gap between them at different locations coming from the curing process. As a result, Eq.(7.11) is utilized to describe the thermal contact conductance between the two surfaces, as a function of air gap thickness [19]:

$$h_{\text{interface}} = \frac{k_{\text{air}}}{\delta} \qquad (7.11)$$

where δ is the air gap thickness. The conductivity values of the liner and composite material were experimentally assessed using [20]. It is expected that the thermal contact conductance will drop significantly with increasing air gap and thus the heat transfer between the liner and composite surface will be reduced. Table 7-2 shows the thermal contact conductance for various distances between the two bodies, (Eq. (7.11)).

Table 7-2: Thermal conductance vs clearance.

δ [m]	$h_{\text{interface}}$ [W/m^{2}K]
0.0001	150.5
0.0003	50.6
0.0005	30.7
0.001	11.3
0.002	10.4
0.005	4.4
0.007	3.1
0.009	2.2

0.015	0

Pressure cycling with gaseous nitrogen (GN_2) at room temperature was carried after obtaining the steady state temperature conditions in the tank. Prior to the FE analysis, it was required to know the boil-off rate when adding a warm pressurant. The thermodynamic conditions considered in [21] were taken into consideration to correlate pressure-rise rate to heat leak rate. The LN_2 boil-off rate throughout pressure cycling was established by using the following relationship based on the first law of thermodynamics for transient problems:

$$BOR_{\text{cycling}} = \frac{\dot{Q}}{\Delta H_{\text{vapLN}_2}}, \tag{7.12}$$

$$\text{where } \dot{Q} = -m\frac{dP}{dt}\left[\frac{h_{\text{fg}}}{v_{\text{fg}}}\left(\frac{dv_{\text{f}}}{dP}+\frac{m_{\text{g}}}{m}\frac{dv_{\text{fg}}}{dP}\right)-\left(\frac{dv_{\text{f}}}{dP}+\frac{m_{\text{g}}}{m}\frac{dv_{\text{fg}}}{dP}\right)+\frac{V}{m}\right] \text{ [21]}$$

and ΔH_{vapLN2} is the enthalpy of vaporization of LN_2, m is the mass and V is the volume of the system, m_g is the mass of GN_2 within the tank, v_f and v_{fg} are the specific volumes of the saturated LN_2 and vapor respectively, h_{fg} is the specific enthalpy of the saturated vapor. The mentioned properties were obtained from [22].

The model of Bourgeois et al. [23] that describes the evolution of ullage temperature as a function of pressure rise was incorporated in the FE analysis at the ullage region:

$$mc_{\text{pGN}_2}\frac{dT}{dt} = V\beta_{\text{GN}_2}T_{\text{vapor}}\frac{dP}{dt} + k_{\text{g}}S_{\text{i}}(T_{\text{wi}}-T) + \dot{m}(h_{\text{e}}-h_{\text{fg}}) \tag{7.13}$$

where c_{pgn2} is the specific heat capacity of nitrogen vapour at constant pressure, β_{GN2} is the CTE of GN_2, k_g is the internal heat exchange coefficient between the wall and the gas, S_i is the internal surface of the tank in contact with gas, T_{wi} is the temperature of the wall in contact with the gas, $\dot{m}$ is the mass flow rate in the tank and h_e is the specific enthalpy of the incoming GN_2 in the system. The value of S_i was based on the obtained boil-off rate from Eq. (7.12), while the value of k_g used in [23] was applied hereby. The corresponding nitrogen properties were obtained from [22].

7.3 Results

7.3.1 Pressure Window at Room Temperature

Throughout the cooling phase of curing, the liner and overwrap were behaving independently since they were not considered as bonded. This resulted in a gap formed in most regions throughout the tank contour, owing to CTE mismatch of the liner and overwrap materials (Fig. 7-10a). More specifically, a gap thickness gradient was obtained along the diagonal direction at the sphere (Fig. 7-10b). Contact throughout curing was obtained in the central tube and polar opening areas. The effect of this contact on the stress field of the liner and composite is presented below.

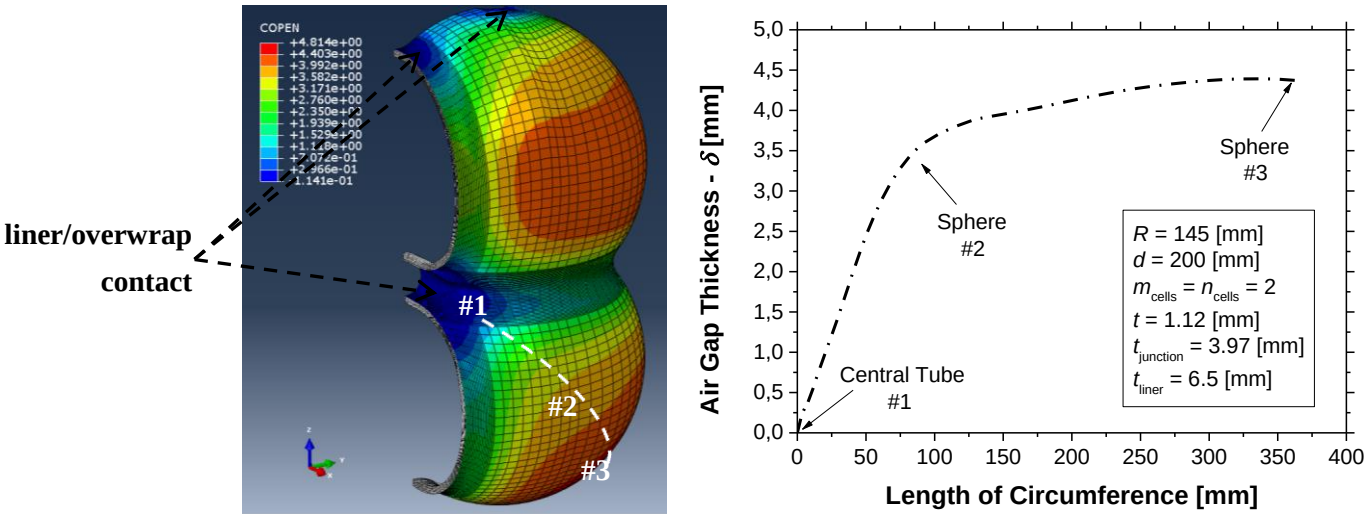

(a) (b)

Fig. 7-10: a) Tank Contour and b) distribution over the spherical shell of liner/ overwrap distance after curing.

i. Low Displacement Rate

The evolution of overwrap strain and structural integrity status throughout the cooling stage of curing and pressurization under low strain rate is shown in Fig. 7-11a,b respectively. These values are associated to discrete FE elements linked to a composite ply in the overwrap. The damage variable for the low displacement rate (depicted in Fig. 7-11b) corresponds to fiber breakage since this was the global failure mechanism (Fig. 7-12c); thus meridional strain history is presented in Fig. 7-11a. The meridional direction at the multi-sphere can be seen in Fig. 7-12b. The location of strain and damage monitoring for the low displacement case is shown in Fig. 7-12c.

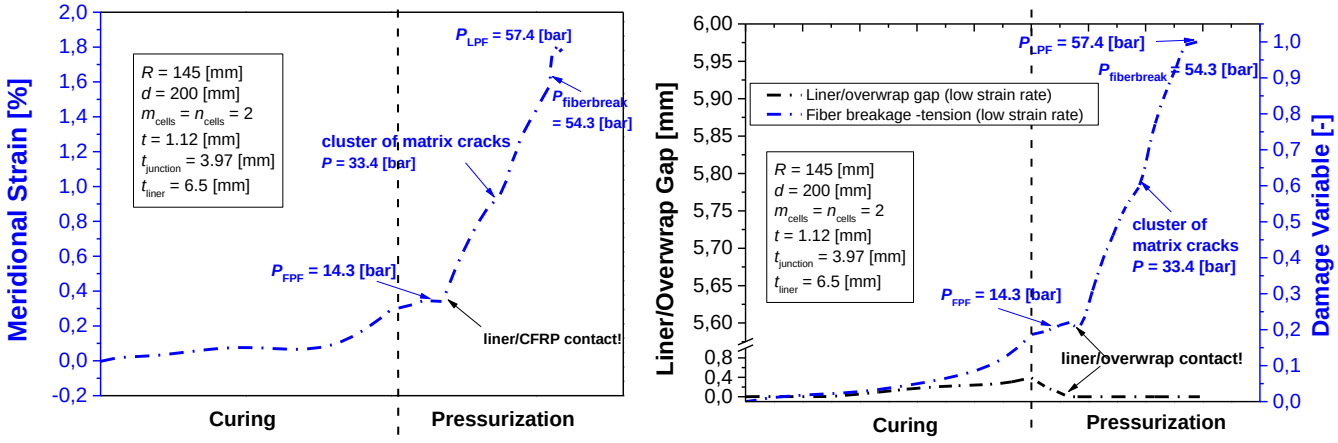

(a) (b)

Fig. 7-11: a) Strain and b) structural integrity history throughout curing and pressurization under low displacement rate.

The cooling phase of curing leads to tensile meridional strain, owing to the negative CTE in the direction parallel to the fibers. At the beginning of pressurization, the meridional strain maintains a near constant value since the composite is not subjected to any load owing to the air gap formed from curing (Fig. 7-10a). A sudden strain increase was obtained from the achieved liner/overwrap contact and the introduction of the pressure load (Fig. 7-11a). It is shown that the cluster of matrix cracks under transverse tension formed nearby (at P = 33.4 [bar]) led to a sudden strain jump (Fig. 7-11a) associated with localized matrix stiffness degradation and stress

re-distribution (Fig. 7-14b). Eventually, fiber freaks were initiated next to the intersections and close to the central tube at P = 54.3 [bar] that progressed through-the-thickness of the laminate signifying global tank failure (P_{LPF} = 57.4 [bar]).

Liner/overwrap contact was achieved throughout the whole tank contour during pressurization (Fig. 7-12a), which resulted in full load transfer from the polymeric liner to the composite. The location of first damage onset during pressurization was at the spherical cell and close to the intersection. This can be associated to the residual stresses from the interaction with the liner, owing to the established contact during curing and the fact that the number of UD straps was chosen on the basis of avoiding damage at the intersections.

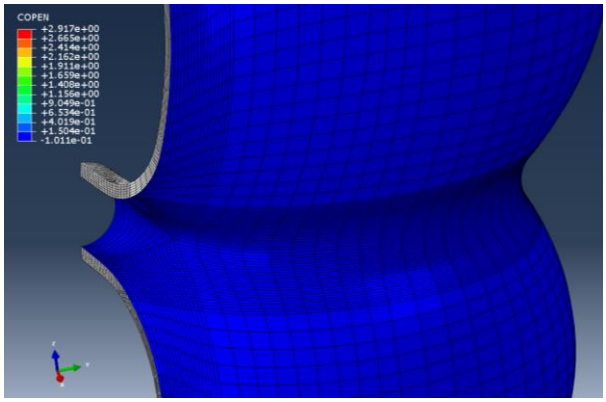

(a)

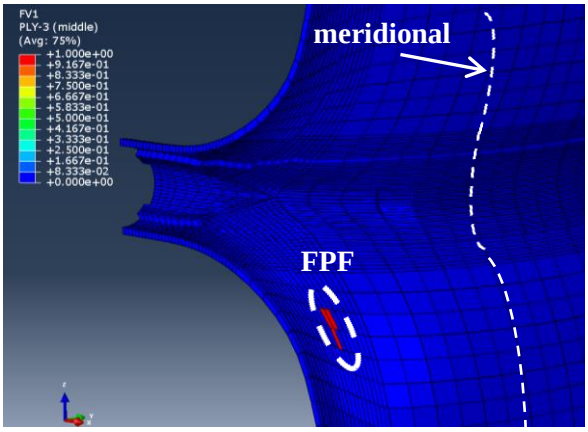

(b)

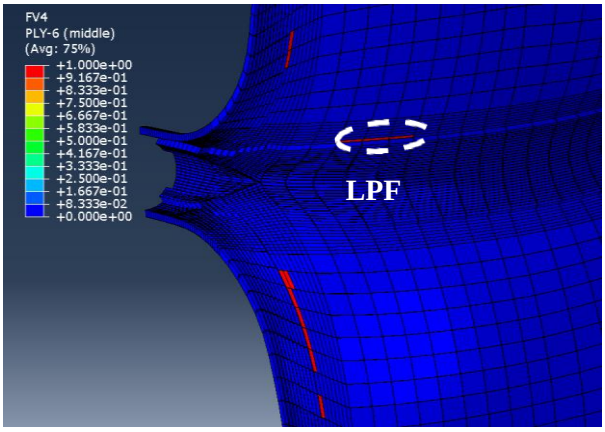

(c)

Fig. 7-12: a) Areas of liner/overwrap contact at burst and locations of b) first damage onset and c) burst for pressurization at a low displacement rate.

The overwrap/liner interaction behaviour and corresponding failure mechanisms -when the multi-sphere is subjected to low pressure rise rate- were identified in this Section. The comparison of the findings of this case with the corresponding ones when the tank is loaded under internal pressure with a high pressure rise rate is presented in the next Section.

ii. High Displacement Rate

The evolution of overwrap strain and structural integrity state throughout the cooling stage of curing and pressurization under high strain rate is depicted in Fig. 7-13a,b respectively. Hoop strain (Fig. 7-11a) and the SDV1 damage variable (see Section 7.2.2) are depicted for this case, owing to matrix cracking under tension being the global failure mechanism (Fig. 7-14d).

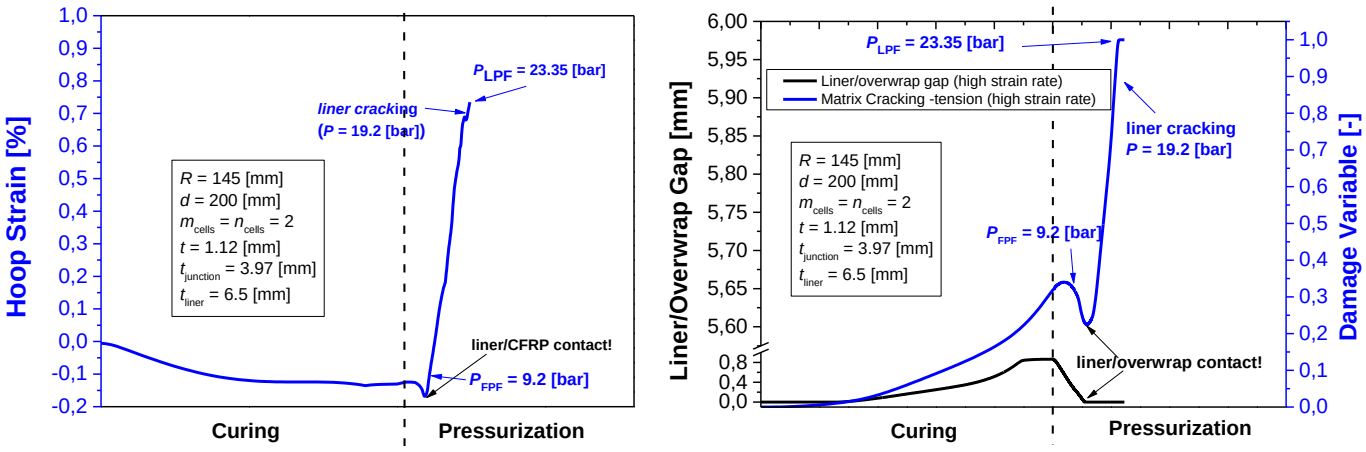

(a) **(b)**

Fig. 7-13: a) Strain and b) structural integrity history throughout curing and pressurization under high displacement rate.

It is shown in Fig. 7-13a that the cooling phase throughout curing resulted in a compressive hoop strain due to a positive CTE. Tensile residual stresses were obtained in the transverse directions throughout cooling, associated with the thermal anisotropy of the layers and the heterogeneity of the laminate [24]. A sudden strain increase was obtained from the achieved liner/overwrap contact and the introduction of the pressure load (Fig. 7-13a). As expected, strain at the overwrap accumulated faster at the high displacement rate case compared to the low displacement rate case (Fig. 7-11a). Liner cracking occurring at P = 19.2 [bar] had a noticeable effect and complete loss of its load carrying capability occurred at P_{LPF} = 23.35 [bar].

Liner/overwrap contact was only achieved throughout the intersections and neighbouring areas right before burst, throughout this loading case (Fig. 7-14a). Localized liner cracking through-the-thickness occurred at the top intersection (Fig. 7-14a) which can attributed to the polymer strain rate sensitivity and the fact that for a great part of the pressurization phase it was not in contact with the overwrap. The location of the first damage onset at the overwrap is similar to the one in low displacement rate case; at the spherical cell and close to the intersection. This can be associated to the residual stresses from the interaction with the liner, owing to the established contact during curing and the fact that the number of UD straps was chosen on the basis of avoiding damage at the intersections. Finally, -as stated above- matrix cracks propagated through-the-thickness which coupled with liner cracking, resulting in loss of load carrying capability (Fig. 7-14d).

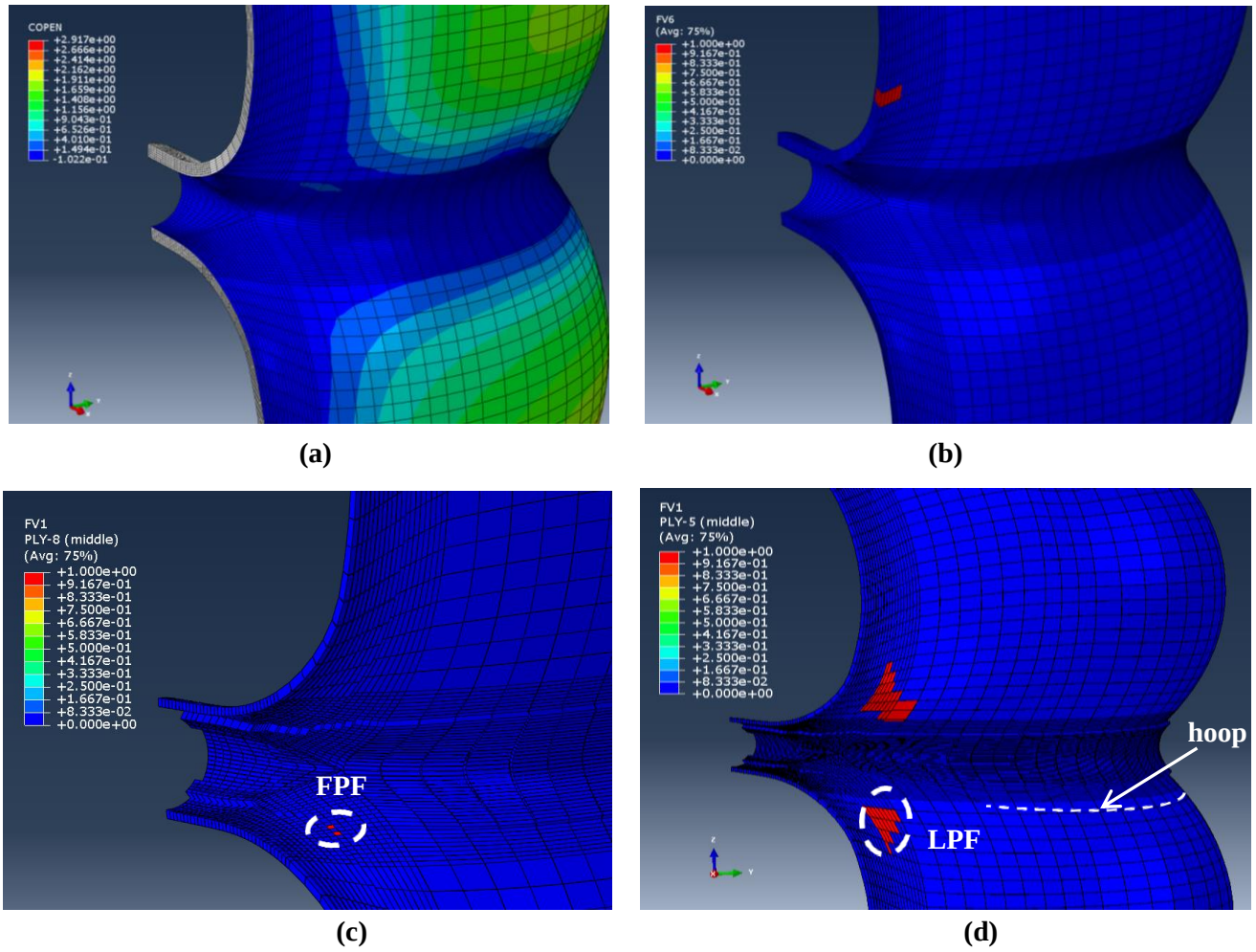

Fig. 7-14: a) Areas of liner/overwrap contact at burst and b) liner cracking through-the-thickness (P = 19.2 [bar] and locations of c) first damage onset (P_{FPF} = 9.2 [bar]) and d) burst (P_{LPF} = 23.35 [bar]) for pressurization at a high displacement rate.

A comparison between the tank pressure window for the low and high displacement cases is presented in Fig. 7-15. It can be seen that safety factors of S_F = 3.81 times the P_{MEOP} and S_F = 2.39 times the P_{MEOP} were obtained for the low and high strain rate cases respectively. The difference in the pressure window between the two load cases lies on the fact that the liner elongated freely without any damage onset when loaded at a low displacement rate and the pressure load was transferred to the overwrap. Subsequently, the strength of the fibers was fully utilized and thus the global failure mechanism was fiber breakage whereas for the high displacement rate, liner fracture and first-ply-failure (FPF) resulted in pressure loss.

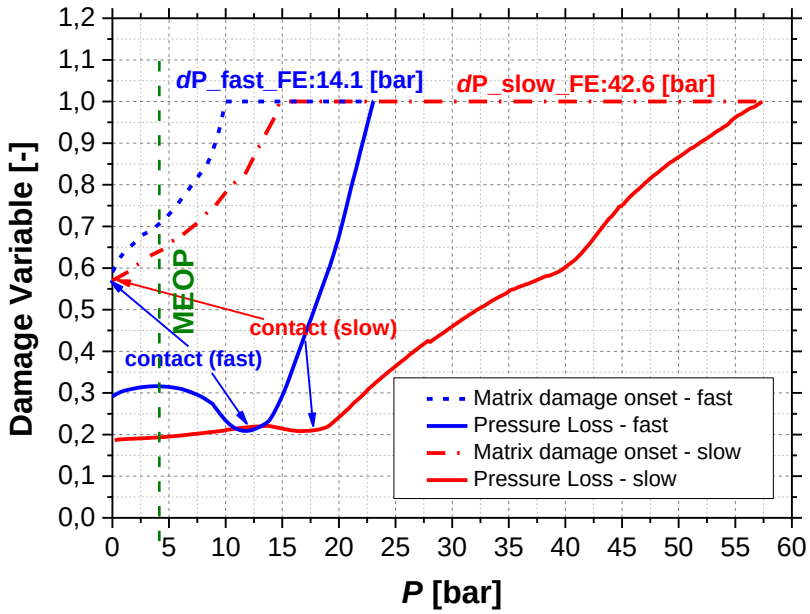

Fig. 7-15: Comparison of the tank pressure window for loading at a low and high displacement-rate.

The behaviour of the multi-sphere under mechanical loading (internal pressure) and under ambient conditions was analysed in this Section. The next Section deals the results on the performance of the multi-sphere under thermo-mechanical loading (normal cryogenic operation).

7.3.2 Cryogenic Operation

The results on the behaviour of the multi-sphere under cryogenic operation are hereby presented. A correlation between the hoop strain and temperature is depicted in Fig. 7-16a for four prescribed positions at the ullage region and below-the-liquid level (shown in Fig. 7-16b) for the chill-down stage. The hoop direction can be seen in Fig. 7-14d. Initially the tank wall was being cooled through natural convection from the nitrogen gas rising from the liquid-gas interface by circumferential conduction. As soon as the liquid front reached a prescribed position, the tank wall was cooled locally by a phase change heat transfer that resulted in a sharp cooling rate causing a large temperature drop. It can be seen that strain there evolved like a wave near the maximum cooling rate. This can be explained by the difference in heat transfer mechanisms right above and below the liquid front and the resulting local thermal deformation incompatibility at the tank wall. After the tank wall was cooled down by LN_2, it would stabilize at a certain temperature in the remaining time of the filling phase. As expected, cryogenic chill-down led to overwrap contraction where the compressive strain trend was in close agreement with temperature history.

The temperature profile of the composite overwrap after chill-down is shown in Fig. 7-16b. The ullage region can be seen at the top of the tank, as well as the areas below the gas/liquid interface. A gap was developed between the liner and overwrap throughout the curing and chill-down stages due to CTE mismatch. A temperature variation along the height of the multi-sphere and below the liquid level can be explained by the varying thickness of the frost layer in that direction that reduces the heat conduction from the exterior.

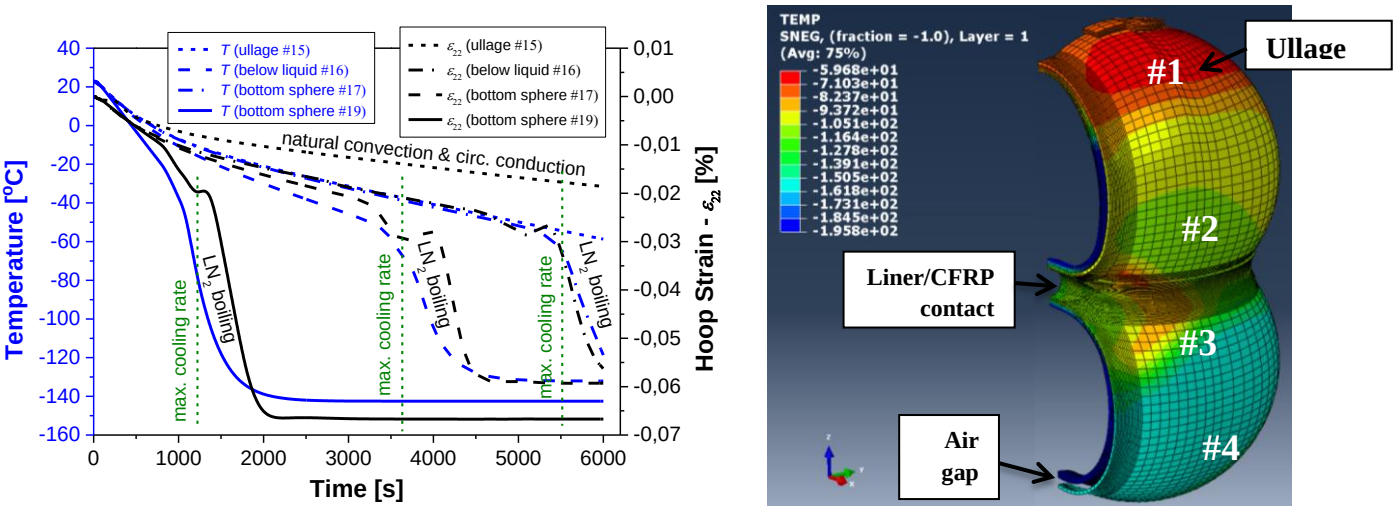

(a) (b)

Fig. 7-16: a) Evolution of hoop strain and temperature at various locations throughout chill-down and b) temperature profile of the composite overwrap after LN_2 filling.

The temperature and structural integrity history of the liner and composite overwrap for the i) chill-down, ii) steady state, iii) pressure cycling and iv) draining stages is presented in Fig. 7-17a and b. The locations monitored were the central hollow tube and the upper sphere below the liquid level (position #2) to analyse the behaviour of the tank wall under free contraction (position #1) and when subjected to thermal restraint (position #2). The structural integrity state in the composite laminate is represented by a damage variable associated with matrix cracking under tension. This damage variable was chosen since a tensile component was obtained at the overwrap in the direction transverse to the fibers during cooling, which is linked to positive CTE. The damage variable of the liner corresponds to the failure criterion of Eq.(7.7).

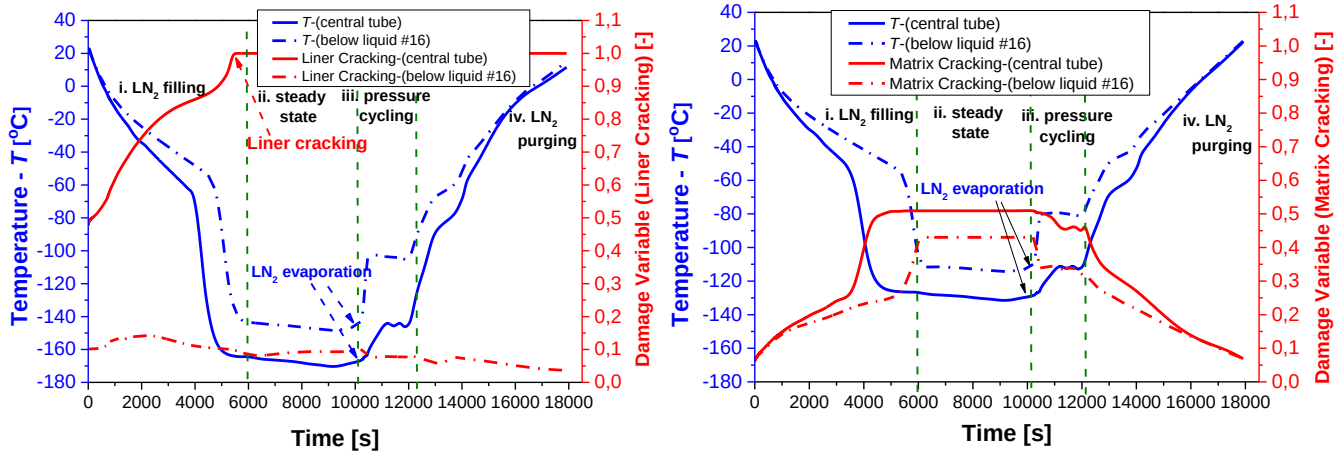

(a) (b)

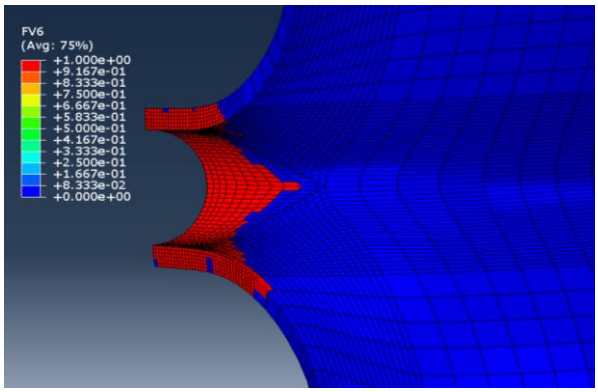

(c)

Fig. 7-17: Temperature and structural integrity of the a) liner and the b) overwrap at the hollow center throughout i) LN_2 filling, ii) steady state, iii) pressure cycling and iv) LN_2 purging phases and c) liner localized cracking at the central tube during chill-down.

Both damage variables had a non-zero value at the beginning of the chill-down stage that is attributed to stress history from curing. It can be seen that while free thermal contraction of the liner at the spheres led to very low stress levels, a thermal restraint imposed from the overwrap at the central hollow cylinder region led to localized cracking at the end of the filling process (Fig. 7-17c). On the other hand, it is important that the composite overwrap maintained its structural integrity throughout all cryogenic operation stages, despite localized liner cracking. It was shown that the sudden temperature drop caused by contact with LN_2 led to a strain jump at the central hollow tube and the upper sphere at t = 4000 [s] and 5500 [s] respectively. Sudden temperature jumps at liner and overwrap at t = 10000 [s] approximately can be linked to LN_2 boil-off, due to the addition of warm pressurant (GN_2). Active pressurization lowered the overwrap damage variable due to temperature increase of the tank wall. The effect of pressure cycling on the liner, overwrap temperature and structural integrity was stronger in the vicinity of the gas-liquid interface (upper sphere) than at the central hollow tube.

7.4 Concluding Remarks

In this chapter, an FE-based transient thermo-mechanical analysis coupled with a PFA algorithm was performed to assess the behavior of the plastic-lined multi-spherical COPV throughout pressurization at low and high displacement rates and normal cryogenic operation (chill-down, pressure cycling, draining). The temperature dependent engineering properties of the liner and overwrap materials -presented in Chapter 6- were hereby incorporated. It was shown that global failure was triggered by polymer liner fracture and matrix cracking at the spheres next to the hollow center tube for the case of pressure loading at ambient conditions under a high displacement rate. On the contrary, pressurization at a low displacement rate led to fiber breakage as the dominant global failure mechanism with the liner remaining intact. In both loading cases first damage onset and global failure have a very localized behaviour, since they were located close to the spherical cells close to the central tube. This is attributed to the residual stresses developed from the liner/overwrap contact throughout curing and the fact that the number of UD straps was chosen on the basis of avoiding damage at the intersections. For the case of cryogenic operation, it was shown that the variation of the thickness of the frost layer along the height direction and the air gap thickness along the tank contour resulted in considerable temperature gradient along the tank's meridional direction. Additionally, it was seen that when the cryogen front reaches a prescribed tank wall location, the cooling rate reaches a peak value that translates to a stress sump. LN_2 boil-off -associated with pressure cycling- led to a temperature increase and a damage variable reduction at both the liner and overwrap. The

thermal restraint that the liner was imposed to from the overwrap at the central hollow cylinder led to localized cracking. However, no damage onset occurred in the composite overwrap at the same load environment. The later may be considered as a positive indication about the suitability of conformal Type IV multi-spherical COPVs for cryogenic storage.

References

[1] I.G. Tapeinos, D.S. Zarouchas, O. Bergsma, S. Koussios and R. Benedictus, 'Evaluation of the Mechanical Performance of a Multi-Cell Tank for Cryogenic Storage: Part I- Tank Pressure Window based on Progressive Failure Analysis', *International Journal of Hydrogen Energy*, **44**, 3917-3930, 2019.

[2] S.T. Peters, Composite Filament Winding, ASM International Materials Park, 2011.

[3] O.K. Bergsma, 'Approximation of mechanical properties of sheared fabrics', *Journal of Thermoplastic Composite Materials*, **15**, 65-75, 2002.

[4] Abaqus 6.13 Documentation, 2016.

[5] V.V. Vasiliev, 'Composite pressure vessels – analysis, design and manufacturing', *Bull Ridge Corporation*, 2009.

[6] L. Zu, 'Design and optimization of filament wound composite pressure vessels', PhD Thesis, TU Delft, 2012.

[7] Z. Hashin, 'Failure Criteria for Unidirectional Fiber Composites', *Journal of Applied Mechanics*, **47**, 329-334, 1980.

[8] P. Papanikos, K.I. Tserpes, G. Labeas and S. Pantelakis, 'Progressive damage modelling of bonded composite repairs', *Theoretical and Applied Fracture Mechanics*, **43**, 189-198, 2005.

[9] G. Agrawal, J. Joseph, D.K. Agarwal and S.S. Kumar, 'Effect of insulation thickness on evolution of pressure and temperature in a cryogenic tank', *Proceedings of the 23rd National Heat and Mass Transfer Conference*, India, 2015.

[10] C.-F., 'Ballistic impact modelling of composite materials', *Proceedings of the 7th International LS-DYNA users Conference*, Michigan, 2002.

[11] K.A. Brown, R. Brooks and N.A. Warrior, 'The static and high strain rate behaviour of a commingled E-glass/polypropylene woven fabric composite', *Composite Science and Technology*, **70**, 272-283, 2010.

[12] Z. Kang, Y. Li, Y. Ma, L. Wang, F. Xie and J. Wang, 'Experimental study on cool down characteristics and thermal stress of cryogenic tank during LN2 filling process', *Applied Thermal Engineering*, **130**, 951-961, 2018.

[13] C.A. Stephens, G. J. Hanna and L. Gong, 'Thermal-Fluid Analysis of the Fill and Drain Operations of a Cryogenic Fuel Tank', NASA Technical Memorandum, 1993.

[14] M. Kida, Y. Kikuchci, O. Takahash, I. Michiyoshi, 'Pool-boiling heat transfer in liquid nitrogen', *Journal of Nuclear Science and Technology*, **18**, 501-513, 1981.

[15] K-H. Kim, H-J. Ko, K. Kim, Y-W. Kim and K-J. Cho, 'Analysis of heat transfer and frost layer formation on a cryogenic tank wall exposed to the humid atmospheric air', *Applied Thermal Engineering*, **29**, 2072-2079, 2009.

[16] J.D. Yonko and C.F. Sepsy, 'An investigation of the thermal conductivity of frost while forming on a flat horizontal plate, *ASHRAE Transactions*, **73**, 1967.

[17] Y. Hayashi, K. Aoki and H.Yuhara, 'Study of frost formation based on a theoretical model of a frost layer', *Heat Transfer*, **6**, 79-94, 1977.

[18] C.A. Schalla, 'Hydrogen liquid level influence on aircraft tank insulation', *Advances in Cryogenic Engineering*, 1966.

[19] C.V. Madhusudana , 'Thermal Contact Conductance', *Springer*, 1996.

[20] ASTM E1530, ‘Standard Test Method for Evaluating the Resistance to Thermal Transmission of Materials by the Guarded Heat Flow Meter Technique’.

[21] Final Report, ‘Investigation of Low-Cost LNG Vehicle Fuel Tank Concepts’, Idaho National Engineering Laboratory, 1998.

[22] J.E. Jensen, W.A. Turttle, R.B. Stewart, H. Brechna and A.G. Prodell, ‘Selected Cryogenic data notebook’, Brookhaven National Laboratory, 1980.

[23] T. Bourgeois, F. Ammouri, M. Weber and C. Knapik, ‘Evaluating the temperature inside a tank during a filling with highly-pressurized gas’, *International Journal of Hydrogen Energy*, **40**, 11748-11755, 2015.

[24] I.M. Daniel and O. Ishai, ‘Engineering mechanics of composite materials, (Second Edition) Oxford University Press, 2006.

Chapter 8: Experimental Assessment of the Mechanical Performance of a Type IV Cryogenic Multi-spherical COPV

The previous chapters have addressed various design issues of a multi-spherical COPV: i) load analysis mapping, ii) volumetric efficiency and performance, iii) tank pressure window under thermo-mechanical loading, iv) draping simulation and v) progressive failure analysis. However, in order to fully understand how the designed tank configuration behaves in the load environment of interest, a tank demonstrator needs to be produced and an experimental assessment must be carried out to assess the accuracy of the analytical and numerical studies.

This chapter outlines all the different aspects in manufacturing a sub-scale Type IV demonstrator and then testing its performance under hydro-burst pressure and pressure cycling at cryogenic temperatures. The evaluation of the temperature profile and respective strain behaviour at cryogenic conditions will provide insight on different phenomena occurring during tank operation and will show whether the accuracy of the CTE (T) and E(T) approximation functions of Chapter 6 and findings of Chapter 7 are realized. This chapter is based on the work conducted in [1].

8.1 Tank Manufacturing

8.1.1 Liner Moulding

As mentioned in Chapters 6 and 7, a plastic liner was chosen because of its material properties (PA12), more specifically, its low density, high ultimate elongation at break, low permeability and the potential to be moulded at complex shapes. Moulding in one piece is an important advantage of the plastic liners, unlike metal liners that have a welding line that can be a weak spot under pressurization. A liner material requirement was to have a melting point higher than the curing temperature of the composite overwrap, and low enough to be compatible with a moulding process. Rotational moulding was chosen as the liner manufacturing process since it can result in a relatively uniform thickness throughout the tank contour. The principle of this technique is to fill-in a metallic mould with the material of interest (in plastic powder form) and to slowly rotate it around two perpendicular axes, while subjecting it to a heating and then a cooling cycle, thus dispersing the softened material and causing it to stick to the walls of the mould. Fig. 8-1a shows the aluminium hollow mould incorporated where the grooves for the resistors (heating elements) can be seen. All the dimensions are given in [mm]. Furthermore, all the holes at the edges for clamping the female with the male mould are shown. The roto-moulding setup involves a robotic arm (to provide a combined rotational movement), and a control system assisting the heating-curing cycle (Fig. 8-1b).

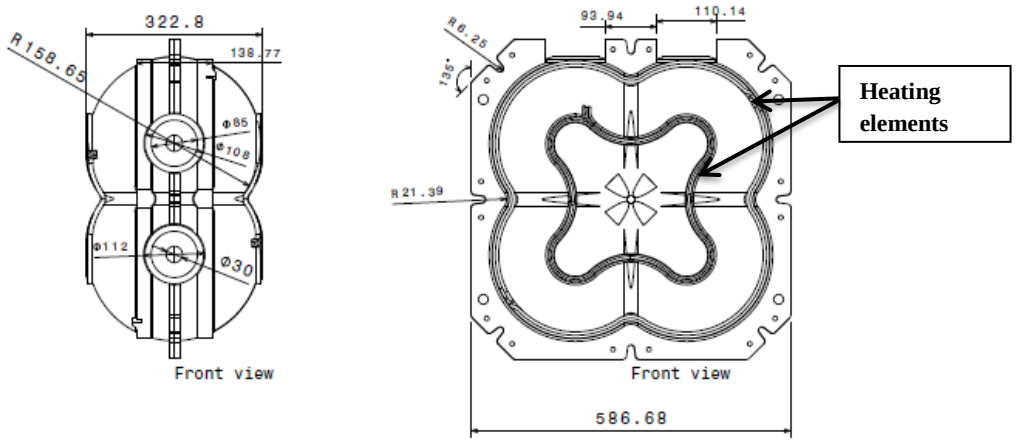

(a)

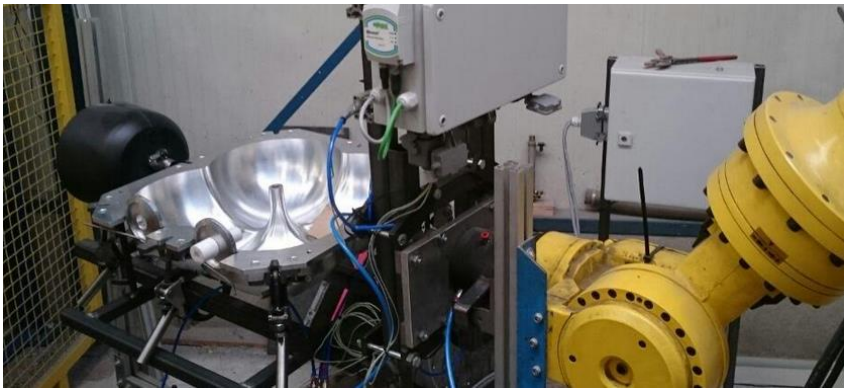

(b)

Fig. 8-1: a) Overview of the aluminium mould and ii) the roto-moulding process for manufacturing of the PA12 liner.

8.1.2 Composite Overwrap

Draping/laying composite patches (with the geometry depicted in Fig. 7-5) was utilized as the composite overwrapping method. Fig. 8-2a depicts the draped patches on the tank contour in conjunction with the UD straps placed at the intersection. The area near the openings was reinforced by both additional doilies and metallic bosses on top of the composite overwrap. The inner and outer metallic boss were threaded together, thus providing a leak-tight tank system. Fig. 8-2b illustrates the central hollow tube, where all the UD straps pass through.

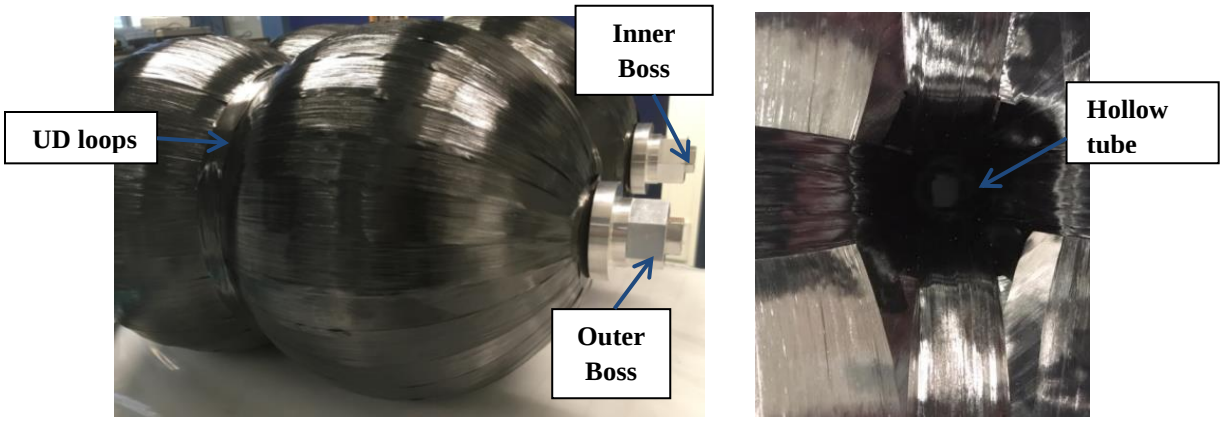

(a) **(b)**

Fig. 8-2: a) Draping of patches from pole to pole and b) reinforcement of the intersections and hollow centre tube.

A fully draped multi-sphere in its i) un-cured and ii) cured forms is illustrated in Fig. 8-3a,b respectively. The compaction of the composite plies can be seen in Fig. 8-3b. The liner and overwrap were expected to expand/contract independently throughout the curing cycle, owing to their CTE mismatch. Sand was internally added as a medium to avoid thermal buckling of the liner during the heating and cooling stages.

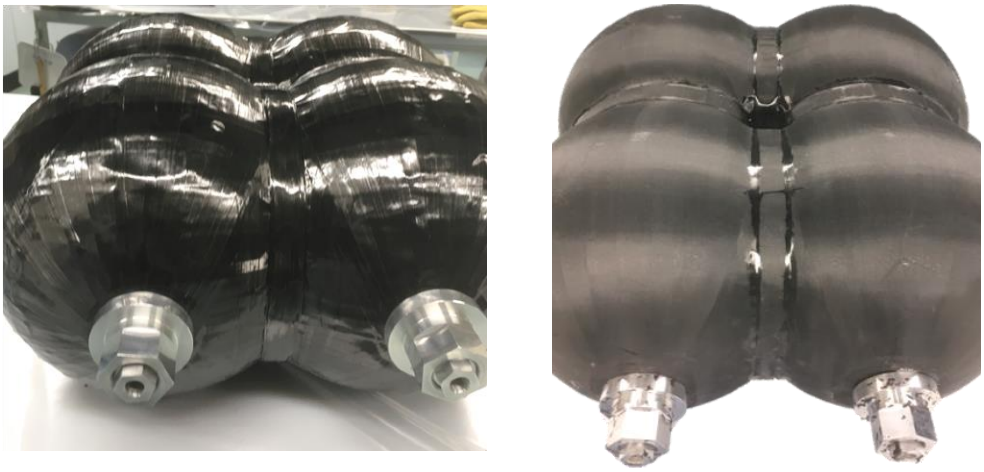

(a) **(b)**

Fig. 8-3: a) Uncured and b) cured multi-shell tank.

8.1.3 Summary of Sub-scale Tank Specifications

The geometrical specifications used throughout the multi-sphere modelling in Chapter 7 were adapted for the sub-scale tank demonstrator. The following specifications were applied:

- Overwrap material: CFRP
- Liner material: PA12
- $m_{cells} = n_{cells} = 2$ ($p_{cells} = 1$)
- R = 145 [mm]
- d = 200 [mm]
- R_{fillet} = 29 [mm]
- QI lay-up*:* $[0,45,-45,90]_s$
- t = 1.12 [mm]
- $t_{junction}$ = 3.97 [mm]
- t_{liner} = 6.5 [mm]
- r_{cyl} = 28.87 [mm]
- l_{cyl} = 110.4 [mm]
- $\pm\varphi = [\pm 45^{o}]$
- i_{ratio} = 2.5 [-]
- s = 60.47 [mm]
- V = 46.1 [l]
- $M_{structural}$ = 2.38 [kg]

In the specifications given above $M_{structural}$ represents the mass of the composite overwrap (Section 5.1.1iii). Additionally the multi-sphere volume (V) is given in liters (l). In the following section the specifications of the tank testing procedures are outlined.

8.2 Tank Testing

8.2.1 Hydrostatic Burst at Room Temperature

i. Test Description

The test campaign was conducted in accordance to the requirements of ANSI/AIAA S-081 standard [2] for composite overwrapped vessels used in reusable launch vehicles. It is stated in the standard that no burst should occur for an internal pressure of less than 1.5 times the P_{MEOP}, which for the case of the SpaceLiner LH_2 tank is 3.8 [bar] [3] (resulting in a proof pressure value of 5.7 [bar]). A hydrostatic burst test at high displacement rate and at ambient conditions was employed to the multi-sphere. The goal was to monitor strain evolution, identify local and global damage locations and mechanisms and consequently to evaluate the pressure allowable.

ii. Instrumentation

Three-dimensional (3D) Digital-Image-Correlation was employed to record the in-plane strain field at one side of the tank. The DIC system utilized Vic3D software from Correlated Solutions. Spraying high contrast dot patterns (speckles) on the tank surface was required to signify all the different strain measurement points throughout the experiment. The speckle size throughout the tank contour was in the range of 1-2 [mm]. Vic3D tracks the displacement at each at each successive pair of images through a correlation algorithm. The DIC system was linked to two digital high-speed cameras that were focused on the top spherical domes, the common intersection and the polar openings (Fig. 8-5a). The camera resolution was set at 2048 x 2048 [pixels]. The strain measurements at the composite overwrap were monitored to quantify the pressure values at which contact would be achieved between the plastic liner and composite overwrap at different locations.

The AE technique was utilized to reveal damage onset and progression as well as the corresponding locations and thus help to pinpoint the multi-spherical COPV pressure allowable. The tank pressure window -the pressure difference from the very first damage event to final failure (ΔP)- can then be evaluated. The AE parameter that was recorded throughout the experiments was the cumulative absolute acoustic energy measure of all the AE hits. Any abnormal change at the acoustic energy response indicates the presence of new damage within the structure [4]. The measurements are here compared with the PFA findings of Chapter 7.

All locations where AE sensors were mounted on the tank are shown in Fig. 8-4. Sensors 1 and 5 were placed at the bottom spheres and close the central hollow tube. They were the most critical sensors, since damage onset as well as global failure was expected to occur at the tank center section primarily. On the other hand, sensors 3 and 4 at the upper spheres were utilized to monitor any unwanted damage onset or even unexpected water leak next to the polar openings. Finally, sensor 2 was mounted next to the horizontal intersection, in order to capture any damage phenomena that could potentially take place at the junctions or their adjacent spherical cells.

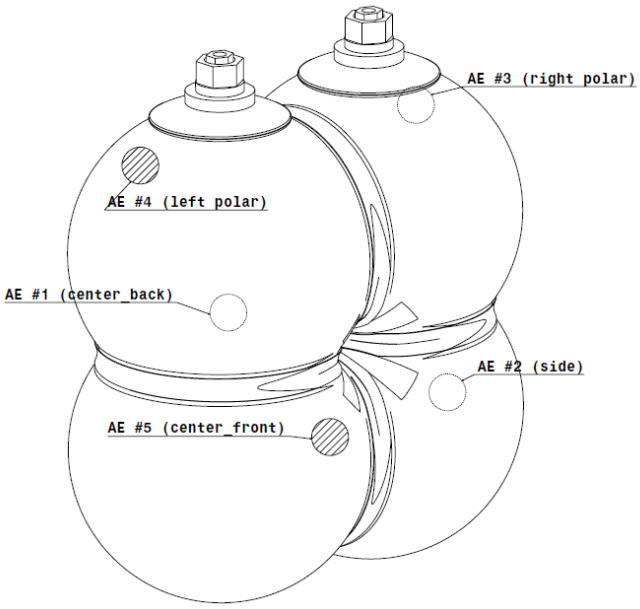

Fig. 8-4: Layout of the Acoustic Emission (AE) sensors at the tank contour.

The complete experimental setup of the tank inside a container is depicted in Fig. 8-5a. A container was used for safety purposes. The DIC cameras were placed under an inclination angle of [15^{o}] from the horizontal axis to have a focus at the upper half of the multi-cell test specimen. AE sensors next to the central cylinder (#5) and at the bottom right sphere (#2) are depicted in Fig. 8-5b. A burst pressure test bench (manufactured by SHINEEAST) with an industrial personal computer (IPC) control unit incorporating LabVIEW Software was employed to build up pressure within the tank. Water was added through hydraulic pressure hoses to the tank where a hydraulic oil pump was the pressure source. By using a digital pressure gauge, real time monitoring of pressure at a high-sampling speed was conducted.

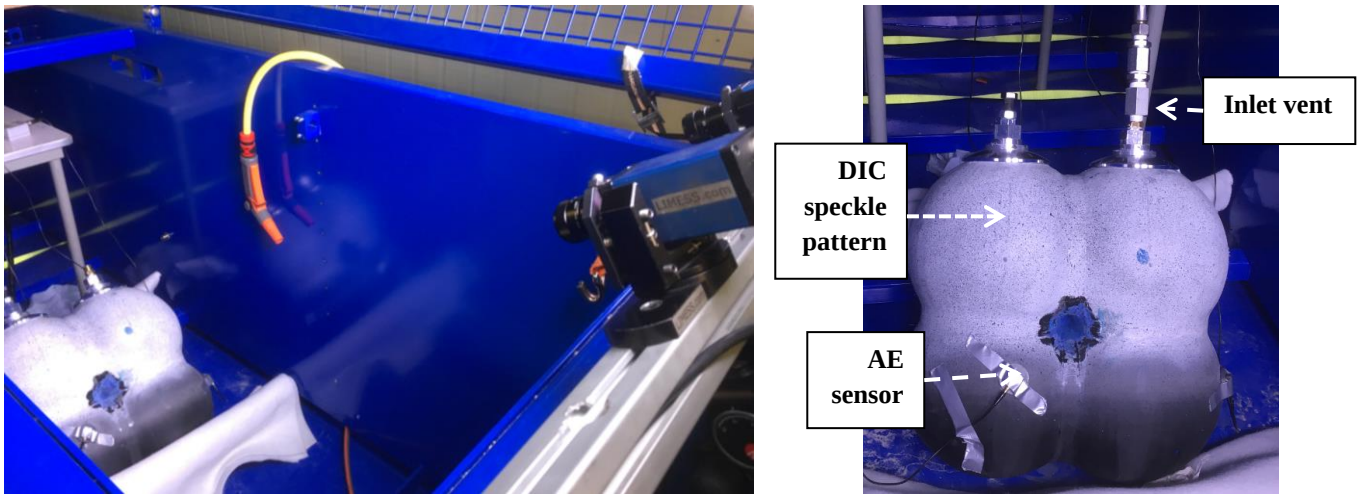

(a) **(b)**

Fig. 8-5: a) Overview of the complete experimental setup and b) tank configuration before hydro-burst pressure testing.

iii. Experimental Procedure

Water was added through hydraulic pressure hoses to increase the pressure. The tank was pressurized at $\frac{dP}{dt} = 1.35$ [bar/s] rate of pressure increase approximately. This pressure rise rate

corresponds to a fast pressure rise rate that a cryogenic tank is facing throughout cryogen evaporation when lacking a thermal insulation layer [5].

8.2.2 Pressure Cycling at Cryogenic Temperature

i. Test Description

According to the ANSI/AIAA S-081 standard [2], the cryogenic tank needs to be subjected to a given number of pressurization cycles at P_{MEOP} while storing a cryogenic liquid, where no burst, nor pressure loss may occur throughout the entire procedure. Repeated pressure cycling at cryogenic temperatures followed by emptying of the tank represents the multiple filling/draining phases during the structure's service life. Throughout pressure cycling at cryogenic temperatures the following information can be acquired: the temperature profile at the tank contour as well as the effect of temperature and internal pressure on the strain behaviour of the composite overwrap.

ii. Instrumentation

Fiber Bragg gratings (FBGs) were employed to evaluate the strain field at different locations during filling with cryogen, pressure cycling, and draining. More specifically, FBGs with an Ormocer coating were employed on the composite overwrap as they have shown the potential to measure strain at low temperatures with a high accuracy [6]. An FBG sensor contains a periodic modulation of the refractive index of the fibre core over a certain gauge length e.g. 8 [mm]. The FBG sensors used in this study were LBL-1550-125 Draw Tower Grating (DTG) type sensors (FBGS International NV). The length of the sensors was 8 [mm] with their nominal Bragg wavelengths distributed in the range of 1520 to 1570 [nm]. Due to their Ormocer coating, these sensors can endure temperatures between -200 to 200 [°C]). The PXIe-4844 optical sensor interrogator (from National Instruments) was used to record the FBG outputs where both strain and pressure were sampled at a 10 [Hz] frequency. The interrogator has a dynamic range of 40 [dB] and a wavelength accuracy of 4 [pm]. Data recording was performed using the National Instruments LabView Software. Additionally, thermocouples (type K) were glued adjacent to every FBG sensor, in order to obtain a collocated temperature-strain relationship

The points where FBGs and thermocouples were mounted can be seen in Fig. 8-6. The fibers were divided into 4 groups: i) spherical cells, ii) top intersection, iii) horizontal intersection and iv) polar openings.

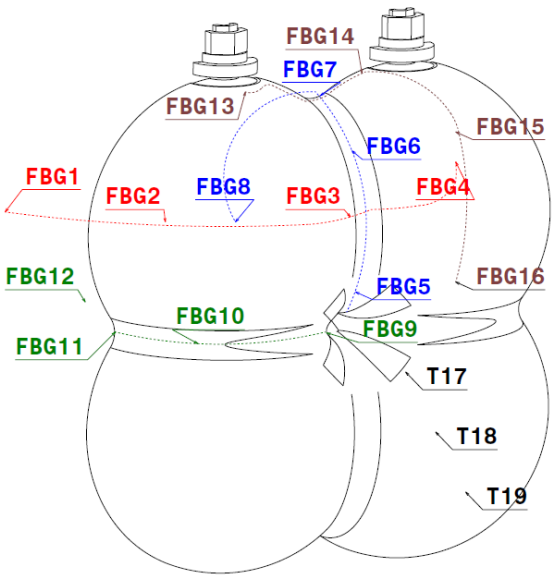

Fig. 8-6: Layout of the various FBGs at the tank contour.

The directions of strain measurement are outlined in Table 8-1. Every fiber group was assigned to assess the temperature and strain gradient along a corresponding path at the tank. The presence of a gradient can be either explained because of the i) location relative to the liquid interface level or ii) the liner and composite overwrap being in contact or not (this affects the mode of heat transfer and thus the strain behaviour).

Table 8-1: Outline of FBGs sensors.

a/a	Local Direction of Strain Measurement	Focus	Group
FBG1	Hoop	Temperature and strain distribution from a sphere to the intersection at liquid interface level	Spheres
FBG2	Hoop		
FBG3	Hoop		
FBG4	Meridional		
FBG5	Meridional	Temperature and strain distribution along the intersection below liquid interface level and at vapour region	Top Intersection
FBG6	Meridional		
FBG7	Meridional		
FBG8	Meridional		
FBG9	Meridional	Temperature and strain distribution along the horizontal intersection and at liner/overwrap contact area in the center	Horizontal Intersection
FBG10	Meridional		
FBG11	Meridional		
FBG12	Meridional		
FBG13	Hoop	Temperature and strain distribution next to openings at vapour region	Openings & Sphere
FBG14	Hoop		
FBG15	Hoop		
FBG16	Hoop		

The surface-mounted FBGs and thermocouples can be seen in Fig. 8-7a. Temperature recordings were performed in another 3 points at different heights along the tank lower sphere, as it can be seen in Fig. 8-6. A pressure gauge was connected to the pipeline for monitoring the internal pressure. Two different vents were used: one for pressurisation and another to drain the system. A pressure relief valve device controlled the pressure level to ensure safety. The complete lay-out of the test setup can be seen in Fig. 8-7b.

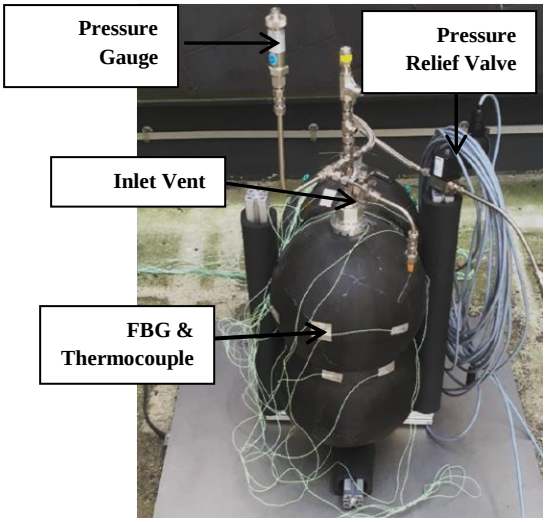

(a)

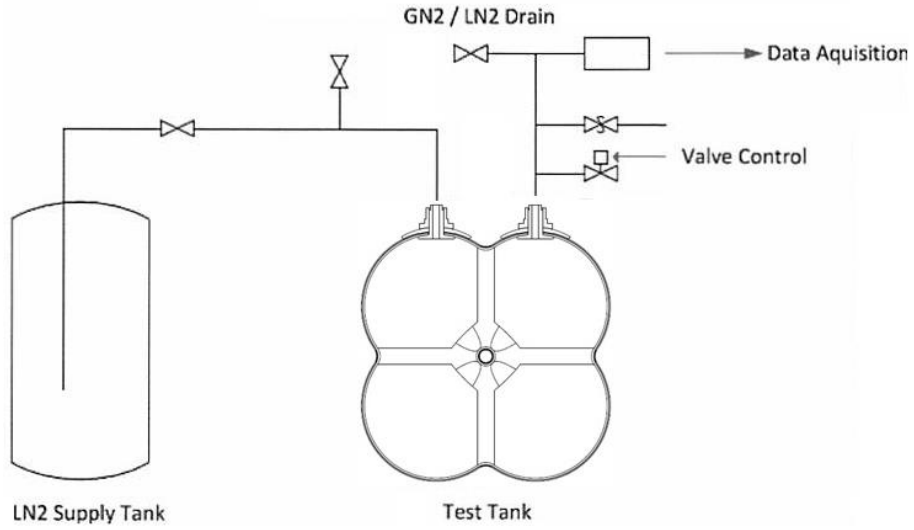

(b)

Fig. 8-7: a) Overview of the experimental setup and sensors before testing and b) complete lay-out of all systems of the test setup.

iii. Experimental Procedure

LN_2 was used instead of LH_2 due to safety reasons. The boiling point of LN_2 is -196 [^oC], slightly higher than LH_2 (-253 [^oC]). All loading stages that the SpaceLiner liquid hydrogen (LH_2) tank is expected to undergo were applied here [3]: i) nominal cryogenic operation at P_{MEOP} (at 3.8 [bar]), ii) nominal empty operation after main engine cut-off (MECO at maximum expected outside temperature under 3 [bar]) and iii) off-nominal operation after early MECO with the remaining fuel (at 3.5 [bar]).

The test procedure consisted of the following steps:

1. Filling of the test tank with LN_2 to a level of 75 [%] by volume with a feed rate of 0.0055 [l/s] at P = 1 [bar] approximately.
2. Active pressurization (with the use of gaseous nitrogen-GN_2 at RT) to 3 [bar], 3.5 [bar] and 3.8 [bar].
3. Unloading.
4. Repetition of steps 2-3 five times.

5. Draining of the tank.

Throughout the cooling process, the ambient air was cooled below its dew point through contact with the colder tank wall surface. This led to water vapour condensation; since the temperature was below the water freezing point, frost was formed all over the tank surface (Fig. 8-8). Complete de-icing occurred only after some time following the draining phase.

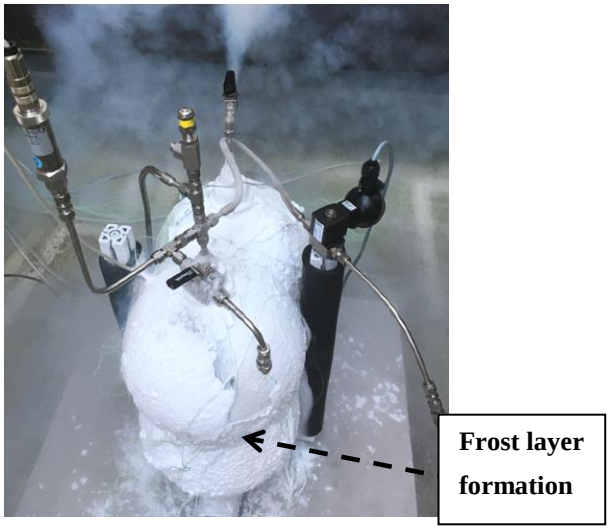

Fig. 8-8: Overview of the multi-spherical COPV at the draining phase.

8.3 Results

8.3.1 Hydrostatic Burst at Room Temperature

The internal pressure as a function of time (hydro burst test) is presented in Fig. 8-9. The following events are illustrated (based on AE and FBG readings):

i) Liner-to-overwrap gradual contact (3.7 [bar] ≤ P ≤ 8.4 [bar]),
ii) Liner/ overwrap damage onset and evolution (7.2 [bar] ≤ P ≤ 18.84 [bar])
iii) Burst at P_{LPF} = 18.84 [bar].

The liner deformation could not be monitored throughout the test, so the focus was given on the composite overwrap.

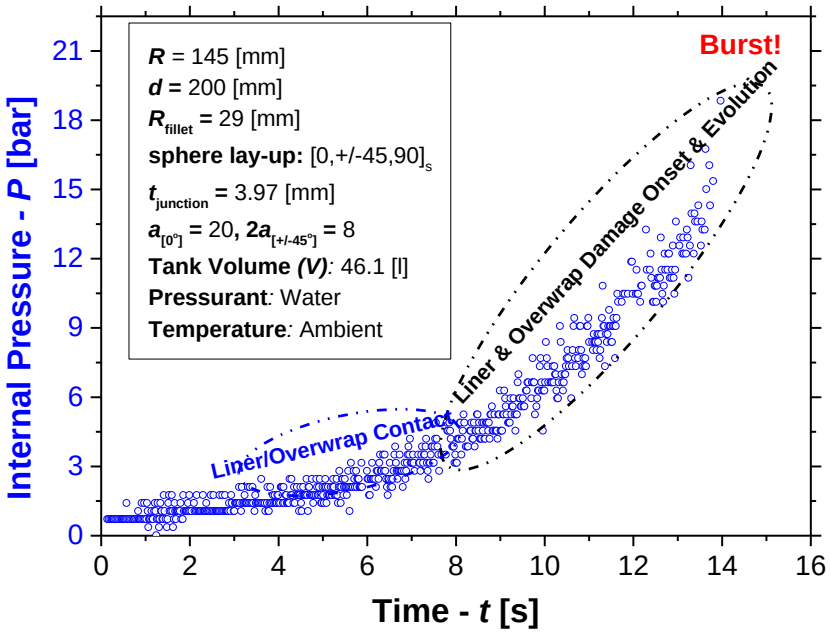

Fig. 8-9: Internal pressure vs time.

It was shown in Chapter 7 that contact between the liner and the composite overwrap took place gradually with increasing pressure, with the central tube being the first contact region. Strain jumps at the overwrap were triggered by liner-overwrap contact through out-of-plane compressive stresses. The meridional strain distribution from the sphere to the junction tip (half-way through the arc length of a junction) is illustrated in Fig. 8-10. These values correspond to contact being achieved at a) the bottom, b) top and c) middle sections of the intersection/spherical shell regions. Fig. 8-10d shows the strain distribution right before burst occurs. Contact was eventually achieved in the whole surface area of the tank. As a result, first damage and complete loss of load carrying capability was expected to occur in that region, owing to the fact that strain accumulated at a faster rate at the intersection/sphere boundary.

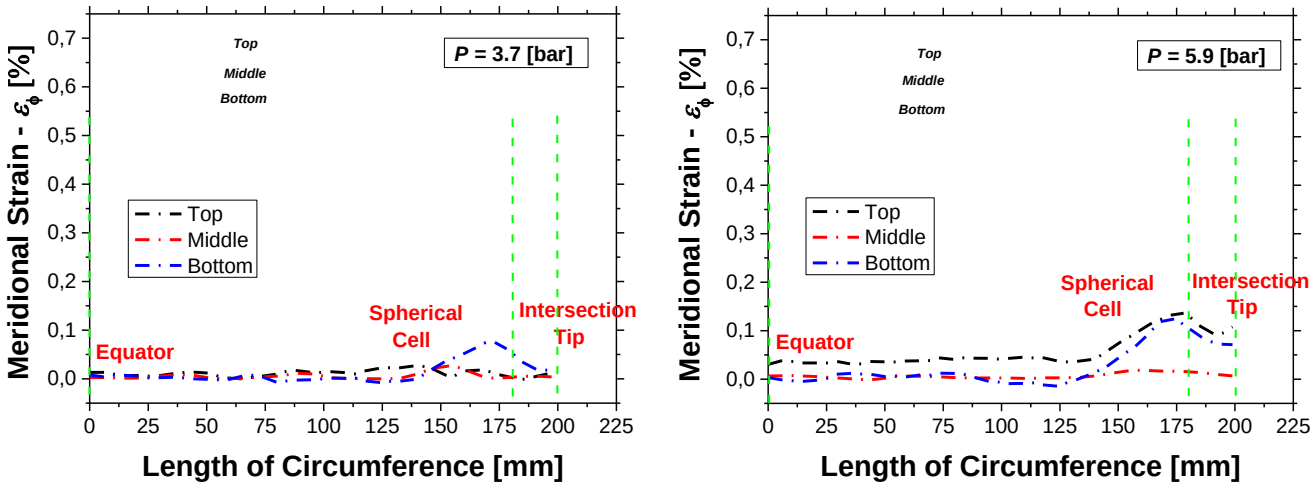

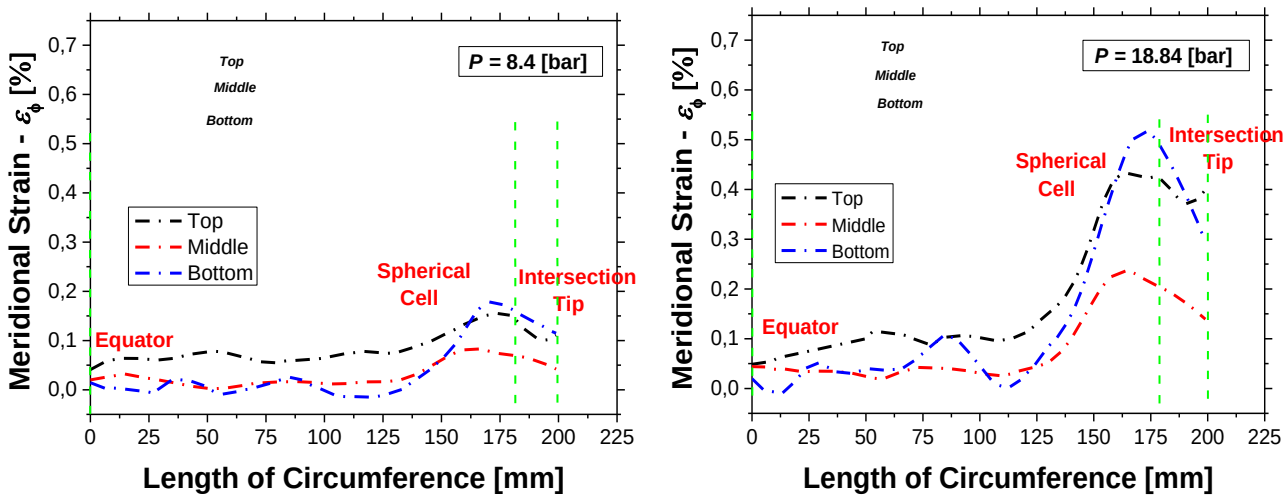

(c) (d)

Fig. 8-10: Meridional strain distribution when contact is achieved at the a) bottom, b) top and c) middle part of the intersection and at d) burst.

Fig. 8-11a depicts the cumulative acoustic energy combined for all sensors as a function of internal pressure. A highly non-linear behaviour was obtained throughout the experiment. A sudden increase at 7.2 [bar] approximately can be attributed to damage onset, while a peak value at 18.84 [bar] is linked to global failure. An analysis of the acoustic energy of individual AE sensors is presented in Fig. 8-11b. The initial low energy levels in AE sensor #4 can be associated to liner/overwrap contact, or even some small water leakage at the polar opening connection. The acoustic energy of all sensors #1,2,3,5 becomes larger than zero at 7.2 [bar] approximately owing to first damage initiation with the largest absolute energy levels recorded in AE sensor #5 right before failure. Hence, it can be assumed that the excessive damage accumulation occurring at the overwrap next to the central tube led to the pressure loss at 18.84 [bar]. However the DIC results are required to verify this assumption.

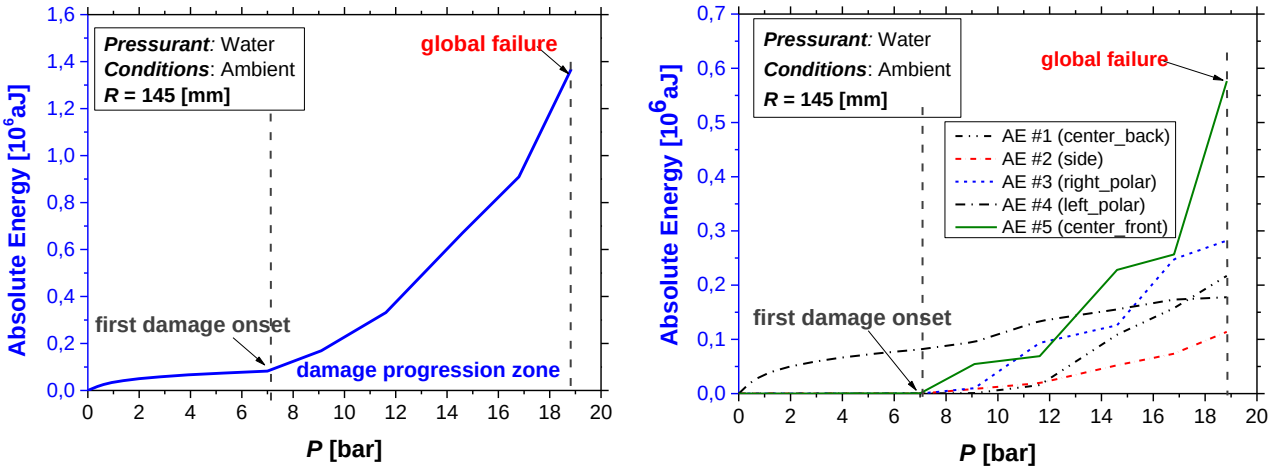

(a) (b)

Fig. 8-11: a) Cumulative absolute acoustic energy of all AE sensors combined and b) cumulative absolute acoustic energy per AE sensor as a function of increasing internal pressure.

A comparison of the FE analysis and the hydrostatic burst pressure test findings on the location and global failure mechanism of the COPV can be seen in Fig. 8-12a,b respectively. Loss of load carrying capability occurred in both cases close to the central hollow cylindrical

tube and at the spherical cells. Failure can be attributed to through-the-thickness matrix cracking of the laminate triggered by liner fracture. The global failure pattern was matrix cracking at 23.35 [bar] in the FE analysis while in the experiment it was matrix cracking at 18.84 [bar] (offset of 23 [%] in the burst pressure value). A water leak occurred next to one metallic boss connection (Fig. 8-12b), at the time of global failure. Hence, it was proven both numerically and experimentally that strain concentration and damage onset can be avoided at the intersections by the introduction of a minimum required number of UD straps.

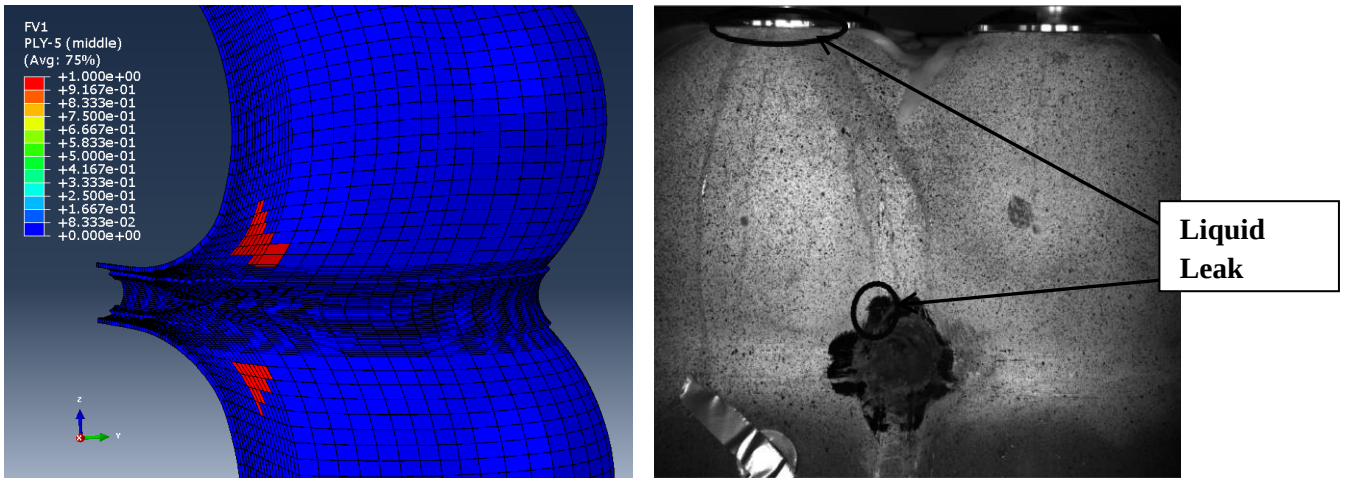

(a) **(b)**

Fig. 8-12: Ultimate structural failure mechanism (pressure loss) (cracked liner & matrix cracks through-the-thickness) in the a) the FE analysis at 23.35 [bar] and the b) the burst test at 18.84 [bar].

A comparison between the FE analysis (Chapter 7) and the AE results on the evolution of damage is presented in Fig. 8-13. The multi-spherical COPV underwent first damage (FPF) at 7.2 [bar] at the test (S_F = 1.94 times the P_{MEOP}) and 9.2 [bar] at the FE analysis (S_F = 2.39 times the P_{MEOP}); this leads to an offset of 17.4 [%] in the tank pressure window ΔP value (P_{LPF} - P_{FPF}) between the experiment and FE analysis.

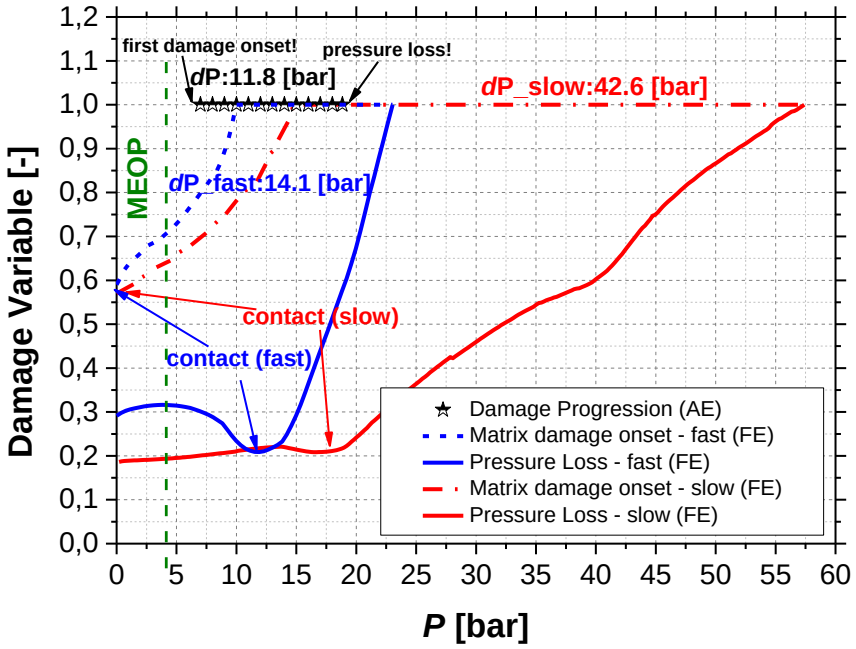

Fig. 8-13: Tank pressure window based experiment and FE analysis.

8.3.2 Pressure Cycling with LN_2

Both the temperature at the upper sphere (FBG16) and internal pressure as a function of time during the cryo test are presented in Fig. 8-14. The stages of the test were:

i) Cryogenic chill-down due to filling of tank with LN_2 (0 [sec] $\leq t \leq$ 6000 [sec]),
ii) Steady state condition (6000 [s] $\leq t \leq$ 10000 [sec]),
iii) Pressure cycling (10000 [s] $\leq t \leq$ 12000 [sec]) and
iv) Tank draining (12000 [sec] $\leq t \leq$ 14000 [sec]).

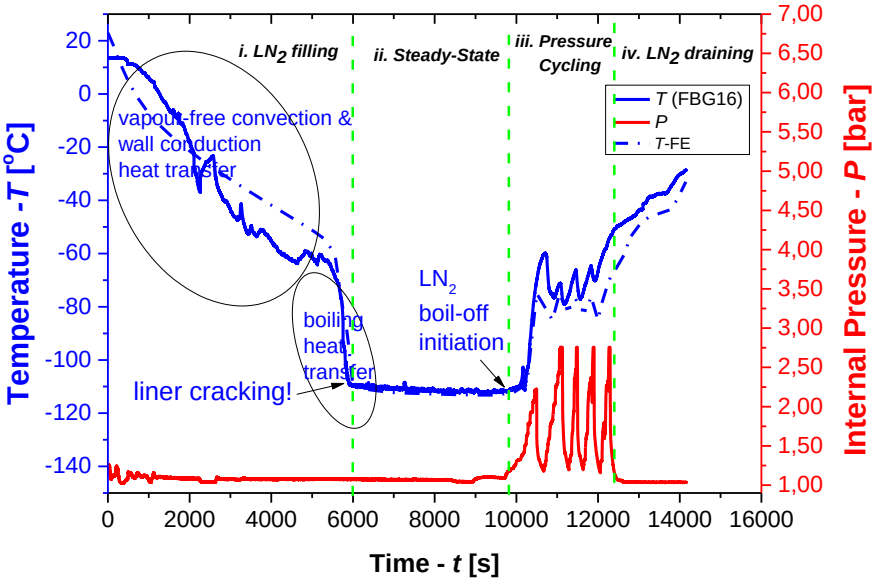

Fig. 8-14: Temperature and internal pressure history at the upper sphere (sensor 16) versus time.

The temperature on the entire tank wall was dictated by the following four ways of heat transfer:

i) Vapour-free convection (at the ullage region),
ii) Radial thermal conduction at the vessel walls,
iii) Circumferential thermal conduction at the vessel walls and
iv) Convection associated with LN_2 boiling (at the gas/liquid interface level)

The liner performance could not be monitored throughout this test, so the focus was given on the composite overwrap. According to the readings of sensor 16 (the location is depicted in Fig. 8-6), the first three heat transfer modes were the primary mechanisms of wall cooling until t = 5500 [sec] approximately (Fig. 8-14). From the moment that the LN_2 level passed sensor 16, a very sudden temperature decrease was recorded from t = 5500 [sec] to 6000 [sec] that can be attributed to liquid boiling. The composite overwrap in this location did not reach the LN_2 saturation temperature due to the fact that the air gap with the liner acted as a thermal insulator. The addition of pressurant (GN_2 at room temperature) at the cycling stage induced rapid LN_2 evaporation, which was reflected by the temperature increase at the overwrap (Fig. 8-14). As last step, tank draining led to a linear temperature increase. A comparison between the findings of the FE analysis of Chapter 7 and the experiment revealed a close agreement in the temperature evolution.

Localized cracking occurred at the liner (central cylindrical tube) at the end of the chill-down stage (t = 5500 [sec]) (Fig. 8-15). This was also shown in the FE study (Chapter 7); this cracking phenomenon can be associated to the CTE mismatch between the liner and the composite overwrap. This mismatch led to a thermal restraint imposed on the PA12 liner by the overwrap,

which in combination with the brittle behaviour of the liner material resulted in cracking. It is important to evaluate whether localized liner cracking would affect the temperature and strain accumulation at the composite overwrap with an increasing number of pressurization cycles.

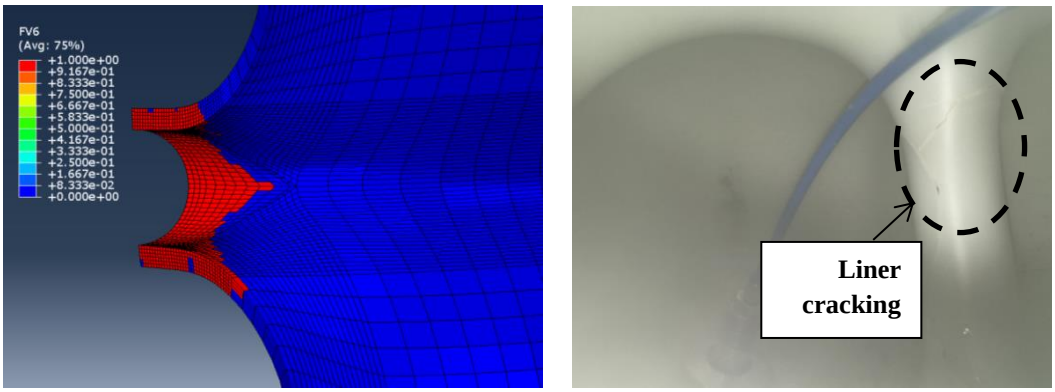

(a) **(b)**

Fig. 8-15: Localized crack formation at the liner at the end of LN_2 filling from a) FE analysis and b) after the experiment.

The temperature history for different locations at the composite overwrap is depicted in Fig. 8-16. The results from thermocouples #2,3,4,8,11,13 (Fig. 8-6) are not plotted since they are placed symmetrically to the thermocouples #1,5,10,14 and thus would give the same response. As expected, the higher the location of a measurement point the more time it stayed in the ullage region, which resulted in a slower cooling rate. With the liquid level increasing, the temperature values at all measurement points were dropping. Lower temperatures were recorded at the bottom spheres (thermocouples #17,18,19) that can be linked to the formation of a thicker frost layer due to more exposure time to cryogenic temperatures. The sensors that were placed below the 75 [%] fill level of the tank (thermocouples #5,6,9,10,12,16,17,18,19) obtained a temperature plateau at the end of the chill-down stage. On the other hand, the sensors at the 75 [%] fill level (thermocouples #1,15) and the ones at the ullage region (thermocouples #7,14) did not reach a temperature plateau, owing to continuous LN_2 boil-off. The introduction of the pressurant (GN_2) (at approximately 1000 [sec]) resulted in a large temperature increase at all the regions close to the 75 [%] fill level (thermocouples #6,9,12,16), due to LN_2 vaporization. This effect was amplified at the central tube vicinity (thermocouple #9) due to liner cracking. It is shown that the temperature fluctuations followed the tank loading-unloading pattern.

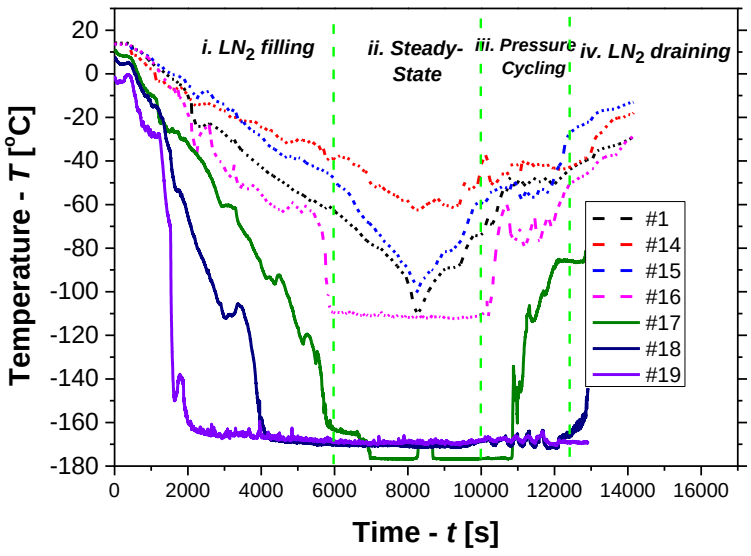

(a)

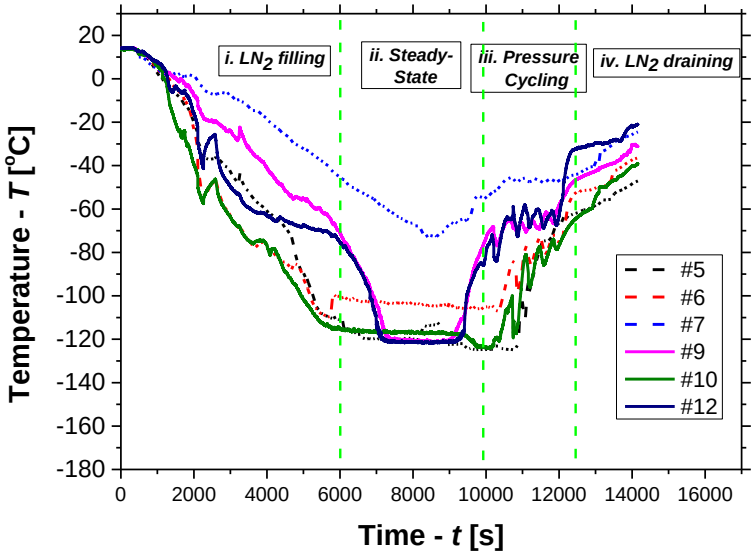

(b)

Fig. 8-16: Temperature distribution over the a) spheres and b) intersections throughout i) LN_2 filling, ii) pressure-cycling and iii) draining stages.

The corresponding strain values at the spheres and intersections are depicted in Fig. 8-17a,b respectively. FBGs#2, 3 correspond to the hoop strain at the upper sphere (at the liquid-tank wall interface level), while FBGs#15,16 represent meridional strain at the upper sphere (above and below the gas-liquid interface level respectively). The cryogenic environment led to the contraction of the tank wall and thus compressive strain; the strain trends are in close agreement with the temperature profile at every sensor (Fig. 8-16). The recorded meridional strain values in all intersection locations were lower in amplitude than the strain levels measured at the undisturbed spherical areas (Fig. 8-17b). This is addressed to the considerably lower laminate CTE in the junction (because of all the added [0^o] plies) as compared to that of the QI laminate at the spherical cell. Additionally, the effect of pressure cycling was more evident in the junctions due to overwrap-liner contact which resulted in the overwrap being loaded in tension next to the central tube (FBGs#8,9). The recorded strain values were significantly lower than the strain allowables and could not result in any damage at the composite overwrap. In addition, visual inspection of the composite overwrap showed no signs of damage.

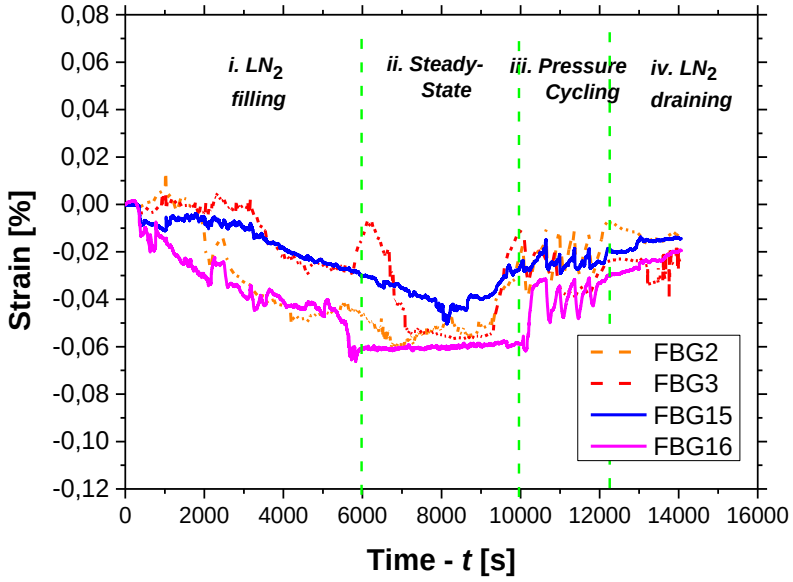

(a)

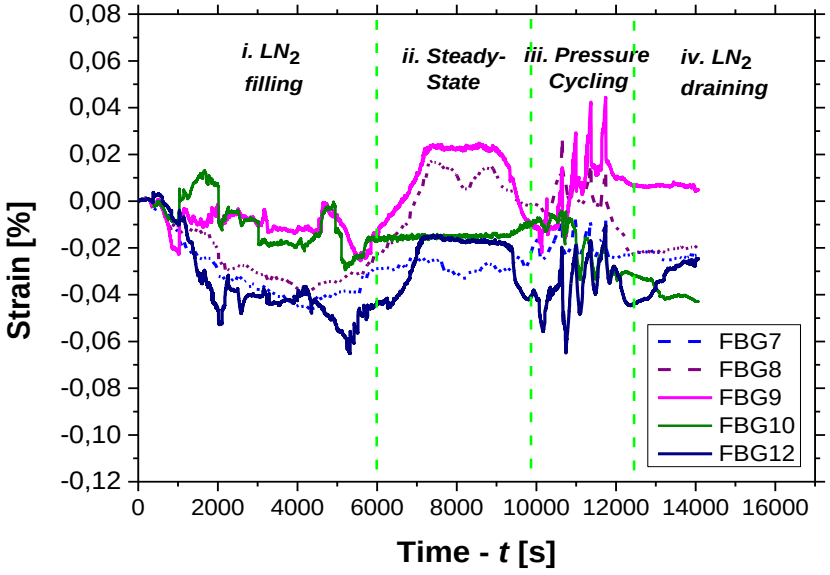

(b)

Fig. 8-17: Strain distribution over the a) spheres and b) intersections throughout i) LN_2 filling, ii) pressure-cycling and iii) draining stages.

A basic thermo-elastic load-deformation relationship is hereby utilized to evaluate strain as a function of temperature and pressure based on Classical Lamination Theory [7]. This will allow a comparison with the findings of FE analysis and the experimental recordings. Strain as a function of temperature (T) and pressure (P) for any ply k of the quasi-isotropic laminate (QI) at the sphere in the material axis system is given by [7]:

$$\boldsymbol{\varepsilon}^{[k]}_{1,2\_\text{sphere}}\left(T,P\right)=\mathbf{T}_{[\varphi]_k}\cdot\boldsymbol{\varepsilon}^{[k]}_{\varphi,\theta\_\text{sphere}}\left(T,P\right) \tag{8.1}$$

where

$$\boldsymbol{\varepsilon}^{[k]}_{\varphi,\theta\_\text{sphere}}\left(T,P\right)=\boldsymbol{\varepsilon}^{o}_{\text{sphere}}+z\boldsymbol{\kappa}^{o}_{\text{sphere}}-\mathbf{e}^{[\varphi_k]}_{\text{free}}=\left(\mathbf{A}_{\text{sphere}}(T)\right)^{-1}\cdot\left[\mathbf{N}_{\text{sphere}}+\mathbf{N}^{T}_{\text{sphere}}\right]-\mathbf{e}^{[\varphi_k]}_{\text{free}}, \tag{8.2}$$

$$\mathbf{e}_{\text{free}}^{[0^o]}=\begin{bmatrix}\alpha_{11}^{\text{T}}\Delta T\\ \alpha_{22}^{\text{T}}\Delta T\\ 0\end{bmatrix},\ \mathbf{e}_{\text{free}}^{[\pm 45^o]}=\begin{bmatrix}\alpha_{11}^{\text{T}}\cos(\pm 45)^2+\alpha_{22}^{\text{T}}\sin(\pm 45)^2\\ \alpha_{11}^{\text{T}}\sin(\pm 45)^2+\alpha_{11}^{\text{T}}\sin(\pm 45)^2\\ 2(\alpha_{11}^{\text{T}}-\alpha_{22}^{\text{T}})\cos(\pm 45)\sin(\pm 45)\end{bmatrix}\Delta T,\ \mathbf{e}_{\text{free}}^{[90^o]}=\begin{bmatrix}\alpha_{22}^{\text{T}}\Delta T\\ \alpha_{11}^{\text{T}}\Delta T\\ 0\end{bmatrix}, \tag{8.3}$$

$$\mathbf{N}_{\text{sphere}}^{\text{T}}=2t_{\text{ply}}\left(\mathbf{C}_{[0^o]}(T)\cdot\mathbf{e}_{\text{free}}^{[0^o]}+\mathbf{C}_{[\pm 45^o]}(T)\mathbf{e}_{\text{free}}^{[\pm 45^o]}+\mathbf{C}_{[90^o]}(T)\cdot\mathbf{e}_{\text{free}}^{[90^o]}\right) \tag{8.4}$$

and $\boldsymbol{\varepsilon}_{\varphi,\theta\_\text{sphere}}^{[k]}(T,P)$ is the strain vector in the laminate coordinate system (φ,θ,φθ) and $\boldsymbol{\kappa}_{\text{sphere}}^{\text{o}}$ are the mid-plane strains and curvatures respectively and $\mathbf{e}_{\text{free}}^{[\varphi_k]}$ is the free expansion strain vector of layer *k*. Curvatures ($\boldsymbol{\kappa}_{\text{sphere}}^{\text{o}}$) due to ΔT are zero at the sphere, owing to the balanced and symmetric QI lay-up. The symbol $\mathbf{N}_{\text{sphere}}^{\text{T}}$ corresponds to the thermal forces vector. The parameter $\left(\mathbf{A}_{\text{sphere}}(T)\right)^{-1}$ represents the QI laminate extensional compliance matrix as a function of temperature. The temperature drop (ΔT) is assumed as uniform through the thin-walled overwrap.

The strain vector at the intersections can be calculated by employing Eqs.(8.5-8.9) [7]:

$$\boldsymbol{\varepsilon}_{1,2\_\text{junction}}^{[k]}(T,P)=\mathbf{T}_{[\varphi]_k}\cdot\boldsymbol{\varepsilon}_{\varphi,\theta\_\text{junction}}^{[k]}(T,P) \tag{8.5}$$

$$\boldsymbol{\varepsilon}_{\varphi,\theta\_\text{junction}}^{[k]}(T,P)=\left(\mathbf{A}_{\text{torus}}(T)\right)^{-1}\cdot\left[\mathbf{N}_{\text{junction}}+\mathbf{N}_{\text{junction}}^{\text{T}}\right]+z\left(\mathbf{D}_{\text{torus}}(T)\right)^{-1}\cdot\left[\mathbf{M}_{\text{junction}}+\mathbf{M}_{\text{junction}}^{\text{T}}\right]-\mathbf{e}_{\text{free}}^{[\varphi_k]} \tag{8.6}$$

$$\mathbf{N}_{\text{junction}}^{\text{T}}=t_{\text{ply}}\left(a_{[0^o]}\mathbf{C}_{[0^o]}(T)\cdot\mathbf{e}_{\text{free}}^{[0^o]}+a_{[\pm 45^o]}\mathbf{C}_{[\pm 45^o]}(T)\mathbf{e}_{\text{free}}^{[\pm 45^o]}\right) \tag{8.7}$$

$$\mathbf{M}_{\text{junction}}^{\text{T}}=z_k t_{\text{ply}}\left(a_{[0^o]}\mathbf{C}_{[0^o]}(T)\cdot\mathbf{e}_{\text{free}}^{[0^o]}+a_{[\pm 45^o]}\mathbf{C}_{[\pm 45^o]}(T)\cdot\mathbf{e}_{\text{free}}^{[\pm 45^o]}\right) \tag{8.8}$$

$$\mathbf{D}_{\text{torus}}(T)=\frac{1}{3}\sum_{\kappa=1}^{n}\left(\mathbf{C}_{[\varphi]_k}(T)\right)\left(z_k^3-z_{k-1}^3\right),\quad n=a_{[0^o]}+2a_{[\pm 45^o]} \tag{8.9}$$

and $\left(\mathbf{D}_{\text{torus}}(T)\right)^{-1}$ is the bending laminate compliance matrix of the toroidal shell as a function of temperature, z_k is the distance of a ply from the laminate mid-plane and *n* is the number of plies at the intersection and, as mentioned in Chapter 4, the laminate at the toroidal shell consists of [0^o] and [±45^o] plies, given by of $a_{[0^o]}$ and $2a_{[\pm 45^o]}$ respectively. The symbols $\mathbf{N}_{\text{junction}}^{\text{T}}$ and $\mathbf{M}_{\text{junction}}^{\text{T}}$ correspond to the thermal forces and moment vectors respectively at the sphere/intersection junction. The mechanical forces ($\mathbf{N}_{\text{junction}}$) and moments ($\mathbf{M}_{\text{junction}}$) vectors at the junction are given in Chapter 4. The approximation functions for the engineering properties $E_{11}^{\text{T}}, E_{22}^{\text{T}}$ and G_{12}^{T} and $\alpha_{11}^{\text{T}}, \alpha_{22}^{\text{T}}$ derived in Chapter 6 can be used to construct the strain curve over a specific temperature range.

The CTE of the overwrap at the spheres and intersection in the longitudinal and transverse directions is illustrated in Fig. 8-18. The CTE at the intersection is close to zero while the effect of temperature is negligible in the longitudinal direction, owing to the fact that mostly [0^o] layers were employed there. The CTE in the transverse direction varies from 11 to 18 [10^{-6} mm/mm^{o}C]. On the other hand, the CTE of the QI laminate at the sphere is 2 [10^{-6} mm/mm^{o}C] approximately in both the longitudinal and transverse directions.

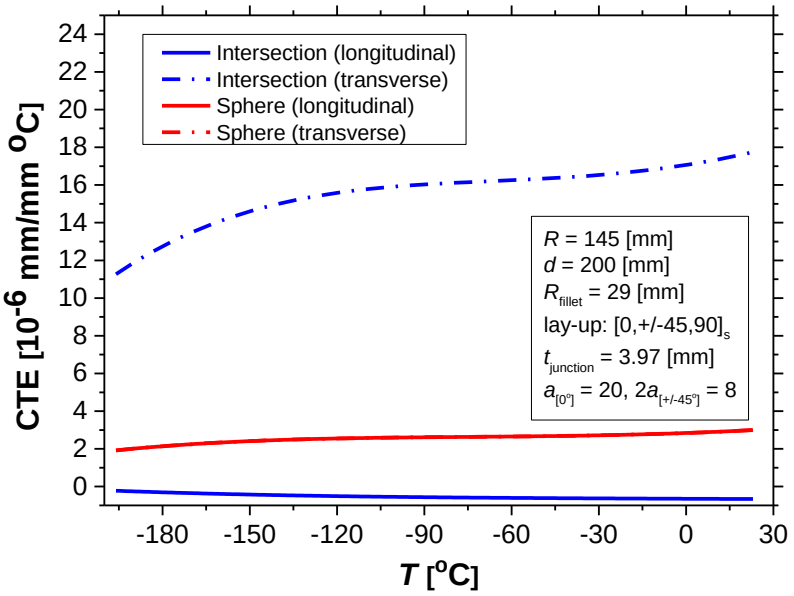

Fig. 8-18: Longitudinal and transverse CTE of the laminate at the intersection and spheres as a function of temperature.

Hoop strain at the spheres as a function of temperature is illustrated in Fig. 8-19 for two different locations: at the vapour region (FBG#15) and below-the-liquid level (FBG#16). A comparison between the results of the CLT, FE analysis and experimental recordings is hereby presented. The initial strain was assumed zero in this case and no strain from curing was taken into consideration. A non-linear relationship between meridional strain and temperature can be seen in both Fig. 8-19a and Fig. 8-19b.

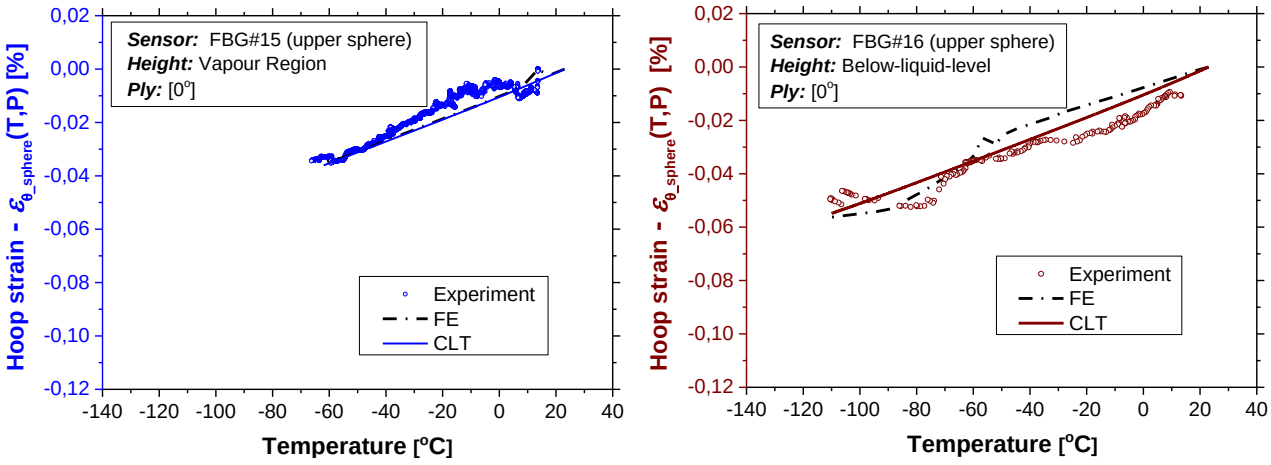

(a) **(b)**

Fig. 8-19: Correlation between hoop strain and temperature for the sphere at the a) vapour region (FBG#15) and b) below-the-liquid level (FBG#16).

Higher compressive strain values can be seen below the liquid level, which can be associated to the larger ΔT that the overwrap is subjected to. It was shown that the temperature effect for FBG#16 was not so strong below -70 [°C] approximately, owing to the stiffness increase of the overwrap at lower temperatures. The FE and experimental values of strain showed good agreement (average offset of 9.5 [%]) with a small offset for $-40 \leq T \leq 10$ [°C] (and a maximum offset of 19 [%] offset for -10 [°C]) for FBGs#15,16. On the other hand, CLT and experimental values had an average offset of 8.3 [%]. As a result, the accuracy of the approximation functions of Chapter 6 and FE model of Chapter 7 is verified.

The ply stresses in the principal material axes system at the spheres and at the intersections are derived by (Eq. (8.10)) and (Eq. (8.11)) respectively [7]:

$$\boldsymbol{\sigma}^{[k]}_{1,2\_\text{sphere}}\left(T,P\right)=\mathbf{T}_{[\varphi]_k}\cdot\mathbf{C}_{[\varphi]_k}(T)\cdot\boldsymbol{\varepsilon}^{[k]}_{\varphi,\theta\_\text{sphere}}\left(T,P\right) \tag{8.10}$$

$$\boldsymbol{\sigma}^{[k]}_{1,2\_\text{junction}}\left(T,P\right)=\mathbf{T}_{[\varphi]_k}\cdot\mathbf{C}_{[\varphi]_k}(T)\cdot\boldsymbol{\varepsilon}^{[k]}_{\varphi,\theta\_\text{junction}}\left(T,P\right) \tag{8.11}$$

The pressure allowable of the experimentally assessed multi-sphere as a function of varying ΔT is presented in Fig. 8-20. The effect of overwrap curing (prior to cryogenic operation) is also taken into consideration. The approach is based on the evaluation of ply stresses at the spheres (Eqs. 8.1-8.4,8.10) and the intersections (Eqs. 8.5-8.9,8.11) and applying the Hashin failure criterion (Eqs. 7.2-7.6) to check for first-ply failure (FPF) at the fiber or matrix [8]. The ply strength allowables in the parallel and transverse to fiber as well as the in-plane shear directions as a function of temperature are identified in Chapter 6. The curve depicted in Fig. 8-20 corresponds to FPF at the transverse direction to the fibers at the sphere.

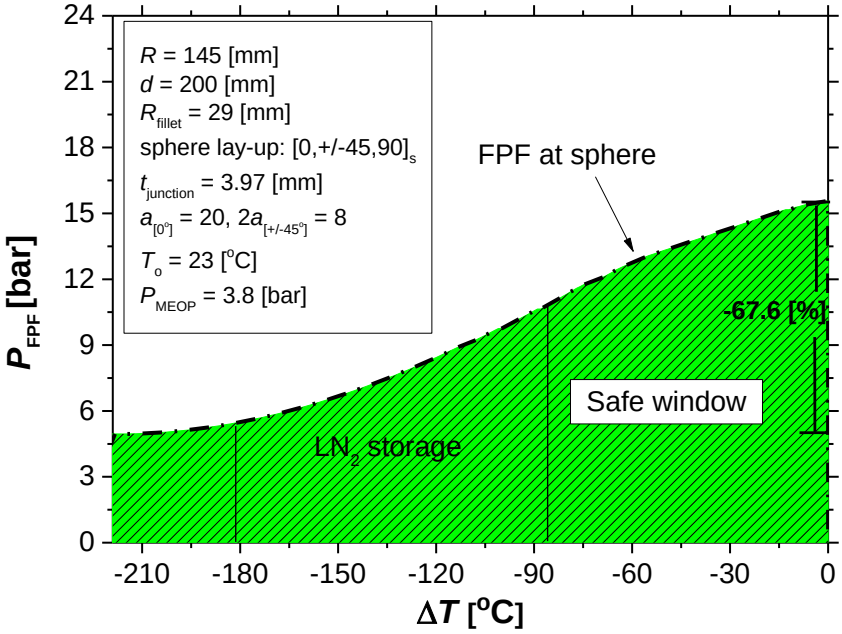

Fig. 8-20: Pressure allowable as a function of ΔT for the overwrap based on Hashin criterion.

The pressure allowable follows a sigmoidal trend (s-curve), owing to the nature of the $E(T)$ and $CTE(T)$ functions. A reduction of 67.6 [%] in the P_{FPF} value was obtained for ΔT = -219 [°C] compared to the P_{FPF} value at RT (ΔT = 0 [°C]), linked to the overwrap embrittlement at cryogenic temperatures.

8.4 Potential of Polymer Use in Cryogenic Environment

In this part the engineering properties of the polymeric liner material will be evaluated on the basis of avoiding damage during cryogenic chill-down. As seen in the experiment, the critical area for the liner is the central cylinder due to thermal restraint imposed by the CFRP overwrap. The range of the Young's modulus and CTE values of the liner material that will lead to an intact liner are identified below.

Initially the radial temperature distribution at the multi-layered tank wall at the central tube needs to be evaluated based on one dimensional heat rate equilibrium [9]. Knowing the radial temperature distribution at the liner and overwrap layers enables the derivation of stresses. The

equation below is used to calculate the hoop strain of the multi-layered tank wall and shows the effect of the material properties and temperature differences [10]:

$$\varepsilon_{\theta\theta\text{inter}} = \frac{A_{\text{liner}} E_{\text{liner}} a_{\text{liner}} \Delta T_{\text{inner}} (v_{\text{torus}} - 1) + A_{\text{UD}} E_{\text{torus}} a_{\text{torus}} \Delta T_{\text{out}} (1 - v_{\text{liner}})}{2[A_{\text{liner}} E_{\text{liner}} (v_{\text{torus}} - 1) + A_{\text{UD}} E_{\text{torus}} (1 - v_{\text{liner}})]} \tag{8.12}$$

$$A_{\text{liner}} = 2\pi R\,,\ \Delta T_{\text{inner}} = \frac{(\Delta T_1 + \Delta T_2)}{2}\,,\ \Delta T_{\text{out}} = \frac{(\Delta T_2 + \Delta T_3)}{2}$$

where ΔT_1 is the temperature change at the inner surface of the liner (ΔT_1 = -219 [^{o}C]) and ΔT_2 is the temperature change at the outer surface of the liner. The total stresses are calculated by [10]:

$$\begin{bmatrix} \sigma_{\text{liner\_in}} \\ \sigma_{\text{liner\_out}} \end{bmatrix} = \frac{E_{\text{liner}}}{1 - v_{\text{liner}}} \begin{Bmatrix} \varepsilon_{\text{hoop}} - a_{\text{liner}} \Delta T_1 \\ \varepsilon_{\text{hoop}} - a_{\text{liner}} \Delta T_2 \end{Bmatrix} \tag{8.13}$$

A maximum stress criterion is employed to check for liner failure at either the inner or outer surface:

$$\sigma_{\text{linerin}} = UTS_{\text{liner}}\,,\ \sigma_{\text{linerout}} = UTS_{\text{liner}} \tag{8.14}$$

The values of t, ΔT_1, ΔT_2 and UTS_{liner} of the liner at the experiment were used. A contour plot of the maximum liner Young's modulus (E_{liner}) and CTE (α_{liner}) -to avoid damage at the central hollow tube- is depicted below (Fig. 8-21). The blue curve corresponds to the inner (R_{in}) liner surface that is in contact with LN_2, while the black curve is associated with the outer liner surface (R_{out}) that is subjected to a thermal restraint by the overwrap during chill-down. It can be seen that the critical zone is the inner liner surface and this is where localized cracking occurred at the PA12 liner at the end of the cryogenic chill-down stage.

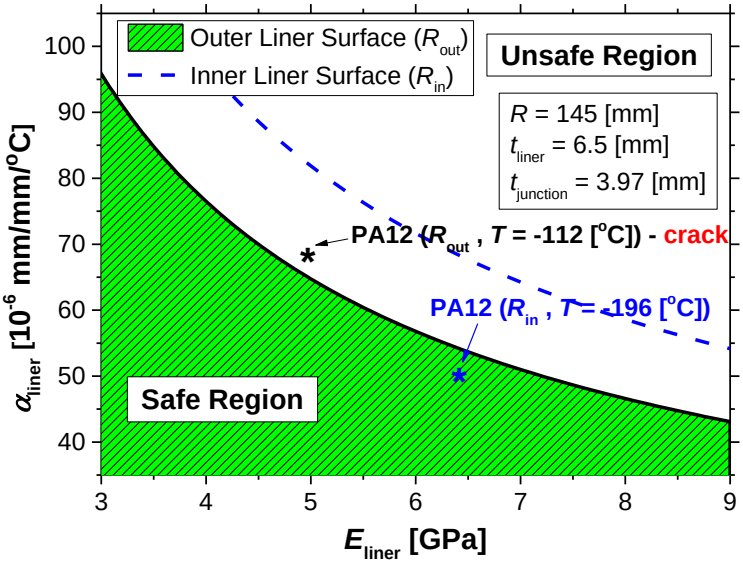

Fig. 8-21: Allowable liner CTE and Young's modulus to avoid damage at the cylinder throughout chill-down for the experimentally assessed geometry.

Consequently, a polymer that will meet the property requirements presented in Fig. 8-21, should be feasible for moulding at this complex shape, and be compatible with the curing cycle of the overwrap. Furthermore, it could potentially be employed as the liner material at the multi-sphere (at the experimentally assessed geometry) when subjected to LN_2 chill-down.

8.5 Concluding Remarks

The main goal of this chapter was to assess experimentally the mechanical performance of the type IV multi-cell tank at both room and cryogenic conditions. The tank was subjected to hydrostatic burst at ambient conditions and pressure cycling at cryogenic conditions. Strain monitoring (with the use of Digital Image Correlation-DIC and Fiber Bragg Gratings -FBGs) in combination with damage progression monitoring (with the use of Acoustic Emissions-AE) provided accurate measurements of the structural integrity state of the COPV. The results are compared with the findings of FE model based on progressive failure analysis (Chapter 7).

Throughout the hydrostatic pressure test, it was shown that the introduction of the right number of UD straps leads to damage onset being avoided in the intersections. Damage onset and evolution is characterized by a very localized behavior (at the sphere and next to the central tube) owing to faster strain accumulation linked to liner/overwrap contact at that region. Global failure is triggered by liner rupture and matrix cracking at the spheres near the central hollow cylinder, which verifies the FE findings of Chapter 7 with an offset of 23 [%] for the burst pressure value. A comparison between the FE of Chapter 7 and AE results on the evolution of damage showed a very good agreement (offset of 17.4 [%]) in the tank pressure window (P_{LPF} - P_{FPF}).

For the case of pressure cycling at a cryogenic temperature (with the use of LN_2), the different heat transfer mechanisms at the tank wall are identified. The obtained temperature profile and corresponding strain recordings over the multi-bubble tank surface verified the results of the FE analysis in Chapter 7. A non-linear relationship between strain and temperature is established, where higher compressive strain values are obtained below-the-liquid level due to larger ΔT that the overwrap. Strain recordings at the composite overwrap verified the accuracy of the approximation functions (with an average offset of 9.5 [%]) for *CTE*(T) and *E*(T) used in the FE model in Chapter 7. It is shown by using the CLT and approximation functions of Chapter 6 that the tank pressure allowable is decreasing in a sigmoid trend (s-curve) with decreasing temperatures. A reduction of 67.6 [%] in the P_{FPF} value is obtained at T = -196 [^{o}C] compared to the P_{FPF} value at ambient conditions.

It was shown that during chill-down of the tank, liner cracking was formed at the central hollow tub, due to CTE mismatch with the composite overwrap. However, liner cracking did not affect the structural integrity of the composite overwrap, and no pressure loss was observed. The required value range of Young's modulus (*E*) and CTE of the suitable polymer materials at cryogenic temperatures were also presented in this Chapter.

References

[1] I.G. Tapeinos, A. Rajabzadeh, D.S. Zarouchas, M. Stief, R.M. Groves, S. Koussios and R. Benedictus, 'Evaluation of the Mechanical Performance of a Multi-Cell Tank for Cryogenic Storage: Part II- Experimental Assessment', *International Journal of Hydrogen Energy*, **44**, 7, 3931-3943, 2019.

[2] J.B. Chang, 'Implementation Guidelines for ANSI/AIAA S-081: Space Systems Composite Overwrapped Pressure Vessels', 2003.

[3] CHATT Project, 'Final Report', 2015.

[4] H-Y. Chou, 'PhD Thesis: Damage analysis of composite pressure vessels using acoustic emission monitoring', RMIT University, Australia, 2011.

[5] G. Agrawal, J. Joseph, D.K. Agarwal and S.S. Kumar, 'Effect of insulation thickness on evolution of pressure and temperature in a cryogenic tank', *Proceedings of the 23rd National Heat and Mass Transfer Conference*, India, 2015.

[6] T. Habisreuther, E. Hailemichael, W. Ecke, I. Latka, K. Schöder, C. Chojetzki, K. Schuster, M. Rothhardt and R. Willsch, 'ORMOCER coated fiber-optic bragg grating sensors at cryogenic temperatures', *IEEE Sensors Journal*, **12**, 2012.

[7] I.M. Daniel and O. Ishai, 'Engineering mechanics of composite materials, (Second Edition) Oxford University Press, 2006.

[8] Z. Hashin, 'Failure Criteria for Unidirectional Fiber Composites', *Journal of Applied Mechanics*, **47**, 329-334, 1980.

[9] T.L. Bergman, A.S. Lavine, F.P. Incropera and D.P. Dewitt, ' Fundamentals of heat and mass tranfer', (Seventh Edition) John Wiley & Sons, 2011.

[10] A.C. Ugural, 'Stresses in beams, plates and shells, (Third Edition) CRC Press, 2010.

Chapter 9: Concluding Comments & Recommendations

9.1 Concluding Comments

The goal of this research was to increase the understanding of the behaviour of multi-spherical composite overwrapped pressure vessels (COPVs) and to examine their potential for use as cryogenic fuel tanks. The geometrical parameters that govern the design process of multi-spheres were identified. Following the design process, development and testing of these structures was performed, in order to evaluate their performance at the given thermo-mechanical loading regime.

The following conclusions are drawn from this Thesis:

- The geometrical variables that have the biggest influence on the volumetric efficiency of the multi-sphere are the i) sphere radius (R), ii) the dimensionless centroid distance (y) and iii) the number of cells in the axial (m_{cells}), transverse (n_{cells}) and height (p_{cells}) directions.

- The minimum multi-sphere weight can be obtained by minimizing the cross-sectional area of the UD straps at the intersections ($A_{UD} = t_{junction}s$). A minimum A_{UD} value for a given dimensionless centroid distance (y) value can be identified for a specific set of fillet radius (r), lamina angle ($\pm\varphi$) and ratio between [0^o] and [$\pm\varphi$] layers at the intersection ($i_{ratio} = a_{[0]}/2a_{[\pm\varphi]}$).

- A safe up-scale of the multi-sphere can be achieved for: $y = \{0.7, 1.4\}$ and $m_{cells} = \{6 , \infty\}$ and by following the strain compatibility principle owing to the fact that performance is nearly constant within these intervals.

- A stepwise linear inverse relationship is attained between performance (n_{PF}) and volumetric efficiency (V_{eff}) of the multi-sphere for increasing aspect ratio of the bounding box (a_{ratio} = box length/box width). Small a_{ratio} values lead to structural efficiency maximization, while large values result in the maximization of V_{eff}.

- The multi-sphere leads to a more lightweight and volumetrically efficient tank configuration when fitted within a prescribed box as compared to packed cylinders.

- An accurate stress prediction at the tank wall requires the evaluation of the temperature dependency of the properties of liner and overwrap materials through mechanical testing and approximation functions with a physical basis.

- The temperature profile at the tank contour is directly affected by the: i) the position of the liquid front, ii) the thickness of the frost layer at the outer surface and iii) the thermal properties of the liner and overwrap materials.

- The effect of in-plane shearing of 2D composite patches throughout the multi-sphere manufacturing process (draping) should be taken into account to accurately predict the stiffness distribution throughout the tank contour.

- Damage at the multi-sphere (due to internal pressure) can have a localized behaviour. It can be redirected from the intersections to the spheres by employing a minimum required number of UD straps at the intersections. The resulting location of first damage onset and ultimate failure is at the spheres next to the central hollow tube, since these are the points of first liner/overwrap contact owing to the gap formed from curing.

- The central hollow cylinder is the critical region at the multi-sphere throughout cryogenic chill-down and throughout testing (localized cracking was seen there). Polymer materials that can result in an intact liner throughout cryogenic operation have theoretically been identified.

- The overwrap maintained its structural integrity throughout cryogenic operation, which along with the volumetric efficiency and weight savings, lead to the conclusion that the multi-sphere can potentially be employed as a cryogenic fuel tank.

- The accuracy of the presented temperature dependency approximation functions was verified by the experimental results. Therefore these relationships can be utilized when modelling the behaviour of liner and overwrap under cryogenic chill-down or draining, at least for the materials employed in this Thesis.

9.2 Recommendations

9.2.1 UD Straps in Intersections

Throughout this work, the stress state at the sphere connecting areas (intersections) was derived analytically. It was shown that by employing a constant fillet radius and an interpolating spline the peak value of junction line forces is very similar; therefore for simplicity the multi-sphere analysis was based on a constant radius. However an interpolating spline can lead to curvature compatibility at the sphere/intersection junction point and a linear curvature and strain distribution as a function of intersection arc length. The use of UD straps following geodesic paths and ply drops at the intersections following an interpolations spline shape would lead to minimization of overwrap weight.

9.2.2 Integration within a Wingbox

The integration of the multi-sphere within a rectangular envelope and the potential of volumetric efficiency and performance enhancement -compared to cylindrical COPVs- was analyzed throughout this Thesis. However the integration within a curved space (e.g. a wingbox) -where the use of spheres with equal radii is no longer volumetrically effective- needs to be considered.

9.2.3 Experimental Assessment of Various Polymeric Liner Materials for Cryogenic Storage

In the present study, polyamide (PA12) was used as the liner material, owing to its low density, its good permeability characteristics, the fact that its melting temperature is above the curing temperature of the composite overwrap, and also because it is suitable for rotational moulding. The rotational moulding process is ideal for obtaining a multi-spherical hollow shell with uniform thickness. It was shown however that localized liner cracking occurred throughout cryogenic chill-down at the hollow cylinder due thermal restraints imposed by the overwrap. This did not affect the structural integrity of the overwrap and no pressure loss was recorded after

5 pressurization cycles. It is however important to prevent liner cracking from happening in future designs by the use of another plastic material. In this study a theoretical assessment of the required stiffness and CTE has been provided to avoid damage throughout chill-down. It is however important to experimentally assess the behavior of various polymers, in terms of strength and ultimate strain under biaxial loading and thermal expansion at cryogenic temperatures.

Acknowledgements

Firstly, I would like to express my sincerest gratitude to my daily supervisor (co-promotor) Dr. Sotiris Koussios for his continuous support and encouragement throughout this study. His scientific ideas/tips and insistence on manufacturing and testing composite-overwrapped multi-spherical demonstrators were extremely significant in terms of revealing their potential as cryogenic fuel tanks. It was very crucial that he allowed me all the freedom I could have asked for, to go after my ideas and initiate collaborations. His solid theoretical background, analytical thinking and rigorous professional attitude are an example to follow.

Secondly, I would like to thank my second supervisor Dr. Roger Groves for helping me finish this Thesis, especially during the last year of this study. His guidance and time management have been of prime importance.

I would also like to thank my promotor Prof. Rinze Benedictus for allowing me to pursue my dream of conducting doctoral research at the Structural Integrity & Composites Group at the TU Delft. His critical questions throughout our meetings have been helpful towards formulating the research questions of this study.

Special thanks to Gemma van der Windt for making everything run so smoothly from an administrative point of view (from my 1st day as a PhD candidate all the way to the PhD Defence). Chats with Gemma have always been very interesting, fun and encouraging.

I would like to take this opportunity to thank Dr. Dimitrios Zarouchas for a successful collaboration on the progressive failure of multi-spherical tank and the utilization of Acoustic Emission to study the damage progression when loaded under pressure. Additionally, I would like to thank PhD Candidate Aydin Rajabzadeh for coming all the way to Bremen, at the German Aerospace Center (DLR) with me to enable the use of Fiber Bragg gratings (FBGs) for strain sensing of the multi-spherical tank when loaded under cryogenic conditions. Furthermore, I would like to thank Victor Horbowiec for helping me prepare the tank for the testing campaigns.

Besides my thesis work, I would like to thank Kleopatra, Amber, Natasa, Petros, George, Sotiris, Giannis, Emma, Konstantinos, Theo, Jesus, Leon for being very good friends. My cousins Giannis, Athina and friends in Greece: Nikos, Giorgos Kyr., Giorgos Mag., Konstantinos, Stathis, Vangelis, Lilian, Theo, Konstantina, Artemis-you guys are a very important part of my life. Additionally, I would like to thank my colleagues: Giacomo, Pedro, Davide, Niels, Luis, Vincenzo, Antonio, Michiel, Nikos Koutras, Nikos Ele (Nick), Maro, Jarret, Lei, Wandong, Adrian, Adrian (the Viking), Eirini, Chirag, Nicola, Megan, Julian, Freek, Zahid, Morteza, Maria, Lucas, Fab, Romina, John-Alan, Leila and Otto for creating a nice and warm working environment as well as tolerating my dorky jokes. I would like to thank Dr. Nikolaos Alexopoulos for believing in me and introducing me to the world of composite materials.

I want to thank my Monicaki for being the greatest source of lightness and craziness. You have helped me to look at the greater picture of things and not caring too much about everything.

Finally, I would like to thank my parents for always being there for me and raising me in a very loving environment. Thank you for teaching me things like being ambitious, optimistic and never giving up. My sousou is the best sister anyone can ask for – it is scientifically proven that sisters help you become a better person .

About the Author..

Ilias Tapeinos is a Greek man (Έλληνας/Ellinas) born in the beautiful city of Athens in the August heat of 1987, one month after Greece winning the European Championship in Basketball. After spending his care-free teenage years in Athens College high school, in 2005 he went on to study Industrial Engineering (BSc) at the University of the Aegean and in 2010 Applied Mechanics (MSc) at the National Technical University of Athens. Over the years he developed a weird passion for composite materials and their applications in extreme environments that led him initially to the Institute of Composite Materials (Kaiserlautern, Germany) and eventually TU Delft at a land far-far away, the Lowlands (a.k.a. Netherlands).

Little did he know that he would enjoy working so much on cryogenic composite over-wrapped fuel tanks for the aerospace sector (for the CHATT project) and being in TU Delft (with the well expected ups and downs in the work/life of a PhD). He decided that he wasn't ready to leave the place and after a discussion he had with his supervisor they both decided that he would stay longer to study the behaviour of thick-walled pressure vessels during manufacturing and operation (Groot Composiet project). He realized the following three things while being in Delft: i) thinking abstract and pursuing the completion of complex ideas (without sticking too much to what's out there) is crucial for research, ii) you should never stop believing in yourself no matter what and that iii) life should not be taken too seriously.

The picture is taken at the basement of the Aerospace laboratory, throughout the draping of one of the multi-spherical tank demonstrators (before that poor thing was burst tested-all in the name of science).

List of Publications

Journals:

1) I.G. Tapeinos, S. Koussios, R.M. Groves and R. Benedictus, 'On the Volumetric Efficiency and Performance of Composite Multi-spheres for Cryogenic Storage', (to be submitted).
2) I.G. Tapeinos, A. Rajabzadeh, D.S. Zarouchas, M. Stief, R.M. Groves, S. Koussios and R. Benedictus, 'Evaluation of the Mechanical Performance of a Composite Multi-Cell Tank for Cryogenic Storage: Part II- Experimental Assessment', *International Journal of Hydrogen Energy*, **44**, 7, 3931-3943, 2019.
3) I.G. Tapeinos, D.S. Zarouchas, O. Bergsma, S. Koussios and R. Benedictus, 'Evaluation of the Mechanical Performance of a Composite Multi-Cell Tank for Cryogenic Storage: Part I-Tank Operating Window based on Progressive Failure Analysis', International Journal of Hydrogen Energy, **44**, 3917-3930, 2019.
4) I.G. Tapeinos, S. Koussios, R.M. Groves, 'Design and Analysis of a Multi-Cell Subscale Tank for LH2 Storage', *International Journal of Hydrogen Energy*, **41**, Issue 5, 3676-3688, February 2016.

Conferences:

1) I.G. Tapeinos, D.S. Zarouchas, O. Bergsma, S. Koussios and R. Benedictus, 'Evaluation of the Mechanical Performance of a Multi-Cell Composite Overwrapped Pressure Vessel for Liquid Hydrogen Storage', *31st ASC Conference*, Virginia, 2016.
2) I.G. Tapeinos, S. Koussios and R. Benedictus, 'Presentation of a Novel Conformable COPV: the multi-sphere', *CPV Symposium*, Berlin, 2015.
3) I.G. Tapeinos, S. Koussios, R.M. Groves and R. Benedictus, 'Design and Analysis of a Multi-cell Tank for Liquid Hydrogen Storage', 20th *ICCM Conference*, Copenhagen, 2015.
4) I.G. Tapeinos, S. Koussios, R. Benedictus, 'Experimental Study on Various Liner Materials for Cryogenic Storage', 5th *ICSAAM Conference*, Kos, 2013.

Propositions

- The minimum weight at the multi-sphere can be obtained by strain compatibility conditions between spheres and intersections and by minimizing the cross-sectional area of the UD straps.

- The multi-sphere is a more lightweight and volumetrically efficient configuration for cryogenic storage when fitted within a prescribed box, compared to arrays of cylindrical composite-overwrapped pressure vessels.

- The effect of in-plane fiber shearing should always be taken into consideration in the manufacturing of complex double-curved structures.

- It is crucial to perform dimensionless studies at a new design and to know the variables interval where it can be up-scaled.

- Cryogenic propellant storage is the future in the aerospace sector.

- A patriarchal society is negative for both men and women.

- Cold climates favour social and financial development.

- Like in other sectors, formalities are a drag on science too.

- A time-lapse of the last year of a PhD could be the video-clip of ‘Under pressure’ by Queen.

- In the future attending an Ajax football match will take longer than commuting from Europe to Australia.

In the field of cryogenic propellant storage the fuel tank should be designed in such a way, that it makes the best possible use of the available space within the aircraft (under a minimum weight).

Spheres have the minimum surface area for a given volume, they result in the minimization of passive heat in the tank and fuel boil-off, thus reducing the weight penalty associated with required thermal insulation thickness in cryogenic environments. Additionally, they can lead to weight savings associated with equal membrane strains, when subjected to uniform pressure.

Therefore a vessel configuration that incorporates partially merged spheres overwrapped with uni-directional (UD) carbon fiber straps applied at the merging points would lead to a lightweight tank structure with high volumetric efficiency.

The aim of this Dissertation is to increase the understanding of the behaviour of multi-spherical composite overwrapped pressure vessels (COPVs) with a polymeric liner under thermo-mechanical loading. This will enable the potential of multi-spherical COPVs to be examined for use as cryogenic fuel tanks.